Optical Properties of Quasiparticles in Monolayer and Bilayer TMDCs

vorgelegt von
M. Sc.
Sophia Helmrich
ORCID: 0000-0002-8737-2370

von der Fakultät II - Mathematik und Naturwissenschaften
der Technischen Universität Berlin
zur Erlangung des akademischen Grades

Doktor der Naturwissenschaften
Dr.rer.nat.

genehmigte Dissertation

Promotionsausschuss:

Vorsitzende: Prof. Dr. Kathy Lüdge
Gutachterin: Prof. Dr. Ulrike Woggon
Gutachterin: Prof. Dr. Janina Maultzsch
Gutachterin: Prof. Dr. Ursula Wurstbauer

Tag der wissenschaftlichen Aussprache: 02.03.2020

Berlin 2020

Abstract

In this thesis, we investigate the optical properties of excitonic quasiparticles in different transition metal dichalcogenides (TMDCs). These novel two-dimensional (2D) semiconductor materials exhibit remarkable mechanical, optical and electronic properties and feature an additional valley degree of freedom. Due to their atomically thin nature, excitons form as quasiparticles with high binding energies in monolayers (ML) and bilayers (BL) of $MoSe_2$ and $MoTe_2$. We combine photoluminescence (PL), pump probe (PP) and 2D coherent spectroscopy (2DCS) to reveal and quantify valley polarization properties and the interaction of phonons with exciton, trion and biexciton.

ML TMDCs are direct semiconductors, whereas BLs in most TMDCs are indirect and less studied. We perform 2DCS measurements of the BL $MoSe_2$ and find a dephasing time for electrons of 20 fs and a scattering of holes of 400 fs, forming an indirect exciton in $MoSe_2$. Moreover, we observe an intra-layer biexciton signature. The BL of $MoTe_2$, which is yet little investigated in literature, shows a bright emission like the ML. We perform a comprehensive spectroscopic study of ML and BL $MoTe_2$ and analyze the lineshape of temperature-dependent PL spectra, comparing ML and BL. The small difference in lineshape can be traced to symmetry and well width, confirming a direct excitonic transition in the BL, unlike in other TMDCs. We further disentangle the homogenous and inhomogeneous parts of the PL linewidth. The inhomogeneous linewidth predicts an inter- and intra-layer trion in the BL separated by 2.2 meV. In general, the trion state in the BL is confirmed by the mass-action law. We deduce a connection between the homogenous linewidth broadening and the phonon-limited mobility, considering acoustical as well as optical phonons. This results in a high acoustical phonon limited mobility of 6000 cm^2/Vs (2000 cm^2/Vs) and 4300 cm^2/Vs for the ML exciton (trion) and BL exciton. The optical phonon limited mobility at room temperature is found to be 300 cm^2/Vs and 150 cm^2/Vs in ML and BL which are the highest values found so far for TMDCs.

Exciton and trion resonances in TMDCs allow for optical manipulation of the valley degree of freedom. We find that resonant excitation of the exciton in PP results in a high negative polarization degree of -65 % which is lost within 1 ps due to electron-hole exchange interactions and bandgap renormalization in $MoTe_2$. The trion is less influenced by these effects resulting in a polarization of 95 % immediately after excitation, depolarizing within 3 ps. Both depolarization timescales are consistent with the fast decay of excitons and trions due to defect-assisted recombination. During the trion formation time of 1.5-2.5 ps, we measure a polarization of about 30 % in ML $MoTe_2$. These are the first observations of valley polarization in $MoTe_2$. Off-resonant excitation results in a non-zero polarization of the PL when exciting higher excitonic states. Phonon assisted cascade processes conserve spin and valley, where the electron transfer is dominated by spin- (valley-) conserving scattering at low (high) temperatures.

Zusammenfassung

In dieser Arbeit studieren wir die optischen Eigenschaften exzitonischer Quasiteilchen in Übergangsmetall-Dichalcogeniden (TMDCs). Dieser zweidimensionale (2D) Halbleiter hat bemerkenswerte mechanische, optische und elektronische Eigenschaften, sowie einen weiteren Valley-Freiheitsgrad. TMDCs sind nur einige Atomlagen dick, und ihre Quasiteilchen weisen hohe Bindungsenergien in Mono- (ML) und Bilagen (BL) auf. Durch die Kombination von Photolumineszenz (PL), Pump-Probe (PP) und 2D kohärenter Spektroskopie (2DCS) untersuchen und quantifizieren wir die Wechselwirkung von Phononen mit Exzitonen, Trionen und Biexzitonen.

ML TMDCs sind direkte Halbleiter, wohingegen BL in den meisten TMDCs indirekt und wenig untersucht sind. Wir führen 2DCS Messungen am $MoSe_2$ BL durch und untersuchen den Transfer von direktem zu indirektem Exziton, wobei das Elektron innerhalb von 20 fs dephasiert und das Loch innerhalb von 400 fs. Außerdem beobachten wir Anzeichen von Biexzitonen. $MoTe_2$ BL wurde bisher wenig untersucht und zeigt eine strake Lumineszenz ähnlich zum ML. Wir führen eine umfassende spektroskopische Studie an ML und BL $MoTe_2$ durch und analysieren temperaturabhängige PL-Linienformen von ML und BL. Wir begründen kleine Veränderungen der BL Linienbreite im Vergleich zum ML durch Veränderungen in der Symmetrie und Schichtdicke. Dies bestätigt eine direkte Bandlücke in $MoTe_2$ BL, welche in anderen TMDCs nicht beobachtet wird. Die PL Linienbreite wird in den homogenen und den inhomogenen Anteil zerlegt. Durch die Analyse des inhomogenen Anteils erwarten wir zwei 2.2 meV energetisch von einander entfernte Trionen: Inter- und Intralagentrionen. Der Trionenzustand an sich wird durch das Massenwirkungsgesetz bestätigt. Homogene Linienbreite und Mobilität hängen zusammen, wobei wir die Einflüsse akustischer und optischer Phononen betrachten. Wir bestimmen hohe, durch akustische Phononen begrenzte, Mobilitäten von 6000 (2000) cm^2/Vs und 4300 cm^2/Vs für das Exziton (Trion) der ML und BL. Die durch optische Phononen limitierten Mobilitäten bei Raumtemperatur liegen bei 300 cm^2/Vs und 150 cm^2/Vs für ML und BL. Dies sind die höchsten gemessenen Mobilitäten in TMDCs.

Der Valley-Freiheitsgrad der Quasiteilchen kann optisch manipuliert werden. Eine resonante Anregung der Exzitonen in PP erzeugt eine Polarisation von -65 %, welche in 1 ps durch Elektron-Loch-Wechselwirkung und Bandlückenrenormierung depolarisiert. Die Trionen sind weniger von diesen Mechanismen betroffen und zeigen eine Polarisation von 95 % direkt nach der Anregung, welche in 3 ps depolarisiert. Defektassoziierte Rekombination zeigt vergleichbare Zeitskalen. Während der Trionformation messen wir etwa 30 % Polarisation in $MoTe_2$ ML. Dies sind die ersten Polarisationsmessungen an $MoTe_2$. Wir messen ebenfalls eine Polarisation, wenn wir höhere exzitonische Zustände anregen. Deren Valley- und Spinzustände werden durch phononische Kaskadenprozesse bis in den Grundzustand erhalten, wobei Spin (Valley) bei tiefen (hohen) Temperaturen erhalten wird.

"A lot of people experience the world with the same incredulity as when a magician suddenly pulls a rabbit out of a hat which has just been shown to them empty. In the case of the rabbit, we know the magician has tricked us. What we would like to know is just how he did it. But when it comes to the world it's somewhat different. We know that the world is not all sleight of hand and deception because here we are in it, we are part of it. Actually, we are the white rabbit being pulled out of the hat. The only difference between us and the white rabbit is that the rabbit does not realize it is taking part in a magic trick. Unlike us. We feel we are part of something mysterious and we would like to know how it all works."

-Jostein Gaarder- Sophie's World: A Novel About the History of Philosophy

Contents

Abstract iii

Zusammenfassung v

1 Introduction 1

2 A brief overview about concepts and methods 3

2.1 The Quasiparticle Zoo . . . 4

2.1.1 Exciton . . . 8

2.1.2 Trion . . . 10

2.1.3 Biexciton . . . 11

2.1.4 Phonon . . . 12

2.2 The secrets of transition metal dichalcogenides . . . 15

2.2.1 Inversion symmetry breaking . . . 15

2.2.2 Spin-orbit coupling and dark and bright quasiparticles . . . 16

2.2.3 Optical selection rules . . . 18

2.2.4 Direct and Indirect optical transitions in ML and BL . . . 20

2.3 How to investigate quasiparticles experimentally . . . 23

2.3.1 Preparing a sample . . . 23

2.3.2 Step one: Photoluminescence spectroscopy . . . 25

2.3.3 Step two - Two Color Pump Probe Spectroscopy . . . 31

2.3.4 Step three - Two Dimensional Coherent Spectroscopy in Austin . . . 33

3 Exciton-phonon coupling in mono- and bilayer $MoTe_2$ 35

3.1 Laser light on - Here comes the ML and BL emission . . . 36

3.1.1 Defect peak analysis . . . 37

3.1.2 Presence of a trion in the BL . . . 38

3.2 Investigating phonons and collecting hints for direct BL emission . . . 42

3.2.1 Which process is shifting the emission energy?-Phonons? . . . 43

3.2.2 Phonons also broadens the linewidth . . . 47

3.2.3 Thermal quenching of emission area by phonons . . . 51

3.2.4 Connecting hints for direct BL emission . . . 54

4 Phonon-limited Mobility in $MoTe_2$ 55

4.0.1 Introductory remarks . . . 56

4.1 The Gaussian linewidth - investigating inhomogeneity . . . 56

4.1.1 Which is the main trion in the ML? . . . 58

4.1.2 Which is the main trion in the BL? . . . 60
4.2 The Lorentzian linewidth and its connection to transport properties . . . 62
4.2.1 Intrinsic broadening and lifetime . . . 63
4.2.2 Quasiparticle coupling to phonons and deformation potentials . . . 64
4.2.3 Transport of carriers . . . 66
4.2.4 Acoustical phonon limited mobility and relaxation time . . . 67
4.2.5 Optical phonon limited mobility and relaxation time . . . 70

5 Valley polarization of $MoTe_2$ 73
5.0.1 Polarization Review . . . 74
5.1 Identification of higher excitonic states . . . 76
5.1.1 Experimental observation of higher excitonic states . . . 76
5.1.2 Theoretical Considerations . . . 79
5.1.3 Connecting theory and experiment . . . 80
5.1.4 Temperature dependence of higher excitonic states . . . 82
5.2 The transfer of valley polarization . . . 84
5.2.1 No polarization from the bilayer . . . 85
5.2.2 Polarization in monolayer - Spin or valley flip . . . 85
5.2.3 The degree of trion polarization . . . 92

6 Exciton and trion formation, decay and polarization dynamics in $MoTe_2$ 95
6.0.1 Introductory Remarks . . . 96
6.1 Decay- and formation time of exciton and trion . . . 98
6.1.1 The mismatch of exciton amplitude and phase decay . . . 98
6.1.2 Trion formation and decay . . . 102
6.2 Degree of polarization of exciton and trion for near-resonant excitation . . . 106
6.2.1 Bandgap renormalization effect in pump probe measurements . . . 106
6.2.2 High degree of valley polarization in the trion . . . 108

7 Coherent exciton dynamics and dephasing in mono- and bilayer $MoSe_2$ 113
7.0.1 Why and how to investigate the indirect transition in bilayer $MoSe_2$ . . . 114
7.1 Dephasing time in ML and BL $MoSe_2$ . . . 116
7.1.1 The second feature in 2DCS spectra of the BL . . . 118
7.1.2 Valley vs. layer polarization in ML and BL $MoSe_2$ . . . 120
7.2 Depopulation in ML and BL $MoSe_2$ . . . 122

8 Summary 125

Publications 131

1 Introduction

In 1931, the Russian scientist Yakov Ilich Frenkel discovered the exciton as "excitation waves" in a crystal [42]. Since then, many properties of this quasiparticle have been investigated and it is well known that an exciton is a Coulomb bound electron-hole pair localized in a crystal [31]. Later in 1958, Murray A. Lampert theoretically proposed the trion and biexciton as "effective-mass-particle complexes", composed of electrons and holes in addition to the exciton [86]. Properties of excitons, trions, and biexcitons have been intensively investigated in many materials, in particular in quantum wells [29, 40, 103, 132, 136, 163, 152]. Excitons are important from an application point of view as their emission enables a deep understanding of the underlying material properties. We use the information contained in the excitonic emission to investigate the properties of two-dimensional transition metal dichalcogenides (TMDCs).

TMDCs are a novel two-dimensional material class supporting excitons with high binding energies [99, 100, 101, 137, 159, 162, 164]. The material in its monolayer (ML) limit has only a few atom layer thickness ($\sim$0.5 nm) and shows binding energies in the range of hundreds of meV for excitons and tens of meV the trions and biexcitons. Most TMDCs emit in the visible spectral range, showing a direct bandgap in the ML limit, and an additional degree of freedom called valley polarization due to the direct excitonic transition emerging at the K/K' points of the Brillouin zone, rather than at the Γ point. They are promising materials to build opto- and valley-tronic devices. By stacking MLs, one can even extend the possibilities for application as in this case the bandgap energy can be adjusted by the twist angle. Most TMDCs MLs have been extensively studied in the recent literature, but it is necessary to understand more-layer systems in particular bilayers of TMDCs. Molybdenum ditelluride ($MoTe_2$) [43, 75, 89, 134, 141, 193] extends the energy range of the TMDCs to the technologically important near-infrared region, promising novel device applications. In particular its infrared bandgap energy makes $MoTe_2$ difficult to study, many laboratories are not equipped for time-resolved experiments in the infrared spectral range. Our group is specialized in time-resolved optical spectroscopy in the infrared, in particular on technologically relevant semiconductor materials. The technical equipment and general expertise contribute well to tackle the yet little studied $MoTe_2$. There are several open questions which we will explore and answer in the cause of this thesis.

An understanding of TMDC bilayers is a necessary step in the investigation of stacked MLs (homo- and heterostructures). To the best of our knowledge, ultrafast coherent dynamics of the bilayer have not been studied in TMDCs. As reference sample we use the $MoSe_2$ BL with its indirect excitonic transition and ask: **which ultrafast dynamics and dephasing processes are observable on the BL TMDCs?**

From the literature it is known that the BL of the infrared $MoTe_2$ shows a bright emission [89,

134]. Theoretical calculations have not been able to unambiguously predict its band alignment [200, 82]. So we ask: **Does the BL of $MoTe_2$ feature a direct excitonic transition?**

By assuming a direct excitonic transition in the BL of $MoTe_2$, it is evident to ask whether one or more trion state exists. The only trion observed in BL so far is in the W-based TMDCs [67]. Refs. [89, 134, 43] observe an additional peak in the BL $MoTe_2$, the nature of which has not yet been definitively established, so: **Is there a trion in BL $MoTe_2$?**

Excitons and trions are the carrier of information in opto-electronics. Materials with high mobility are needed for the applications in devices. Theoretical publications predict high mobility values for $MoTe_2$ of $3000 - 10000$ cm^2 V^{-1} s^{-1} [60, 204] which would be the highest mobility in the TMDCs. We clarify experimentally: **Do exciton and trion mobilities in $MoTe_2$ approach the theoretical limit?**

In addition to the degree of freedom based on excitons and trions in opto-electronics, TMDCs show the so-called valley degree of freedom. Valley is coupled to spin and carries information, as one can selectively excite individual valleys by circularly polarized light. Molybdenum disulfide (MoS_2) shows a high polarization degree [100, 173], a reduced value is found in molybdenum diselenide ($MoSe_2$) [74, 173] and predictions for $MoTe_2$ are even lower [8], though for $MoTe_2$ an experimental observation of valley polarization is still needed. **Is there a measurable valley polarization degree in $MoTe_2$?**

By changing the excitation energy from resonant to off-resonant excitation we excite higher excitonic states [11, 28, 104] even beyond the electronic bandgap which have as far as we know not been invetigated in literature. So the question rises: **Can we measure a polarization of higher excitonic states?**

It is known that the valley polarization is lost within several picoseconds in common TMDCs [159]. Except for a radiative excitonic decay time of 3 ps [134], timescales of exciton and trion depolarization and depopulation have to the best of our knowledge not been studied in $MoTe_2$, so: **Which processes determine the decay dynamics of excitons and trions in $MoTe_2$?**

All in all, this thesis will answer these questions (and some more) and, thus, deliver a deeper understanding of TMDCs exciton, trion, biexciton, phonon interaction and dynamics. We start with a brief introduction of TMDCs in chapter 2 followed by an analysis of temperature-dependent photoluminescence spectra, band parameters and transport properties in chapter 3 and 4. In chapter 5 we extend the analysis to polarization-degree-resolved measurements by off-resonant excitation. By performing pump probe measurements in chapter 6, we investigate the resonant degree of polarization and the fast decay processes. In chapter 7 we close with ultrafast coherent spectroscopy measurements of $MoSe_2$ ML and BL. Finally, we summarize our results in chapter 8.

2 A brief overview about concepts and methods

In this chapter we briefly introduce properties of semiconductors in general, transition metal dichalcogenides in particular and the measurement techniques to investigate this class of materials optically. In the first section, we introduce the Hamilton formalism for electrons moving in a semiconductor under the influence of its periodic lattice potential. Furthermore, the energy band structure, bandgap and localization of quasiparticles will be deduced and the concept of exciton, trion, biexciton and phonon quasiparticles is introduced. We combine exciton- and trion-photon coupling and extract first statements on exciton-phonon coupling. As this thesis focusses on transition metal dichalcogenides, all defined concepts are applied to our class of material.

In the second section, we introduce the particular material properties of transition metal dichalcogenides. We investigate the inversion symmetry breaking/restoring of transition metal dichalcogenides depending on the number of layers. Inversion symmetry has a significant influence on the possibility to define this material optically. Binary selection rules for the high symmetry points of the Brillouin zone are established. Due to a pronounced spin-orbit coupling in transition metal dichalcogenides, the selection rule in momentum space is coupled to spin at the high symmetry points. Finally, the character of quasiparticle transitions is clarified theoretically, i.e. direct or indirect transition as a function of layer number. Especially molybdenum ditelluride shows an ambivalent behavior.

The last section deals with the fabrication and optical characteristics of the samples. Measurement techniques for the investigation of quasiparticles in transition metal dichalcogenides are introduced, namely photoluminescence, two-color pump probe, and two-dimensional coherent spectroscopy which yield complementary information on carrier dynamics and energy level structure. Especially position and polarization control due to the small size of the samples and the binary selection rule are important to establish.

2.1 The Quasiparticle Zoo

In this section we clarify the definition of a semiconductor in general and introduce the lattice, energy bands and localization of quasiparticles. Then we extract basic properties of the quasiparticles like group velocity, effective mass and wave vector. For the general description of semiconductors, we follow Ref. [7] and Ref. [31]. As this thesis focusses on some of the remarkable properties of transition metal dichalcogenides (TMDCs), in this introduction, we directly apply the general assumptions to the special case of TMDCs. By combining this general introduction with a summary of the current research we, thus, introduce TMDCs in the context of classical semiconductors.

In principle semiconductors discussed in this thesis are solids with a crystalline structure, that means an arrangement of the molecules in a lattice. The lattice is a periodic array of points in space. Each semiconductor can be categorized through their lattice structure in three dimensions. In this thesis, we concentrate on the hexagonal honeycomb (2H) lattice of TMDCs, where the lattice constants (the magnitudes of the axis of the primitive unit cell $\vec{a}$, $\vec{b}$, and $\vec{c}$) a and b are equal and differ from c. The lattice constants for $MoTe_2$ and $MoSe_2$ are collected in Tab. 2.1.

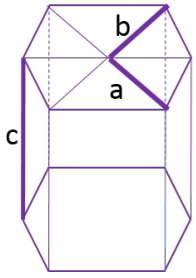

Fig. 2.1: Sketch of the hexagonal lattice.

Table 2.1: Lattice constants for TMDCs [138].

	a, Å	c, Å
$MoTe_2$	3.5	13.9
$MoSe_2$	3.3	13.0

TMDCs are layered semiconductors consisting of transition metals (Molybdenum (Mo), Tungsten (W)) and chalcogenide atoms (Sulfur (S), Selenide (Se), Telluride (Te)) arranged in atom layers. One layer of transition metal atoms is sandwiched between two layers of chalcogenide atoms covalently bonded to each other as illustrated in Fig. 2.2. Each transition metal has six nearest chalcogenide neighbors and each chalcogenide atom has three nearest transition metal atoms forming p-d hybridized transition metal-chalcogenide bonds [6]. We call one of these structures a monolayer (ML). By adding a second one we get a so-called bilayer (BL) consisting of two ML bound by van der Waals interactions. Stacking more and more layers together, we obtain a three-dimensional bulk crystal in the large number of layer limit. The bond between the layers is mechanically not very strong, thus, one can simply isolate single layers, as discussed in section 2.3.1.

Electrons can move in these lattices and their movement is described by the Schrödinger equation $H\psi(r) = E\psi(r)$, where the Hamiltonian is $H = H_0 + V(r) = -\frac{\hbar^2\nabla^2}{2m} + V(r)$ and $V(r)$ is a periodic potential with respect to the periodicity of the crystal structure. Plane wave e^{ikr} wave functions solve the unperturbed (i.e. the free electron) Schrödinger equation with

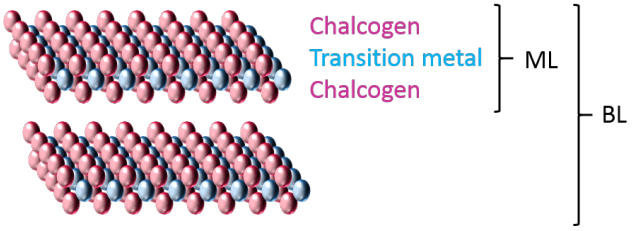

Fig. 2.2: Sketch of TMDC monolayer and bilayer.

an unperturbed energy eigenvalue of $E_0 = \frac{\hbar^2 k^2}{2m}$. To accommodate the potential formed by the crystal atoms, we can extend the solution in terms of perturbation theory. Therefore, we assume that the wave function is a Fourier series approximation to periodic boundary conditions $\psi(r) = C(k)e^{ikr}$. Now, let G (G_0) be the reciprocal lattice vector (constant) which is the Fourier transformation of the lattice vector (constant) and assume that each wavevector k only couples to those other wavevectors k' that differ by reciprocal wave vector G, such that

$$\psi_k(r) = \sum_G C(k-G)e^{i(k-G)r} = e^{ikr}u_k(r). \tag{2.1}$$

That means the movement of an electron in a lattice can be described by a plane wave and a periodic function factor $u_k(r)$, as introduced in the Bloch theorem and $\psi_k(r)$ is the *Bloch function*. The resulting Schrödinger equation reads: $\left(H_0 + \sum_G V_G e^{iGr}\right)\psi_k(r) = E^k\psi_k(r)$, where the (zero order) energy eigenvalue is ($E_0^k = \frac{\hbar^2 k^2}{2m}$)

$$E_k = E_0^k + V_0 + \sum_G \frac{|V_G|^2}{E_0^k - E_0^{k-G}}. \tag{2.2}$$

The solution has a degeneracy at $E_0^k = E_0^{k-G}$ satisfying the Bragg condition for electrons $k\cdot(G_0/2) = |G_0/2|^2$. This results in plane waves with wavevector $k = G_0/2$ forming periodically as a function of the crystal structure. The space spanned by these planes in wavevector space is called Brillouin zones. The first Brillouin zone (BZ) of a hexagonal lattice as found in TMDCs

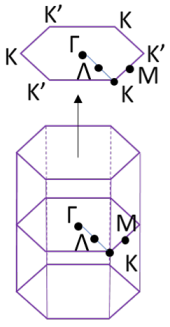

Fig. 2.3: Sketch of the hexagonal three dimensional Brillouin zone (BZ) and projection to two dimensional BZ, with high symmetry points Γ, K, Λ, and M.

[6] is shown in Fig. 2.3. We indicate the high symmetry points which are the most relevant for TMDCs layers, as investigated in section 2.2. The edges of the BZ must follow the Bragg condition. Therefore, the degeneracy in equation 2.2 has to be investigated in detail at the BZ boundary, where $E_0^k = E_0^{k-G_0}$ and we obtain

$$E^k = V_0 + \frac{1}{2}\left(E_0^k - E_0^{k-G_0} \pm \left[\left(E_0^k - E_0^{k-G_0}\right)^2 + 4|V_{G_0}|^2\right]^{1/2}\right) = V_0 \pm 2|V_{G_0}|.$$

The two energy eigenvalue solutions are always separated in energy by at least $2|V_{G_0}|$ creating a separation of energy bands. For intermediate energy, no electrons are allowed, thus, forming a forbidden energy gap or bandgap at the degeneracy points $1/2\ G_0$ (i.e. one half of the reciprocal lattice constant) defining the boundaries of the Brillouin zone. The associated bandgap has a bandgap energy $E_g = 2|V_{G_0}|$. The magnitude of the bandgap is material characteristic for each semiconductor and depends on certain environmental factors, like temperature and excitation intensity. We name the band energetically above or below the bandgap conduction band (CB) or valence band (VB), respectively. In addition to temperature and excitation intensity, the bandgap of TMDCs depends mainly on the number of layers, and the atomic weight of the chalcogenide atom. Exemplarily, the optical bandgap shrinks from 1.90 eV in MoS_2 [101, 162] and 1.55 eV in $MoSe_2$ [171] in the visible range down to 1.10 eV in $MoTe_2$ [141] in the near infrared at room temperature. Fig. 2.4 shows electronic band structure calculations of ML $MoTe_2$ (a), BL $MoTe_2$ (b). The bandgap energy decreases with increasing atomic weight and increasing number of layers.

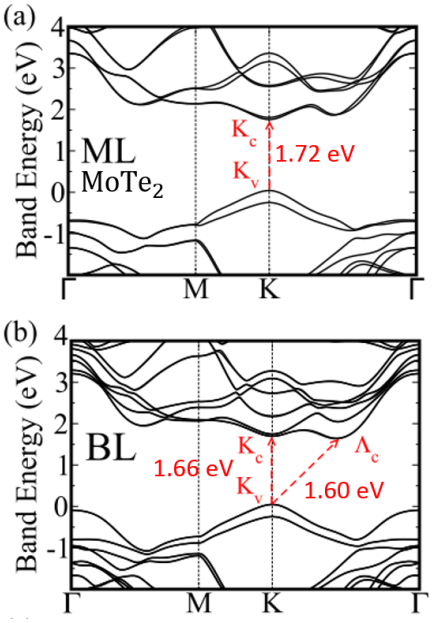

Fig. 2.4: Electronic band structure calculations of $MoTe_2$ (a+b). Reprinted (Fig.1) with permission from [134] Copyright (2019) by the American Physical Society.

So far, we consider the electron as a moving particle in a periodic potential of atom cores,

weakly bound to each other. Now, we assume electrons to be tightly bound to the positive particles. By exciting electrons to the CB, i.e. increasing their energies by at least the bandgap energy, empty electron states called holes form in the VB. The holes thereby have wavevectors $k_h = -k_e$. We can think of these electrons and holes as localized particles where their wave functions can be described as a linear superposition of Bloch functions (time dependent eq. 2.1) for various $k = k_0 + \Delta k$ peaked at k_0. The localized wave function is then

$$\Psi_{nk_0}(r,t) = \int d^3\Delta k \;\; a_{n\Delta k}\psi_{nk}(r,t)$$

where n is the band index. We expand the energy eigenvalue E_{nk} and the periodic function factor u_{nk} of the Bloch function in Δk:

$$\begin{aligned}
\psi_{nk} &= e^{ikr}u_{nk}(r)e^{-i(E_{nk})/\hbar\ t} \\
&= e^{i(k_0+\Delta k)r}(u_{nk_0}(r) + \Delta k\nabla_{k_0}u_{nk_0} + ...)e^{-i(E_{nk_0}+\Delta k\nabla_{k_0}E_{nk}+...)/\hbar\ t} \\
&= \underbrace{e^{ik_0r}u_{nk_0}(r)e^{-i(E_{nk_0})/\hbar\ t}}_{constant\ in\ \Delta k}\ exp\left[-i\Delta k(\underbrace{\nabla_{k_0}E_{nk_0}/\hbar}_{=v_g}\ t - r)\right] + ...
\end{aligned}$$

where we only consider the leading order in the periodic factor function. We call v_g the group velocity. Considering the equation above we can think of v_g as the velocity of the motion of the envelope of the wave packet of localized states. It describes rather the transport of mass, than motions of particles charge and energy. In the following we want to semiclassical investigate the attributed mass analogous to classical mechanics:

$$\text{Let: } \frac{d}{dt}v_g = \frac{1}{\hbar}\frac{d}{dt}(\nabla_k E_{nk}) = \frac{1}{\hbar}\nabla_k\left(\frac{d}{dt}E_{nk}\right) \text{ and assume: } \frac{dE}{dt} = F\cdot v \text{ and } F \text{ is } k\text{-independent}$$

$$\text{then: } \frac{d}{dt}v_g = \frac{1}{\hbar}F\ \nabla_k v_g = \frac{1}{\hbar^2}F\ \nabla_k\nabla_k E_{nk}. \text{ By comparing this to } F = m\frac{d}{dt}v \text{ we get}$$

$$\boldsymbol{m^*} = \hbar^2\left(\frac{d^2E}{dk^2}\right)^{-1}$$

where m^* is a mass equivalent term of the wave packet which we call the *effective mass* of electrons or holes. This simple trick allows us two treat the electrons and holes moving along the energy bands as fermionic quasi-particles with a quasi-mass and a quasi-velocity analogous to the particles in classical mechanics. This eases the handling of a complex quantum mechanical many-body problem.

As mentioned earlier electrons and holes are tightly bound. The binding force in this case are Coulomb interactions. A Coulomb bound electron hole pair complex is a bosonic (integer spin) quasiparticle called exciton. More complex bound structures including either an extra electron or hole are called trion. Two bound pairs of electron and hole are called biexciton. In

the following subsections we want to give an overview over the quasiparticle nature of excitons, trions and biexcitons and summarize previous investigations in TMDCs.

2.1.1 Exciton

Excitation appears as two plane waves, one for the CB electron and one for the VB hole. An exciton X is formed if the exited electron hole pair (e-/h pair) is localized due to Coulomb processes. Analogous to the hydrogen model, excitons have a Bohr radius $a_{B,X}$ and a Rydberg energy R_X which is linked to their binding energy by

$$\begin{aligned} a_{B,X} &= \frac{\hbar^2 \epsilon_{SC}}{\mu_X e^2} = 2 \text{ nm} \\ R_X &= \frac{\mu_X e^4}{\epsilon_{SC}^2 \hbar^2} = 509 \text{ meV} \end{aligned} \tag{2.3}$$

where $\epsilon_{SC} = \epsilon_0 \epsilon_r = \epsilon_0 (\epsilon_\parallel \epsilon_\perp)^{1/2} = 16.9 \cdot \epsilon_0$ [130, 169] is the dielectric constant in the semiconductor and the exciton reduced mass is $\mu_X^{-1} = m_e^{*-1} + m_h^{*-1} = (1/0.64 + 1/0.65) \cdot 1/(9.109 \cdot 10^{-31} \text{ kg})$, where m_e^* and m_h^* are the electron and hole effective masses [128]. We directly calculate the Bohr radius and the Rydberg energy for the TMDC $MoTe_2$. The calculated numbers are a good approximation as exciton binding energies from $200 - 600$ meV have been found in TMDCs [127, 193]. Therefore, TMDCs have large exciton binding energies and small Bohr radii compared to other semiconducting materials exhibiting binding energies of only several meV [96, 113]. Thus, the excitons are strongly coupled in TMDCs. The Hamiltonian of an exciton reads as Hamiltonian of an electron and a hole bound by the Coulomb potential:

$$H_X = \frac{p_e^2}{2m_e} + \frac{p_h^2}{2m_h} - \frac{e^2}{\epsilon_{SC} |r_e - r_h|}.$$

Electron hole pairs with angular momentum $(0, \pm 1)$ are excitons where the hole and the electron have the same spin, thus, allowing radiative recombination. These pairs can undergo interband processes called *electron-hole exchange interactions* (e-/h exchange) . The principle of e-/h exchange is sketched in Fig. 2.5: a CB electron returns to the VB and a VB electron is excited to the CB via the emission and reabsorption of a virtual photon p (Fig. 2.5 b). Electron hole exchange interactions play an important role in exciton physics as excitons couple strongly to photons. We have measured a timescale for exciton e-/h interactions of less than one picosecond [159]. Theoretical investigations predict e-/h exchange timescales of 13 fs [199] being at least one order of magnitude faster than the lifetime of an exciton in TMDCs of several ps. How important these e-/h exchange interactions are in the case of TMDCs will be investigated in chapter 5 and 6.

On the other hand, dark excitons do not couple to photons (i.e. they do not emit light)

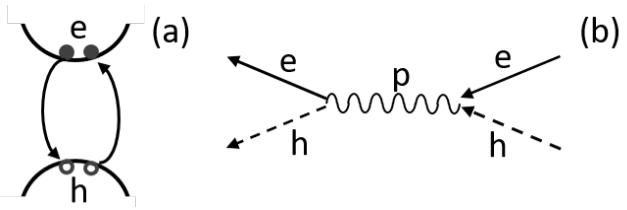

Fig. 2.5: (a) Sketch of electron hole exchange interactions. (b) Sketch of electron hole interactions in Feynman diagram by the exchange of a virtual photon p. Both diagrams are equivalent.

and thus do not exchange e-/h pairs. This results in an energy separation of bright and dark excitons. Usually bright excitons exhibit a higher energy than dark excitons. There are two classes of TMDCs, molybdenum based and tungsten based TMDCs, distinguishable by their bright dark exciton ($E_{bright} - E_{dark}$) splitting. The first one features a negative splitting and the second one a positive [93, 209]. A detailed investigation will follow in section 2.2.

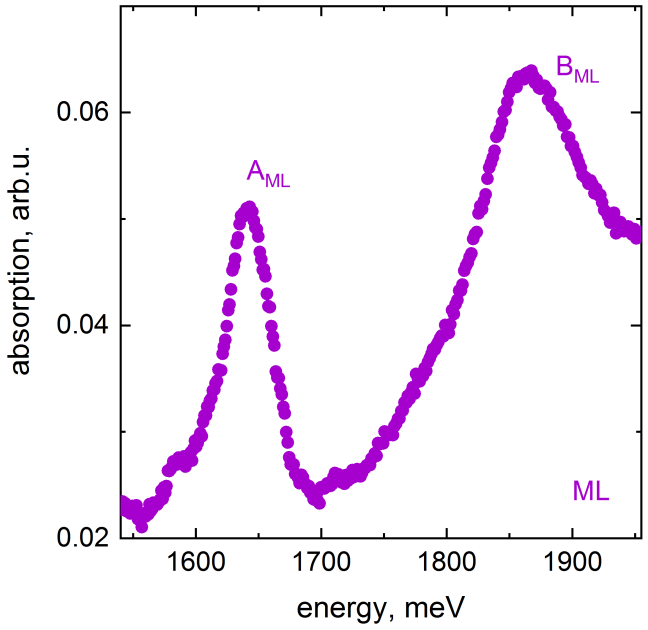

Fig. 2.6: Absorbance spectrum of excitons (A, B) in ML of $MoSe_2$ at 30 K.

Excitons can be created by the absorption of a photon p with center of mass momentum Q_p forming an exciton with the same center of mass momentum $Q = k_e + k_h = Q_p$ where k_e (k_h) is the wave vector of the electron (hole). The photon absorption rate of the exciton is

$$A(Q_p, \omega_p) = 2\pi \; N_p \; |\Omega_{Q_p}|^2 \; L^D \sum_{v_i} |\; \langle v_i | r = 0 \rangle \; |^2 \; \delta \left(E_g + E_{v_i} + Q_p^2 / 2M_X - \omega_p \right) \tag{2.4}$$

where ω_p is the photon energy, N_p is the photon number linked to the laser intensity, Ω_{Q_p} is the exciton-photon coupling, L^D is the size of the sample over space dimension D (in principle this is the volume over which the exciton has a well-defined momentum), v_i is the relative motion of the exciton, and the last term is a set of delta functions. The delta functions are peaked

at ω_p equals to all possible bound exciton energies $E_g + E_{v_i} + Q_p^2/2M_x \sim E_g + E_{v_i}$, where E_g is the bandgap energy and $E_{v_i} = -R_X/(i+1)^2$ possible Rydberg state binding energy (cf. eq. 2.3). The equation above indicates that one should measure clear peaked spectra at the energy of an exciton. Experimentally we do not observe delta peaks, we observe broad peaks where the linewidth originates inter alia from exciton lifetime broadening. One can investigate linewidth broadening Γ mechanisms by replacing E_{v_i} via $E_{v_i} + i\Gamma$ in eq. 2.4. An example absorption spectrum for ML TMCD $MoSe_2$ is shown in Fig. 2.6. It is obvious that the peaks of the excitons (labeled A and B) are not only lifetime broadened. There are a number of other mechanisms. In chapter 3 and 4, this thesis clarifies which processes broaden the linewidth.

The absorbed energy is directly proportional to the laser intensity. Note, there is a critical value, the Mott transition, directly linked to the particle properties by $\eta = N_p(a_X/L)^D$. If the Mott transitions is smaller than one, we form bound e-/h states, for a Mott transition larger than one there are dense, overlapping particle functions. In this regime, we do not observe individual e-/h pairs, but rather we found an electron hole plasma. Thus, it is important to choose a laser intensity below the Mott density to assure a measurement of exciton properties and dynamics.

2.1.2 Trion

Trions are made of one exciton plus one extra charge, either an electron or a hole. Due to the odd number of fermionic components, trions are fermions allowing spin values of $\pm 1/2$ or $\pm 3/2$ which must be considered in the description of a trion. In contrast to the bosonic excitons, the trion is a fermionic particle and the energy of a trionic gas spreads out when the trion density increases. In this thesis, we consider trions consisting of two electrons and one hole, due to the reason that the bulk material (cf. section 2.3.1) is slightly negatively doped for $MoTe_2$ and $MoSe_2$ samples. In TMDCs, however, both types of trions can be investigated. We can assume that the electrons have the same or opposite spin resulting in odd orbital functions or odd for $S = 1$ and even for $S = 0$ orbital functions, respectively. Thus, the ground state trion is made from two electrons with opposite spin. The mass of the trion is $m_T = 2m_e^* + m_h^*$. The Hamilton of the trion reads like an exciton Hamilton plus Coulomb interactions with the extra electron e'

$$H_T = \frac{p_e^2}{2m_e} + \frac{p_{e'}^2}{2m_{e'}} + \frac{p_h^2}{2m_h} - \frac{e^2}{\epsilon_{SC}|r_e - r_h|} - \frac{e^2}{\epsilon_{SC}|r_{e'} - r_h|} - \frac{e^2}{\epsilon_{SC}|r_e - r_{e'}|}.$$

The energy eigenvalue of the Schrödinger equation is then $E_T = K^2/2m_T + E_\xi$, where $E_\xi \sim E_{Bind}^T$ is the trion binding energy, and K is the center of mass momentum. Similar to the excitonic binding energy, the binding energy of trions in TMDCs is significantly larger than in other semiconductor materials. Binding energies for the trion in order of tens of meV have been found [12, 23, 56, 89, 193]. Therefore, trions can be investigated independently of the exciton due large separation in energy to the exciton, i.e. the trion emission/absorption is not within

the exciton linewidth. This renders TMDCs an ideal class of materials for studying trions, as will be done in this thesis.

Modeling the trion being an exciton with an extra charge, we assume to have an electron with momentum k_e and an exciton with center of mass motion Q_X so that the trion momentum is $p = \beta_X k_e - \beta_e Q_p$. Compared to excitons trions have a poor coupling to photons, i.e. the trion absorption spectrum does not consist of a "bound" trion absorption, rather, it stems from many-body effects between photo-created excitons and free carriers and can be calculated by:

$$S_T = N_p |\Omega_{Q_p}|^2 L^D \sum_{\xi_i} |\langle \xi_i | r = 0, p \rangle|^2 \, \delta \left((\omega_p + \frac{k_e^2}{2m_e}) - (E_g + E_{\xi_i} + \frac{(k_e + Q_p)^2}{2(2m_e + m_h)}) \right). \quad (2.5)$$

$\omega_p + \frac{k_e^2}{2m_e}$ is the initial energy and is the energy of the photon plus the energy of the electron. The trion fulfills $\omega_p + \frac{k_e^2}{2m_e} = E_g + E_{\xi_i} + \frac{(k_e+Q_p)^2}{2(2m_e+m_h)}$. As the electron can have a momentum between $k_e = 0$ and $k_e = k_F$ assuming a Fermi sea with Fermi vector k_F. So the absorbed energy can range between $E_g + E_\xi$ and $E_g + E_\xi - k_F^2/2m_e$. That means by increasing the Fermi wave vector (for example by doping) the low energy side of the trion will spread out. At finite temperature the sharp low energy edge can be broadened by thermal excitation. This leads to an asymmetric line shape of trions at higher temperature [30]. At low temperatures the number of trions scales with the electron density.

2.1.3 Biexciton

Biexcitons are made of two excitons, being bosonic particles. Unlike excitons biexcitons also have a spin state as trions, to be considered because the wave functions contain both a spin part and an orbital part. The two electrons and holes can have the same or the opposite spin. Mostly we understand the biexcitons as two interacting bright exciton states. The biexciton binding energy is much smaller than the exciton binding energy as the attraction of two opposite charged particle has to be considered. The binding energy and the center energy of the biexciton have been under discussion. We found that [166] the biexcitons have a binding energy depending on the configuration of the electrons and holes at the high symmetry points K and K'. The lowest bright biexciton is located energetically in between the exciton and the trion emission. Moreover, biexcitons have a small coupling to photons compared to excitons. The Hamiltonian of the biexciton is the Hamiltonian of two excitons and the interactions of their respective electrons and holes:

$$H_{XX} = \frac{p_e^2 + p_{e'}^2}{2m_e} + \frac{p_h^2 + p_{h'}^2}{2m_h} + \sum_{ij} \frac{e^2}{\epsilon_{SC} |r_i - r_j|}; \quad i, j = e, e', h, h'$$

The probability of forming a biexciton increases with the number of excitons.

2.1.4 Phonon

Previous investigations in this thesis have been made without inducing movement of the lattice atoms. This is reasonable as in a stable crystal each atom has an equilibrium position. If an atom receives (for any reason) kinetic energy the atom starts to vibrate around its equilibrium position. As there are forces between the atoms, the movement is global in the lattice called lattice vibrations. This is as thinking of particles linked by springs as sketched below and after a certain time particles start to move simultaneously. One can solve the equation of motion of such a system: First, we assume one particle per unit cell, then the mode frequency (i.e. the frequency of the normal modes of vibration) is given by

$$\omega_q = \left(\frac{4\sigma}{M}\right)^{1/2} \sin(qa/2),$$

where σ is the force constant, M is the mass of the atom, a is the separation between the atoms, and q is the wave vector specified by the boundary conditions of the lattice: $q = 2\pi n/Na$. N is the number of atoms in the chain, thus, the number of normal modes.

Definition 1. *A phonon is a quasiparticle characterized by the energy $\hbar\omega_q$ and a group velocity $v_g^p = \nabla_q \omega_q$. The evolution of the phonon frequency dependent on the wavevector is known as phonon dispersion.*

Phonon modes parallel to the axis are called longitudinal and phonons perpendicular to the axis are named transversal. For two atoms per unit cell the wave factor is given by

$$\omega_q^2 = \frac{\sigma}{M^*}\left(1 \pm \left[1 - \frac{4M^{*2}}{M_a M_b}\sin^2(qa/2)\right]^{1/2}\right),$$

where $M^{*-1} = M_a^{-1} + M_b^{-1}$. Thus, the branches in the lattice vibration spectrum split to the $+$ and the $-$ sign in the equation above. The minus sign is attributed to the acoustic branch ω_q^- and the plus sign is linked to the optical branch ω_q^+. For three-dimensional crystal structures and/or more atoms per unit cell, the equation of motion can only be solved by numerical calculations. The number of solutions and, therefore, the number of phonon bands, can be calculated by the number of unit cells N and the number of atoms per unit cell R to be: dNR in d dimensions.

In TMDCs ML and bulk, the phonon dispersion has been investigated in first principle density functional theory calculation and Raman experiments [6, 48]. In Fig. 2.7 (a) an example phonon dispersion for ML $MoTe_2$ is shown along prominent symmetry points sketched in Fig. 2.3 [48]. The ML TMDC has nine phonon branches. There are three acoustical phonon modes: the out of plane (ZA), the transversal (TA), and the longitudinal acoustic (LA) phonon mode. The acoustical phonon (A) mode represents modes where the atoms vibrate in phase as shown in Fig. 2.7 (a). In contrast, for optical phonons (O) the atoms vibrate out of phase, yielding lager

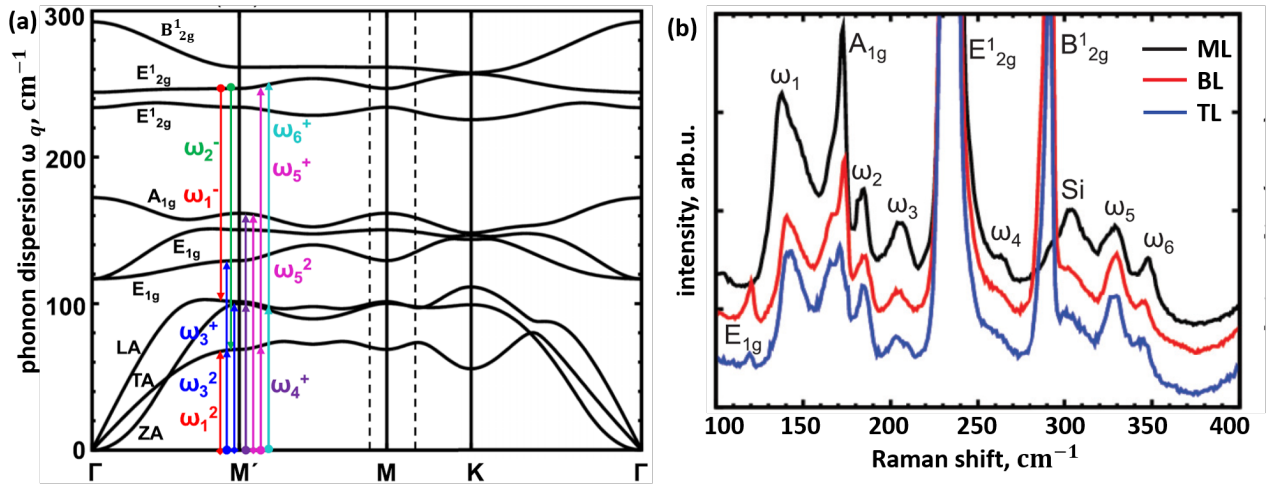

Fig. 2.7: (a) Phonon dispersion relation of ML $MoTe_2$ along high symmetry point of the Brillouin zone. (b) Raman spectra of ML, BL, and trilayer (TL) showing small intensity peaks (ω_i) and typical $MoTe_2$ Raman modes and the for normalization used Silicon mode. Reprinted (Fig4b, Fig1a) with permission from [48] Copyright (2019) by the American Physical Society.

energies than the A phonons. The next two branches are non-polar TO and LO modes (E_{1g}), followed by the transversal (TO, A_{1g}) and the longitudinal (LO, E^1_{2g}) optical phonon mode. The homopolar LO mode (E^1_{2g}) is even higher in energy. [69].

Fig. 2.7 (b) show first order Raman modes, namely in-plane E^1_{2g}, out of plane A_{1g}, and additionally in the BL and trilayer (TL) the E_{1g} and B^1_{2g} modes [48]. These peaks correspond to optical Γ point phonons. In Raman experiments mostly optical phonons can be investigated. Acoustical phonons change the broadening of Raman peaks.

Exciton Phonon interactions

In this subsection we investigate the interactions of excitons with phonons. We follow Refs. [10, 69]. As investigated in chapter 2.1.1, excitons with momentum $Q(k) = k_e + k_h$ are created by photons of center of mass momentum Q_p. The exciton then interacts with a phonon q and arrives at a final state $Q'(k')$. The phonon processes which can be included are acoustical and optical phonons. The scattering from one Bloch state $|k\rangle$ to another Bloch state $|k'\rangle$ can be described by the transition/scattering rate

$$W(k,k') = \frac{2\pi}{\hbar}\sum_{q,k'} |M^j(q)|^2 \left[N'(E')+1\right] N(E)\cdot \\ \left[N_q \cdot \delta(E'-E-\Delta E_q)\delta_{k'-k,q} + (N_q+1)\cdot\delta(E'-E+\Delta E_q)\delta_{k'-k,-q}\right], \tag{2.6}$$

where $|M^j(q)|$ is the matrix element for scattering with j either acoustical or optical phonons and is equivalent to the number of the phonon branch. The δ functions ensure the conservation of energy and momentum, and N and N' are the exciton populations for the state $|k\rangle$ and $|k'\rangle$

having energies E, E'. For excited states we assume that $|k\rangle = 0$ and $[N'(E') + 1]\, N(E) = 1$. $N_q \sim k_B T/\hbar v_S q = k_B T/\hbar\omega_q$ is the number of phonons for equipartition, where v_S is the sound velocity, being material specific. We set q to be the phonon in-plane wavevector.

The matrix element can be described by $M_q^j = \langle k + q|\delta V_{q,j}(r)|k\rangle$, where $\delta V_{q,j}$ is the change in the effective periodic lattice potential along the vibrational phonon mode and is directly linked to the so called deformation potential D_e for electrons.

Definition 2. *A deformation potential describes how the carriers interact with the local changes in the crystal potential sourced by lattice vibrations.*

Therefore, it is obvious that the phonons influence the physical properties of the quasiparticles (like excitons and trions). It is one of the major topics of this thesis to quantify how phonons couple to excitons and trions. So, it is necessary to examine a couple of important properties of TMDCs unlikely for most of the other semiconducting materials. The secret of the TMDCs lie in their symmetry as investigated in the next section.

2.2 The secrets of transition metal dichalcogenides

In this section, we investigate the special symmetry of TMDCs and link this to spin-orbit coupling, optical selection rules and a direct/indirect transition of ML and BL $MoTe_2$. The ML is characterized by the absence of inversion symmetry [189] and a large spin-orbit coupling. This is complemented by an excitonic transition coupled to σ^+-polarized light at the K point and spin up electron and hole pair [82, 101, 141, 162, 171]. Consequently, valley and spin are coupled for ML TMDCs [189]. In the BL, inversion symmetry is restored and, therefore, the spin and the valley are no longer good quantum numbers. The Bulk form is generally indirect in TMDCs and undergo a transition from indirect to direct semiconductor in the ML limit. In most TMDCs the BL exhibits an indirect bandgap. Due to its high luminescence brightness, the type of the optical bandgap in BL $MoTe_2$ is under discussion [89, 134]. This has important implications for $MoTe_2$ as an active medium of light emitting devices, as the photon yield favor the BL over the ML and their carrier mobility is in comparable range. $MoTe_2$ emitting in a technologically relevant wavelength in the near infrared [56, 141] seems to be a promising candidate for opto-electronic devices, with applications ranging from short-range telecommunications to medical imaging.

2.2.1 Inversion symmetry breaking

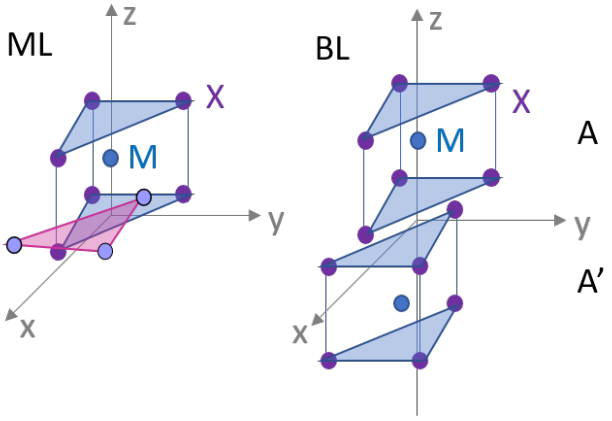

Fig. 2.8: ML and BL inversion symmetry breaking and restoring in the TMDCs MX_2. M (blue dot) denotes the transition metal, X (violet dot) the chalcogenide atoms. In case of the ML, the magenta plane pictures the inversion-symmetry-restored hypothetical second chalcogenide atomlayer.

As mentioned in the previous section, the lattice structure of monolayer TMDCs MX_2 consist of one atomlayer of transition metal (M) atoms sandwiched between two atomlayers of chalcogenides (X). A schematic of the atomic structure of the ML is displayed in Fig. 2.8, we only show one atom of M (blue dot) and two atomlayers of X (violet dot). Inversion symmetry requires a symmetry center with coordinates (i_x, i_y, i_z) which is in case of ML TMDCs the M atom. Each point of the lattice is mirrored at the inversion center such that each point in

the lattice $(i_x + x, i_y + y, i_z + z)$ has an inversion point $(i_x - x, i_y - y, i_z - z)$. In Fig. 2.8 we construct a inversion symmetric atomlayer (magenta rectangle) to the upper atomlayer (upper blue rectangle). The lower blue rectangle represents the atomic lattice structure of TMDCs. By comparing the real lattice structure to a hypothetic inversion symmetry restored lattice it is obvious that the inversion symmetry in the ML is broken [189]. Instead, the ML shows a mirror symmetry in z direction.

The heavy M atoms in first approximation have d orbitals that means an angular momentum l=2. The d orbitals hybridize into $m_l = 0, \pm 1, \pm 2$ represented by d_z^2, d_{xz} & d_{yz}, d_{xy} & $d_{x^2-y^2}$, respectively. In ML due to the mirror symmetry only d_z^2 and d_{xy} & $d_{x^2-y^2}$ are permitted [189]. Therefore, the valence (VB) and conduction band (CB) wave functions at the high symmetry point K read [189]

$$|\phi_{CB}\rangle = |d_z^2\rangle\,, \quad |\phi_{VB}^{\tau}\rangle = \frac{1}{\sqrt{2}}\left(|d_{x^2-y^2}\rangle + i\tau\,|d_{xy}\rangle\right),$$

where τ is the valley index ± 1 for K or K' valley. The Hamiltonian has the form

$$H_0 = at(\tau k_x \sigma_x + k_y \sigma_y) + \frac{\Delta}{2}\sigma_z, \tag{2.7}$$

where a is the lattice constant, t is the nearest neighbor hopping energy, Δ is the bandgap energy, and $\sigma_{x,y,z}$ denote the Pauli matrices. The values for a, t, and Δ can be estimated in band structure calculations. The Hamiltonian is comparable to the ML graphene Hamiltonian [191]. In contrast to graphene, ML TMDCs show strong spin-orbit coupling which will be discussed in detail in the next subsection.

By adding a second monolayer, a BL is formed. Depending on the space group of the TMDC, a special alignment of the layers is expected. In our case we are dealing with a 2H structure MX_2 indicating the presence of two atoms per unit cell. Naturally forming BL, i.e. exfoliated BL, typically exhibits AA' stacking. The stacking sequence is sketched in Fig. 2.8 and implies that the M atom of layer one is stacked over the X atom of layer two [55]. In contrast to the ML, the BL inversion center is located between the two layers. Thus, the inversion symmetry is restored in the BL.

2.2.2 Spin-orbit coupling and dark and bright quasiparticles

In this subsection, we introduce spin-orbit coupling resulting in a splitting of valence and conduction band in ML and BL TMDCs. Moreover, we introduce the excitonic transitions A and B and dark and bright excitons.

An electron has both orbital **L** and spin **S** angular momentum, interacting through their magnetic moments and, thus, influencing the energy of the electron, so that the spin-orbit

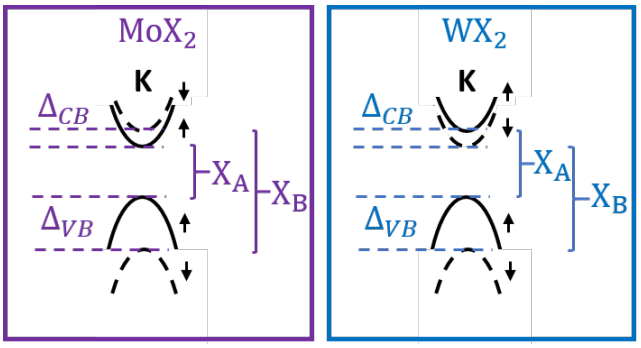

Fig. 2.9: Schematic of conduction and valence band splitting for Mo- and W- based TMDCs in electron-hole picture. Spin up (down) bands sketched by solid (dashed) curves. X_A and X_B denotes the optically bright exciton states.

coupling (SOC) gives a contribution to the Hamiltonian [7, 93]

$$H_{SOC} = \lambda \, \mathbf{L} \cdot \mathbf{S}, \tag{2.8}$$

where λ characterizes the strength of the SOC. As mentioned in section 2.2.1, in TMDCs the transition metal atom (M) is heavy, so the SOC can be large. Including the M orbitals d_z^2, d_{xy}, $d_{x^2-y^2}$, nearest neighbor M-M hoping, and on-site spin-orbit interactions of the M atoms results in a large valence band spin splitting at the K point of $\Delta_{VB} = 2\lambda$ [93]. For $MoTe_2$ a large valence band splitting of 215 meV [93] to 275 meV [127, 134] is expected in theory. The values are larger compared to other Mo-based TMDCs and smaller than in the W-based TMDCs due to the higher mass of the W atom [93, 127].

The splitting of the conduction band is underestimated in this approach. One has to include interactions of the M d_{xz}, d_{yz} and the chalcogenide atom (X) p_x and p_y orbitals by a second order perturbed Hamiltonian such that the wave function of the conduction band reads $|\phi_c'^{\tau}\rangle = \frac{1}{\sqrt{2}} |d_{xz} + i\tau d_{yz}\rangle$ and a first order perturbed effect from the X p_x and p_y orbitals [189]. The former is dominating for the heavier W atoms, the latter especially has to be considered for the Mo-based TMDCs [93]. Moreover, intra-valley short range e-/h Coulomb exchange interactions within the exciton have to be included to find an estimate for the splitting of the dark and bright excitons [39]. This result in an opposite dark bright splitting for W- and Mo-based TMDCs as sketched in Fig. 2.9. In W-based TMDCs the lowest exciton state is dark [39, 93]. For Mo-based compounds, the lowest excitonic transition is bright [39, 93]. All in all, the conduction band splitting together with the Coulomb interaction results in a splitting $\Delta_{CB} = 34$ meV [39] up to 58 meV [134] in ML $MoTe_2$. These are the highest values for the conduction band splitting in the TMDC family [39].

We can attribute the optically bright transitions to the X_A exciton being the 1s exciton transition, where electron and hole have the same spin. In case of MoX_2 the bright transition is the energetically favorable one unlike for most semiconductors [31], and it is sketched in

Fig. 2.9. This makes the excitons exceptionally stable and resistant to dephasing. In WX_2 the dark exciton is the lowest in energy instead of the bright X_A exciton. Therefore, dark states have more influence especially on non-radiative scattering channels in WX_2 than in MoX_2. The X_B exciton is the energetically next higher bright optical transition having the opposite spin of electrons and holes compared to the X_A exciton. The center energies of both the A exciton and the B exciton for $MoTe_2$ are found to be (1.095 ± 0.005) eV and (1.345 ± 0.005) eV at room temperature by absorbance measurements [141].

The giant SOC together with the absence of inversion symmetry allows a strong coupling between spin and valley [189], described in the following section.

2.2.3 Optical selection rules

In this section, we follow Refs. [189, 191, 192, 194] to link valley to the circular polarization. As introduced in chapter 2.1 electron wave functions can be described by Bloch functions. Now we assume a wave packet of these Bloch functions carrying an orbital magnetic momentum $\mathbf{m}$ which arises from self-rotations of the electron wave packets [191] such that

$$\mathbf{m}(k) = -\frac{ie}{2\hbar} \cdot \langle \nabla_k u_k | H(k) - E_k | \nabla_k u_k \rangle \,, \tag{2.9}$$

where u_k is the periodic function (cf. eq. 2.1), H_0 is the Bloch Hamiltonian defined in eq. 2.7, and E_k is the band energy (cf. eq. 2.2). For a two dimensional system the magnetic momentum is perpendicular to the plane $\mathbf{m}(k)\ \hat{z}$, and we set $\mathbf{m}(k)$ to be identical for the upper and lower band. Thus, in the vicinity of the K point, the magnetic moment reads

$$\mathbf{m}(k)\hat{z} = \frac{2a^2t^2\Delta\tau m_e^*}{4a^2t^2k^2 + \Delta^2}, \tag{2.10}$$

where τ, Δ, a, t defined in eq. 2.7, and m_e^* is the effective electron mass. As seen in the equations above $\mathbf{m}(k)$ is valley dependent. Let $\mathcal{P}_\alpha^{i,j}(k) = -i\hbar \langle u_{i,k} | \nabla_{k_\alpha} | u_{k,j} \rangle$ be the inter-band matrix element for a band i so from eq. 2.9 it follows

$$\mathbf{m}(k) = -i\frac{e\hbar}{m_e^2} \sum_{i \neq j} \frac{\mathcal{P}^{i,j}(k) \times \mathcal{P}^{j,i}(k)}{E_{i,k}^0 - E_{j,k}^0}. \tag{2.11}$$

By assuming

$$|\mathcal{P}_\pm(k)|^2 = |\mathcal{P}_x^{CB,VB} \pm i\mathcal{P}_y^{CB,VB}|^2 \tag{2.12}$$

the degree of circular polarization can be described by [194]

$$\begin{aligned}\eta(k) &= \frac{|\mathcal{P}_+(k)|^2 - |\mathcal{P}_-(k)|^2}{|\mathcal{P}_+(k)|^2 + |\mathcal{P}_-(k)|^2} \\ &\underbrace{=}_{eq.\ 2.11+\ 2.12} -\frac{\mathbf{m}(k)\hat{z}}{\mu_B^*(k)} \underbrace{=}_{eq.\ 2.10} -\frac{1}{e\hbar}\ \frac{4a^2t^2\Delta\tau m_e^{*2}}{4a^2t^2k^2 + \Delta^2},\end{aligned} \tag{2.13}$$

where $\mu_B = e\hbar/(2m_e^*)$ is the Bohr magneton.

The K/K' valleys can be selectively addressed by controlling the photon angular momentum i.e. the helicity of the excitation light [194]. Left (σ^-) corresponds to $|\mathcal{P}_-(k)|^2$ and right (σ^+) corresponds to $|\mathcal{P}_+(k)|^2$ circularly polarized light exciting the lowest bright exciton (A exciton) in the K' and the K valley, respectively. The connection of the degree of polarization with the inter-band matrix element results from the normalized oscillator strength for left and right circular polarized light [72, 198]. By directly investigating inter-band transitions at the K point $\eta(\pm K) = -\tau$, where $\tau = \pm 1$, thus, we can specifically optically address each valley.

Connecting valley and spin

In the band structure of ML TMDCs shown in Fig. 2.4, the valence and conduction bands are curved such that the lowest optical transition is located at the edge of the BZ K/K', sketched in Fig. 2.3. As mentioned above, TMDCs have a strong spin-orbit coupling originating from the M d orbitals. This interatomic contribution has to be investigated in the Hamiltonian by combining eq. 2.7 and eq. 2.8 to

$$H = H_0 + H' = at\left(\tau k_x\sigma_x + k_y\sigma_y\right) + \frac{\Delta}{2}\sigma_z - \lambda\tau\frac{\sigma_z - 1}{2}s_z, \tag{2.14}$$

where s_z is the spin quantum number up $\uparrow$ or down $\downarrow$. Time reversal symmetry $E_\uparrow(k) = E_\downarrow(-k)$ implements that the spin splitting in different valleys K and K' is opposite in the ML TMDCs [189, 192]. The resulting bands and spin splitting of the K and K' (often denoted "-K") valleys are shown in Fig. 2.10. We can include SOC into the valley-helicity of light dependence by replacing the energy gap Δ in eq. 2.10 and 2.13 by $\Delta' = \Delta - \tau s_z\lambda$, where 2λ is the valence band splitting making the band-gap spin dependent. Thus, the valley selection rule becomes spin dependent. This has several implications: (i) Spin and valley are locked at the band edges, so spin can be selected by the valley selection rules. As shown in Fig. 2.10 right-circular (σ^+) polarized light can address the K valley and either spin up electrons for the lowest optical transition or spin down electrons for the next higher CB state and vice versa for left circular (σ^-) polarized light. (ii) Inter-valley scattering (e.g. from K to K') requires a simultaneous spin flip. This makes both spin and valley robust and useable in valleytronic applications. The recombination of electrons and holes only takes place when the selection rules are fulfilled, that means e-/h pairs have to have same spin and valley to recombine. (iii) Valley and spin

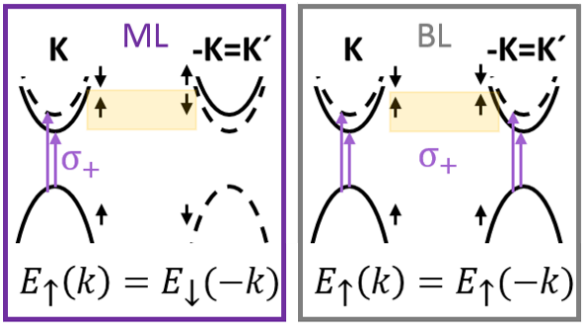

Fig. 2.10: Schematic of conduction and valence-band and spin splitting ML (violet) and BL (gray) TMDCs due to time reversal symmetry. Spin up (down) bands sketched by solid (dashed) curves. The arrows indicating excitation with right circular polarized light (σ^+)

define the polarization of the emitted photon. (iv) Holes have longer spin and valley lifetimes, therefore, the electrons depolarize (i.e. electrons are equally distributed to the valleys) first and combine with the still spin and valley polarized holes and emit photons with oppositely polarized light.

In contrast, in BL TMDCs, the restored inversion symmetry implies a time symmetry $E_\uparrow(k) = E_\uparrow(-k)$. Thus, the spin splitting is not opposite in different valleys as shown in Fig. 2.10. Therefore, valley and spin are not locked, spin is not a good quantum number, and K and K' valley are degenerate. Consequently, selective excitation in one particular valley is not possible [192]. Thus, we do not expect to measure a polarization in BL TMDCs. Note, there are several possibilities to break the inversion symmetry in BL for example by electrically controlled tuning [190] or AB stacking [192] layering M over M atoms.

2.2.4 Direct and Indirect optical transitions in ML and BL

We call a semiconductor direct if its electrons and holes reside in valleys at the same point in the Brillouin zone, sketched in Fig. 2.11 (a) as black arrow for the example of $MoSe_2$. In detail, the CB minima and VB maxima are at the same point in k-space (K) provided that $k_h - k_e \sim 0$ [37]. An indirect quasiparticle is characterized by electron and hole being in different valleys shown in Fig. 2.11 (b) for example the hole in the K and the electron in the Λ valley. Thus, indirect quasiparticles can only radiatively decay with assistance of e.g. a phonon [37].

In their bulk form, TMDCs are indirect semiconductors, while a TMDC ML features a direct lowest optical excitonic transition at the K or K' point of the Brillouin zone [82, 101, 141, 162, 171]. Most TMDCs undergo a transformation from an indirect centrosymmetric transition at the Γ point to a direct non-centrosymmetric transition at the K point of the hexagonal Brillouin zone in the ML limit. This has been confirmed for MoS_2 and $MoSe_2$ [82, 101, 162, 171] due to strong distinctions in photon yield in photoluminescence experiments, band structure calculations [55, 82, 135] and ARPES measurements [65, 205]. For the MoS_2 and $MoSe_2$ compounds only minimal luminescence is observed from BLs [87, 172], unless strain is

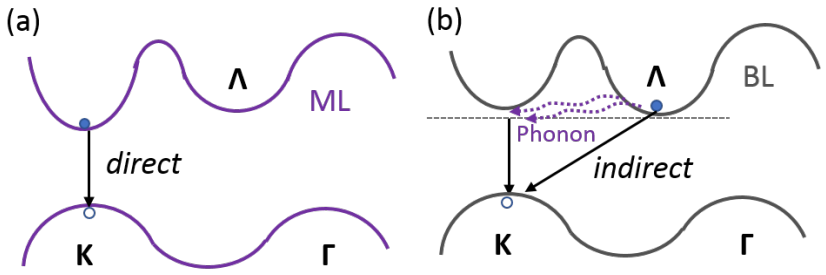

Fig. 2.11: Direct (a) and indirect (b) bandgap (violet arrow) exemplary illustrated for $MoSe_2$.

applied [32]. It is established that for these materials the unstrained BL has an indirect bandgap with the valence band maximum located at the Γ_{VB} or the K_{VB} point [82, 101, 162, 171], the latter especially in $MoSe_2$. The conduction band minima are located at the Λ_{CB} valley sometimes also called Q_{CB}. The ML has a direct bandgap in the K_{VB} and K_{CB} valleys. Early density functional studies found that ML MoX_2 show less quantum confinement compared to the bulk, instead their electronic structures are dominated by surface states near the Fermi level [90].

$MoTe_2$ is an exception. An additional feature peculiar to $MoTe_2$ is the large luminescence yield obtained from a BL of $MoTe_2$ sheets [89, 134]. The evidence for a indirect/direct bandgap in case of BL $MoTe_2$ is controversial. There are hints of an indirect bandgap in band structure calculations [82, 200], but the majority of the experimental evidence [43, 89, 134] suggest that this is not the case.

To better understand this feature and the mismatch between experiment and theory in the BL $MoTe_2$, we investigate the band structure calculations in more detail. We refer to the really nice review article from the group of Prof. Xiadong Xu [92]. The band structure calculations for the BL strongly depend on the calculation parameters like lattice constant, interlayer distance [90], and interlayer hopping. The variation in band structure is significant for the visible TMDC material, such that the lowest optical transition can be attributed either to Γ_{VB} to Λ_{CB}, Γ_{VB} to K_{CB}, or K_{VB} to Λ_{CB}. The latter is not observed in MoS_2. Additionally, a K_{VB} to K_{CB} direct transition is observed in $MoSe_2$. However, there are a few statements that can be made: (1) The energies of the K_{VB} and K_{CB} do not change much as they are dominated by metal d orbitals that remain identical for different compounds. (2) The energy of the Γ_{VB} is raised and that of Λ_{CB} is lowered as both have admixtures of X p_z orbitals. This is a consequence of the interlayer hopping, i.e. the band extrema split with increasing layer number. Interlayer hoping is allowed (forbidden) between the VB (CB) states. (3) The Γ_{VB}, K_{VB} splitting decreases with increasing weight of the chalcogenide atom from 500 meV in MoS_2, to 100 meV in $MoSe_2$ to ~ 0 meV in $MoTe_2$ [50, 65, 205]. This allows a direct emission in the BL $MoTe_2$. To clarify the mismatch from theory to experiment, we investigate the photoluminescence lineshape of ML and BL $MoTe_2$ in chapters 3 and 4.

In this section, we have clarified that inversion symmetry breaking leads to an optical selection rule where the helicity of the light selects the valley (K or K'). The strong SOC in TMDCs due to the heavy transition metal atoms leads to a coupling of valley and spin. That makes the polarization of the quasiparticles stable to dephasing resulting in a stable polarization in photoluminescence spectroscopy for the lowest optical transition. The question arises whether higher exitonic states show a polarization as well. The BL does conserve inversion symmetry; thus, valley and spin are not coupled, and we expect to see no measurable polarization. In addition, we summarize the discussion of a direct transition in BL $MoTe_2$, finding that there is no clear conclusion for $MoTe_2$. To investigate the open questions, we perform further optical experiments. The setups and methods used in this thesis will be investigated in the next chapter.

2.3 How to investigate quasiparticles experimentally

In this section we introduce the fabrication and pre characteristics of the samples and measurement techniques, namely Photoluminescence, Two Color Pump Probe, and Two Dimensional Coherent Spectroscopy to investigate quasiparticles in TMDCs. We specify the aspects of position and polarization control of the Photoluminescence setup and adapt this to the other measurement methods.

2.3.1 Preparing a sample

In this thesis, we investigate mechanically exfoliated mono and bi-layers of bulk $MoSe_2$ and $MoTe_2$. The bulk material is ordered from the commercial provider *2D Semiconductors* [150]. The company synthesize the bulk crystals using the flux zone technique ensuring a good atomic structuring, thus, low impurities and defect concentration (10^9 to $10^{10}\,cm^{-2}$). This allows experiments on un-encapsulated samples. Moreover, the bulk crystal is slightly negatively doped, enabling the formation of negatively charged trions. The bulk crystal grows in the 2H semiconducting phase composed of 2D-layers that are weakly hold together by van der Waals interactions [6] and can be easily exfoliated into 2D layers. Mechanical exfoliation has been previously performed to produce graphite ML and more-layer [114] and was adapted to TMDCs in 2010 [101, 162]. There, a sticky tape (scotch tape or mobile phone protective film) is pressed on to the 3D bulk material, carefully removed and pressed multiple times on the substrate. The resulting flake landscape is characterized by an optical microscope at different magnification and mono- and few-layer flakes are identified by their optical contrast.

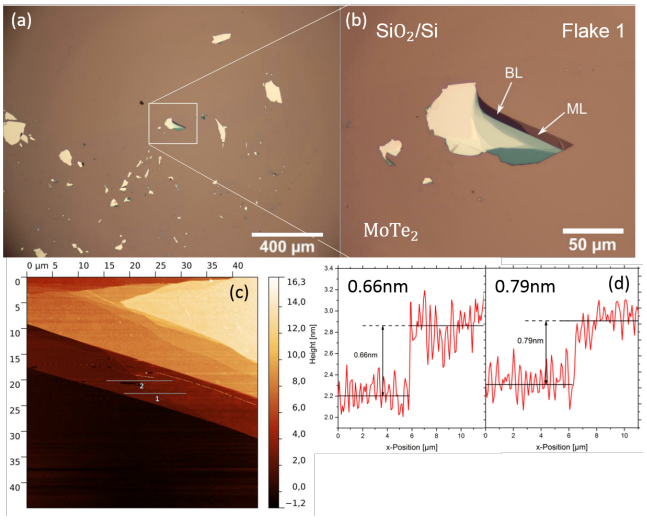

Fig. 2.12: (a+b) Optical microscope image of $MoTe_2$ ML and BL flake 1 at different magnifications on SiO_2/Si substrate. (c) Atomic force microscopy image of ML and BL edge. 1 and 2 denotes the scan area. (d) Sample height according to atomic force measurement.

For our investigations, we use $MoTe_2$ flakes mechanically exfoliated from a bulk sample onto a

$SiO_2 = 80\,nm/Si$ substrate by *Robert Schneider* from the group of *Prof. Dr. Rudolf Bratschitsch* from the *Westfälische Wilhelms-Universität Münster* at Münster. The identification of ML and BL is achieved by optical contrast and atomic force microscopy. Optical microscope image of the flake used in our experiments are shown in Fig. 2.12 (a+b). The investigated flake exhibits a lateral extension of about 120 μm and mainly consists of largely bulk material which is thinning at one edge down to a ML. The ML and the BL parts of the flake are marked in the figure. In addition to optical contrast measurements, the thickness of the layers is quantified by atomic force microscopy measurements presented in Fig. 2.12 (c). The thickness (Fig. 2.12 (d)) of one layer is estimated by two cuts at different ML-BL edge positions to be 0.66 nm and 0.79 nm, respectively. The change of thickness along the edge elucidates the need of position control of the laserspot on ML and BL as introduced in the experimental section. A second $MoTe_2$ ML flake is produced under the same exfoliation conditions shown in Fig. 2.13 (a). The second ML has a lateral extension of 10 μm x 50 μm comparable to that of flake 1. For both flakes we chose SiO_2/Si substrate as all experiments performed on these flakes are in reflection geometry.

The $MoSe_2$ ML and BL are produced in *Prof. Dr. Xiaoqin (Elaine) Li's* research group at the *University of Texas at Austin* by using mechanical exfoliation by *Marshall Campbell* and *Matthew Staab* on Polydimethylsiloxane, respectively. Then both flakes are transferred to the same sapphire substrate by *Kha Tran* to ensure measurements within the same cooling process in transmission geometry displayed in Fig. 2.13 (c+d).

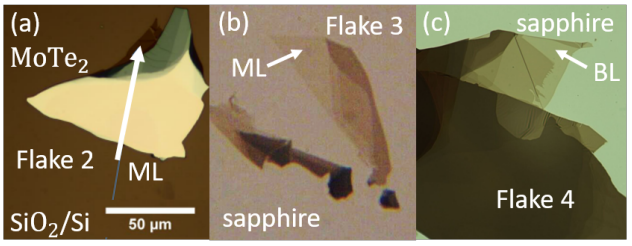

Fig. 2.13: (a) Optical microscope image of ML (flake 2) $MoTe_2$ on SiO_2/Si. (b+c) Microcopy image of ML (flake 3) and BL (flake 4) $MoSe_2$ on sapphire.

All flakes investigated in this thesis are directly connected to the bulk material. We also investigated a set of isolated ML $MoTe_2$ flakes and found that they show no measurable emission. We assume that flakes which are connected to the bulk material are separated from the substrate, thus, dielectric screening effects of the substrate are significantly reduced compared to isolated flakes. This assumption is supported by position control measurements on different points of the ML-BL edge (cf. next chapter). An enhanced dielectric screening leads to a blue shift of the excitonic and trionic emission and a reduced ratio of trion to exciton intensity [91].

2.3.2 Step one: Photoluminescence spectroscopy

Photoluminescence spectroscopy is a linear optical method analyzing optical transitions in semiconductors. Mainly due to absorption of photons with energies higher than the bandgap an electron promotes from the VB to the CB resulting in the creation of a hole in the VB (cf. section 2.1). The excited electron decays either non-radiatively, i.e. by scattering to a triplet state of lower lying energy or quenching trough the ground state, or radiatively by emitting a photon of a characteristic energy. The resulting emission of a photon can be detected by a spectrometer. The emitted light contains information of the inner state of the sample, like carrier population and type, broadening mechanisms, bandgap energy, defect and impurity scattering, making the photoluminescence spectroscopy a rather simple but effective primal measurement method.

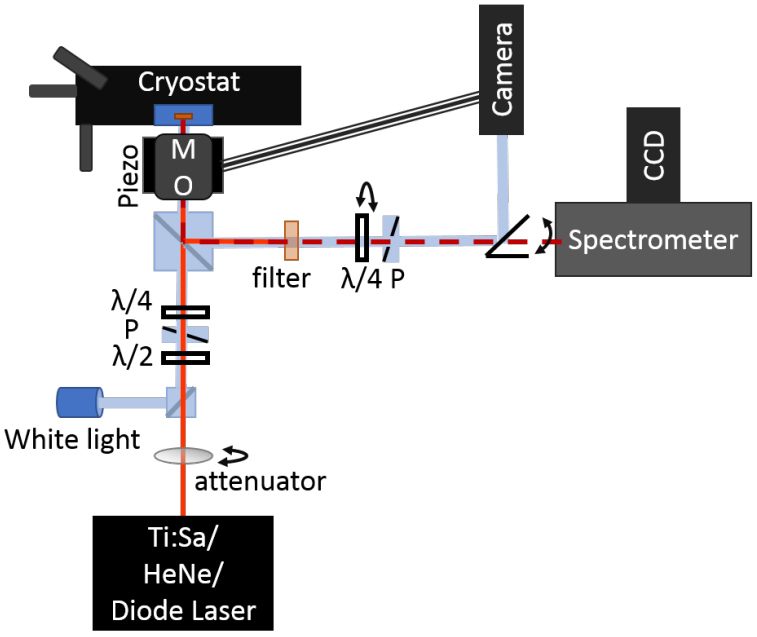

Fig. 2.14: Experimental photoluminescence setup. MO: microscope objective; CCD: charge-coupled device sensor; λ/i, i=2,4 : polarization retarder plate, P: polarizer

In our PL experiment (cf. Fig. 2.14), we excite particles either with a *Ti:Sapphire Mira HP* pumped by a *Verdi V-18* from *Coherent* operating between 1.124 eV (1000 nm) and 1.797 eV (690 nm), a helium-neon laser at 1.960 eV (633 nm), or laser diodes at 1.907 eV (650 nm) and 1.850 eV (670 nm). The laser light is directed to a 50x NIR-micro objective (*Mitutoyo, R79005809A*, 0.5 NA) focusing the beam on the sample with a spot size of $\sim 6\,\mu$m. The sample is kept in a helium-flow cryostat in vacuum ($\sim 10^{-6}$ mbar). We control the position of the sample due to micrometer screws in x,y, and z direction. The resulting emission is coupled into the same MO confocal geometry and guided to the spectrometer passing a filter to strip the pump beam and excise laser reflection. We detect the emission by a *Horiba iHR550* spectrometer connected to a nitrogen-cooled *Horiba IGA detector* from *Jobin Yvon GmbH*.

As you can see in the sketch of the setup in Fig. 2.14, we can control various parameters like excitation power, sample temperature, excitation energy, pulsed or continuous wave excitation, and polarization to investigate the nature and behavior of quasiparticles. The results are discussed in the next chapters. Note, the control of the polarization optics will be discussed in the next subsection separately.

The need of controlling the position

Based on the results of the atomic force microscopy measurements, where it is found that the thickness of the layer changes slightly with the position on the sample and the restricted lateral extension of the flake, a precise positioning of the sample is necessary. Therefore, we develop a camera feedback piezo-fine-alignment LabVIEW control program which scans and adjusts the position of the laser spot on the sample. To realize this in experiment, we extend the classical PL setup (cf. Fig. 2.14) by mounting the microscope objective (MO) on a *TRITOR 102 Piezoelement* from *Piezosystem Jena*, and adding a white light source (illumination of the sample), and a monochrome camera *Chameleon 1.3* from *FLIR*. The control program facilitates, firstly, manual positioning in the μm range with direct camera feedback and, secondly, saving chosen positions and using this for automatic positioning on the sample. Details on the LabVIEW control program can be found in the BSc-thesis of my student *Matthias Kunz* [84].

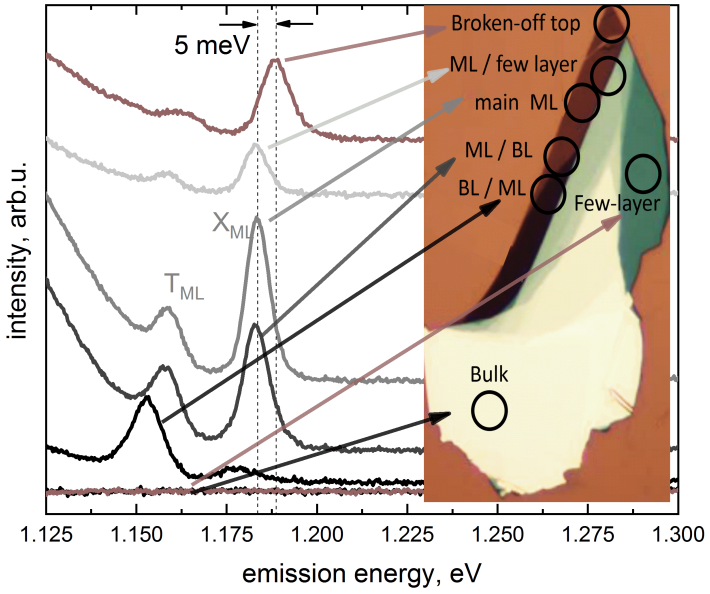

Fig. 2.15: Photoluminescence of Flake 1 dependent on the position of the laser spot (black circle) on the flake.

As we measure the emission from ML flake 1 for different positions we clearly see changes along the ML edge, as illustrated in Fig. 2.15. The main ML emission is characterized by exciton (X_{ML}) and trion (T_{ML}) resonances. By moving along the long axis of the flake, we

clearly observe a change of the exciton and trion emission in intensity, bandwidth, and center energy. For measurement positions exhibiting overlap with the BL we see a contribution of the BL exitonic emission. For measurements on the top witch is broken off from the rest of the flake we see a clear drop in trion to exciton intensity ratio from 0.66 to 0.30 and a blue shift in center energy of about 5 meV attributed to increased screening of the substrate [91] bringing up the question of substrate supported and suspended ML flake which will be investigated in chapter 5. Besides, the bulk and few-layers do not show a significant emission.

Polarization control

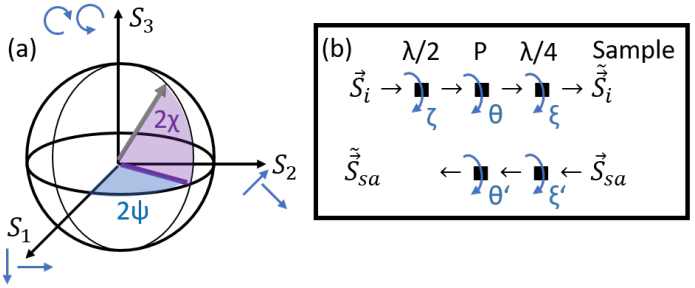

Fig. 2.16: (a) Poincaré sphere. The axes denote the Stokes parameters. (b) Sketch of polarization optics and Stokes parameter.

As introduced in section 2.2, the direct excitonic formation in TMDC is restricted by optical selection rules of the K and the K' point of the hexagonal Brillouin zone, controllable by the helicity of the circularly polarized light. Left or right circularly polarized light can be transformed from arbitrarily polarized light by inserting a set of polarization optics ($\lambda/4$, P, $\lambda/2$) in our setup, as seen in Fig. 2.14. The polarization of the electromagnetic radiation can be described in terms of the so called Stokes vectors on a Poincaré sphere illustrated in Fig. 2.16 (a) in spherical coordinates:

$$\begin{aligned} S_0 &= I \\ S_1 &= Ip\ \cos(2\phi)\ \cos(2\chi) \\ S_2 &= Ip\ \sin(2\phi)\ \cos(2\chi) \\ S_3 &= Ip\ \sin(2\chi), \end{aligned} \tag{2.15}$$

where I is the total intensity of the electromagnetic wave, $0 \leq p \leq 1$ the degree of polarization, and ϕ and χ are the spherical coordinates visualized in Fig. 2.16 (a). The Stokes coordinates mathematically describe the polarization of the light, for example linear ($\leftrightarrow$ / $\updownarrow$), 45° linear

(↗ / ↖), circular (↻ / ↺), and arbitrarily (A) polarized light can be expressed by

$$\leftrightarrow / \updownarrow \mathrel{\widehat{=}} \begin{pmatrix} 1 \\ \pm 1 \\ 0 \\ 0 \end{pmatrix}; \nearrow / \nwarrow \mathrel{\widehat{=}} \begin{pmatrix} 1 \\ 0 \\ \pm 1 \\ 0 \end{pmatrix}; \circlearrowright / \circlearrowleft \mathrel{\widehat{=}} \begin{pmatrix} 1 \\ 0 \\ 0 \\ \pm 1 \end{pmatrix}; A = \begin{pmatrix} a \\ b \\ c \\ d \end{pmatrix}.$$

We use linear film polarizers *LPNIR050* (510-800 nm) and *LPVISC050* (650-2000 nm) from *Thorlabs* consisting of prolate ellipsoid nanoparticles embedded in sodium-silicate glass. They offer superior performance compared to conventional polymer-based polarizers, like significantly higher damage threshold and a dramatically better extinction ratio [47]. Note, still better polarization quality can be obtained using Glan-Taylor prism, however, the experimental signal-to-noise ratio does not require this further improvement. The extinction ratio describes the ratio of maximum transmission of linearly polarized signals for a aligned polarizer axis to the minimum transmission signal of a 90°rotated polarizer [47]. Polarizers can be mathematically described in terms of Müller matrices M_i (the four-dimensional equivalent of the Jones matrices) and applied to a Stokes vector by $S_f = M_2(M_1 S_i)$ for final (S_f) and initial (S_i) Stokes vectors. The Müller matrix for a horizontal linear polarizer is

$$P_h = \frac{1}{2} \begin{pmatrix} 1 & 1 & 0 & 0 \\ 1 & 1 & 0 & 0 \\ 0 & 0 & 0 & 0 \\ 0 & 0 & 0 & 0 \end{pmatrix}.$$

We can rotate these matrices in each lab system by the angle Θ towards the fast axis via $P_\Theta = R(\Theta) P_h R^{-1}(\Theta)$, where $R(\Theta)$ is the rotation matrix.

Retarders change the polarization of the transmitted light, by inducing a phase shift between orthogonal states of polarization. The most common retarders are $\lambda/2$ to rotate a linear polarization and $\lambda/4$ to change the polarization from linear to circular polarization and vice versa. We use achromatic retarder plates from the company *Bernhard Halle* in two different wavelength regimes: 460-680 nm and 600-1200 nm. The achromatic retarders are zero-order double plates made from two distinguish materials, Quartz and MgF_2, with different material dispersion resulting in a nearly constant phase shift over the whole spectral range. Between the two plates is an air-gap producing a low group delay dispersion of 37 fs^2 for the $\lambda/4$ and 61 fs^2 for the $\lambda/2$ retarder, perfectly working for ultrashort laser pulses as we use in our pump probe measurement [51]. Retarder plates can be described as well in terms of Müller matrices

and can be rotated analogous to the polarizers:

$$\lambda/2_h = \begin{pmatrix} 1 & 0 & 0 & 0 \\ 0 & 1 & 0 & 0 \\ 0 & 0 & -1 & 0 \\ 0 & 0 & 0 & -1 \end{pmatrix}; \quad \lambda/4_h = \begin{pmatrix} 1 & 0 & 0 & 0 \\ 0 & 1 & 0 & 0 \\ 0 & 0 & 0 & 1 \\ 0 & 0 & -1 & 0 \end{pmatrix}$$

The polarization optics are included in the beam guidance as presented in Fig. 2.16 (b). Starting with arbitrarily polarized light $\vec{S}_i = A$. The light reaching the sample is described by

$$\begin{aligned} \tilde{\vec{S}}_i &= R(\xi)\lambda/4_h R^{-1}(\xi) \;\; R(\Theta)P_h R^{-1}(\Theta) \;\; \lambda/2_{vertically}\; \vec{S}_i = \lambda/4_{135}\; P_h\; \lambda/2_h\; \vec{S}_i \\ &= \begin{pmatrix} 1 & 0 & 0 & 0 \\ 0 & 1 & 0 & 0 \\ 0 & 0 & -1 & 0 \\ 0 & 0 & 0 & -1 \end{pmatrix} \frac{1}{2} \begin{pmatrix} 1 & 1 & 0 & 0 \\ 1 & 1 & 0 & 0 \\ 0 & 0 & 0 & 0 \\ 0 & 0 & 0 & 0 \end{pmatrix} \begin{pmatrix} 1 & 0 & 0 & 0 \\ 0 & 0 & 0 & 1 \\ 0 & 0 & 1 & 0 \\ 0 & -1 & 0 & 0 \end{pmatrix} \begin{pmatrix} a \\ b \\ c \\ d \end{pmatrix} \\ &= \frac{1}{2} \begin{pmatrix} a+b \\ 0 \\ 0 \\ -(a+b) \end{pmatrix} \widehat{=} \begin{pmatrix} 1 \\ 0 \\ 0 \\ -1 \end{pmatrix} \widehat{=} \circlearrowleft \end{aligned}$$

assuming $\lambda/2_h = \lambda/2_{vertically}$, $\Theta = 0°$, and $\xi = 135°$. Thus, we excite the sample with left circular polarized light. By comparing this to the valley selection rules (cf. section 2.2.3) we excite carriers in the K' valley. We keep the orientation of the polarization optics of the excitation beam constant for the complete measurement. If we need to change the retarders and polarizers (due to a change in wavelength) we choose the same orientation of the optics.

The sample emits light of a certain polarization $\vec{S}_{sa} = (\sigma_a, \sigma_b, \sigma_c, \sigma_d)^T$ in Fig. 2.16 (b). For simplicity we assume to have arbitrarily polarized light and interpret the results in the end of this section. The light passes a second $\lambda/4$ retarder rotatable between two possible adjustments: (i) $\xi'_s = 135°$ having the same orientation as the $\lambda/4$ plate in the excitation beam and (ii) $\xi'_o = 45°$ having the opposite orientation as the $\lambda/4$ plate in the excitation beam. Afterwards, the light passes a second linear polarizer in horizontal linear polarized orientation (same orientation as in the excitation beam path). We calculate the two cases in the following:

$$\begin{aligned} (i)\;\; same \qquad \tilde{\vec{S}}_{sa} &= \lambda/4_{135}\; P_h\; \vec{S}_{sa} \\ &= \frac{1}{2} \begin{pmatrix} 1 & 1 & 0 & 0 \\ 1 & 1 & 0 & 0 \\ 0 & 0 & 0 & 0 \\ 0 & 0 & 0 & 0 \end{pmatrix} \begin{pmatrix} 1 & 0 & 0 & 0 \\ 0 & 0 & 0 & 1 \\ 0 & 0 & 1 & 0 \\ 0 & -1 & 0 & 0 \end{pmatrix} \begin{pmatrix} \sigma_a \\ \sigma_b \\ \sigma_c \\ \sigma_d \end{pmatrix} = \frac{1}{2} \begin{pmatrix} \sigma_a + \sigma_d \\ \sigma_a + \sigma_d \\ 0 \\ 0 \end{pmatrix} \end{aligned}$$

$$(ii)\ \ opposite \quad \tilde{\vec{S}}_{sa} = \lambda/4_{45}\ P_h\ \vec{S}_{sa}$$
$$= \frac{1}{2}\begin{pmatrix} 1 & 1 & 0 & 0 \\ 1 & 1 & 0 & 0 \\ 0 & 0 & 0 & 0 \\ 0 & 0 & 0 & 0 \end{pmatrix}\begin{pmatrix} 1 & 0 & 0 & 0 \\ 0 & 0 & 0 & -1 \\ 0 & 0 & 1 & 0 \\ 0 & 1 & 0 & 0 \end{pmatrix}\begin{pmatrix} \sigma_a \\ \sigma_b \\ \sigma_c \\ \sigma_d \end{pmatrix} = \frac{1}{2}\begin{pmatrix} \sigma_a - \sigma_d \\ \sigma_a - \sigma_d \\ 0 \\ 0 \end{pmatrix}$$

Both results in horizontal linear polarization considering only the components in the circular polarized component of the emitted light. Assuming now the sample emits light of the same circular polarization as we excite with, that means emission from the K' valley $\vec{S}_{sa} = (1, 0, 0, -1)^T$, thus,

$$(i)\ \ same: \quad \tilde{\vec{S}}_{sa} = \frac{1}{2}\begin{pmatrix} 0 \\ 0 \\ 0 \\ 0 \end{pmatrix} \quad (ii)\ \ opposite: \quad \tilde{\vec{S}}_{sa} = \begin{pmatrix} 1 \\ 1 \\ 0 \\ 0 \end{pmatrix}.$$

So polarized light of the same polarization will be suppressed completely (maximized) using the same (opposite) retarder orientations and vice versa for light emitted from the K valley. As we are interested in a polarization transfer process we call the intensity of the light excited and emitted from the same valley $I_{K'K'}$ and excited and emitted from different valley $I_{KK'}$. So $I_{K'K'}$ ($I_{KK'}$) is correlated with excitation retarder $\lambda/4_{135}$ and detected with (ii) $\lambda/4_{45}$ ((i) $\lambda/4_{135}$). Starting from this assumption we can calculate the degree of polarization by

$$polarization = \frac{I_{K'K'} - I_{KK'}}{I_{K'K'} + I_{KK'}}. \tag{2.16}$$

2.3.3 Step two - Two Color Pump Probe Spectroscopy

In the following, we explain the principles of our pump probe method with heterodyne balanced detection and investigate the polarization of each beam to address the K or the K' valley of the hexagonal Brillouin zone. Thereby, we follow Refs. [71, 76, 77, 116]. The setup is presented in Fig. 2.17. In principle, pump probe spectroscopy uses two ultrashort light pulses. In our case

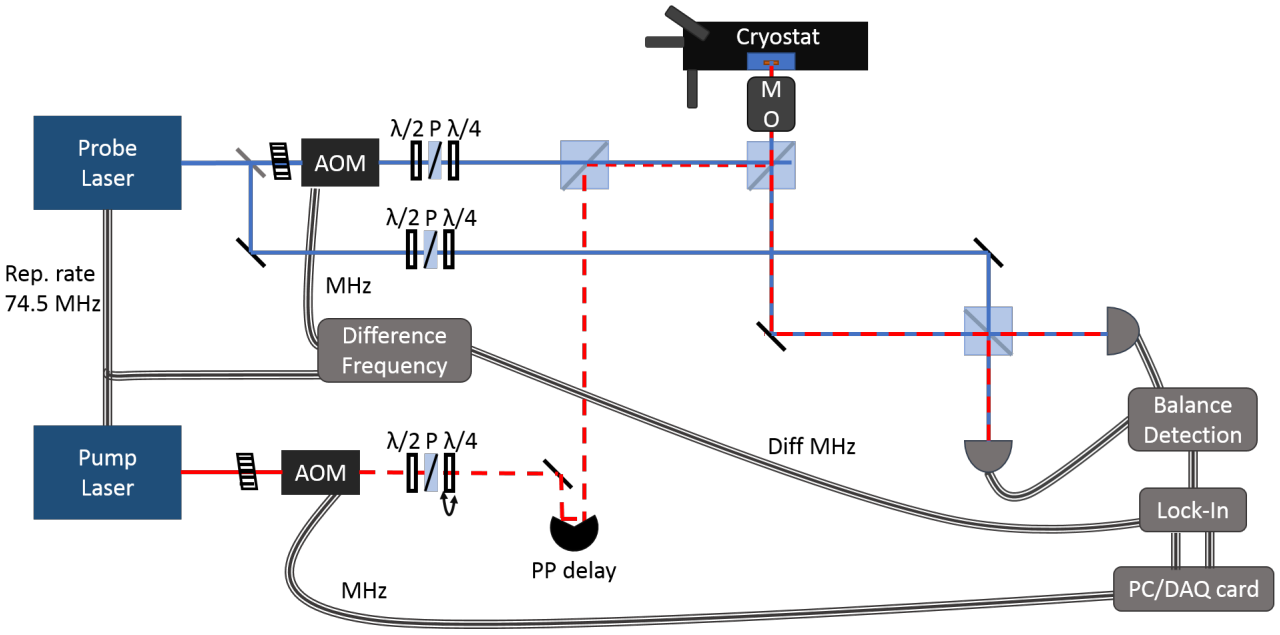

Fig. 2.17: Experimental Two Color Pump Probe setup.

we use two white light *Toptica FemtoFiber Pro* SCIR-systems, generating a supercontinuum in the NIR/IR that can individually be tuned in wavelength by amplitude masks in the Fourier plane of a pulse shaper. The temporal pulse length is estimated to be 180 fs by autocorrelation measurements. The pump pulse as the first pulse perturbs the sample at time zero. The probe pulse, the second pulse, reaches the perturbed sample and probes it delayed by τ with respect to the pump pulse. One can set the pump probe delay τ by an optical delay line. We choose a collinear geometry of our pulses. To make the pulses distinguishable we set frequency markers by shifting the original laser frequency with an acoustic optical modulator (AOM). After interaction with the sample the probe beam is interfered with the unshifted reference beam to distinguish the pulses. The experimental method is described in greater detail in Ref. [76]. We acquire data by switching the pump on and off and getting a signal on our *Zürich Instruments* lock in *ZI HF2LI* S_{on}, S_{off}. The differential reflection signal (dR/R) and phase signal ($d\phi/\phi$) is then

$$\frac{\ln 10}{10}\frac{dR}{R}(\tau) + i\frac{d\phi}{\phi}(\tau) = \ln\left|\frac{S_{on}(\tau)}{S_{off}}\right| + i\left(\phi^{(on)}(\tau) - \phi^{off}\right). \tag{2.17}$$

The delay between pump and probe τ can be tuned to measure dynamics of the perturbed system. The heterodyne detection enables the simultaneous tracking of both amplitude and phase which has previously not been used in the study of 2D systems. We note that a camera feedback white light adjusting tool and low temperature capability is also included in this pump probe setup. The details on these components can be found in the PL section.

Helicity of the light in pump probe measurements

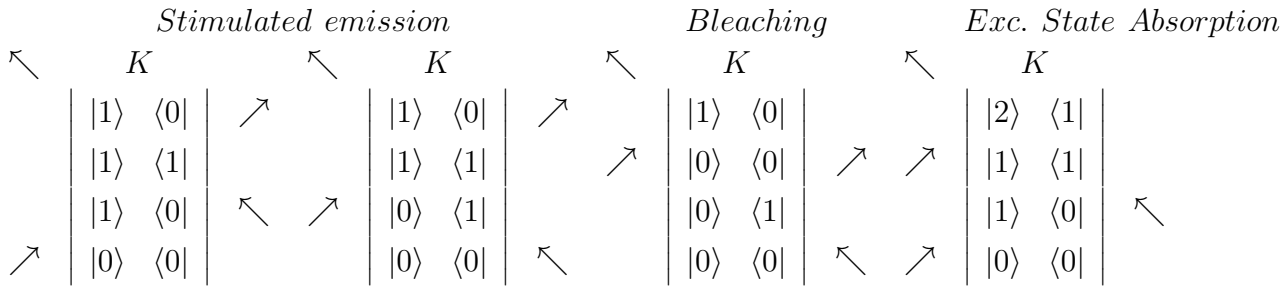

In this section, we follow Ref. [112]. For a better understanding of the processes we illustrate them in terms of the Feynman diagrams above. The time increases from the bottom to the top of each diagram and the arrows indicate the pulses. First, we discuss the stimulated emission. In pump probe spectroscopy we have two beams: pump and probe. Quantum mechanically the pump acts twice (illustrated by the first two arrows in the diagram). The first pump pulse creates a microscopic polarization by occupying one state from $|0\rangle$ to $|1\rangle$ and the second pump pulse creates a population at the sample, $\langle 0|$ to $\langle 1|$. As both steps (pump pulse one and two) originate from the same laser beam, the two pump pulses reach the sample nearly at the same time, so we cannot distinguish which step acts first. This is shown by the two stimulated emission diagrams above where the two steps result in the same population. In both cases the pump pulse results in a populated excited state $|1\rangle\ \langle 1|$. For a delay $\tau\ \sim 0$ between pump and probe we assume to observe no population decay. After the delay τ, the probe pulse stimulates the excited state back to the ground state. The last arrow in each diagram indicates the emitted light pulse. As this emission is stimulated by the probe it has the same frequency and, thus, can interfere with the reference beam as explained before. Increasing the time delay, the population of the exited state starts to decay, and we can probe the evolution of the population decay. In addition to stimulated emission, there are two other main processes observed in pump probe. These are ground state bleaching and excited state absorption, as sketched above. Ground state bleaching describes particles that are in the ground state after the pump pulse. The probe pulse then interacts linearly with the sample and we get absorption at the sample. In excited state absorption one creates a first excited state polarization and population by the pump and the probe pulse induces a second excited state absorption. For all different types of pump probe processes, we assume to populate the same valley (K valley) in ML TMDCs due to the same helicity of the light, namely left circularly polarized light (σ^-) for pump and

probe introduced in section 2.2.3. We adjust the polarization using the same polarizers and retarders as discussed in the previous section. By changing the helicity of the pump beam to right circularly polarized light (σ^+) we pump the K' and probe the K valley. We sketch this for zero-time delay and a delay $\tau > 0$ for the probe (K) valley.

$$\begin{array}{cc|cc|cc|cc|c} \nwarrow & & K, \tau = 0 & & & \nwarrow & & K, \tau > 0 & \\ & & |1\rangle & \langle 0| & & & x\,|1\rangle & x\,\langle 0| & \nearrow \\ \nearrow & & |0\rangle & \langle 0| & & & x\,|1\rangle & x\,\langle 1| & \\ & & |0\rangle & \langle 0| & & & |0\rangle & \langle 0| & \\ & & |0\rangle & \langle 0| & & & |0\rangle & \langle 0| & \end{array}$$

Choosing opposite circular polarization results in an absorption-like process of the excited state for the K valley at zero delay induced by the probe. As the pump populates the opposite valley, we cannot observe the other processes. After a certain time $\tau > 0$ the K valley is populated by a certain probability $0 \leq x \leq 1$ due to valley exchange interaction and we measure stimulated emission and excited state absorption from the K valley. The exact mechanisms involved in the valley exchange interactions will be investigated in chapter 6. We assume a uniform occupancy for the two valleys after a characteristic interaction-time. Consequently, we can measure a valley polarization equivalent to a preferred population of one valley as a function of the pump probe delay. We denote that, the resulting differential reflection for pump and probe beam have the same (opposite) helicity $dR/R_{\circlearrowleft\circlearrowleft}$ ($dR/R_{\circlearrowleft\circlearrowright}$) and thus investigate the signal from the same (opposite) valley. The resulting valley polarization is calculated by

$$valley\ polarization = \frac{dR/R_{\circlearrowleft\circlearrowleft} - dR/R_{\circlearrowleft\circlearrowright}}{dR/R_{\circlearrowleft\circlearrowleft} + dR/R_{\circlearrowleft\circlearrowright}}. \tag{2.18}$$

2.3.4 Step three - Two Dimensional Coherent Spectroscopy in Austin

In this section, we briefly present two-dimensional coherent spectroscopy (2DCS), the corresponding setup is shown in Fig. 2.18. We follow thereby the thesis of *Dr. Galan Moddy* [110] and Ref. [18]. This approach is implemented in *Prof. Dr. Xiaoqin Li*'s lab at the *University of Texas at Austin* where I spent four months in a research exchange program funded by the *GRK 1558*. In contrast to the other setups in this thesis, this setup is limited in energy to visible light in the emission range of the titan sapphire laser (Ti:Sa). The mode-locked Ti:Sa produces 53 fs pules with a repetition rate of 76 MHz and a center wavelength of 750 nm (1.65 eV). The light is guided through the JILA-Monster [18] producing four phase stable beams with tunable delays. Three of them with wavevectors k_1, k_2, and k_3 are focused in a typical four wave mixing (FWM) box geometry on the sample with a spot size of 30 μm, interacting with the sample and creating the FWM signal $k_S = -k_1 + k_2 + k_3$. The pulses are interfered with the reference beam (the fourth beam from the JILA Monster) to extract the FWM amplitude that is subsequently detected using a spectrometer. The signal is Fourier transformed to the time-domain, positive

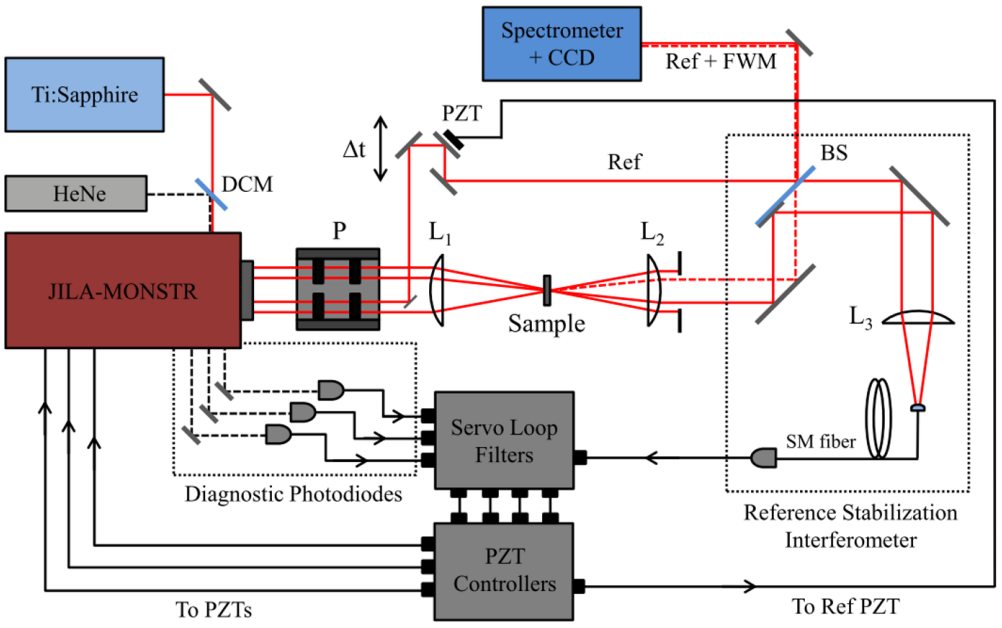

Fig. 2.18: Two Dimensional Coherent Spectroscopy setup in the group of *Prof. Dr. Elaine Li* at the *University of Texas at Austin* from Ref. [110].

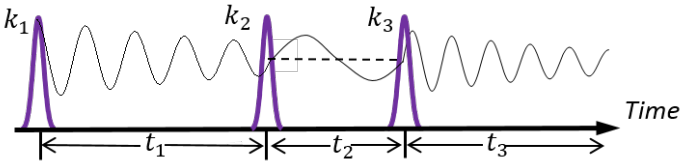

Fig. 2.19: Sketch of the four wave mixing time ordering of the three exciting pulses k_1, k_2, and k_3 with time-delays t_1, t_2, and t_3 between the pulses.

time terms are isolated and back transformed into the energy-domain.

The time ordering and time delays of the FWM geometry are sketched in Fig. 2.19. To do so, we either scan the time delay t_1 between the first and the second pulse or t_2 between the second and the third pules. Thereby, we reproduce a 2D excitation spectrum of the signal either $S(\hbar\omega_{t1},\ t_2,\ \hbar\omega_{t3})$ keeping the delay between the second and the third pulse t_2 constant or $S(t_1,\ \hbar\omega_{t2},\ \hbar\omega_{t3})$ keeping the delay between the first and the second pulse t_1 constant. In the first case, we measure an excitation energy ($\hbar\omega_{t1}$) vs. emission energy ($\hbar\omega_{t3}$) map where we can extract homogenous line width. These are directly linked to dephasing rates for $MoSe_2$. In the second configuration we measure the zero quantum energy ($\hbar\omega_{t2}$) vs. the emission energy ($\hbar\omega_{t3}$) to determine population decay rates. The results are presented in chapter 7.

3 Exciton-phonon coupling in mono- and bilayer $MoTe_2$

We study the temperature- and power-dependent photoluminescence of monolayer and bilayer molybdenum ditelluride in the temperature range between 5 K and room temperature. In this chapter, we aim to investigate the exciton-phonon coupling in molybdenum ditelluride for monolayer and bilayer to extract key parameters like line broadening and temperature shifts of emission lines of excitons and trions. We disentangle the effects of interactions of excitons with acoustic and optical phonons and show that molybdenum ditelluride excitons have an exceptionally small coupling with acoustical phonons. This observation, together with the large luminescence yield which can be obtained from the bilayer, puts forward molybdenum ditelluride as a robust and bright light source in the near-infrared spectral range. The scaling of luminescence energy and linewidth of the molybdenum ditelluride bilayer differs from the observations in the monolayer by effects that can be traced to symmetry and well width. This suggests a similar band alignment of mono- and bilayer, in contrast to other transition metal dichalcogenides. Moreover, we confirm the existence of an optically active trion state in the bilayer emission, by assuming an electron capture process from a low density two-dimensional free electron gas.

3.1 Laser light on - Here comes the ML and BL emission

In this section we give an overview about the analysis of PL spectra of ML and BL $MoTe_2$, identify peaks and confirm the existence of a trion emission in the BL $MoTe_2$ for the first time.

We study the temperature- and power-dependent PL of ML BL $MoTe_2$. Details on the measurement method and sample preparation are described in section 2.3. Exemplary emission spectra at 10 K and 10 μW excitation power of ML (violet squares) and BL (gray circles) $MoTe_2$, recorded under the same experimental conditions, are presented in Figure 3.1. ML and BL lineshape and linewidth are extremely well resolved and directly comparable. The ML and BL luminescence can be decomposed into a set of Voigt functions. These are shown exemplary for the sharp emission peaks as shaded areas in Fig. 3.1. A Voigt function is defined by:

Definition 3. *A Voigt function is the convolution ($\otimes$) of a Gaussian function and a Lorentzian function $V(x) = (G \otimes L)(x)$. The fit function*

$$V(x) = A\,\frac{2\,\ln 2}{\pi^{3/2}}\,\frac{\Gamma_L}{\Gamma_G^2}\int_{-\infty}^{\infty}\frac{e^{-t^2}}{(\sqrt{\ln 2}\,\frac{\Gamma_L}{\Gamma_G})^2+(\sqrt{4\,\ln 2}\,\frac{x-x_C}{\Gamma_G}-t)^2}\,dt$$

depends on the parameters: area A, center of the profile x_C, Gaussian linewidth Γ_G, and Lorentzian linewidth Γ_L. The full with at half maximum (FWHM) of the Voigt profile is given by $\Gamma = 0.5346\ \Gamma_L + \sqrt{0.2166\ \Gamma_L\Gamma_L + \Gamma_G\Gamma_G}$ [34].

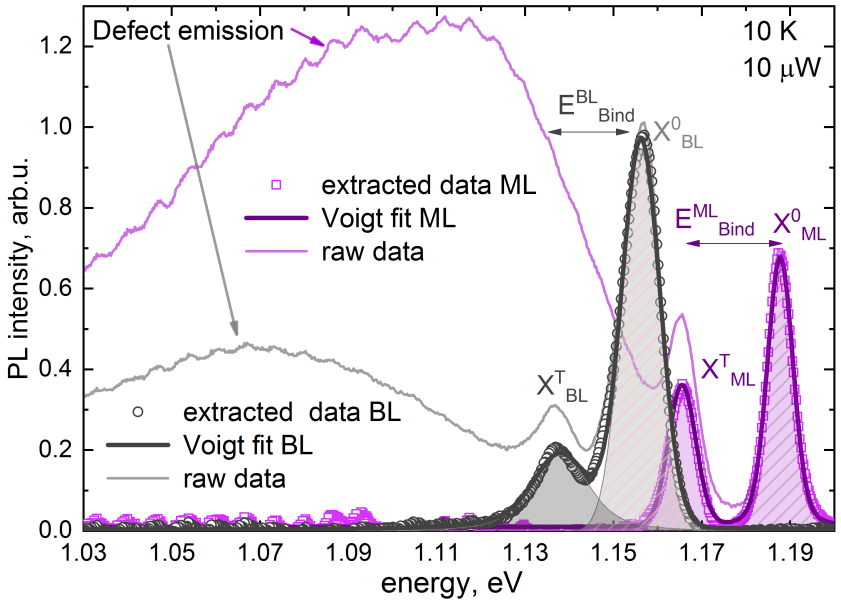

Fig. 3.1: Normalized PL spectra of ML (violet squares) and BL (gray circles) $MoTe_2$ at 10 K fitted by sums of Voigt functions (solid dark violet and gray lines). The solid areas indicate the respective Voigtian components of the main peaks. Light violet and gray lines represent the raw data including the defect emission of ML and BL $MoTe_2$.

Thus, the Voigt fit provides information about energy position (x_C), integrated area of emission (A), and linewidth (Gaussian and Lorentzian) for each peak. These spectral characteristics

provide quasiparticle (introduced in section 2.1) properties which will be analyzed in the following. There are three main peaks for both ML and BL $MoTe_2$, measured on flake 1. The highest energetic one is identified by its emission energy as A exciton emission of the ML X^0_{ML} at 1.190 eV and the BL X^0_{BL} at 1.155 eV, consistent with previous studies [56, 89, 134, 75]. The position in energy of the second peak corresponds to the trion peak X^T_{ML} at 1.165 eV as observed in Ref. [75] at low temperature. The emission of the $MoTe_2$ BL, also shows a second peak at 1.135 eV. This peak has been observed previously in literature and is attributed to the trion transition [89, 64], though a final proof in $MoTe_2$ is still lacking. In WS_2 [208] and WSe_2 [67] the BL trion has been confirmed through gate dependent PL measurements. Thus, the assumption of a charged particle in the BL emission is reasonable. A detailed investigation of power- and temperature-dependent measurements will confirm the quasiparticle nature of this peak in section 3.1.2. Finally, there is a broad bulky peak at low energy fitted by a set of three (ML) or two (BL) Voigtians. We ascribe this as defect-related emission due to scattering with particles and power dependent measurements underline the non-quasiparticle nature evaluated in the following section.

3.1.1 Defect peak analysis

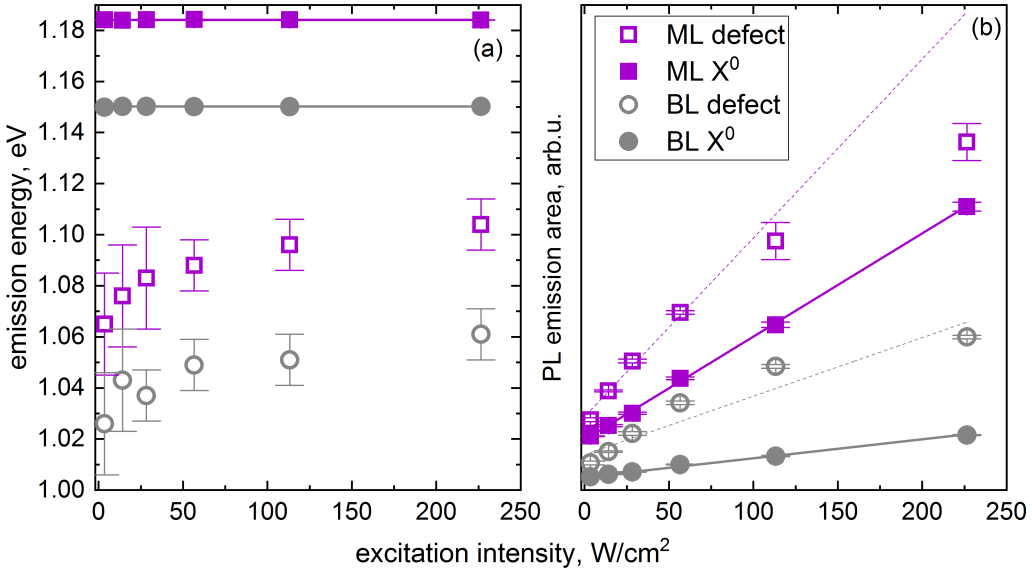

Fig. 3.2: ML (violet) and BL (gray) exciton (closed symbol) and defect (open symbols) emission energy (a) and integrated area of emission (b) versus excitation intensity. ML and BL excitation energy are linearly fitted. The dotted lines in (b) are the best possible linear approximation of the defect emission intensity. Note: The ML emission area (b) is offset above the BL for better illustration.

We perform a set of power dependent PL measurements varying the excitation power from 1 μW to 64 μW at a constant temperature of 10 K and a spot size of 6 μm. We calculate the excitation intensity as laser power divided by spot area. As can be seen by the linearly rising excitonic emission area, the power is low enough to avoid thermal heating effects of the sample.

We choose an excitation energy of 1.797 eV to obtain a reasonably good signal-to-noise ratio up to room temperature [193]. The integrated area of emission or briefly emission area and the emission energy position are extracted for all peaks. In case of the defect peak we estimate the emission area from the sum over the area of the single Voigt peaks. The emission energy is attributed to the energy at maximal intensity. The results are presented in direct comparison to the exciton trends in Fig. 3.2 (a+b) for ML and BL $MoTe_2$.

The emission energy of the exciton in (a) stays constant over the hole excitation intensity range, as expected for quasiparticles under low power excitation below the Mott transition (introduced in chapter 2.1.1) and at low temperature [29, 60, 120, 44]. The defect emission energy increases with increasing excitation power indicating more than one scattering process with distinguishable saturation threshold unlikely for single particle emission. Moreover, the PL emission area (cf. Fig. 3.2 (b)) of the defect does not rise linearly with excitation intensity in contrast to the quasiparticle emission (closed symbols) [60, 120, 44]. As the defect shows no quasiparticle behavior, we will not include this peak in the following analysis.

3.1.2 Presence of a trion in the BL

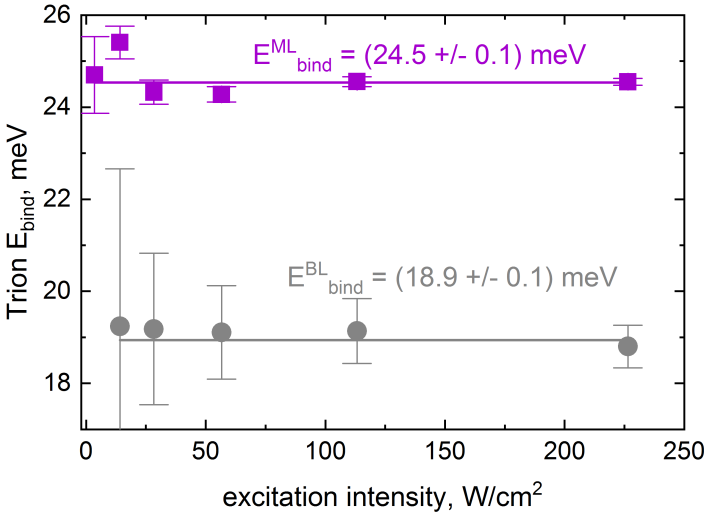

Fig. 3.3: Excitation-intensity-dependent trion binding energy E_{Bind} of ML (violet squares) and BL (gray circles) $MoTe_2$ fitted by constant functions (solid lines).

As the power dependent emission energy and emission intensity show a clear linear behavior for quasiparticles, we confirm the quasiparticle nature of the second BL peak by analyzing ML and BL exciton and trion emission in direct comparison. Therefore, we extract the trion binding energy E_{Bind} (Fig. 3.1), by subtracting the trion emission energy from the exciton emission energy, of (24.9 ± 0.5) meV and (19.1 ± 0.5) meV for ML and BL, respectively. The ML trion binding energy is comparable with previous measurements particularly confirmed in gate voltage dependent PL measurements [89, 134, 193]. By compare the trion binding energy

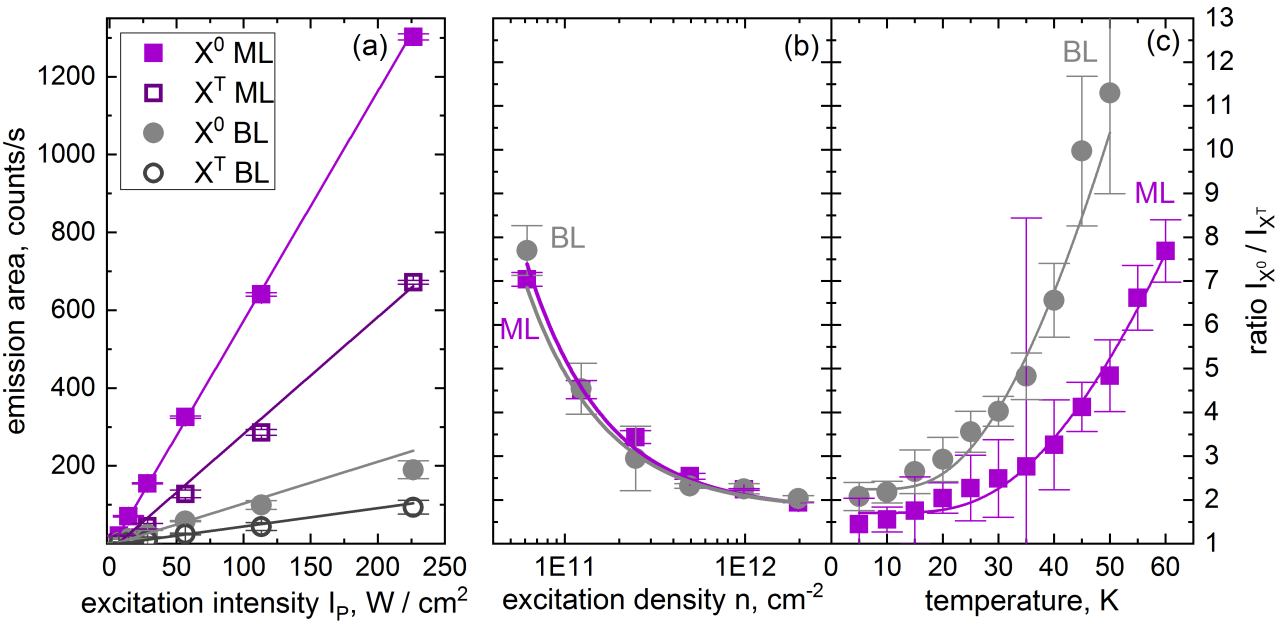

Fig. 3.4: (a) Excitation intensity dependent quasiparticle emission area of ML (violet squares) and BL (gray circles) fitted by a linear function (solid lines). (b) Exciton to trion intensity ratio of ML and BL as a function of excitation density n at 24 K. (c) Temperature-dependence of ML and BL exciton to trion ratio. The data in (b+c) are fitted simultaneously by eq. 3.1.

of $MoTe_2$ to other TMDCs we except that the binding energy gets smaller with increasing atomic weight of the chalcogen atom. Binding energies of MoS_2 and $MoSe_2$ are estimated to be 26 meV and 21 meV [12]. Our trion binding energy is somewhere in between. By taking substrate effect into account and assuming a less substrate coupling higher binding energy for MoS_2 and $MoSe_2$ are expected [23]. This underlines the assumption of a less supported ML and BL flake from section 2.3.1. The BL trion binding energy is $1-2\,\mathrm{meV}$ larger compared to previous publications [89, 134]. The lower binding energy of the bilayer is an effect of the increased screening of the e-h interaction towards increasing thickness as previously established for semiconductor quantum wells [152]. By tuning the excitation intensity as seen in Fig. 3.3, we confirm the trion binding energy values by constant fits, this being the first evidence for the trionic nature of the second BL peak.

Apart from emission energies, we as well evaluate the integrated area of emission as sketched in Fig. 3.1 as shaded areas for ML (violet) and BL (gray) quasiparticle emission. The intensities are in the same order of magnitude for ML and BL $MoTe_2$. To investigate the underlying quasiparticle nature, especially the trionic nature of the second BL peak, we tune excitation intensity, excitation density, and temperature as illustrated in Fig. 3.4 for ML and BL.

Fully consistent with observations on other TMDCs [44, 60, 120], we observe in Fig. 3.4 (a) a linear increase of the emission area with excitation intensity. Here, the power dependence is connected with the recombination process of free excitons and trions. If one increases the temperature, non-radiative processes should become more important, and the intensity should

scale quadratically with power [29]. In this process, the exciton emission rises faster than the attributed trion emission. To understand the physics behind we calculate the ratio of exciton to trion emission area for both, ML and BL $MoTe_2$, in Fig. 3.4 (b) as function of the excitation density. We calculate the excitation density from PL measurements using the Ti:Sa laser in the mode lock regime. To calculate the excitation density, we firstly calculate the laser fluence

$$laser\ fluence = \frac{laser\ pulse\ energy}{spot\ area} = \frac{average\ power}{repetition\ rate\ \cdot\ spot\ area}$$

assuming a round spot of 10 μm diameter, a repetition rate of the Ti:Sa Laser of 75.4 MHz, the average power is tuned from 2 μW doubling in each step up to 64 μW. Then the excitation density is calculated

$$n = \frac{fluence\ \cdot\ 4/(1+n_s)^2\ \cdot\ absorbance}{photon\ energy},$$

where we assume a refractive index n_S for SiO_2 of 1.45, a absorbance of $\sim 25\%$, and a photon energy of 1.190 eV. The ratio decreases with increasing excitation density. ML and BL show a similar evolution with n. This abatement can be explained by assuming a trion formation by excitons capturing extra electrons from the two dimensional free electron gas of low density [103, 137], where the exciton to trion ratio scales inversely proportional to the excitation density. The capture process is investigated in detail in chapter 6. This assumption predicts a temperature dependence in the equilibrium state with a chemical potential (ideal fermionic gas)

$$\mu_{chem} = k_B T\ \ln[e^{\pi\hbar n/k_B T M_{XT}} - 1]$$

of the exciton to trion ratio

$$\frac{X^0}{X^T} = \frac{g_e^2 g_X}{g_T} e^{-E_{bind} - \mu_{chem}/k_B T},$$

where $g_{e,X,T}$ is the spin degeneracy for electrons, excitons and trions. Inserting the chemical potential results in

$$\frac{X^0}{X^T} = \frac{g_e^2 g_X}{g_T} e^{-E_{bind}/k_B T} \frac{1}{e^{\pi\hbar n/k_B T M_{XT}} - 1}.$$

We assume a non-degenerated electron gas that means $g_{e,X,T} = 2$ and $\pi\hbar^2 n/M_{XT} \gg k_B T$ [13, 136] then expanding the second term to first order results in a exciton to trion ratio of

$$\frac{X^0}{X^T} = 4 \cdot e^{-E_{bind}/k_B T}\ \frac{k_B T M_{XT}}{\pi\hbar^2 n}.$$

The ratio of exciton to trion X^0/X^T reads as intensity ratio I_{X^0}/I_{X^T} times radiative lifetimes τ_X/τ_T for exciton and trion [106, 136]. Therefore, the exciton to trion intensity ratio can be

described comparable to the Saha equation [13] and mass action law [132] by

$$\frac{I_{X^0}}{I_{X^T}} = 4\frac{\tau_T}{\tau_X} \cdot e^{-E_{bind}/k_BT} \ \frac{k_BTM_{XT}}{\pi\hbar^2 n}, \tag{3.1}$$

where $M_{XT} = M_{X^0}/M_{X^T}\ m_e = 0.66\ m_e$ is the mass ratio of exciton to trion [128]. Plotting the excitation density- and temperature-dependent ratio for excitation densities between $6 \cdot 10^{10}$ cm^{-2} and $2 \cdot 10^{12}$ cm^{-2} in Fig. 3.4 (b) and temperatures in between 5 K and 60 K in Fig. 3.4 (c) and fitting the data by eq. 3.1 for ML (violet squares) and BL (gray circles) simultaneously we extract values for the exciton to trion radiative lifetime ratio of $\tau_T/\tau_X = (6 \pm 2)$ and $\tau_T/\tau_X = (3 \pm 1)$ for ML and BL, respectively. The radiative trion lifetime is larger compared to the exciton for both ML and BL $MoTe_2$. The estimate for the trion to exciton radiative lifetime ratio gives the ratio of the corresponding trion and exciton wave functions [40]. By compare the trion radiative to the exciton radiative lifetime for $MoSe_2$ of 15 ps to 1.8 ps, we found a comparable ratio of the radiative lifetime of the ML $MoSe_2$ of (8 ± 1) [133]. Moreover, outgoing from measurements of the radiative lifetime in ML and BL exciton $MoTe_2$ of 3 ps and 4 ps [134], we can estimate the radiative lifetime of the trion to be ~ 18 ps ~ 12 ps. Therefore, we assume a mixed phase of free electrons (with a low free electron density), excitons, and trions confirming a trion state in both ML and BL $MoTe_2$.

In this section, we investigate the ML and BL luminescence and exemplary explain one spectrum. We rule out that the defect peak shows an excitonic transition. We confirm the trion nature of the second BL peak by analyzing the ML and BL temperature- and excitation density dependent data in terms of the mass-action law.

3.2 Investigating phonons and collecting hints for direct BL emission

In order to obtain quantitative results on the exciton-phonon coupling and the direct or indirect nature of the bandgap of the BL, we perform a series of temperature-dependent PL measurements between 5 K and room temperature on the ML and BL. The results for an excitation power of 10 μW are shown in Fig. 3.5 (a) and (b) for ML (violet) and BL (gray), respectively. The solid black lines represent Voigt fits. As motivated in the previous section, we corrected the data for the defect peak emission. ML and BL PL emission are remarkably similar in shape and intensity on first look. The BL, shows a pronounced bright emission of excitons and trions at low temperatures compared to the ML. The evolution of the temperature of ML and BL seems to be comparable on first look. A closer inspection shows a stronger emission energy shift with temperature for the $MoTe_2$ BL than for the ML, investigated in detail in section 3.2.1. The trion peak shows up to 60 K in the ML and 50 K in the BL. This temperature range, especially the trion emission, will be investigated in the next chapter. The exciton peaks remain clearly visible up to room temperature. Large broadening mechanisms and a strong decrease in signal intensity leads to a decreasing signal-to-noise ratio with increasing temperature, especially pronounced for the BL emission. In the following we extract the emission parameters (intensity, energy, linewidth) in terms of Voigt fits (cf. section 3.1) with respect to temperature.

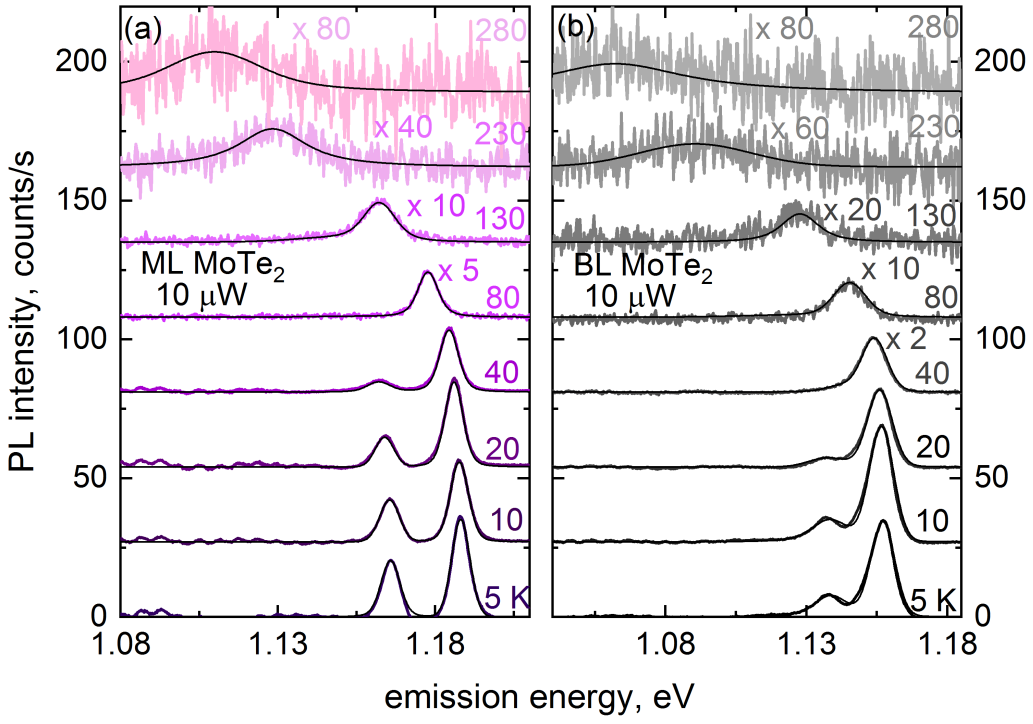

Fig. 3.5: Temperature-dependent PL of ML $MoTe_2$ (a) and BL $MoTe_2$ (b) at 10 μW excitation power.

3.2.1 Which process is shifting the emission energy?-Phonons?

In this section we investigate the emission energy of the exciton and the trion of ML and BL. We attribute the change of emission central energy with temperature as optical bandgap narrowing and find responsible mechanisms by examining a set of different equations. The main process turns out to be quasiparticle-lattice interactions with phonons. Moreover, we analyze ML and BL in direct comparison and find hints for direct optical transitions in the BL $MoTe_2$.

First, we extract the spectral maximum of the exciton emission which is directly related to the optical bandgap of the material. The optical bandgap is linked to the electronic bandgap by the binding energy of the excitons (as introduced in chapter 2). The exciton binding energy is hundreds of meV large, therefore, there is a clear difference of electronic and optical bandgap. The exciton binding energy temperature-dependence has to be separately investigated to extract electronic bandgap temperature shift. However, as introduced in chapter 2.1. the optical bandgap describes the energy necessary to excite a particle from the valance (VB) to the conduction band (CB). TMDCs have bandgap energies in order of 1-2 eV [56, 74, 101, 127] fits seamlessly in to values of classical III-V semiconductors [129, 176]. The decrease of the optical bandgap with increasing temperature is a usual semiconducting behavior known for decades [176]. There are two main bandgap shifting mechanisms: (i) Temperature-dependent electron/exciton-lattice interaction leads to a shift which scales quadratically (linearly) with temperature below (above) the Debye temperature. (ii) Temperature-dependent dilatation of the lattice results in a position shift of the VB and CB scaling nonlinearly (linearly) at low (high) temperature [9, 129, 176], associated with acoustic waves. Both terms are attributed to lattice interactions, this being an important mechanism in 3D semiconductors. As TMDC ML and BL are 2D materials, lattice interactions are even more important. However, these mechanisms equally effect both direct and indirect emission [176].

To investigate the emission shift in detail, we plot the temperature dependence of ML (violet symbols) and BL (gray symbols) for exciton (light colored symbols) and trion (dark colored symbols) in Fig. 3.6. Outgoing from the two bandgap shift mechanisms Ref. [176] proposed the so called Varshni equation, which was previously investigated by Ref. [74] in MoS_2 and $MoSe_2$. The fits with the Varshni equation

$$E_g(T) = E_g(0) - \frac{\alpha T^2}{T + \beta}, \tag{3.2}$$

are shown as dashed lines in Fig. 3.6. Here, $E_g(0)$ is the exciton peak energy (originally the free carrier/electronic bandgap energy) at zero temperature, and α and β are material constants. The shift is related to linear or non-linear temperature dependencies where the critical value is the Debye temperature. Thus, β is assumed to be related to the Debye temperature of the material.

For the ML exciton we obtain $\alpha = 5.05 \times 10^{-4}\,\mathrm{eV\,K^{-1}}$ and $\beta = 191\,\mathrm{K}$ which is in agreement with the results obtained in Ref. [75]. The correspondence to the Debye temperature as introduced by Ref. [129] cannot be confirmed for $MoTe_2$ as expected by Ref. [115]. We now extend our considerations to the BL. Results obtained for direct and indirect gap germanium [176] show a significantly different temperature dependence of the exciton peak energy. The energy shift we observe for the $MoTe_2$ BL exciton peak, however, is only slightly larger than that in the ML. Still, in particular for temperatures higher than 50 K, differences in the line broadening also become apparent. Consequently, the BL data are not described by the same set of parameters as the ML data. The Varshni fit of the BL data over the whole temperature range, yields $\alpha = 6.01 \times 10^{-4}\,\mathrm{eV\,K^{-1}}$ and $\beta = 236\,\mathrm{K}$, both slightly larger compared to the ML. However, the values are very close and in their combination result in almost identical slopes for both systems. We observe a red-shift of the emission with increasing temperature of altogether 83 and 90 meV from 5 K up to room temperature for ML and BL, respectively.

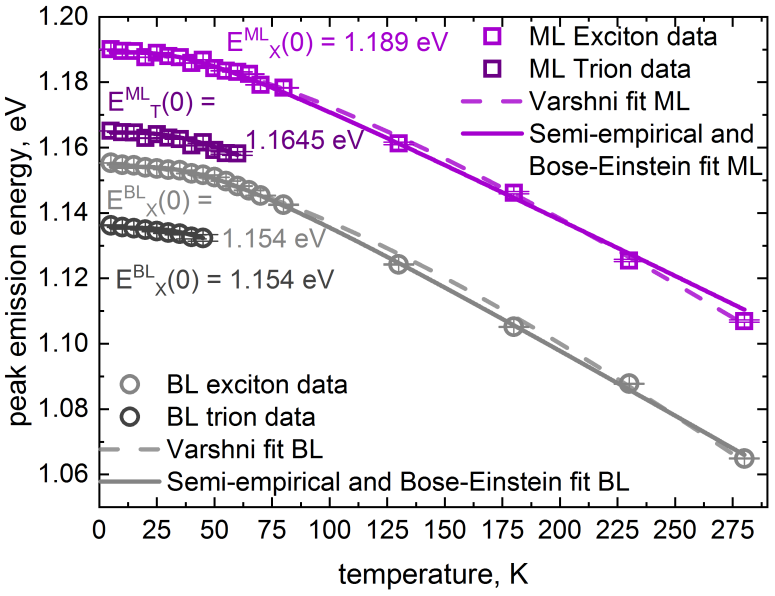

Fig. 3.6: Exciton and Trion peak emission energy of BL (gray circles) and ML (violet squares) $MoTe_2$ versus temperature. $E(0)^{ML/BL}$ indicates the extrapolated spectral energy position of the exciton at zero temperature. The dashed (solid) lines represent fits by the Varshni function (semi-empirical fit function).

The Varshni function has been used here to describe the bandgap shift empirically in experiments and does not carry a more complex physical meaning, as the β factor turns out to differ strongly from the Debye temperature. As already mentioned above the shift of the bandgap is due to lattice dilatations, so, acoustical and optical vibrations of the lattice have to be included [9, 41]. Ref. [105] introduces a general expression

$$E_g = E_0(1 + AT^x) + B\left[\Theta_A \ \coth(\Theta_A/2k_BT) + \Theta_O \ \coth(\Theta_O/2k_BT)\right]$$

including a variable dependency in x-order on T (first term) and acoustical (second term) and optical (third term) phonon-carrier coupling. Θ_i denotes the average phonon energy. The second and the third term correspond to Bose-Einstein statistical phonon factors including both emission and absorption of phonons. As the equation above contains six fitting parameters one can bring together the phonon terms in the practicable Bose-Einstein factor equation. It was formulated for semiconductors by Viña et al. in Ref. [177] and first applied to TMDCs (bulk $MoSe_2$) in Ref. [59]. Here, the energy of the bandgap is described as

$$E_g(T) = E_g(0) - s_{\text{ep}} \left[1 + \frac{2}{\exp(\Theta/k_B T) - 1}\right] = E_g(0) - s_{\text{ep}} \coth(\Theta/2k_B T),$$

where s_{ep} is a scaling factor of the mean occupancy of an average phonon mode [177].

As an alternative a semi-empirical fitting function has been introduced in Ref. [115] for GaAs and adapted to TMDCs in Ref. [74, 171]. The temperature dependence of the bandgap is described by

$$E_g(T) = E_g(0) - S \langle \hbar\omega \rangle \left[\coth(\langle \hbar\omega \rangle / 2k_B T) - 1\right], \tag{3.3}$$

where S is a dimensionless coupling constant describing the strength of electron/exciton-phonon coupling and $\langle \hbar\omega \rangle$ is the average phonon energy. Thus, this semi-empirical equation provides information about electron-phonon interactions in the material and enables calculation of the entropy and enthalpy. The fits using this description are displayed as solid curves in Fig. 3.6. Fitting results also in terms of the Bose-Einstein factor equation are equivalent for the semi-empirical fit equation due to the same underlying Bose-Einstein statistics.

With the semi-empirical equation, we obtain values of $S = (2.03 \pm 0.13)$ and $\langle \hbar\omega \rangle = (10.2 \pm 0.9)$ meV for ML $MoTe_2$ which is lower than the values for ML MoS_2 ($\langle \hbar\omega \rangle = 19$ meV) and $MoSe_2$ ($\langle \hbar\omega \rangle = 14.5$ meV)[74], indicating a coupling of excitons with lower-energy phonons in $MoTe_2$ compared to the compounds with lighter chalcogenides. In agreement with our results and as introduced in section 2.2.4, acoustic (A) phonons in ML $MoTe_2$ have been found to have an energy of 7.4 to 12 meV [48], and thus the lowest activation energy in Mo-based TMDCs [6]. There is a set of acoustical phonon modes (the phonon dispersion relation is found in section 2.2.4). The energetically lowest are the ZA (out of plane acoustic modes) followed by the transverse and longitudinal acoustical phonon (TA+LA) modes with comparable energies at the K and the M point. As the average phonon energy is around 10 meV we conclude that mostly LA phonons contribute to the lattice vibrations, supporting the early studies of Ref. [9].

Extending the fit to the trion emission we determine values of $S = (2.1 \pm 0.2)$ and $\langle \hbar\omega \rangle = (10.2 \pm 0.9)$ meV for the ML trion. Exciton and trion bandshift can be described by comparable $< \hbar\omega >$, that means the same phonon modes induces their respective bandgap shifts. The coupling constant however slightly increases from exciton to the charged trion. In terms of the Bose-Einstein factor equation the coupling constant is linked to a scaling factor of the mean

Table 3.1: Fitting constants for ML and BL luminescence.

Varshni fit and Debye temperature ML			
	α (10^{-4} eV K^{-1})	β (K)	Θ_D (K)
MoS_2	3.3 [73], 5.9 [79]	238 [73] , 430 [79]	275 [73]
$MoSe_2$	5.67 [3]	330 [3]	197 [59], 240 [74]
$MoTe_2$	5.05	191	169 ± 14
Varshni fit and Debye temperature BL			
	α (10^{-4} eV K^{-1})	β (K)	Θ_D (K)
MoS_2			414 [206]
$MoSe_2$	5.56 [3]	330 [3]	314 [3]
$MoTe_2$	6.01	236	202 ± 10
Semi-empirical fit ML			
	S	$\langle\hbar\omega\rangle$ (meV)	$\langle\hbar\omega\rangle / k_B$ (K)
MoS_2	1.16 [74], 1.82 [171]	19 [74], 22.5 [171]	220.5 [74], 261.1 [171]
$MoSe_2$	2.18 [74], 2.23 [3]	14.5 [74], 19 [3]	168.3 [74], 220.5 [3]
$MoTe_2$	2.03 ± 0.13	10.2 ± 0.9	118.4 ± 10.0
$MoTe_2$ X^T	2.13 ± 0.23	10.2 ± 0.9	118.4 ± 10.0
Semi-empirical fit BL			
	S	$\langle\hbar\omega\rangle$ (meV)	$\langle\hbar\omega\rangle / k_B$ (K)
MoS_2 [206]	2.2	25	290
$MoSe_2$ [3]	2.18	19	220
$MoTe_2$	2.38 ± 0.05	12.2 ± 0.6	141.6 ± 7.2
$MoTe_2$ X^T	2.58 ± 0.31	12.2 ± 0.7	141.6 ± 7.2

occupancy of the phonons [177]. We estimate $s_{\text{ep}} = (20 \pm 2)$ meV for the ML exciton and (21 ± 2) meV for the trion, indicating that the excitons are less strongly coupled to phonons than trions. We will investigate this in the next chapter in more detail. Besides, $< \hbar\omega > /k_B$ is the average phonon temperature [177] and is related to the Debye temperature via $0.5 < \frac{\langle\hbar\omega\rangle}{k_B}/\Theta_D < 0.7$ for semiconductors [117]. The upper limit is considered a good approximation for TMDCs. Thus Θ_D is in $MoTe_2$ lower than in other Mo-based TMDCs [59, 118], as expected by the lower bandgap energy of ML $MoTe_2$. The values for all parameters we obtained for $MoTe_2$ along with literature values for MoS_2 and $MoSe_2$ are collected in Table 3.1.

Fits of the BL data by the semi-empirical equation are carried out using $S = (2.38 \pm 0.05)$ and $\langle\hbar\omega\rangle = (12.2 \pm 0.6)$ meV which is slightly larger than the 10.2 meV obtained for the $MoTe_2$ ML. This indicates a change in the underlying phonon process. The phonon modes do not shift in energy with increasing thickness from ML to tri-layer according to Raman measurements [48]. Thus, the origin of the change in average phonon energy may be found in an optical phonon mode at 15 meV which is present in the BL but absent in the ML [48], namely the homopolar transversal optical (TO) phonon mode. Taking into account the results of experiments of ML and multi-layer MoS_2 [206] for temperatures above 100 K, where the average phonon energy increases with increasing number of layers, this is a systematic behavior of TMDCs. The change

in the average phonon energy of MoS_2 [206] is six times larger than observed for $MoTe_2$. The increase in the dimensionless coupling strength we observe is of the same order as in MoS_2 [206]. Moreover, from these values, we can estimate a change in the Debye temperature with increasing layer thickness of about 30 K. Then we expand our considerations to the BL trion and fit the emission energy change by $S = (2.6 \pm 0.3)$ and $\langle \hbar\omega \rangle = (12 \pm 1)$ meV. The parameters for the semi-empirical equation confirm an equivalent behavior to the ML $MoTe_2$, namely the same average phonon energy and a small increase in the phonon-coupling. The same values accentuating the quasiparticle nature of the trion and comparable phonon interactions of the trions. All fitting parameters for the $MoTe_2$ BL are collected in Table 3.1.

Hint 1. Comparable bandgap shifts and fits for ML and BL underline a similar band alignment.

Note. Phonons also redshift with increasing temperature, but the effect is small compared to the exciton bandgap shift. For MoS_2 Ref. [87], a net redshift of 4.4 meV (5 meV) for the LO (homopolar LO) mode from 5 K to room temperature has been measured.

3.2.2 Phonons also broadens the linewidth

In this section we investigate linewidth broadening mechanisms of excitons and can directly confirm that acoustical phonons dominate at low temperatures, where the coupling to excitons is the smallest in TMDC family. In the high temperature limit, we found optical phonons to be the major process. Moreover, we clarify limitations which will be solved in chapter 4.

There are a couple of linewidth broadening mechanisms. The most probable broadening of the homogenous linewidth is phonon induced broadening. The Bose-Einstein like phonon induced bandgap shift discussed in section 3.2.1 gives a reasonable fit of the broadening

$$\Gamma(T) = \Gamma_0 \left(1 + \frac{2}{e^{\Theta/k_B T} - 1}\right) + \Gamma_1.$$

There, the equation fits the broadening of the data with the same values as for the bandshift [177] for temperatures above 100 K. This assumes that mostly polar optical phonons contribute to the lattice interaction, which we can confirm for our data for >80 K. As predicted by Ref. [88] this is a high temperature process for temperature above 100 K. At low temperatures, as the linewidth of the quasiparticles is proportional to the phonon population. Fittingly, the acoustical phonon population increases linearly with temperature. On the other hand, the optical phonon population is insignificant. Ref. [88] estimates the line broadening from the wave function and scattering rates due to phonon-exciton interactions. The transition rates for different phonon processes are introduced in section 2.2.4 and directly linked to deformation potentials and mobility, which is the topic of the following chapter. Lee et al. [88] implement a formula for linewidth broadening including optical and acoustical phonon, impurity induced,

and (in)homogenous scattering mechanisms by:

$$\Gamma_{tot}(T) = \Gamma_0^{tot} + \gamma_A T + \Gamma_O \frac{1}{\exp(E_O/k_B T) - 1} + \Gamma_{imp} e^{-<E_B^{imp}>/k_B T}, \tag{3.4}$$

where Γ_0^{tot} include the intrinsic linewidth and broadening due to inhomogeneous fluctuations of the sample thickness in particular due to a number of non-radiative processes, γ_A is the exciton-acoustic phonon coupling strength including the deformation and piezoelectric potential, the second term arises from the interaction with longitudinal optical (LO) phonons, and the last term is due to impurity scattering with the average binding energy over all possible locations of impurities. Comparable equations to estimate the influence of exciton-phonon coupling in the linewidth broadening have been applied in GaAs-quantum wells in Ref. [139, 163].

We observed a pronounced broadening of the exciton emission peaks with increasing temperatures, as shown in Fig. 3.5. At low temperature, the peak has a FWHM of 7.9 meV, this broadening is comparable to previous observations [75, 89, 134]. We determine the FWHM of the exciton of the Voigt fit components Γ_L and Γ_G (cf. Def. 1) for ML and BL emission and plot it versus temperature for five different excitation energies, as shown in Fig. 3.7. We observe a nearly constant FWHM for temperatures below 50 K followed by an increase of the linewidth with increasing temperature for both ML and BL $MoTe_2$.

We fit our data with eq. 3.4 neglecting of the impurity-induced scattering for simplicity. Moreover, in order to reduce the uncertainty of the fit, we simultaneously fit the FWHM for five different excitations energies between 1.798 eV and 1.653 eV for ML and BL $MoTe_2$, respectively. Fig. 3.7 shows the fitting results (solid lines) for ML and BL in violet and gray on the background of the linewidth data. The linewidth broadening shows a similar behavior for all different excitation energies and does not depend on the excitation energy for this totally off-resonant excitation. This enables a global fit using all five data sets for ML and BL with to the linewidth broadening equation. The large data set allows us to extract values for all parameters (intrinsic linewidth, A-phonon coupling, O-phonon coupling and O phonon energy) without applying fitting constraints. We confirm a non-linear behavior of the linewidth broadening, where acoustical phonon scattering dominates for temperatures below 60 K (50 K) for ML (BL) $MoTe_2$. Above these temperatures optical phonons start to influence and dominate above 80-100 K. By having a closer look (cf. next chapter) on temperatures below 60 K we observe the influence of impurities and inhomogeneously broadened scattering in detail. Explaining the inadequate linear approximation for low temperatures.

We obtain $\Gamma_0^{tot} = (7.3 \pm 0.1)$ meV and (10.6 ± 0.1) meV for ML and BL, respectively, which is of the order of results obtained for $MoSe_2$ by Ref. [3] and increases analogously for the BL. It is comparable to non-encapsulated $MoTe_2$ [134] and encapsulated $MoSe_2$ and MoS_2 [147, 187], thus underlining the good quality of our sample and making $MoTe_2$ a ideal candidate to study pure excitonic and trionic effects without the influence of hBN. The intrinsic linewidth includes

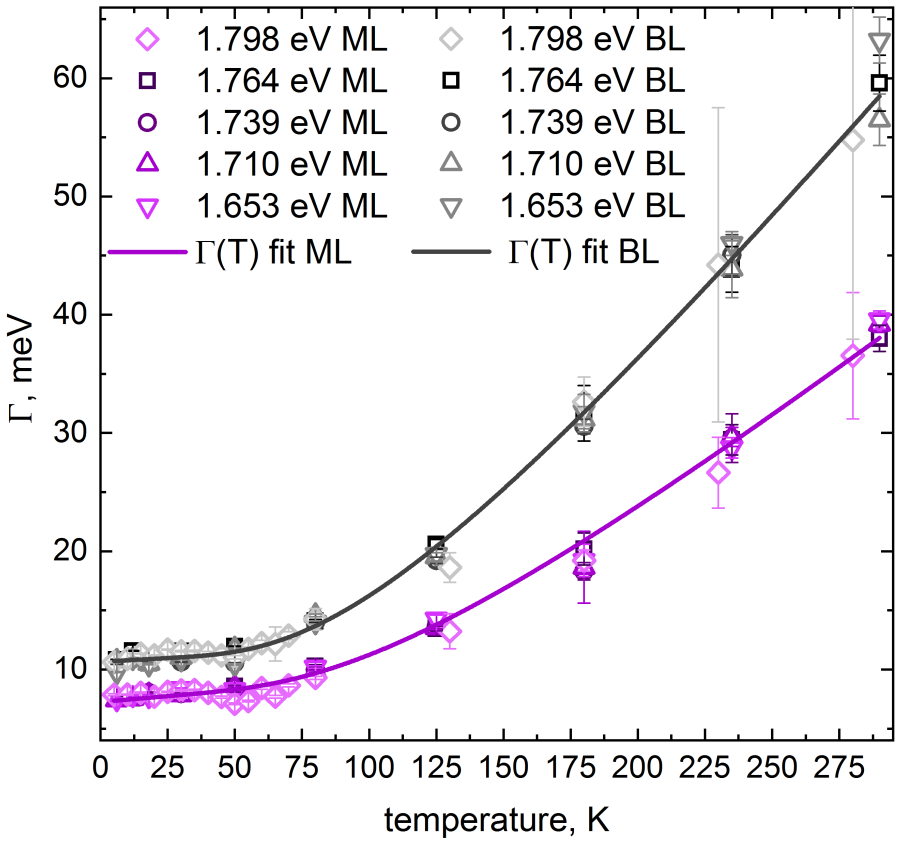

Fig. 3.7: Full width at half maximum (Γ) of the exciton emission for ML (violet symbols) and BL (gray symbols) versus temperature. The results of simultaneous fits by eq. 3.4 for five excitation energies in a range of 1.798 to 1.653 eV are shown as solid lines.

processes like radiative recombination, spin-flip scattering, exciton-exciton scattering, and so forth. One can investigate related radiative recombination lifetimes, if inhomogeneous broadening can be excluded, as done in chapter 4. ML and BL show comparable Γ_0 we assume that the difference is attributed to inhomogeneous broadening, as a thicker sample likely contains more defects and impurities [16].

Hint 2. A comparable homogenous Γ_0 indicates that ML and BL $MoTe_2$ behave similar to a direct quantum well of variable thickness.

Still, γ_A is a widely used characteristic number, providing an estimate for the upper limit of exciton-A phonon coupling. We derive $\gamma_A = (20 \pm 4)\,\mu\text{eV K}^{-1}$ and $(13 \pm 6)\,\mu\text{eV K}^{-1}$ for ML and BL, respectively. Interestingly, this agrees well with the assumption of a quantum well-like decrease of the acoustic phonon coupling with increasing well width L via $\gamma_A \sim \text{const}/L$ [10]. This effect has been observed also in other 2D materials like Nanosheets [1], the smaller phonon coupling is attributed to a smaller electron hole coulomb interactions and an increase of the lateral size of electron and hole wave functions.

Hint 3. The quantum-well-like behavior of ML and BL $MoTe_2$ supports the direct semiconductor nature of both.

Table 3.2: Fitting constants for ML and BL linewidth broadening.

Linewidth broadening ML			
	Γ_0 (meV)	γ_{LA} (μeV K^{-1})	Γ_{LO} (meV)
MoS_2 [21]	4 ± 0.2	70 ± 5	42.6 ± 1.2
$MoSe_2$	7.5 [3]	91 [148]	72 [3]
$MoTe_2$ ($E_{LO} = (30 \pm 4)$ meV)	7.3 ± 0.1	20 ± 4	61 ± 15
Linewidth broadening BL			
	Γ_0 (meV)	γ_{LA} (μeV K^{-1})	Γ_{LO} (meV)
MoS_2			
$MoSe_2$ [3]	12		93
$MoTe_2$ ($E_{LO} = (25 \pm 4)$ meV)	10.6 ± 0.1	13 ± 6	77 ± 25

Unlike Ref. [75] we observe only a very small broadening at low temperature, confirming a very small exciton-acoustic phonon coupling in our sample. The coupling strength extracted from the line broadening is of the same order as obtained from the semi-empirical fit function above. The numerical value of $\gamma_A = (20 \pm 4)\,\mu\mathrm{eV\,K^{-1}}$ for $MoTe_2$ is smaller than estimated for WSe_2 ($60\,\mu\mathrm{eV\,K^{-1}}$)[109], $MoSe_2$ ($91\,\mu\mathrm{eV\,K^{-1}}$) [148], MoS_2 ($70\,\mu\mathrm{eV\,K^{-1}}$) [21] and is of the same order as in WS_2 ($28\,\mu\mathrm{eV\,K^{-1}}$) [148]. These values are similar to the values obtained for $MoSe_2$ and MoS_2 in Ref. [156]. The small influence of acoustic phonon coupling is thus an effect of relative low exciton mass and high material density in $MoTe_2$. Note, we do not exclude inhomogeneous broadening at this point, for more information see chapter 4.

In the high temperature limit where optical phonons dominate, the fit for the ML returns an O-phonon energy E_O of (30 ± 4) meV consistent with the E_{2g} homopolar longitudinal optical (LO) phonon mode at 30 meV for $MoTe_2$ [6, 48] and discussed in detail in section 2.2.4. The BL linewidth broadening is described best using a slightly lower optical phonon energy of $E_O = (25 \pm 4)$ meV (gray line Fig. 3.7). This effective lower energy providing superior fitting may be due to an additional nonpolar optical (E_{1g}) phonon mode for the BL at ~ 14 meV and a stronger coupling to the polar TO phonons with a energy of 19 meV [48]. LO phonon lattice interaction induces a macroscopic electric field coupling to the carriers. The resulting Coulomb interactions between excitons and LO phonons can be described in terms of Fröhlich interactions in 3D and slightly differently in 2D [69]. The interactions strongly depend on the order of the deformation potential which for its part depends on the mode (polar, homopolar; LO, TO) of the phonon. The coupling to optical phonons $\Gamma_O = (61 \pm 15)$ meV for the ML is smaller than $\Gamma_O = (77 \pm 25)$ meV for the BL. This is reflected by the large linewidth displayed by the BL emission at high temperature. In an ideal quantum well, the exciton-LO phonon coupling is expected to scale linearly with the well width [153]. Our results show that the increase of Γ_O for BL $MoTe_2$ compared to the ML is only about 15%. A similar dependence has been observed also for the BL of $MoSe_2$ in Ref. [3]. This shows that the sublinear dependence of exciton-LO phonon coupling does not result from the peculiar band structure of $MoTe_2$ but is rather

universal for TMDCs. The underlying reason might be an offset caused by the contribution of the polarizability of the substrate to the overall charge distribution. The fitting results are collected in table 3.2.

3.2.3 Thermal quenching of emission area by phonons

In this section we investigate the emission area, that means the exciton population with increasing temperature. There, we found that the main process causing a decay in intensity with temperature by the escape of carriers due to interactions with optical phonons. At low temperatures we observe a twice as intense BL emission compared to the ML, supporting the direct optical transition in BL $MoTe_2$.

The simplest concept of PL emission intensity is assuming a two level system with radiative and non-radiative transitions for carriers from the CB to the VB. Measurable emission results from bright radiative transition. The emission area is the area approximated by the Voigt-profile fit of the emission spectrum (cf. Def. 1). In Fig. 3.8, the emission area for ML and BL is plotted as violet squares and gray circles, respectively, versus temperature. For temperatures above 25-30 K the intensity of the emitted light decreases with increasing temperature, fully consistent with observations on other Mo-based TMDCs [3, 79, 171]. This process is called thermal quenching [155]. In principle, if the energy separation between the CB and the VB is sufficiently large compared to the temperature ($E_g \gg k_B T$), we do not expect a thermal activation of the system. Therefore, with increasing temperature the number of particles in the CB decreases due to more efficient scattering.

At temperatures below 30 K the integrated area of emission shows a slight dependence on the excitation energy and an increase of the emission area with temperature. Thus, more processes than thermal quenching have to be included. Shibata [155] attribute the rising to "negative thermal quenching" through states in between the CB and the VB and/or additional CB states. The energy separation between these states is then low enough to make thermal activation of carriers possible which can also explain the dependence on the excitation energy. Note that at low temperature, the BL shows an intensity which is approximately twice the ML emission intensity as previously observed by Ref. [89, 134]. In contrast, the BL of MoS_2 and $MoSe_2$, with a confirmed indirect exciton in the BL, is almost dark [101, 171]. Based mainly on the large photon yield from the BL, it has been conjectured in Refs. [43, 89, 134] that the $MoTe_2$ BL has a direct excitonic transition. Varying the excitation energy in the range from 1.798 eV to 1.653 eV demonstrates that this high brightness of the BL emission is systematic for a wide range of excitation wavelengths, see Fig. 3.8. The BL shows a very bright luminescence and is more intense than the ML consistently for all excitation energies. The large photon yield does not depend on the excitation conditions. To compare absolute values of the intensity we determine the ratio of BL and ML intensity. The results are shown as blue rectangles in Fig. 3.8 (Inset).

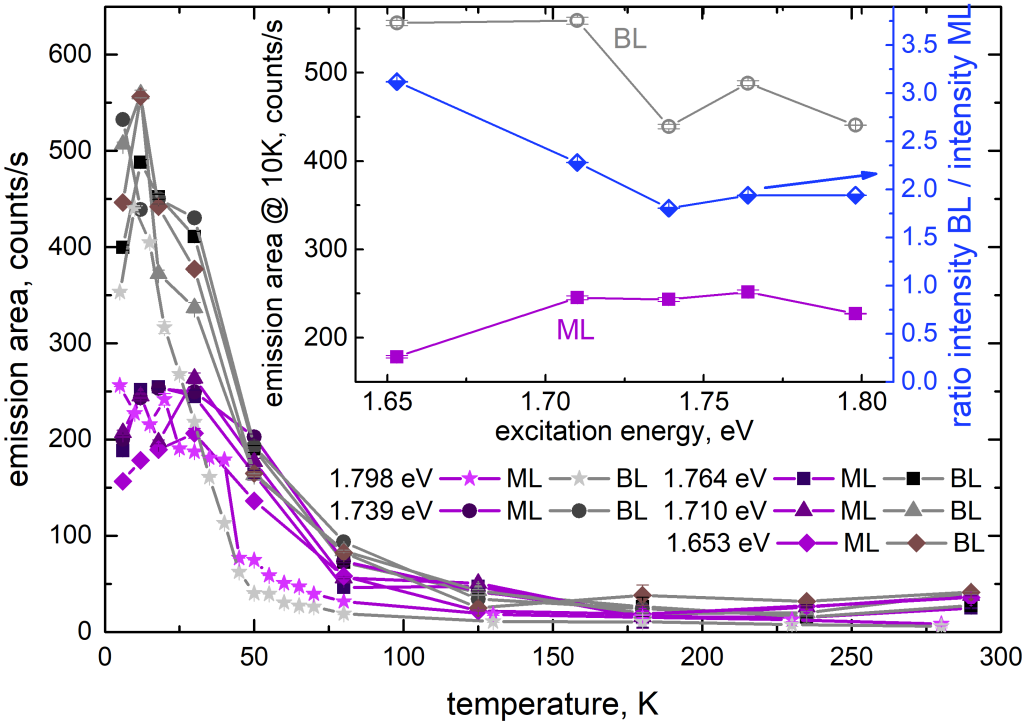

Fig. 3.8: (Main) Excitation energy dependent ML (violet symbols) and BL (gray symbols) PL intensity. (Inset) (Left axis) Integrated area of PL emission for ML (violet squares) and BL (gray circles) $MoTe_2$ as a function of excitation energy at 10 K. (Right axis) Ratio of BL and ML integrated area of emission (blue rectangle).

At large excitation energies we observe an approximately twice as large emission intensity of the BL compared to the ML. The ratio increases nearly linearly with decreasing energy up to 2.7, thus, this large BL photon yield is systematic for a wide range of excitation energies.

Hint 4. The high BL emission intensity suggest that the $MoTe_2$ ML and BL display the same band alignment, with a similar direct transition.

We choose an excitation energy of 1.798 eV for optimal signal to noise ratio and investigate the functional form of the temperature dependence of the luminescence (cf. Fig. 3.9), which is well established for a range of semiconductors, where thermally activated scattering processes cause the loss of intensity [155]. We assume that a thermal escape of quasi-particles due to scattering via optical phonons established for quantum dots embedded in quantum wells by Ref. [175] and adapted to the TMDC-regime by Ref. [133] is responsible for the decrease in excitonic emission. Therefore, we make the ansatz following Ref. [175] that the PL intensity is the integral over the PL intensity per time unit

$$I_{PL}(T) = \int_0^\infty I_{PL}(t)dt = \int_0^\infty \frac{n(t)}{\tau_{rad}}dt,$$

where, τ_{rad} is the radiative recombination time and $n(t)$ is the carrier population, assessable by a rate equation $dn/dt = g(t) - n/\tau$ with respect to the generation rate g(t) and the PL

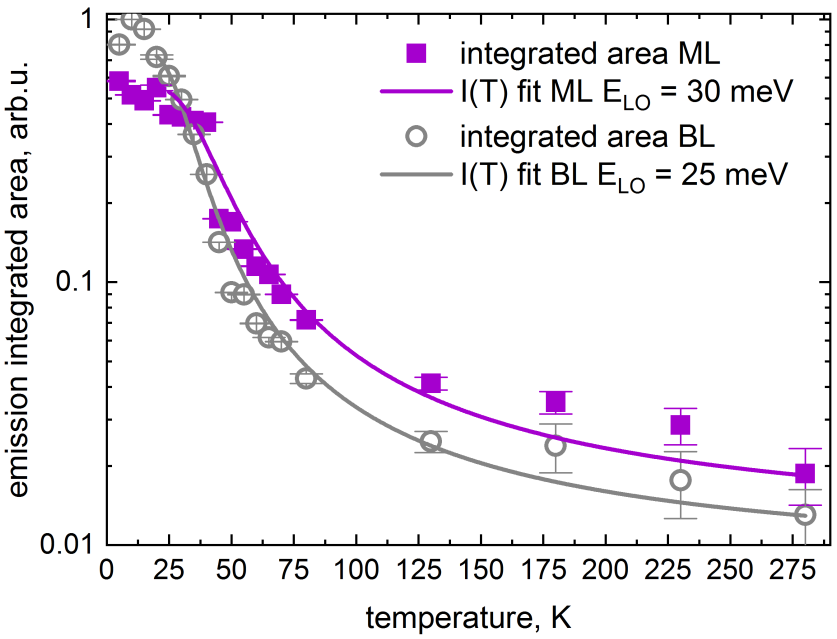

Fig. 3.9: Integrated intensity of the emission spectrum for ML (violet squares) and BL (gray circles) versus temperature. The solid lines are fits with Eq. 3.5.

decay rate τ. Thus $n(t) = n_0 e^{-t/\tau}$, where n_0 is the initial carrier population. Then we assume that $1/\tau$ includes the radiative decay $1/\tau_{rad}$ and the non-radiative decay in terms of a thermal escape rate of the carriers $1/\tau_{esc} = 1/\tau_0 (e^{E_O/k_B T} - 1)^{-m}$ due to scattering with m involved optical phonons of energy E_O which is the main loss process for higher temperatures. Thus the emission area is [175]

$$I(T) = \int_0^\infty \frac{n_0}{\tau_{rad}} e^{-t} e^{1/\tau_{rad} + 1/\tau_{esc}} \, dt = \frac{I(0)}{1 + \tau_{rad}/\tau_0 \, (e^{E_O/k_B T} - 1)^{-m}}, \tag{3.5}$$

where $I(0) \sim n_0$ is the PL intensity at zero temperature, E_O is the O-phonon energy which was taken to be 30 meV for ML and 25 meV for the BL consistent with the best fits of the FWHM of the emission lines in Fig. 3.7, and $m \sim 1$ is the number of O phonons involved in the process. We estimate a $\tau_{rad}/\tau_0 = (30 \pm 15)$ and (60 ± 23) for ML and BL $MoTe_2$, respectively. One can find an estimate for the radiative decay in section 3.1, whereas the non-radiative decay is investigated in chapter 6. The values are in the same range within the error bars for ML and BL. The temperature dependence for $T > 20$ K of the emission of ML and BL appears to be well described without having to resort to an additional thermally activated process as it would be the case if the band alignments were different. This analysis neglects the thermally activated part at low temperatures which we found to be dependent on the excitation wavelength.

Hint 5. The same temperature dependence for temperatures above 20 K indicates the same direct band alignment for ML and BL.

3.2.4 Connecting hints for direct BL emission

In conclusion, we have analyzed the temperature dependence of the energy, linewidth, and intensity of the exciton luminescence of ML and BL $MoTe_2$. The linewidth exhibited by $MoTe_2$ at low temperature is comparable to other Mo-based TMDCs, but we find a very low coupling to acoustic phonons. This leads to a stable narrow linewidth of the $MoTe_2$ emission in particular at low temperatures, where optical phonons still play a little role. The coupling to optical phonons is more pronounced for the BL, however, the adverse effect of a somewhat stronger line broadening is compensated by the very bright luminescence of the $MoTe_2$ BL. In the linear excitation regime at low temperature, we observe an approximately twice as large emission intensity of the BL compared to the ML. The shift of the emission wavelength and the intensity decay of the emission with increasing temperature both support the assumption that the $MoTe_2$ BL has the same direct band alignment as the ML, in contrast to BLs of all other TMDC materials.

4 Phonon-limited Mobility in $MoTe_2$

In this chapter, we study the temperature dependence of Gaussian and Lorentzian linewidths of the quasiparticle photoluminescence of monolayer and bilayer molybdenum ditelluride in the temperature range between 5 K and room temperature. In an analysis of the Gaussian linewidth we disentangle the effects of local defect potential induced fluctuations of the layer width and the influence of trions with slightly different (~ 2.2 meV) energies, particularly in the bilayer. The Lorentzian part of the Voigt lineshape function for exciton and trion emission in monolayer and bilayer gives an estimate of values for exciton and trion deformation potentials and acoustic and optic phonon limited mobility in molybdenum ditelluride. We estimate a lower limit of 6000 $cm^2V^{-1}s^{-1}$ (2000 $cm^2V^{-1}s^{-1}$) and 4300 $cm^2V^{-1}s^{-1}$ for the exciton (trion) acoustic phonon limited mobility at 5 K for ML and BL, respectively. At higher temperatures, the optical phonons dominate, limiting the mobility. Compared to estimated values for molybdenum diselenide in the literature, [69] molybdenum ditelluride is an excellent candidate for designing opto-electronic devices based on this high mobility combined with the semiconducting behavior essential for optoelectronic applications. Combining the two properties is necessary to satisfy the growing demand for touchable and wearable electronic devices. TMDCs can be an adequate material in addition to the zero bandgap material graphene, which features a high quasiparticle mobility [15, 20]. In the following sections, we extract upper and lower mobility values for excitons in monolayer and bilayer. All in all, the finite direct bandgap of the monolayer and bilayer, the robustness and the non-necessity of encapsulation make molybdenum ditelluride a promising material for opto- and valley-tronic applications.

4.0.1 Introductory remarks

The previous chapter deals with the Voigt linewidth of the PL and raises a number of questions about homogenous and inhomogeneous parts of the linewidth and how they connect to quasiparticle behavior. Therefore, we base the following analysis on the temperature dependent photoluminescence of ML and BL $MoTe_2$ from flake 1 (cf. section 2.3) investigated in chapter 3. Here, we focus on the Gaussian and Lorentzian linewidth part of the Voigt functions in more detail. By investing the individual linewidth parts, we are able to disentangle the effects of homogenous and inhomogeneous linewidth and the corresponding broadening mechanisms. In the previous chapter, we confirm a trion transition in the BL $MoTe_2$. Now we investigate which trions in particular participate in the bright optical transition for both ML and BL $MoTe_2$. To do so, we compare the Gaussian linewidth of exciton and trion for both ML and BL $MoTe_2$. In addition, the Lorentzian part gives us information about intrinsic linewidth and lifetimes of the related processes. The temperature evolution of the Lorentzian linewidth clearly shows a phonon dominated broadening. The phonon broadening is estimated by phonon coupling to the excitons. Relaxation times of the carriers depend on their energy and on scattering mechanism with phonons. Starting from this assumption, we can directly link linewidth broadening to deformation potentials, scattering, relaxation lifetime and, thus, address the transport properties like mobility.

4.1 The Gaussian linewidth - investigating inhomogeneity

In this section, we focus on the Gaussian part of the Voigt profile. The Gaussian linewidth is indicative of inhomogeneous broadening due to defect induced broadening and several non-radiative processes, as it would be the case for a randomly fluctuating local potential via defects. In principle, we understand the inhomogeneous broadening as a number of sharp emission peaks overlapping slightly in energy, thus, forming a much broader band [10].

Figure 4.1 (a) shows the FWHM of the Gaussian portions of the linewidths for ML (violet squares) and BL (gray circles) exciton (closed symbols) and trion (open symbol) versus temperature at an excitation intensity of 35 Wcm^{-2}. We observe an approximately constant Gaussian FWHM (Γ_G) for the whole temperature range. The data below 60 K are especially interesting for a detailed consideration of the trion, as the trion signature vanishes at higher temperature as investigated in chapter 3. The Gaussian linewidth in the temperature range is linearly fitted (solid lines). The ML exciton has a $\Gamma_G = (6.9 \pm 1.8)\,\mathrm{meV}$ and is comparable to the Voigt FWHM as exemplary shown in Fig. 4.1 (b) as a function of excitation intensity at 24 K. This indicates that especially at lower temperatures the dominating broadening process is inhomogeneous. The ML trion in Fig. 4.1 (a) (violet open squares) shows a similar broadening compared to the exciton of $\Gamma_G = (6.8 \pm 1.4)\,\mathrm{meV}$ indicating that similar processes and local

potential changes influence the emission energy of the quasiparticles in ML. We can estimate the broadening due to layer thickness fluctuations induced by defect potentials by [10]

$$\Gamma_G = (2\cdot)\delta E_e + \delta E_h = \frac{\hbar^2\pi^2}{2L^3}\left[(2\cdot)\frac{1}{m_e^*} + \frac{1}{m_h^*}\right]\delta L,$$

where in case of the trion we have to consider the factor 2, L is the layer thickness, and δL is the change in layer thickness. We estimate for the ML exciton and trion a change in layer thickness of $\delta L \sim ((4.7 \pm 1.2)\% \cdot a$ and $\delta L = (3.1 \pm 0.6)\% \cdot a$ in percentage of the lattice constant a. Thus, a comparable change in layer thickness due to the influence of a potential induced by defects of exciton and trion results in a stronger inhomogeneous broadening of the trion. At temperatures between 45-55 K the change of the layer thickness δL is smaller compared to lower and higher temperatures indicating that the electrons are interacting more and more with the same defect states resulting in a modified Gaussian shape.

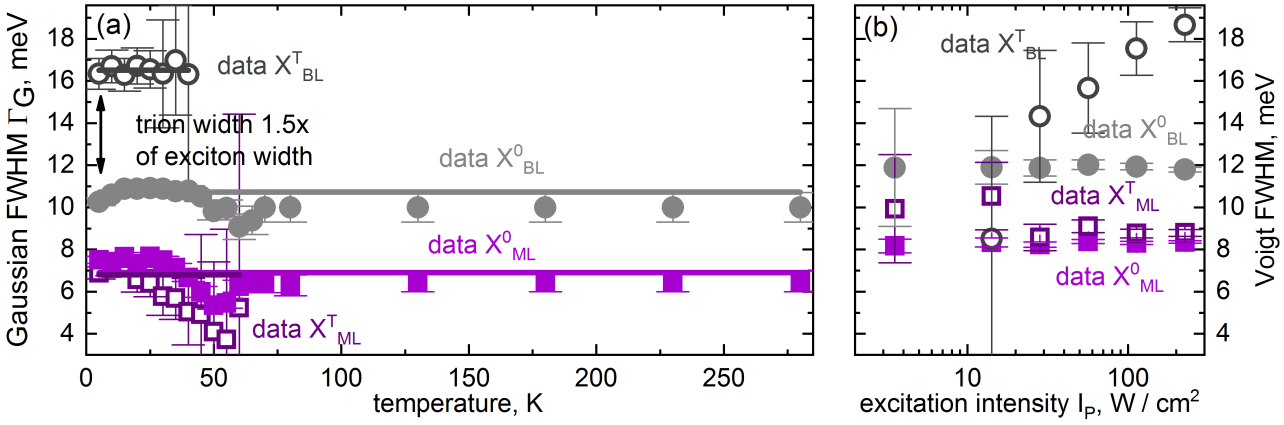

Fig. 4.1: FWHM of the Gaussian (a) part of the Voigt fit for ML (violet squares) and BL (gray circles) excitonic (closed symbol) and trionic (open symbol) emission versus temperature at 35 Wcm^{-2}. The solid lines represent linear fits with zero slope. (b) Excitation intensity dependence for ML and BL Voigt FWHM at 24 K.

The broadening process is dominating for thin layers as it scales with $1/L^3$. The BL exciton shows a pronounced broadening compared to the ML of $\Gamma_G = (10.7 \pm 0.6)$ meV in Fig. 4.1 (a, gray closed circles) at low temperatures resulting in a change of layer thickness of $(11.4 \pm 0.3)\% \cdot a$ which is in principle twice as much as the ML, as we expect. The BL trion (gray open circles) shows a pronounced broadening of $\Gamma_G = (16.5 \pm 0.6)$ meV exceeding the broadening of the exciton, in contrast to the ML data. We found that the broadening is ~ 1.5 times of the broadening of the BL exciton. As the ML trion broadening does not differ drastically from the exciton, at least trions of two different energies have to be considered for the BL. To study this problem in detail, we investigate the trion nature in ML and BL $MoTe_2$ in the following sections.

4.1.1 Which is the main trion in the ML?

For the ML, Γ_G of exciton and trion remain similar through the whole temperature range. This indicates the presence of only one trion species which we confirm by an equal excitation intensity dependence in Fig. 4.1 (a, violet symbols). To identify the trion state we discuss the level schemes of exciton and trion for the ML. We start with the ML exciton. The level schemata for the exciton are represented in Fig. 4.2. There are eight possible exciton states. Due to the special band structure of the Mo-based TMDCs, as introduced in section 2.1, the lowest optical transition is bright, and electrons and holes have the same spin. Therefore, the dark excitons, where the electron and hole have opposite spins are not the energetically preferred. In (a) and (c) bright excitons within the same valley are created. We call this type of exciton an intra-valley exciton. Both excitons are energetically identical and can be excited by left or right circular polarized light. The second pair of bright excitons (b,d) is a so called inter-valley exciton as electrons and holes located in opposite valleys. This exciton configuration is energetically not favorable compared to the bright exciton state. (e,g) and (f,h) represents dark exciton states which cannot be detected with PL measurements. In typical semiconductors where the binding energy of the dark exciton is smaller than the one of the bright exciton [31] these states are preferred scattering states of the bright excitons due to non-radiative decay. In the case of $MoTe_2$, the dark inter-valley exciton (f,h) is a possible scattering channel. However, the exciton state we can observe in PL has to the bright intra-valley exciton. We use the observations made on the exciton to now investigate the trion states.

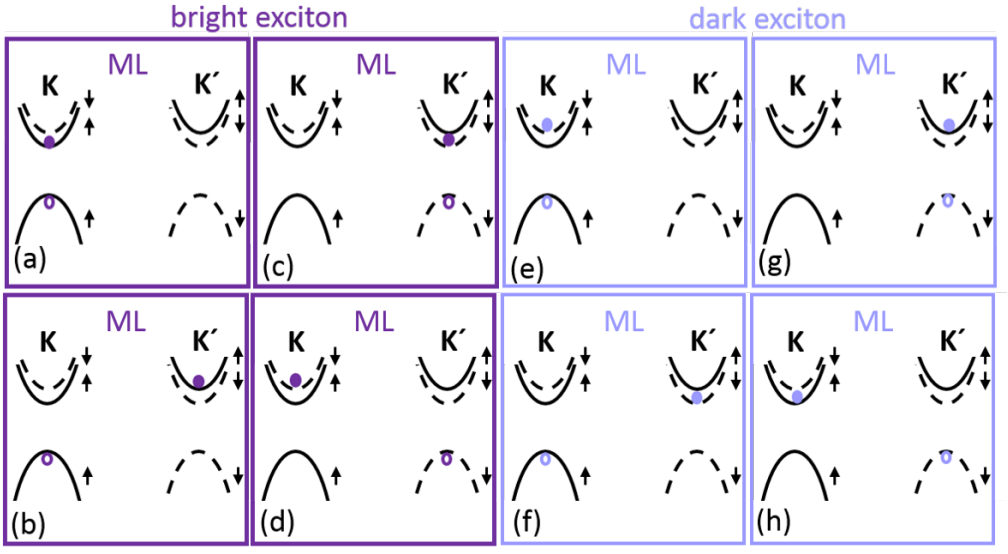

Fig. 4.2: Sketch of the ML, bright (violet) and dark (light violet) excitons in the K and K′ valleys. (a,c), (e,g), (b,d), and (f,h) represents excitons with the same energy where the electron and hole are located in the opposite valleys, respectively.

The possible trion states are sketched in Fig. 4.3 for bright (violet) and dark trions (light violet). There are 12 possible trion states, we only show six in Fig. 4.3 as the other six correspond

to the trion states where the carriers are located in the opposite valley. The three dark trion states all being inter-valley trions. (e) and (f) have the opposite spin for the electron/hole pair and the extra electron (excess electron). (d) has the same spin for the e-/h pair and the excess electron. (d) and (e) are non-degenerate in energy though due to identical spin of the excess electron and the e-/h pair the energy of trion (d) is enhanced [35, 197]. In addition, there are three bright trion states. (b) is the intra-valley trion and it is energetically comparable to the inter-valley trion (c) apart from the small separation in energy due to the same spin states of the e-/h pair and the excess electron in (c). With the lowest-energy exciton of $MoTe_2$ being bright, the most relevant trion state in particular at low temperature is an inter-valley trion (a) with the exciton occupying the K/K' valley and the extra electron residing in the lowest energy level of the conduction band of the K'/K valley [159]. It has the lowest energy of all possible trion states, bright or dark. As the inter-valley trion is bright and low in energy it dominates the PL emission. We expect these trions to form from intra-valley excitons by capturing an extra charge [122]. The responsible processes will be investigated in detail in chapter 6 in pump probe measurements. However, the trion and its opposite valley trion have the same bright exciton as initial state consequently exciton and trion show comparable inhomogeneous broadening of the linewidth.

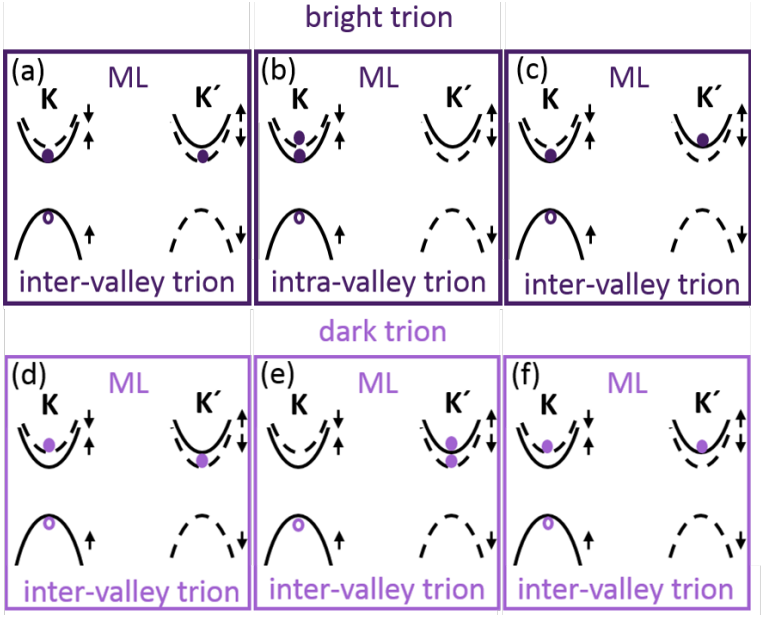

Fig. 4.3: Sketch of the ML, bright (violet) and dark (light violet) inter- and intra-valley trions in the K and K' valleys.

4.1.2 Which is the main trion in the BL?

As presented in the BL, values for Γ_G differ from exciton to trion by a factor of 1.5. As observed previously in WSe_2 [35, 159, 197], spin degenerate trion states split in energy. Therefore, we first investigate the level schema of the exciton in the BL in Fig. 4.4. The BL is in principle a set of two ML stacked together by Van der Waals forces as introduced in chapter 2.1. In a homo-bilayer the K and K' valleys are no longer coupled to spin as introduced in section 2.2, so that we cannot distinguish valley K from valley K' point in terms of spin as observed in the ML. We illustrate this in Fig. 4.4. Due the AA' stacking in the natural homo-bilayer, the upper and lower layers have opposite spin. That means a bright exciton is either located in the upper or the lower valley as sketched in Fig. 4.4. There are eight possible bright excitons, we only sketch the energetically lowest ones chosen equivalent to the ML case. For the BL trion, more possible configurations can be imagined, with the extra charge being confined to either of the two layers due to restored inversion symmetry, thus weakening valley selection rules.

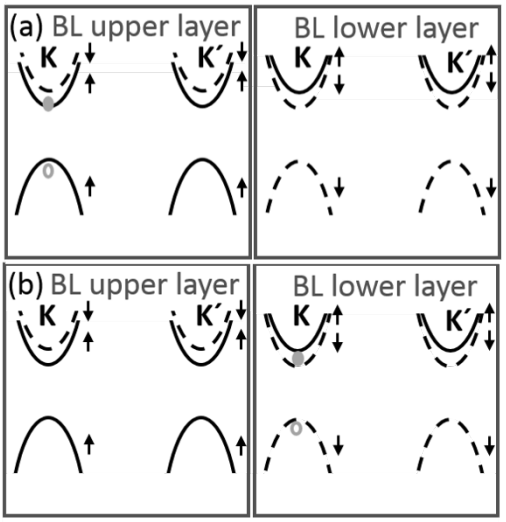

Fig. 4.4: Sketch of the upper, and lower BL K and K′ valleys plus energetically optimal bright excitonic states.

There are 28 possible optically active bright trion states in BL TMDCs. 12 of these are so-called intra-layer trions, whereas the others are upper and lower inter-layer trions. 16 out of 28 are energetically unfavorable at low temperature and small excitation density. The remaining states are sketched in Fig. 4.5 for the exciton in the K valley and upper layer. A fine structure trion splitting (trion states with distinguishable energy) is observed in WSe_2 due to short range contributions to electron-electron and electron-hole (J'_{eh}) Coulomb exchange interactions [35, 197]. According to Ref. [197], only trion states where electron-hole pair and the extra electron have the same spin show a non-zero exchange interaction between the excess electron and the electron hole pair. Consequently, we do not expect to see a splitting in ML inter- to intra layer trions. However, the non-zero J'_{eh} causes a shift of the intra-layer trion to higher

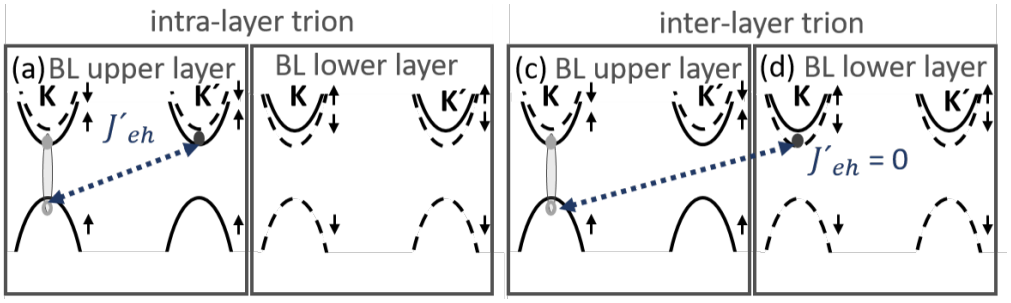

Fig. 4.5: Sketch of the upper, and lower BL K and K′ valleys plus energetically optimal bright excitonic and trionic states. Thereby, the bright exciton is highlighted by an ellipse color. J'_{eh} denotes the exchange interaction energy between the excess electron and the electron-hole pair.

energies in BL. The splitting can be estimated by [197]

$$J'_{eh} \sim \frac{0.6a}{4a_{eh}} \frac{e^2}{\epsilon_{SC} a_{eh}} = \frac{0.6a}{4a_{eh}} \frac{E_{bind} * a_B}{a_{eh}} \sim 2.2\,\text{meV}, \tag{4.1}$$

where we use the estimate of the Bohr radius and Rydberg energy in eq. 2.3 and assume the binding energy is equivalent to the Rydberg energy so that $E_{bind} \sim 509$ meV in agreement with chapter 5 and Ref. [134], $a_B = 2$ nm is the Bohr radius, $a = 0.352\,\text{nm}$ [78] is the lattice constant, and $a_{eh} \sim 2.5 \cdot a_B$ [197, 203] is the distance from the excess electron to the hole.

As discussed above in Fig. 4.1 (a), the BL trion shows a linewidth broadening 1.5 times of the BL exciton in contrast to the ML. This observation agrees with the assumption of a split trion state in the BL with a splitting of $\sim$ 2.2 meV. We observe in Fig. 4.1 (a, violet open symbols) the envelope of two energy separated inhomogeneous broadened trion states. Therefore, the measured Gaussian linewidth consist of a mixture of the inter- and the intra-layer trion states. The Voigt FWHM in Fig. 4.1 (b) varies for the BL trion with excitation intensity from broadening comparable to the ML to a twice as large FWHM at higher excitation intensity. As the excitation intensity is directly linked to carrier densities as shown in section 3.1.2 we can understand this process as population of the intra-layer trion state with an energy separation to the inter-layer exciton of 2.2 meV. So, this means at low excitation density one of the trion states is preferentially populated. By increasing the excitation intensity, more carriers are able to populate the layers and so both trion states are populated equally.

In conclusion, we investigate the inhomogeneous linewidth and find that the broadening is dominated by fluctuations of the layer thickness (δL) by local potential changes for example by defects. In addition, we find the main trion, namely the bright inter-valley trion in the ML and the bright intra- and inter-layer trions in BL, to be responsible for the measurable emission in PL spectroscopy. Additionally, the two trions in BL are energetically separated and explain the unusual strong broadening in the BL trion emission. In pump probe experiments (cf. chapter 6) we can further investigate the dark states which cannot been measured in PL.

4.2 The Lorentzian linewidth and its connection to transport properties

In this section, we analyze the homogenous linewidth and address parameters of intrinsic linewidth, exciton-acoustical and -optical phonon coupling and optical phonon energy. We directly link the parameters to dephasing time, deformation potentials, and transport properties like phonon limited mobility and relaxation time. We find out that especially at low temperature $MoTe_2$ has promising transport properties usable in opto-electronic devices.

Firstly, we investigate scattering induced broadening of the linewidth. As clarified in the previous chapter in detail, broadening of the linewidth is attributed to phonon processes by equation 3.4. By disentangling the Lorentzian and Gaussian parts of the linewidth we can ignore influences of inhomogeneous broadening. Homogenous effects affect the whole exciton population equally, such as scattering with phonons, and can be analyzed by the Lorentzian linewidth Γ_L. To do so, we repeat the linewidth broadening analysis from chapter 3 and separate the problem into two temperature ranges. For temperatures below 60 K we assume dominant scattering by acoustical phonons and for the whole temperature range we take optical phonons additively into account. At low temperature, we can also investigate trions introduced in chapter 2.1.2, which vanish for higher temperatures. As we only consider trions at these low temperatures we ignore fermionic broadening of the linewidth, the more so as we do not observe an asymmetric trion lineshape typical for the fermionic broadening [31].

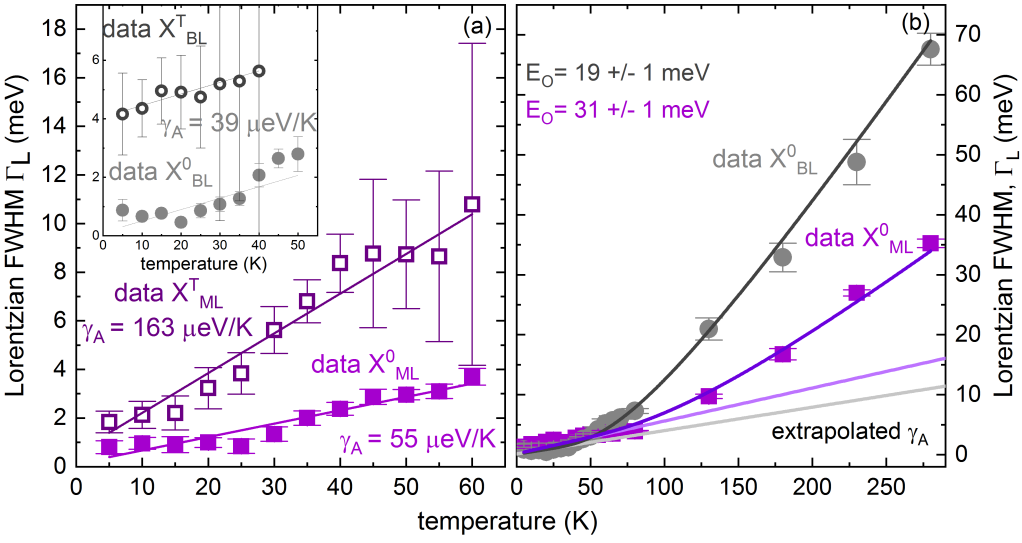

Fig. 4.6: FWHM of the Lorentzian part Γ_L of the Voigt fit for ML (violet squares) and BL (gray circles) excitonic (closed symbol) and trionic (open symbol) emission versus temperature for two different temperature ranges. The data in (a+b) are fitted by broadening equation 3.4 where we in (a) set $\Gamma_O \sim 0$.

The data for homogenous broadening are presented in Fig. 4.6 (a+b) for ML (violet squares) and BL (gray circles) for the two different temperature ranges. For low temperatures the

Table 4.1: Fitting constants for ML and BL linewidth broadening.

	Γ_0 (meV)	γ_{LA} (μeV K^{-1})	Γ_O (meV)	E_O (meV)
ML X^0	0.1	55 ± 5	50	31 ± 1
ML X^T	0.6	163 ± 15		
BL X^0	0.1	39 ± 6	70	19 ± 1
BL X^T	4.0	39 ± 6		

Lorentzian FWHM increases linearly with temperature (Fig. 4.6 (a)) for all quasiparticles. Thus, we analyze the low temperature data by only considering acoustical phonons by a linear version of eq. 3.4, namely $\Gamma_L = \Gamma_0 + \gamma_A T$. Please note, Γ_0 now only describes intrinsic broadening mechanisms. Considering the whole temperature range, we observe the same non-linear increase of the linewidth with increasing temperature as in the previous chapter. We fit the data of Fig. 4.6 (b) by eq. 3.4, assuming the same values for γ_A and Γ_0 as extracted from the fit of the low temperature range. Γ_O is chosen within the errors of chapter 3. Fig. 4.6 (b) indicates that 55-60 K are well chosen as turn-off temperature by comparing the variation of the data to the extrapolated γ_A. The resulting parameters for ML and BL $MoTe_2$ are summarized in table 4.1. In the following sections we analyze the fitting parameters in more detail and connect them to transport properties and dephasing time.

4.2.1 Intrinsic broadening and lifetime

The first term in the linewidth broadening fit Γ_0 is called intrinsic linewidth. The values for Γ_0 are extracted from the fit and summarized for ML and BL exciton and trion in table 4.1. Γ_0 is determined by a number of scattering processes like radiative recombination, exciton-exciton scattering or spin-flip scattering. In addition, the intrinsic linewidth is linked to a dephasing time $T_2 = \frac{2\hbar}{\Gamma_0}$. We estimate T_2 times of 13 ps and 2.2 ps for ML exciton and trion and 13 ps and 0.3 ps for BL exciton and trion, respectively. The T_2 for ML and BL exciton are similar, indicating that comparable processes on similar timescales are responsible for the intrinsic broadening. The trion dephasing time is smaller than the exciton in case of the ML indicating that we are dealing with intrinsic linewidth, otherwise the exciton T_2 should be smaller than the one of the trion due to non-radiative phonon mediated exciton to trion scattering channels. The Γ_0 of the BL trion is high compared to the ML exciton and trion and BL. We attribute this high value due to the energy shift in between two different trion modes in the BL of 2.2 meV. Taking these separations into account, comparable intrinsic linewidths for both trion modes are possible. Further measurements on the BL for example on electrically gated samples may allow to better resolve each trion separately.

4.2.2 Quasiparticle coupling to phonons and deformation potentials

As investigated in chapter 2.1.4, excitons interact with phonons, which is modeled by the transition rate $W(k, k')$ in equation 2.6. The acoustic phonon limited Lorentzian linewidth is directly linked to the rate by [10]

$$\Gamma_L = \frac{\hbar}{2} W(k, k'). \tag{4.2}$$

The transition rate is determined by the deformation potential. Def. 2 indicates that the deformation potential changes with the involved phonon modes/branches.

Scattering with acoustic phonons, especially TA and LA as introduced in section 2.1.4 is elastic as the energy of the phonons is small compared to $k_B T$, thus, $q = 2k \sin(\theta/2)$, where θ is the angle between k and k'. The coupling matrix element scales linearly in q such that $M_q = D_X \cdot q$. Note the ZA phonon mode scales quadratically in q and is not investigated in the long-wavelength limit [69]. The deformation potential for an exciton reads $D_X = D_e - D_h$ [10, 156], where $D_{e(h)}$ is the electron (hole) deformation potential. Thus, we can estimate the scattering rate $W(k, k')$ for optical excitation with $k = 0$ analogous to a quantum well of thickness L for + absorption and − emission of a phonon [10] by

$$W_{\pm}(k = 0) = \frac{3 k_B T M_X (D_e - D_h)^2}{4 \hbar^3 \rho v_s^2 L},$$

where M_X is the exciton mass, ρ is the density of $MoTe_2$, v_s is the sound velocity, and L is the well thickness. Combining the equation with eq. 4.2, we can directly link the temperature dependence of the homogenous linewidth displayed in Fig. 4.6 (a) to the deformation potential $(D_e - D_h)^2$. The slope of the linear function is associated with the exciton-acoustic phonon coupling $\gamma_{A,X} = 55\,\mu\text{eV K}^{-1}$ (For more details we refer to chapter 3). Taking into account a thickness dependence of the coupling as derived for quantum wells in Ref. [10], the relation of exciton deformation potential due to acoustical phonons and linewidth broadening is given by

$$\frac{2 \cdot 3 k_B T M_X (D_e - D_h)^2}{8 \hbar^2 \rho v_s^2 L} = \gamma_{A,X} T, \tag{4.3}$$

where the factor of 2 originates from absorption and emission of phonons. The exciton mass $M_X = m_e^* + m_h^* = 1.29\ m_e$ [128] of ML and BL is calculated by the effective electron (m_e^*) and hole (m_h^*) masses. The material density is $\rho = 7.7$ g cm^{-3}. The published values for the speed of sound in $MoTe_2$ differ by 50% from 3.5 km/s (Ref. [27]) to 5 km/s (Ref. [61]), however it allows an estimate of the deformation potential. Atomic force microscope measurements yield a layer thickness of 0.66 nm, cf. section 2.3.1. We obtain upper and lower limits for $D_X = D_e - D_h$ of 6.3 eV and 4.4 eV, respectively. These values are very similar to the results obtained for MoS_2 and $MoSe_2$ by Shree et al. in Ref. [156]. In the BL, the exciton coupling to acoustic phonons $\gamma_A^{BL} = 39\mu\text{eV K}^{-1}$ is weaker than for the ML exciton as already investigated

in chapter 3. The resulting upper and lower limits for $D_X = D_e - D_h$ of 7.5 eV and 5.2 eV, respectively, are larger than for the ML exciton. We assume this can be the result of larger carrier interactions with local changes in the crystal potential by lattice vibrations due to either a larger lattice or additional interactions with the out of plane ZA phonon mode in the BL. Besides, the deformation potential is directly linked to the shift in the bandgap [9] investigated in section 3.2. Thus, a higher deformation potential observed in the BL compared to the ML induces a higher bandgap shift, matching our observations of a net shift of (83 ± 2) meV and (90 ± 2) meV for ML and BL, respectively. The ratio of the bandgap shift is similar to the ratio of the deformation potentials for ML and BL $\Delta E_{ML}/\Delta E_{BL} \sim D_X/D_T$. This agrees with the statement that the bandgap shift is induced mostly by lattice interaction with acoustical phonons made in the previous chapter. Trions display a three times larger phonon coupling of $\gamma_{A,T} = 163\,\mu$eV K^{-1} than excitons which is due their extra charge. This is also confirmed by a vanishing trion emission for temperatures higher than 60 K, whereas the exciton emission is observable up to room temperature. We assume that the trion has a deformation potential consisting of one hole and two electron deformation potentials [123]

$$D_T = 2D_e - D_h,$$

where we assume that the scattering rate $W(k,k')_X = \frac{3k_BT(D_e m_e^{*2} - D_h m_h^{*2})^2}{4\hbar^3 \rho v_s^2 L}$ and follow the argument that the trion emission reads as a many body effect between excitons and free carriers (cf. Ref. [31] and section 2.1.3). Therefore, we can estimate a similar exciton-acoustic phonon coupling for the trion deformation potential

$$\frac{2 \cdot 3k_BTM_T(2D_e - D_h)^2}{8\hbar^2\rho v_s^2 L} = \gamma_{A,T}T, \tag{4.4}$$

where $M_T = 2m_e^* + m_h^* = 1.93\ m_e$ is the trion mass. We obtain upper and lower limits for D_T of 8.88 eV and 6.22 eV, respectively. Thus, we can estimate upper and lower electron (hole) deformation potential to be $D_e = 2.58$ eV and 1.82 eV ($D_h = -3.6$ eV and -2.6 eV) being in the same order of magnitude as the theoretical estimates in Refs. [61, 204]. As trions have a stronger phonon coupling, they are suited for detection of small vibrations of the lattice structure. Especially TMDCs are an ideal model system to study these trion effects as the binding energy is large enough to separate the trion emission from the exciton and to entangle phonon-coupling effects. In addition, the calculable trion deformation potential allows to estimate the effects of electrons and holes only in theory calculations.

The coupling matrix element for optical phonons is inelastic and scales in zero and first order in q, thus $M_q^j = D_j^0 + D_j^1 \cdot q$, where D_j^0 and D_j^1 are the zeroth and first order optical deformation potentials. Thereby, the symmetry of the deformation potential in k space determines which phonons are allowed in zeroth or first order. TO phonons are describable by the first order

deformation potential, the homopolar and the LO mode correspond to a zero order deformation potential and have finite values [69]. From our temperature-dependent Lorentzian linewidth broadening in Fig. 4.6 (b), we can extract the phonon energy of the optical phonons E_O to be (31 ± 1) meV and (19 ± 1) meV for ML and BL, respectively. Comparing E_O to the calculated phonon dispersions in Fig. 2.7 (a) and the associated Raman measurements for the ML and BL in Fig. 2.7 (b) from Ref. [48] we can compare the energies of the phonon modes. We find that $E_O = 31$ meV and 19 meV for ML and BL mostly overlaps with the energy of longitudinal optical phonons, mainly polar and homopolar LO phonons (E^1_{2g}) in case of the ML and polar TO and LO (A_{1g} and E^1_{2g}) phonons in case of the BL. Therefore, mainly LO phonons contribute to the exciton phonon coupling for the ML in perfect agreement with Ref. [69]. Under the assumption that both LO modes (polar+homopolar) correspond to a zeroth order deformation potential in q as predicted by Ref. [69] we can restrict our considerations to scattering described by zeroth order deformation potential D^0 theory for the ML. Note the homopolar phonon mode dominating in the ML is induced by vibrations perpendicular to the layer changing layer thickness rapidly [69]. This can explain why the mode is less dominant in the BL as vibrations of two layers can cancel out each other. In the case of the BL first order deformation potentials have to be considered further, due to the strong TO mode interactions, thus $M_q = D^0_{LO} + D^1_{TO} \cdot q$. In contrast to interaction with acoustic phonons, for inelastic scattering we cannot neglect the phonon energy in the calculation of the scattering rate. Thus, equation 2.6 cannot be solved analytically. As an approximation, we estimate the zeroth order deformation potential from calculations of electron deformation potentials of $D^0_{LO} = 1.34 \cdot 10^8$ eV cm^{-1} for the LO phonons. Consistent with Ref. [69], the zero order deformation potential dominates the first order deformation potentials at low and moderate energies. We assume a first order TO phonon deformation potential of $D^1_{TO} = 1$ eV to investigate the effect on the transport properties with or without the first order approximation.

4.2.3 Transport of carriers

The transport of carriers plays an important role in opto-electronic devices. So, it is necessary to determine how particles behave under external force, like electric field, heat, and external concentration. In an environment without external force particles move Brownian like with interactions between carriers, impurities, and lattices resulting in a mean thermal speed of v. The time between collisions is called the relaxation time τ, directly linked to the distance the carrier travels without collisions. The relaxation time is temperature-dependent and impurity-dependent. Applying a force, carriers start to move along the bands due to the equation of motion, where the mass is characterized by the effective mass m^* as introduced in chapter 2.1. The ratio of the charge of the carrier e times the average relaxation time $\langle\tau\rangle$ and the effective

mass m^* yields the mobility [7]

$$\mu = \frac{e\langle\tau\rangle}{m^*}. \tag{4.5}$$

Note, the carriers in our case move in a crystal with periodic lattice potential and are assumed to be described by Bloch states (cf. section 2.1.1)). Vibration of the lattice (phonons) results in scattering transitions of these Bloch states from $|nk\rangle$ to $|nk'\rangle$ assuming intra- and inter-band scattering, with a scattering rate $W(k,k')$. Thus the relaxation time τ can be described in terms of scattering rate [7, 69]

$$\frac{1}{\tau(E_k)} = \int W(k,k')d^3k', \tag{4.6}$$

i.e. the scattering mechanisms define the relaxation time. There are several different scattering mechanisms like impurity and phonon scattering. As we are dealing with temperature evolution, especially scattering with phonons is assessable. Here, we can connect the previous discussion of linewidth with the relaxation time: Scattering broadens the linewidth and scattering defines the relaxation time. Thus, linewidth broadening can quantify scattering mechanisms which can in turn reveal insights into the relaxation time. And from the relaxation time, the mobility can be computed according to eq. 4.5.

We can determine acoustical or optical phonon limited mobility. We neglect other processes such as impurity scattering or electron scattering which further can be summed up via the Mathissen rule [61] to the phonon limited mobility. As discussed above acoustic phonons dominate mostly at low temperatures, optical phonons play an increasing role especially at elevated temperatures up to room temperature due to small optical phonon energies as calculated by Ref. [69] for MoS_2. For $MoTe_2$ the phonon energies are even smaller than for MoS_2 [6, 48], thus acoustical and optical phonons are expected to limit the mobility early on [61], resulting in $1/\mu_P = 1/\mu_A + 1/\mu_O$ with μ_P the total phonon-limited mobility, μ_A the acoustical and μ_O the optical-phonon-limited mobility.

4.2.4 Acoustical phonon limited mobility and relaxation time

In the case of acoustical phonons, i.e. assuming elastic scattering, the resulting relaxation time is estimated by eq. 2.6 and eq. 4.6 to be [156]

$$\begin{aligned}\frac{1}{\tau} &= \frac{2\pi}{\hbar}\sum_{k',q}|M^j(q)|^2(1+2N_q)\delta E_k - E_{k'} - \hbar\omega_q \\ &= \frac{Mk_BTD^2}{\hbar^3\rho_{2D}v_S^2}\end{aligned}$$

where E_k is defined in eq. 2.2 under the assumption of parabolic bands, M and D are either M_X or M_T and D_X or D_T, and we neglect the energy of the acoustical phonon $\hbar\omega_q$. Using

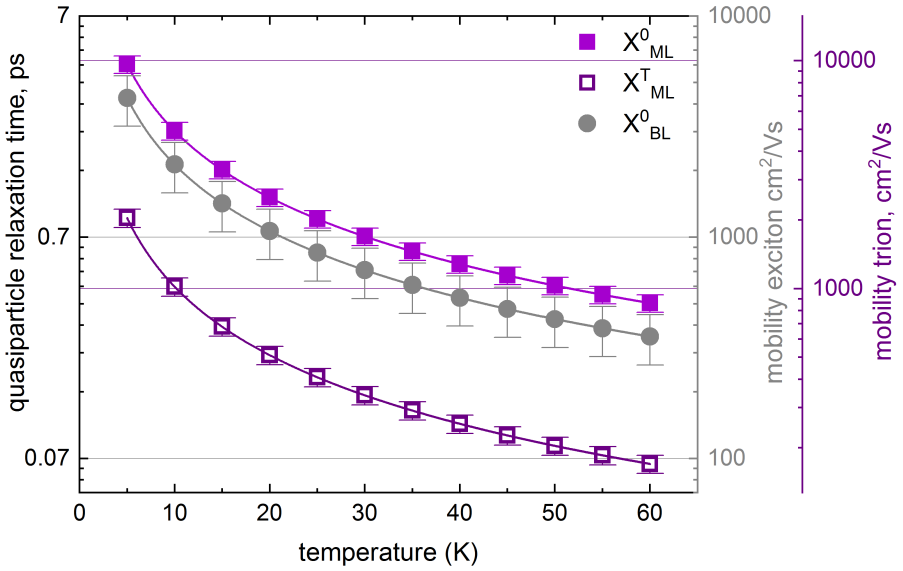

Fig. 4.7: Exciton (closed symbols) and trion (open symbol) mobility and relaxation times versus temperature for ML (violet squares) and BL (gray circles) $MoTe_2$.

eq. 4.5 the acoustical phonon limited mobility is

$$\mu_A = \frac{e\hbar^3 \rho_{2D} v_S^2}{M^2 k_B T D^2}, \tag{4.7}$$

where ρ_{2D} is the two dimensional density. The literature values for exciton mass M and sound velocity v_S differ significantly, thus, the deformation potentials can be obtained only as a rough estimate, whereas the mobility can be expressed in terms independent of these values (cf. eq. 4.8). It is possible to obtain a good approximation of the acoustical phonon limited carrier mobility μ_A for excitons and trions. By combining equations for mobility and deformation potential for exciton eq. 4.3 and trion 4.4 [61, 156, 204] and assuming that the 2D density (ρ_{2D}) is the density times half lattice constant c=1.39 nm (cf. section 2.1 and [138, 156]) μ_A can be estimated via

$$\mu_A = \frac{3e\hbar c}{8ML} \quad \frac{1}{\gamma_A T} = \frac{e}{M} \tau_k, \tag{4.8}$$

and is directly linked to the relaxation time for exciton acoustic phonon scattering [70]. Here, e is the elementary charge. The resulting mobility and relaxation times are plotted in Fig. 4.7 for ML (violet squares) and BL (dark gray circles) exciton (closed symbol) and trion (open symbol). Please note that the values for the relaxation time differ from exciton to trions due to varying effective quasiparticle mass M and quasiparticle phonon coupling γ_A. The mobility scales inversely with temperature, reaching high values at low temperature. Besides, a temperature independent parameter to study the transport properties of excitons (trions) is the so called diffusion coefficient [36] $C_{Diff} = \mu_A / e k_B T = (2.6 \pm 0.2)\,\mathrm{cm}^2 s^{-1}$ ($(0.9 \pm 0.1)\,\mathrm{cm}^2 s^{-1}$).

We observe relaxation times in the order of 3 ps for the exciton decreasing with increasing

temperature as interactions with phonons become more intense. This is comparable to the radiative lifetime measured in $MoTe_2$ ML [134]. Impacts on the lifetime of the excitons will be investigated in detail in chapter 6 by pump probe measurements. The trion has a lower relaxation time than the excitons, this is unusual compared to measurements of $MoSe_2$ in Ref. [133] where the trion lifetime is larger than the one of the exciton. Thus, especially in the case of the trion other processes instead of phonon limited lifetimes have to be considered. The BL exciton on the other side shows comparable relaxation times in good agreement with Ref. [134] supporting the hypothesis of a direct semiconductor transition from chapter 3 which make the BL $MoTe_2$ an adequate candidate for TMDC hetero-structures.

We estimate a lower limit of 6044 $cm^2\ V^{-1}\ s^{-1}$ (2038 $cm^2\ V^{-1}\ s^{-1}$) and 4260 $cm^2\ V^{-1}\ s^{-1}$ for the exciton (trion) acoustical phonon limited mobility at 5 K for ML and BL, respectively. The associated values for the electrons and holes in ML at the same temperature are even higher, we calculate values of 61122 $cm^2\ V^{-1}\ s^{-1}$ for the electron and 29035 $cm^2\ V^{-1}\ s^{-1}$ for the holes as expected by the smaller deformation potentials compared to the exciton. As expected for TMDCs, the holes are less mobile than the electrons. The growing demand for touchable and wearable electronic devices has sparked a great amount of research activity in the direction of flat and flexible electronically active materials. The most prominent example is the two-dimensional (2D) material graphene, which is readily manufactured and features a high quasiparticle mobility [15, 20] as an essential prerequisite for efficiently functioning devices. Graphene, however, is lacking a finite direct bandgap limiting its applicability in opto-electronics. So TMDCs with the non-zero bandgap and high exciton and trion binding energies will be adequate candidates.

Most of the theory papers in the literature only investigate the mobility at room temperature [61, 66, 204]. Only few, like Ref. [70] calculate MoS_2 mobility for temperatures below 100 K. Ref. [70] estimates that the acoustical phonon limited mobility depends further on the carrier density influencing the temperature-dependence of the mobility $\mu \sim T^{-i}$, i.e. with increasing carrier density i increases. For carrier densities used in our experiments (cf. chapter 3, $n \sim 10^{11}\ cm^{-2}$) the T^{-1} dependence is justified. So Ref. [70] finds an electron mobility at 4 K of $1.5 \cdot 10^5\ cm^2\ V^{-1}\ s^{-1}$, perfectly comparable to our results. Comparing this to the mobility found in graphene of $2 \cdot 10^5\ cm^2\ V^{-1}\ s^{-1}$ at the same carrier density [15], the values are in the same order of magnitude. Increasing the carrier density, e.g. by increasing excitation power can further improve the mobility. Comparing our results to other commonly used semiconductors like Silicon (Si) having a comparable but indirect bandgap [14] and a mobility at low temperature of $10^4\ \ cm^2\ V^{-1}\ s^{-1}$ [167], we find $MoTe_2$ to provide superior mobility. Thus $MoTe_2$ is a promising material for opto- and valley-tronic applications due to its high mobility, finite direct bandgap of the monolayer and bilayer, the robustness, and the non-necessity of encapsulation. For a better comparison at higher temperature optical phonon mobility has to be taken into account.

4.2.5 Optical phonon limited mobility and relaxation time

Optical phonon scattering have been previously investigated in calculations [61, 66, 69] on ML TMDCs at high temperatures. Comparable to the acoustical phonon scattering we combine eq. 4.6 and eq. 2.6, with two major differences (i) the phonon energies are too high to neglect them and (ii) the phonon scattering with optical phonons in inelastic. To handle the problem we split the inelastic scattering in a part describing out-scattering contributions and a part describing in-scattering where the out-scattering part can be simplified analytically to an inelastic scattering rate proportional to the inverse carrier lifetime τ_{inel} and inverse optical phonon limited mobility μ_O for both zero and first order deformation potential in q by [69]

$$\begin{aligned}\mu_O &= \frac{\tau_{\text{inel}} e}{M} = \frac{2e\hbar\rho_m E_O}{M^2 (D^0_{LO})^2} \left[1 + e^{E_O/k_B T}\Theta(\epsilon_K - E_O)\right]^{-1} N_0^{-1} \\ \mu_O &= \frac{\tau_{\text{inel}} e}{M} = \frac{e\hbar^3\rho_m E_O}{M^3 (D^1_{TO})^2} \left[(2\epsilon_k + E_O) + e^{E_O/k_B T}\Theta(\epsilon_K - E_O)(2\epsilon_k + E_O)\right]^{-1} N_0^{-1},\end{aligned} \tag{4.9}$$

where $N_0 \sim k_B T/E_O$ is the Bose-Einstein distribution in first approximation, ϵ_K is the carrier energy, and $\Theta(\epsilon_K - E_O)$ is the Heaviside step function [69], which assures that only excitons with a certain energy can emit a phonon. Precisely, the equation above is designed for fermionic particles describing the mobility of electrons. In $MoTe_2$ electrons and holes have comparable masses [128], thus, a comparable curvature of the band structure and group velocity. The exciton is a localized electron hole pair moving in the lattice, thus, we assume a comparable description for the exciton movement limitations. However, as investigated in detail in section 4.2.2 we assume a zero order deformation potential for LO phonons of $D^0_{LO} = 1.34 \cdot 10^8\,\text{eV cm}^{-1}$ [61] and a first order deformation potential for TO phonons of $D^1_{TO} = 1\,\text{eV}$. In case of the ML we only consider LO phonons. In contrast, in the BL both LO and TO phonons have to be included in the investigation. As proposed by Ref. [69] the zero order deformation potential should dominate the mobility. Therefore, we calculate the mobility by $\mu_O = 1/(1/\mu^0_O + 1/\mu^1_O)$ and without first order deformation potential for the BL.

The results for the optical phonon limited mobility as a function of carrier energy are presented in Fig. 4.8 (a) for ML (violet squares) and BL (without D^1_{TO}: gray circles, with D^1_{TO}: blue line) at room temperature. Here, the mobility differs for ML and BL more than in the case of acoustical phonons (cf. chapter 3) supporting the higher coupling of excitons to optical phonons for the BL. Thus, optical phonons limit the mobility at high temperature stronger for the BL as for the ML. As expected, the first order deformation potential does not influence the optical phonon limited net mobility. For higher carrier energies above 250 meV the TO phonon modes further limits the mobility.

Now, we investigate the temperature dependence by calculating the mobility for a carrier energy ϵ_K above and below the phonon energy E_O, and plot this in Fig. 4.8 (b) versus temperature as open and solid symbols, respectively. The calculations are limited to excitons

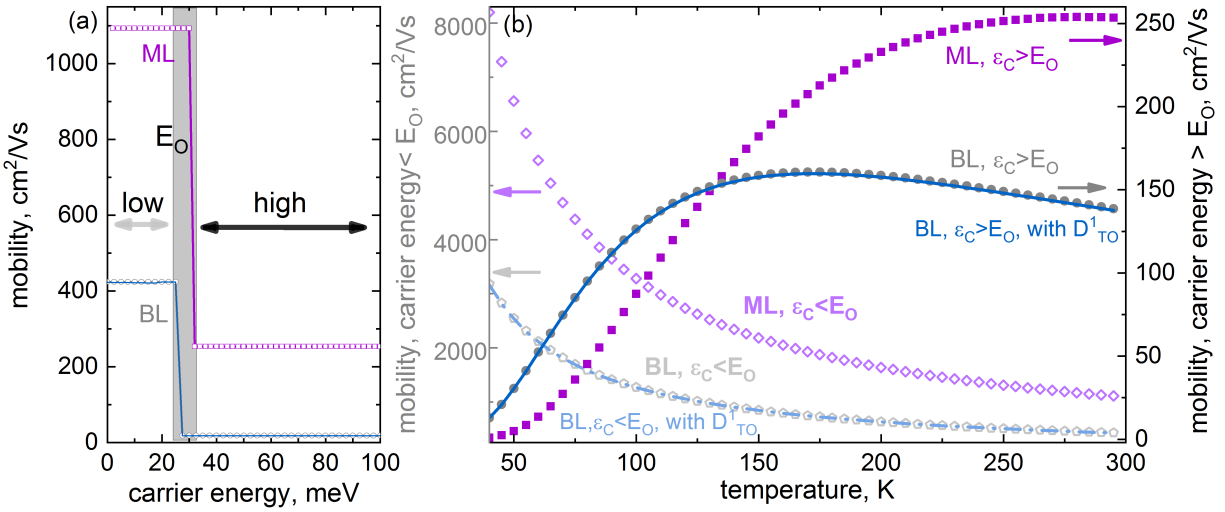

Fig. 4.8: Exciton optical-phonon-limited mobility dependent on carrier energy at 300 K (a) and temperature (b) for ML (violet) and BL with (blue) or without (gray) first order deformation potential D^1_{TO}. In (b) we present the mobility evolution for carrier energies ϵ_K lower (open symbols) and higher (closed symbol) than the phonon energy E_O versus temperature for $MoTe_2$.

here, as the trion signature disappears at higher temperatures, and the optical phonon interaction becomes significant only at temperatures above 40 K. Remember, below 40 K mainly the acoustical phonons limit the mobility. For lower temperatures, we get an extremely high optical-phonon-limited mobility for $\epsilon_K < E_O$ indicating that such excitons are not impaired by optical phonons. For high temperatures (around room temperature) optical phonons limit the mobility of these low-energy carriers strongly. The opposite trends are observed for carrier energies exceeding E_O. We can estimate an upper and a lower value of 1126 cm^2/Vs and 295 cm^2/Vs for the optical-phonon-limited mobility in ML and 251 cm^2/Vs and 140 cm^2/Vs for the BL at room temperature. Compared to other TMDCs, the ML displays a high mobility in the room-temperature limit [61, 66, 69, 70, 204], whereas the BL shows values comparable to the ML mobility of other members of the TMDC family [66]. Moreover, there is a set of experimental observations on room temperature mobility yielding 3-10 cm^2 V^{-1} s^{-1} for MoS_2 [114, 125] indicating that beside the phonon limited mobility discussed here further processes like ionized or neutral impurity scattering dominate the mobility processes at room temperature. We confirm that the zero-order deformation potential is a good approximation for the BL, as taking into account the first order deformation potential does not change the mobility at all. The deformation potential, acoustical phonon limited mobility at 5 K and optical phonon limited mobility at room temperature are summed up in table 4.2.

All in all, we investigate the trion nature of the second peak in BL, and attribute it to two trion states, inter- and intra-layer trion, which are separated by 2.2 meV. Thereby, we can explain the mismatch in Gaussian FWHM at exciton and trion in BL. Moreover, mobility restricted by acoustical and optical phonons has been estimated for exciton, trion, electron, and hole and directly linked to relaxation dynamics in ML and BL $MoTe_2$. We determine a

Table 4.2: Deformation potentials upper and lower D^{max} and D^{min} limit, acoustical μ_A and optical μ_O^{max}; μ_O^{min} phonon limited mobility for ML exciton, trion, electron, hole, and BL exciton.

Deformation potential and mobility ML					
	D^{max} (eV)	D^{min} (eV)	μ_A (cm^2/Vs)	μ_O^{max} (cm^2/Vs)	μ_O^{min} (cm^2/Vs)
X	6.3	4.4	6000	1100	300
T	8.9	6.2	2000		
e	2.6	1.8	61000		
h	-3.6	-2.6	29000		
Deformation potential and mobility BL					
	D^{max} (eV)	D^{min} (eV)	μ_A (cm^2/Vs)	μ_O^{max} (cm^2/Vs)	μ_O^{min} (cm^2/Vs)
X	7.5	5.2	4300	250	150

high mobility in both ML and BL making $MoTe_2$ an adequate candidate for opto-electronic applications especially at low temperature where only acoustical phonons limit the mobility. The low temperature mobility is graphene like for the electron in the ML $MoTe_2$. The BL exciton also shows a promising mobility and lays the foundation of understanding hetero-structure mobility. In addition, we confirm that LO phonons (polar and homopolar) linked to a zero-order deformation potential are the major optical phonon modes coupling to excitons and limiting their mobility in the ML and BL $MoTe_2$.

5 Valley polarization of $MoTe_2$

In this chapter, we study the excitation energy dependence of the circular polarization of the photoluminescence from monolayer and bilayer molybdenum ditelluride in the temperature range between 5 K and room temperature. The excitation energy is tuned from near resonant excitation of the A exciton at 1.24 eV to far above bandgap excitation at 1.96 eV. We identify the X^A exciton, X^B exciton, and X' ($X^{A'}$ and $X^{B'}$) exciton resonances by comparing photoluminescence spectra and photoluminescence excitation spectra to density functional theory calculations for the monolayer. The density functional theory calculations were performed by *Dr. Malte Rösner* from the *Radboud University*. The bilayer shows the same excitonic states, where the X^A and $X^{A'}$ are slightly red-shifted by ~ 30 meV and the X^B and $X^{B'}$ stay remarkably similar in energy. We expand photoluminescence excitation spectroscopy measurements to the trion and find signatures of these higher exitonic states in both ML and BL trion emission. This shows that the trion is an excellent scattering channel even for higher exitonic states.

We study the degree of circular polarization of the A exciton and trion emission of monolayer and bilayer molybdenum ditelluride. In prior experiments on transition metal dichalcogenides, the observed valley polarization under non-resonant excitation condition has been found to be low, measurements with the excitation covering the higher lying excitonic states (B and A') have been limited to the B exciton [11]. To the best of our knowledge, nothing has been published so far on the A' and B' exciton. This is surprising, as the excitation of higher excitonic states is a natural way to invert a system from an application point of view. We find that if the excitation is circularly polarized and resonant to higher exciton states, the resulting emission from the X^A shows a finite polarization. Our measurements reveal that the polarization transfer is temperature-dependent. The exciton resonance dependence will be considered by density functional theory calculations. *Dr. Matthias Florian* and *Dr. Alexander Steinhoff* from the group of *Prof. Dr. Frank Jahnke* at the *University of Bremen* calculated the polarization dependence of the density functional theory extracted absorption. Due to the binary selection rule and spin-valley coupling, the change of polarization requires both a valley and spin flip, where the latter is highly temperature dependent. Complementary experiments on the inversion-symmetric bilayer show no observable circular polarization in the emission. The trion polarization simply follows the polarization of the exciton. Consequently, even the monolayer trion can be used for valley-tronic applications.

5.0.1 Polarization Review

In section 2.2, we briefly introduce mechanisms leading to a spin-valley coupling and selective excitability by circularly polarized light. The spin-valley coupling stabilizes the polarization of one valley. As one wants to change valleys one also has to consider that spin is still a good quantum number [189]. If selectively excited, excitons in K/K' valleys always emit light in a fixed polarization, this mechanism can be exploited to design binary information encodes or binary storage media. To facilitate these applications, it is necessary to understand the processes limiting or supporting the valley-spin polarization.

The binary valley addressability of ML TMDCs has been demonstrated in experiments by polarization resolved PL spectroscopy. Extensive research has been performed in particular on ML MoS_2, measuring a valley polarization in PL from 32 % to 100 % under near-resonant excitation [22, 100, 143, 202], and $\sim$ 30 % under non-resonant excitation [143]. A lower valley polarization of $\sim$ 20 % has been observed for $MoSe_2$ [74] under near-resonant excitation and $\sim$ 5 % [74, 179, 183] for non-resonant excitation. The available data for ML $MoTe_2$ confirm this trend, showing no measurable valley polarization for excitation from 50-460 meV above the A exciton [134] in the absence of an additional magnetic field [4].

Results for WSe_2 show that the circular polarization of the excitation beam can be transferred to the A exciton emission if the excitation is resonant to the energetically higher B exciton state [11, 104]. The B exciton is the second bright exciton in the K/K' valley. It is energetically located above the A exciton due to the valence and conduction band splitting. Furthermore, it features an opposite spin compared to the A exciton due to spin-valley selection rules as seen in Fig. 2.9, section 2.2.2. If one considers applications of TMDCs in photonics, pumping a higher excitonic level is a convenient way to create a population inversion. In addition to the B exciton, there is a large amount of higher excitonic Rydberg-like states (2s, 2p,...) studied in Mo- [25, 49, 124, 180] and W-based [11, 28, 104, 181, 182] TMDCs materials. The A' (2s or 2p) exciton $X^{A'}$ is the next higher bright excitonic state with the hole located within the same valence band minimum as for X^A and, thus, is associated with the same circular polarization and spin as X^A (cf. Fig. 5.1 left). The $X^{A'}$ is energetically followed by the next higher bright B exciton state $X^{B'}$. The hole is located in the same valley as the hole of the B exciton and has the same spin as the hole of the B exciton.

In this section, we investigate the polarization transfer of these states by scanning the excitation energy over a wide range from near resonant with the A exciton via the B exciton and the A' exciton up to the wings of the B' exciton. To identify the peaks energetically, we measure excitation energy resolved photoluminescence (PLE), i.e. taking PL spectra with the setup described in section 2.3.2 at different excitation energies in the range of 1.24 eV to 1.96 eV at the same excitation intensity of 35 Wcm^{-2}.

Besides, we also investigate the BL $MoTe_2$. As shown in the previous section, BL $MoTe_2$

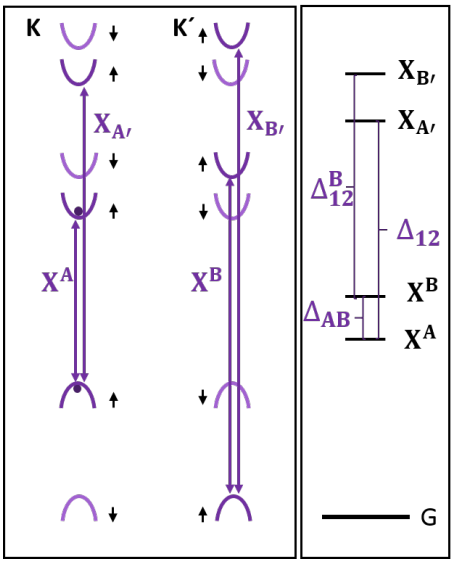

Fig. 5.1: (Left) Schematic of higher excitonic transitions in the K, K‘ valleys of ML $MoTe_2$. (Right) Possible energy difference between higher excitonic transitions are sketched.

behaves like a direct semiconductor and has an exceptionally bright emission. Thus, it is worthwhile revisiting the higher excitonic states and the polarization of emission of this particular material. As investigated in section 2.2.1, the lattice structure of ML TMDCs displays an explicitly broken inversion symmetry whereas the inversion symmetry can be restored if a second layer is added to form a BL [6]. Thus, valley and spin are coupled for ML TMDCs [189]. Left (σ^-) and right (σ^+) circularly polarized light excites the lowest bright exciton (A exciton) in the K' and the K valley, respectively. In contrast, in BL TMDCs spin and valley are no longer coupled and, thus, selective excitation in one particular valley is not possible [189]. We investigate the polarization behavior of higher exitonic states in ML and BL in the second part of this chapter by performing polarization resolved PLE measurements. We examine the main polarization conserving rules and investigate the influence of phonons. Considering the low momentum associated with acoustic phonons, it is conventionally assumed that acoustic phonon scattering preserves the K index, whereas scattering by optical phonons leads to valley depolarization. We investigate whether this assumption holds in $MoTe_2$ by measurements on the degree of circular polarization of the emitted light. To do so, we measure polarization-dependent/independent PLE as a function of temperature in the range of 5 K up to room temperature.

Measurements are performed on flake 1 for the BL and on flake 1 and 2 for the ML $MoTe_2$. Properties and images of the flakes can be found in section 2.3.1.

5.1 Identification of higher excitonic states

In this section, we address higher excitonic states by PLE measurements on ML and BL $MoTe_2$. We derive the energetic position of the higher excitonic states by analyzing the intensity of the emission from exciton or trion in both layer structures. We identify the peaks in ML $MoTe_2$ by comparing the PLE spectra to absorption spectra calculated by using density functional theory. These calculations were performed by *Dr. Malte Rösner* from the *Radboud University*. Details of the calculation method can be found in the previous publication Ref. [165].

5.1.1 Experimental observation of higher excitonic states

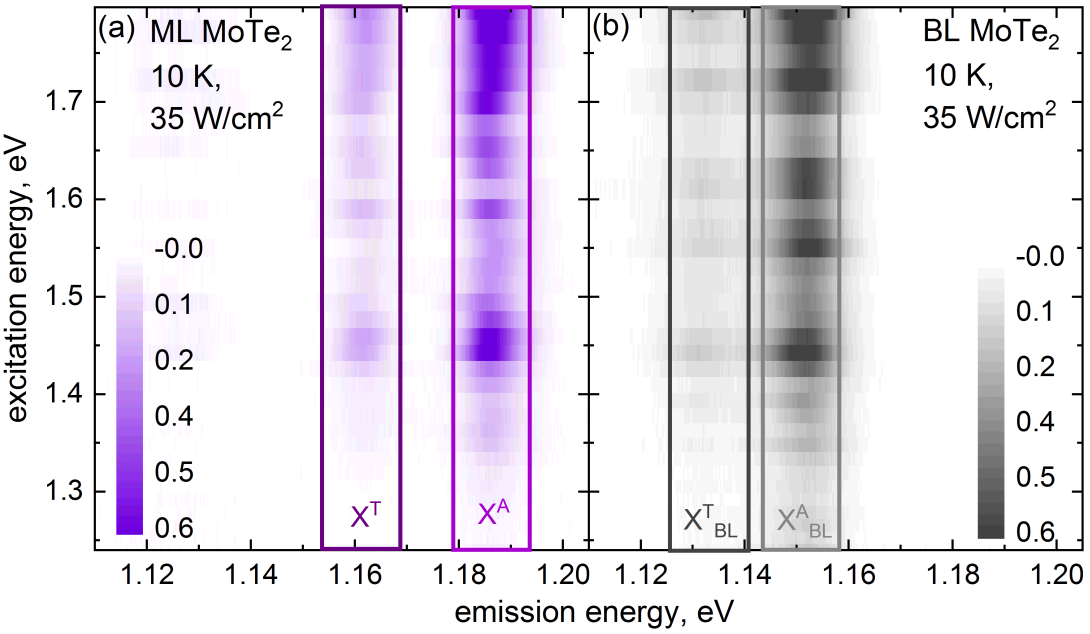

Fig. 5.2: Normalized PLE maps of ML (a) and BL (b) $MoTe_2$ measured at 10 K and 35 W cm^{-2} excitation intensity. The boxes indicate the position of the X^A exciton and X^T trion emission area.

Normalized PLE maps of flake 1 taken at a temperature of 10 K are shown in Fig. 5.2 (a) and (b) for the $MoTe_2$ ML and BL, respectively. The excitation energy was varied from 1.24 eV to 1.79 eV with a resolution of 11 meV and an excitation intensity of 35 Wcm^{-2}. The spectra were recorded under identical conditions for ML and BL. Consistent with chapter 3, we identify the two peaks of the ML emission centered at 1.190 eV and 1.162 eV as the A exciton X^A (violet box in Fig. 5.2 (a)) and trion X^T (dark violet box) emission, respectively. Following chapter 3, we assign the peaks of the BL at $E_{X^A_{BL}} = 1.155$ eV and $E_{X^T_{BL}} = 1.135$ eV to the A exciton (gray box in Fig. 5.2 (b)) and trion (dark gray box) emission. The intensity varies significantly over the excitation energy range, due to absorption changes. The position in emission energy of the exciton and trion does not change with increasing excitation energy for ML and BL. This indicates that the trion binding energy stays constant over the whole excitation energy

range. The stability of the observed emission is an indication of the good structural quality of our sample. Moreover, the linewidth, i.e. Voigt, Gauss, and Lorentzian FWHM do not change over the whole excitation energy range. This clearly indicates that the change in intensity is not due to phonon or defect assisted local potential changes as observed in chapter 4 but is induced by changes in the underlying population of excitons and trions. The extracted data on linewidth and energy can be found in the thesis of my student *Hery Ahmad* [2].

For a quantitative evaluation of the emission spectra, we fit the complete spectra by a sum of two Voigtian functions representing the A exciton and trion (cf. chapter 3), respectively. Subsequently, we extract the integrated area of emission (or shortly emission area) for the exciton and trion on ML and BL $MoTe_2$. Fig 5.3 (b and d) show the emission area as a function of excitation energy for ML (b, violet squares) and BL (d, gray circles) $MoTe_2$ for the A exciton (closed symbols) and trion (open symbols) emission. For better visibility of the energy difference of the excitonic peaks we show the exciton X^A and trion X^T emission in Fig. 5.3 (a+c) for ML and BL on the same energy scale as the emission area measurements.

In all cases in Fig. 5.3 (b+d) we observe a clear maximum of emission between 1.4 eV and 1.5 eV excitation energy, a double peak feature at $\sim$ 1.6 eV, and a strongly increasing emission upon approaching the blue end of the Ti:Sa laser energy range. These peaks coincide well with higher exciton resonances observed in reflectance contrast experiments for ML and BL $MoTe_2$ in Ref. [141], second harmonic generation spectroscopy on $MoSe_2$ [180], theoretical calculations on MoS_2 [124], and bulk $MoTe_2$ transmission measurements [188]. Following the convention of these references, we refer to these peaks as the B, A' (2s or 2p), and B' (2s or 2p) exciton resonances X^B, $X^{A'}$, and $X^{B'}$ associated with the transitions sketched in Fig. 5.1.

According to prior observations, both B and B' exciton only slightly decrease in energy from ML to BL TMDCs [4, 134] which is also reproduced in our data. We determine the X^B peak position at 10 K as (1.455 ± 0.005) eV and (1.445 ± 0.005) eV for ML and BL. This is in perfect agreement with transmission measurements of bulk $MoTe_2$, where an energy of 1.455 at 77 K is estimated [188]. The A exciton shows a pronounced offset of $\sim$ 155 meV from ML to bulk [188]. That means that the B exciton resonance shift less with increasing number of layers, compared to the A exciton. We estimate an A-B exciton splitting (Δ_{AB}) of (265 ± 5) meV and $\Delta_{AB}^{BL} = (290 \pm 5)$ meV in experiment. This perfectly fits the band structure calculations of Ref. [134]. Therefore, $MoTe_2$ has the largest Δ_{AB} in the Mo-TMDC family [49, 124, 180].

Discerning $X^{A'}$ and $X^{B'}$ is hard as the literature does not provide a good mapping and is limited to high temperature measurements [141, 193]. Therefore, we investigate the absorption spectra of ML $MoTe_2$ in DFT calculations in the next subsection. Based on our measurements, we estimate a center position for the $X^{A'}$ of (1.621 ± 0.005) eV and (1.589 ± 0.005) eV in ML and BL. This is a separation of (32±5) meV from ML to BL $X^{A'}$ exciton, in perfect agreement with the separation of the A exciton of $\sim$ 35 meV. The double-feature shows a clear splitting of $\sim$ 60 meV and 70 meV in ML and BL. We estimate an $A - A'$ exciton splitting Δ_{12} of

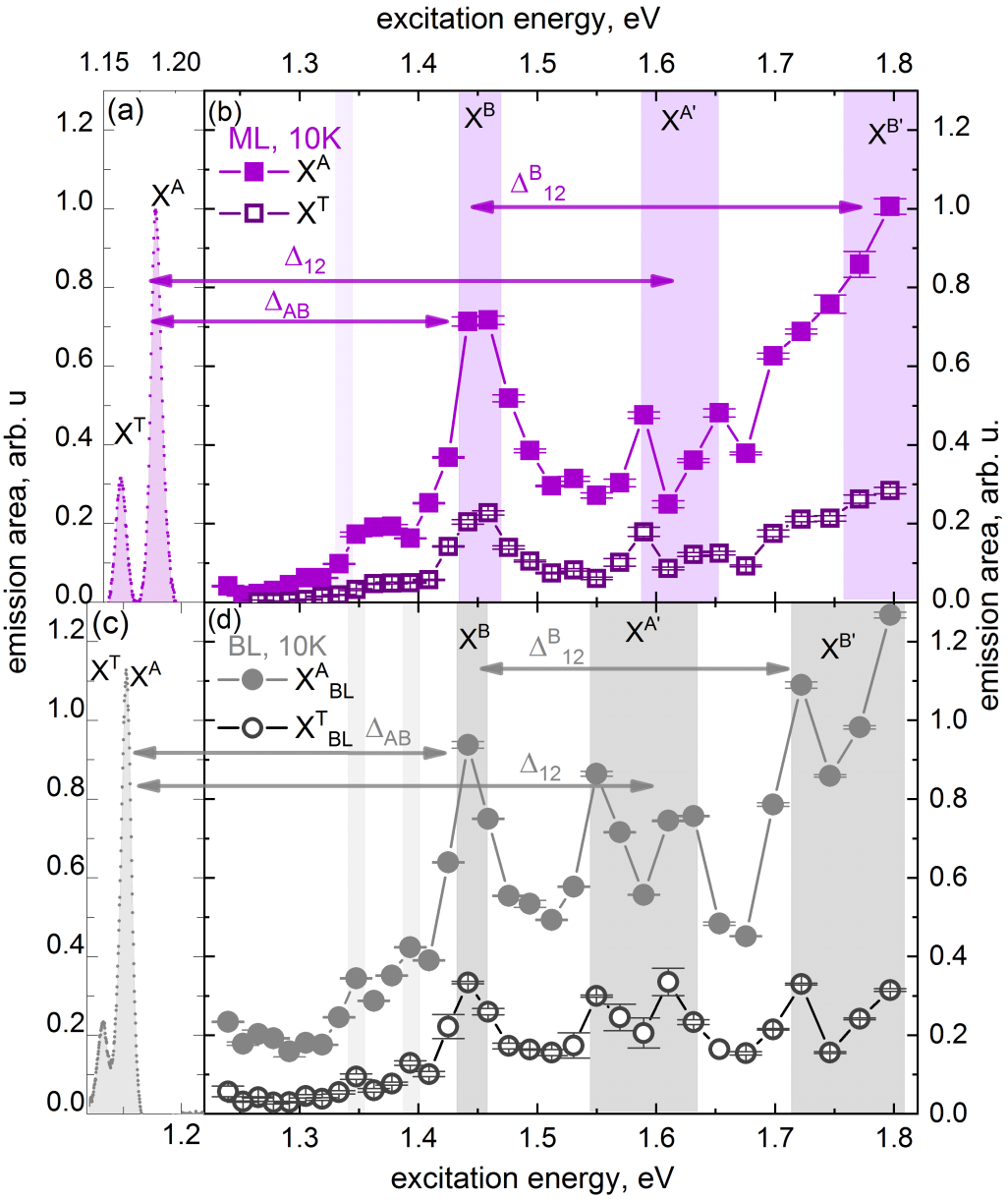

Fig. 5.3: Photoluminescence spectra of ML (a) A exciton X^A and trion X^T and BL (c) X^A and X^T. Excitation energy-resolved emission area of ML (violet squares, b) and BL (gray circles, d) $MoTe_2$ at 10 K and 35 W cm^{-2}. We identify the peaks of higher order excitons X^B, $X^{A'}$, and $X^{B'}$ and the energy difference between the excitonic peaks Δ_{AB}, Δ_{12}, and Δ^B_{12}.

(430 ± 10) meV and (435 ± 10) meV for ML and BL in experiment. The splitting between the A and A' stays constant from ML to BL which is a confirmation of the direct exciton transition in BL.

The remaining excitonic transition at the high energy side is not fully covered by the Ti:Sa laser energy. To extend the measurement we repeat the PL measurement exciting either with two diode-lasers or a Helium-Neon laser at 1.85 eV, 1.91 eV, and 1.96 eV, respectively. The results are presented for the ML in section 5.1.3. By assuming a similar splitting between A' and B' and A and B, we can find a first estimate for the $X^{B'}$ center position at ~ 1.885 eV and ~ 1.880 eV for ML and BL. This agrees with the assumption that the B excitonic transitions do not shift in energy with increasing number of layers. Assuming conservation of conduction- and valence-band splitting through higher exitonic states [124] ($\Delta_{12} \sim \Delta_{12}^{B}$). We obtain the same values for the $X^{B'}$ excitonic transition of 1.885 eV and 1.880 eV for ML and BL.

We determine the emission area with respect to the trion emission in Fig. 5.3 (b+d, open symbols). For both ML and BL, the trion emission area follows the exciton emission area (closed symbols). This indicates that we observe a population from the same higher excitonic states. The trion lies energetically below the exciton, therefore, it is as well an excellent scattering channel for excitons from higher states. Moreover, the constant ratio of emission area underpins that the cascade process from higher states down to the ground state excitation is comparable to trion formation, otherwise one has to observe additional higher trionic states. This is reasonable due to a observed cascade process of $\sim 1.5 - 2$ ps in $MoSe_2$ [17] and a trion formation time of $1.5 - 2.5$ ps (cf. chapter 6). Thus, we expect to measure a trion polarization comparable to the exciton polarization (cf. section 5.2.3).

5.1.2 Theoretical Considerations

The experimental studies in the literature and theoretical calculations mostly focus on the A and B excitonic transition and visible TMDC materials excluding $MoTe_2$. Therefore, the comparison of our results is rather difficult, especially the correct assignment of the higher excitonic transitions is challenging. Thus, in the scope of a collaboration with *Dr. Malte Rösner* from the *Radboud University* and *Dr. Matthias Florian* and *Dr. Alexander Steinhoff* from the group of *Prof. Dr. Frank Jahnke* at the *University of Bremen* we calculate the absorption spectra for ML $MoTe_2$ by DFT calculations. Details on the calculation method and process can be found in Ref. [165]. The resulting spectra are calculated for a fully substrate supported (thick light violet line) and a free standing (thin violet line) ML in Fig. 5.4. The energy is presented relative to the bandgap energy. We can estimate a binding energy $E_{Bind} = E - E_{Bandgap}$ of (430±5) meV. This is lower than the estimate of the Rydberg-like binding energy in eq. 2.3. Ref. [92] confirms the trend that DFT calculations underestimate the bandgap energy. Moreover, the calculated binding energy is comparable to band-structure related calculations of

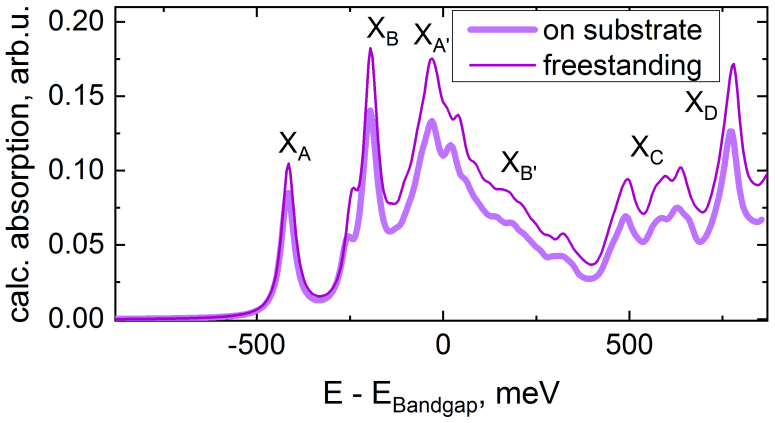

Fig. 5.4: Absorption spectra for ML $MoTe_2$ on substrate (light violet thick line) and freestanding ML (thin violet line) versus energy relative to the bandgap energy. The excitonic transitions are indicated.

the binding energy in $MoTe_2$ of ~ 500 meV [134]. We confirm the assumption that the binding energy of the ML is comparable to the $A - A'$ splitting. We can assign the peaks with the higher excitonic transitions in energetically increasing order: A exciton, B exciton, A' exciton, B' exciton, C and D excitons. The C and D excitons are beyond the scope of this thesis.

Moreover, we can directly compare the influence of substrate adhesion in ML $MoTe_2$. The calculations indicate a decrease in absorption for substrate supported flakes. Furthermore, a constant center energy of the peaks is predicted within the resolution of the calculation of 5 meV. As estimated in section 2.3.2, the shift resulting from changing substrate screening is around 5 meV and, therefore, cannot be resolved here.

For a better comparison we choose a smaller energy range and normalize the energy to the B exciton transition energy. The results are presented in the next subsection in Fig. 5.5.

5.1.3 Connecting theory and experiment

We now connect the experimental and theoretical results from section 5.1.1 and 5.1.2, by shifting the theoretical absorption spectra energetically to the B exciton resonance and normalize the absorption to the emission area. Fig. 5.5 show the combined result. There, we extend the measurements of the ML shown in Fig. 5.3 by PL measurements exciting with laser diodes and a Helium Neon laser (HeNe) with energies of 1.85 eV, 1.91 eV, and 1.96 eV, respectively. We use the same excitation energy as for the Ti:Sa excitation, but a direct comparison of absolute emission areas is non-trivial as the measurements where performed on different days and different beam profiles lead to slightly varying spot sizes. We present these results in Fig. 5.5 as symbols in the blue shaded area. All other measurements were performed with the Ti:Sa.

The B exciton emission area perfectly agrees in shape and FWHM with the calculated absorption and is centered at (1.455 ± 0.005) eV. We estimate an A-B exciton splitting (Δ_{AB}) of (265 ± 5) meV in experiment and an spin-orbit induced valence band splitting (SOC) of

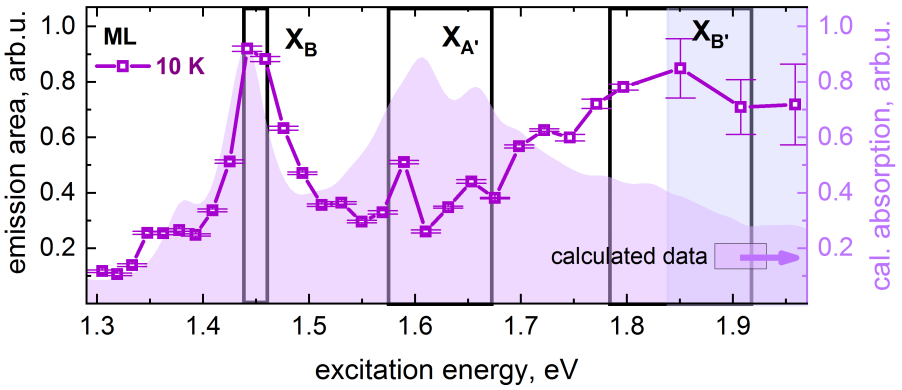

Fig. 5.5: (Right) Absorption spectra for ML $MoTe_2$ (violet shaded area) versus excitation energy. The excitonic transitions are indicated. (Left) Integrated area of emission of the exciton versus excitation energy for ML (violet squares). The blue shaded areas on the panel indicating excitation with two different diodes and a HeNe laser. All other measurements where performed by using a Ti:Sa laser.

(226 ± 5) meV in theory. The offset is related to a conduction band splitting of 30-70 meV in $MoTe_2$ [39, 134] not considered in DFT calculations. Therefore, the identification of the B exciton is confirmed by DFT calculations and we approve that $MoTe_2$ has the largest Δ_{AB} and SOC in Mo-TMDC family [49, 124, 180]. Moreover, by comparing our results to the estimates in section 2.2.2 we can confirm the values of Refs. [93, 127, 134]. We also observe a phonon side band on the red side of the B exciton separated by 60 meV from the main transition. This is twice the longitudinal optical (LO) phonon energy [6, 48] (cf. section 2.1.4).

The second feature, the double peak, is associated with the $X^{A'}$ transition. We clearly observe the double feature in both calculation and experiment. The features are centered at 1.59 eV and 1.65 eV in experiment and 1.60 and 1.655 in theory. We observe a separation of the peaks of 60 meV in agreement with the 55 meV obtained from theory. We estimate an $A - A'$ splitting (Δ_{12}) of (430 ± 10) meV in experiment and (430 ± 5) meV in DFT. Analog to the B exciton, the Δ_{12} splitting in $MoTe_2$ is the largest in Mo-based TMDCs [124]. As the separation of the peaks corresponds to nearly twice the LO phonon energy, we assume that one of the peaks is the phonon replica of the other one. Due to the DFT calculations for freestanding ML in Fig 5.4 the energetically lower peak is stronger in absorption, thus, we identify it as the main $X^{A'}$ excitonic transition. Thus, we can confirm the A' excitonic nature of this peak.

The remaining feature is related to the $X^{B'}$ exciton. Both theory and experiment show a broad exciton absorption. We identify the center position to be 1.83 eV from DFT calculations. This deviates from the expected value by 50 meV. Considering that the energetically higher peak of the $X^{A'}$ peaks is a phonon replica, we correct the estimated value of the $X^{B'}$ to 1.85 eV which corresponds very well to the calculated value. So, we estimate a B-B' splitting of approximately 390 meV being slightly smaller than the $A - A'$ separation. This is in perfect agreement with GW-Bethe-Salpeter calculations of MoS_2 [124]. Thus, we can confirm the B' nature of the highest excitonic peak measured in our PLE experiments. Changing the temperature and

investigating the optical bandgap energy improves the peak nature which will be done in the following.

5.1.4 Temperature dependence of higher excitonic states

In addition to the PLE measurements on ML and BL, we also perform temperature resolved PLE measurements with a resolution of 25 nm from 6 K to room temperature and temperature resolved PL measurements at 1.46 eV, 1.80 eV, and 1.85eV with 5 K temperature resolution up to 65 K. We extract the temperature evolution of the ML emission area peaks shown in Fig. 5.5. There we especially take into account the excitonic energy shifts.

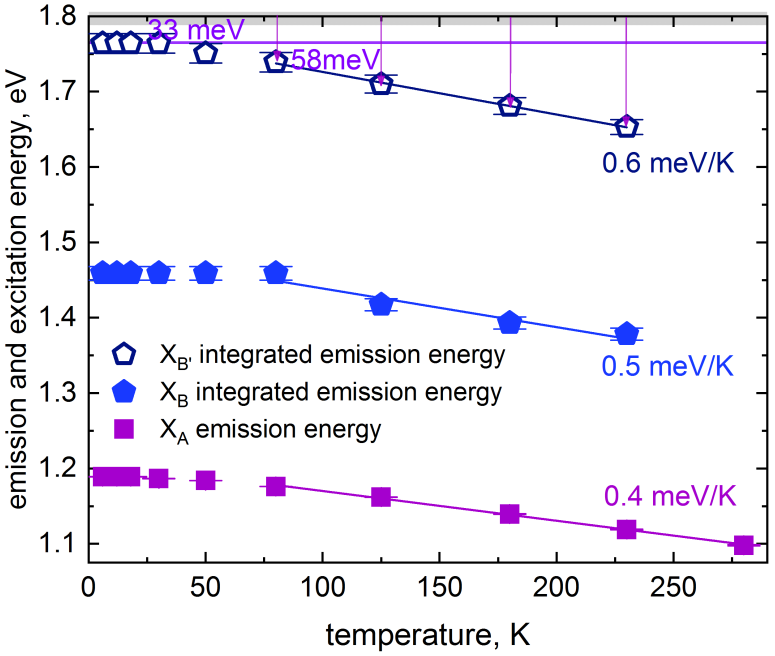

Fig. 5.6: Spectral shift of the X_A (violet squares) exciton emission maxima versus temperature and temperature dependence of the excitation energy correlated with the maximal emitted energy for X_B (blue closed hexagon) and $X_{B'}$ (blue open hexagon) excitation. The solid lines are linear dependences approximating the high temperature data points.

The temperature dependence of the spectral maximum of the A exciton emission is plotted in Fig. 5.6 as violet squares. The second and third set of data trace excitation energies giving rise to the maximum integrated area of A exciton emission, and thus the spectral positions of the B exciton (closed pentagons) and the B' exciton (open pentagons). The spectral position of the A' exciton cannot be tracked as the excitation energy resolution is too coarse and the A' exciton is less intense in A emission area compared to the other higher excitonic transitions. The solid lines approximate the high-temperature data points, the slope in meV/K is displayed. The rate of change with temperature increases from the A exciton via the B exciton up to the B' exciton, as the increasing spatial extension of the excitons favors the exciton-phonon interaction. The shift in energy position is typical for excitonic transitions as introduced in

section 3.2.1 in semiconductors and agrees very well with the shape of the A exciton for the B and B' exciton, underlining the excitonic nature of the peaks. The shift of the resonances with increasing temperature has also important consequences for the change of polarization, as with increasing temperature the detuning energy starts to increase indicated by the violet arrows in Fig. 5.6.

In this section we experimentally observe higher excitonic states by excitation energy resolved PL measurements in ML and BL $MoTe_2$. We identify the individual peaks by comparing their energy position and shift relative to the lowest A exciton with literature data and absorbance spectra calculated by DFT for the ML. We identify the peaks of the BL emission analogue to the ML for the first time on $MoTe_2$ and in particular observe the $X^{B'}$ for the first time experimentally in TMDCs. Due to its emission energy in the near infrared, $MoTe_2$ is a perfect candidate to study higher excitonic states as their energy lies in the visible range and can, thus, be easily resolved. Moreover, we show that the trion is an excellent scattering channel for excitonic states. We confirm the excitonic nature of the ML high energy states by temperature resolved PLE. We take that knowledge and measure polarization across these higher excitonic transitions in ML and BL taking into account either the excitonic or the trionic emission.

5.2 The transfer of valley polarization

In this section, we study the degree of circular polarization of the exciton emission of ML and BL $MoTe_2$ while scanning the excitation wavelength over a wide range from near resonance with the A exciton via the B exciton and the A' exciton and up to the B' exciton. Schematic level schemes and helicity-dependent selection rules for the ML and BL of this material are shown in Fig. 5.7 (a) and (b), respectively. As spin and valley are no longer coupled, we do not observe a polarization from the BL. We find a non-zero polarization of the A exciton emission for the pump photon energy being resonant to either the B or the B' exciton transition. Moreover, the degree of polarization is highly temperature dependent due to temperature dependent changes in the underlying spin conserving and spin flipping scattering mechanisms with flexural phonons [161].

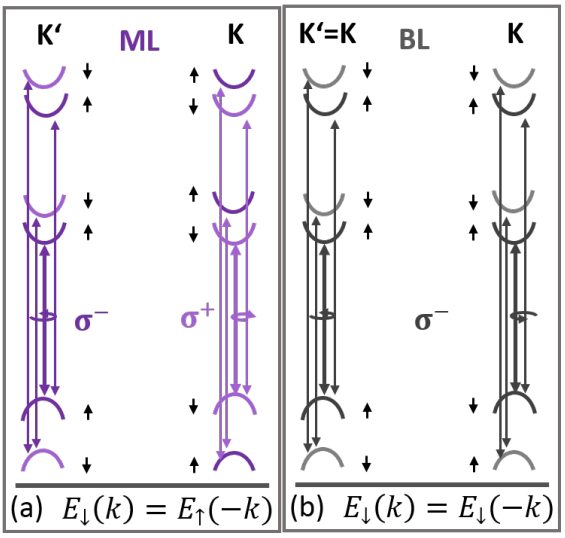

Fig. 5.7: Sketch of optical selections rules by exciting with left σ^- or right σ^+ circular polarized light, respectively for ML (a) and BL (b).

In the following, we excite the sample with σ^- polarized light and record polarization-resolved PLE spectra for both ML and BL $MoTe_2$. The setup is presented in section 2.3.2. We measure the degree of polarization by taking PL spectra with opposite polarized retarder plates, cf. section 2.3.2 and extract the emission area at different excitation energies for the emission on the exciton X^A or the trion X^T. The resulting emission is denoted by $I_{K'K'}$ ($I_{KK'}$) when investigating the same valley (opposite valleys). The degree of polarization, and hence the valley polarization [202], is determined by eq. 2.16. The section is organized as followed: Firstly, we investigate the polarization of the BL exciton. Secondly, we examine the polarization on the ML exciton emission by tuning the excitation over a wide energy range and correlate a non-zero polarization with the estimated position of the higher excitonic states. Thirdly, we investigate the temperature dependence of the polarization. And finally, we determine the trion degree of polarization.

5.2.1 No polarization from the bilayer

The results are presented in Fig. 5.8 for the BL (dark gray circles) at 10 K and 35 Wcm^{-2}. The gray shaded area represents the error interval for zero polarization extracted from the signal to noise ratio of the luminescence data. For clarity we include the PLE results from the previous section to identify energetically higher excitonic transitions (open gray circles).

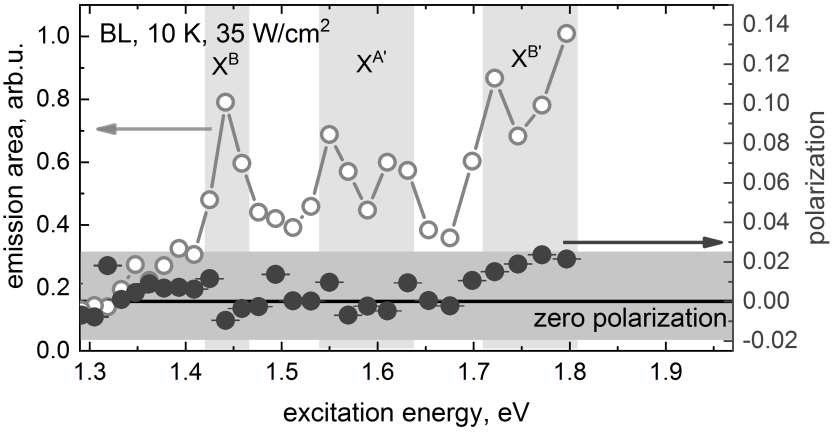

Fig. 5.8: (Left) Integrated area of emission of the exciton versus excitation energy for BL (open circles). (Right) Excitation energy dependence of PL circular polarization under σ^- polarized excitation for $MoTe_2$ BL (closed circles).

The dark gray circles in Fig. 5.8 show that the A exciton emission from the BL of $MoTe_2$ has zero polarization for all excitation energies, independent of the total emitted intensity. This is owing to the preservation of inversion symmetry in the BL as sketched in Fig. 5.7 (b). As investigated in section 2.2, excitation with σ^- polarized light addresses both valleys equally, thus, in the emission no polarization direction is preferred. This is consistent with measurements on natural 2H-structured BL showing little or no polarization even under resonant excitation [64]. For AB stacked homo-bilayers due to inversion symmetry breaking a large polarization can be obtained as established in Ref. [67, 68]. The results on the BL confirm the theoretical estimates of Refs. [189, 191, 192] and [194]: Restoration of inversion symmetry leads to a strongly depolarized system.

5.2.2 Polarization in monolayer - Spin or valley flip

The results for the ML $MoTe_2$ at 10 K are presented in Fig. 5.9 (b) (violet squares). The gray shaded area represents the error interval for zero polarization as extracted from the signal to noise ratio of the luminescence data. The violet shaded areas around the data points represent the errors of the ML polarization estimated by the difference in polarization of flake 1 and 2. While for all practical purposes, an off-resonant excitation seems to be favorable, little or no valley polarization has been observed so far under these conditions, even for MoS_2 and $MoSe_2$ [8, 73, 74]. We include the calculated polarization as thick violet line in Fig. 5.9 (b).

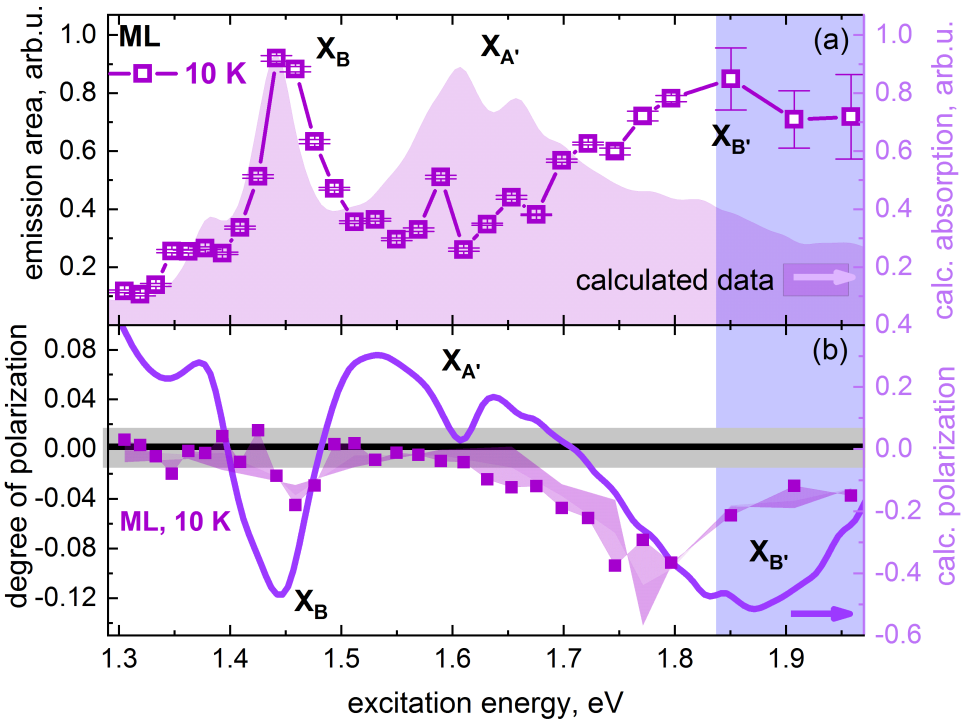

Fig. 5.9: (a, Left) Integrated area of emission of the exciton versus excitation energy for ML (violet squares). (a, Right) Absorption spectra (light violet area) from DFT calculations for ML $MoTe_2$. The excitonic transitions are indicated. (b, Left) Excitation energy dependence of PL circular polarization under σ^- polarized excitation for $MoTe_2$ ML (violet squares). The blue shaded areas on the panel indicating excitation with two different diodes and a HeNe laser. All other measurements where performed by using a Ti:Sa laser. (b, Right) Polarization estimated from DFT calculations (solid violet line).

We estimate the theoretical polarization by calculating absorbance spectra for opposite spin orientation and estimate the degree of polarization by eq. 2.16. To assign non-zero polarization through higher excitonic states, we include the ML emission area spectrum and the absorbance spectra from DFT calculations in Fig. 5.9 (a). A detailed investigation of this figure can be found in the previous section.

In contrast to the BL, the ML in Fig. 5.9 (b) shows strong deviations from zero polarization in two distinct excitation energy ranges. A clear circular polarization around an excitation energy of 1.46 eV of (-0.04 ± 0.01) and in the energy range from 1.69 eV to 1.90 eV is observed, with a maximum polarization of (-0.11 ± 0.02) for 10 K, respectively. The low energy peak coincides with the X^B resonance at 1.46 eV, cf. Fig. 5.9 (a) and the high energy peak is assigned to the $X^{B'}$ resonance. Thus, the polarization of the A exciton emission follows the polarization of higher excitonic resonances. This agrees with the DFT calculations, where we calculate a clear non-zero polarization across the B, A', and B' exciton resonance. From DFT we estimate a polarization of around (0.5 ± 0.01) for both B and B'. The polarization of the A' exciton is less, we estimate values of (0.3 ± 0.02) and (0.16 ± 0.2) for the lower and higher A' exciton peak. This decrease in the degree of polarization from B to A' explain why we cannot resolve

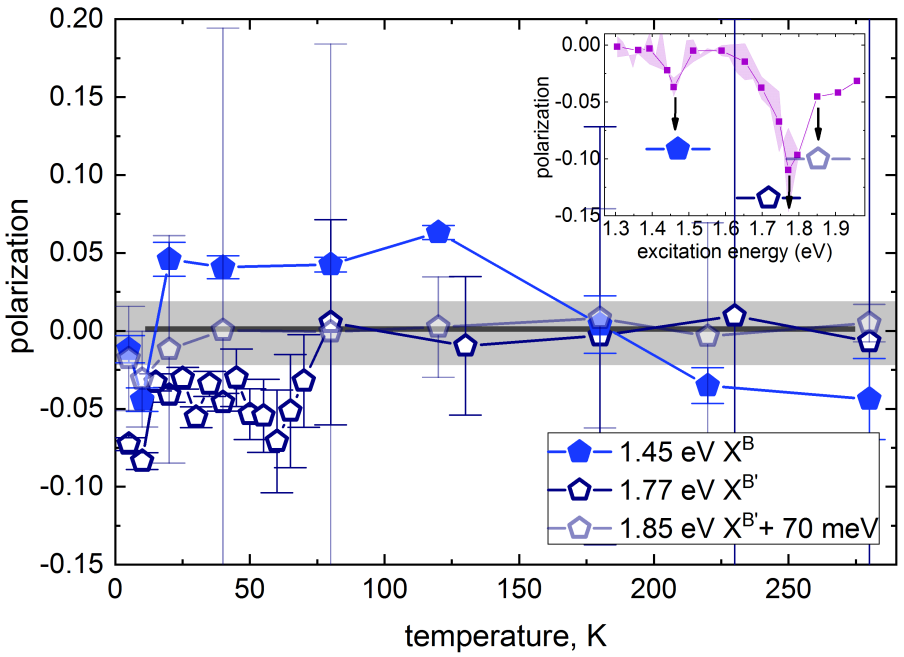

Fig. 5.10: Temperature dependence of PL valley polarization using σ^- circular polarized light of ML $MoTe_2$ for an excitation energy of 1.46 eV (open blue pentagons) 1.77 eV (open blue squares), and 1.85 eV (solid blue circles). Inset: Polarization at 10 K to illustrate the spectral positions of the excitation light of the respective polarization data.

this polarization in experiment. The decrease in polarization degree from theory to experiment is assumed to be due to additional phonon, defect and dark state related scattering channels.

We now change temperature for constant excitation energies resonant to the high excitonic transitions to investigate phonon influence on the degree of polarization. Fig. 5.10 shows the temperature dependence of the degree of polarization of A exciton emission for an excitation at the B exciton (closed blue pentagons), the B' exciton resonance (open blue pentagons) and at the blue shoulder of the B' resonance (open light blue pentagons). The latter does not result in a measurable polarization. We observe two main processes: First, we measure a finite polarization at low temperature for both B and B' where the degree of polarization changes signs for excitation resonant to the B exciton. Second, polarization is only measurable up to 80 K for a B' excitation and 120 K for a B excitation. The latter is explained by excitonic energy shifts with temperature in Fig. 5.6. Keeping in mind that the data of Fig. 5.10 were taken with constant excitation energy, it is reasonable that the excitation energy misses the B' and B resonances, and in both cases the polarization has decayed to zero at about 50-60 meV detuning. The larger shift of the B' peak explains why in this case the observed polarization is lost earlier, namely at 80 K. This is confirmed by temperature dependent measurements of valley polarization at a detuning energy of 70 meV (Fig. 5.10, light blue open pentagon), where the polarization vanishes already at low temperature, and the 2-LA-phonon polarization degree model of Ref. [8] being an upper limit for depolarization [173]. This cannot explain the change of sign for the B exciton resonance. Apart from 10 K, we choose a second temperature where

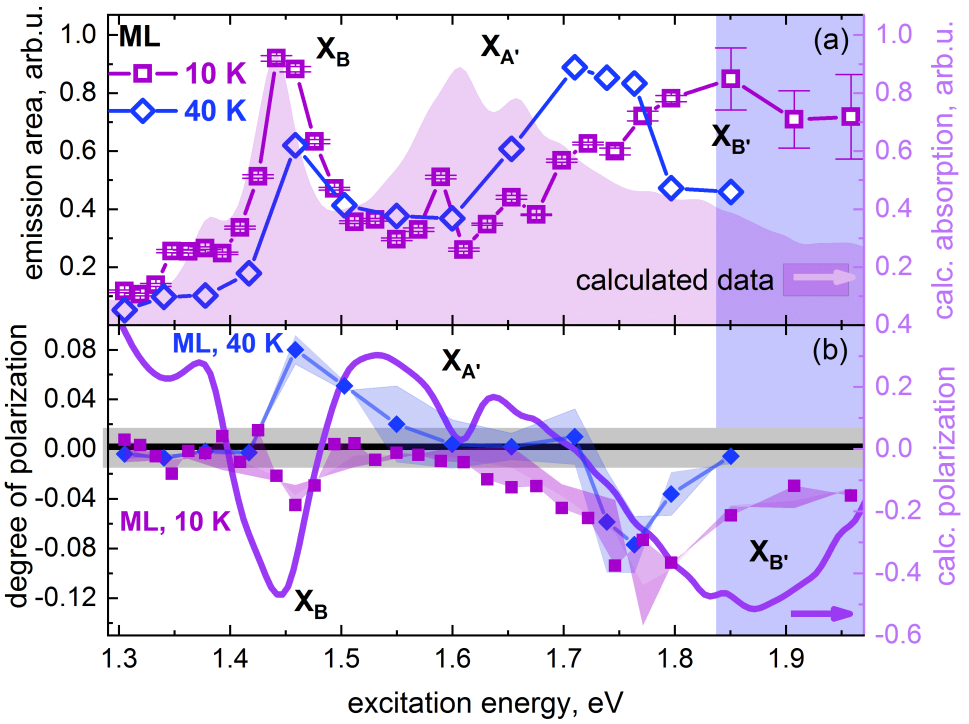

Fig. 5.11: (a, Left) Integrated area of emission of the exciton versus excitation energy for ML (violet squares: 10 K, blue diamonds: 40 K). (a, Right) Absorption spectra (light violet) from DFT calculations for ML $MoTe_2$. The excitonic transitions are indicated. (b, Left) Excitation energy dependence of PL circular polarization under σ^- polarized excitation for $MoTe_2$ ML (violet squares, blue diamonds). The blue shaded areas on the panel indicating excitation with two different diodes and a HeNe laser. All other measurements where performed by using a Ti:Sa laser. (b, Right) Polarization estimated from DFT calculations (solid violet line).

the sign of the B exciton is inverted and the B' exciton polarization is decreased, namely 40 K.

The results for the ML at 40 K are added to the Fig. 5.9 and are presented in Fig. 5.11 (a+b) as blue diamonds. In (a) the emission area at 40 K follows the emission area of 10 K. They overlap very well for the B exciton. For the B' exciton, we observe a higher shift at 40 K, and the A' exciton is not resolvable due to a larger separation of the energy points. With increasing temperature, the polarization (b) of the $X^{B'}$ resonance decreases from (-0.11 ± 0.02) to (-0.08 ± 0.02), respectively. At the X^B resonance the polarization degree changes signs and we measure a degree of polarization of (-0.04 ± 0.01) at 10 K and (0.08 ± 0.02) at 40 K. This change of sign can be not reproduced in the DFT calculations as they do not include any dynamics.

Starting from the high conduction band splitting in ML $MoTe_2$ compared to other TMDCs, a bright lowest optical transition in Mo based TMDCs [93, 80] and the low LA phonon energy in $MoTe_2$ [48], no valley polarization is to be expected for ML $MoTe_2$ for our high detuning energies $E_{excitation} - E_{X^A} \approx 490 - 600\,\text{meV}$ [8]. So there have to be additional processes included to the ones discussed so far for ML MoS_2 and $MoSe_2$ [74, 8]. We illustrate the underlying processes in Fig. 5.12 schematically to clarify valley and spin transitions. With

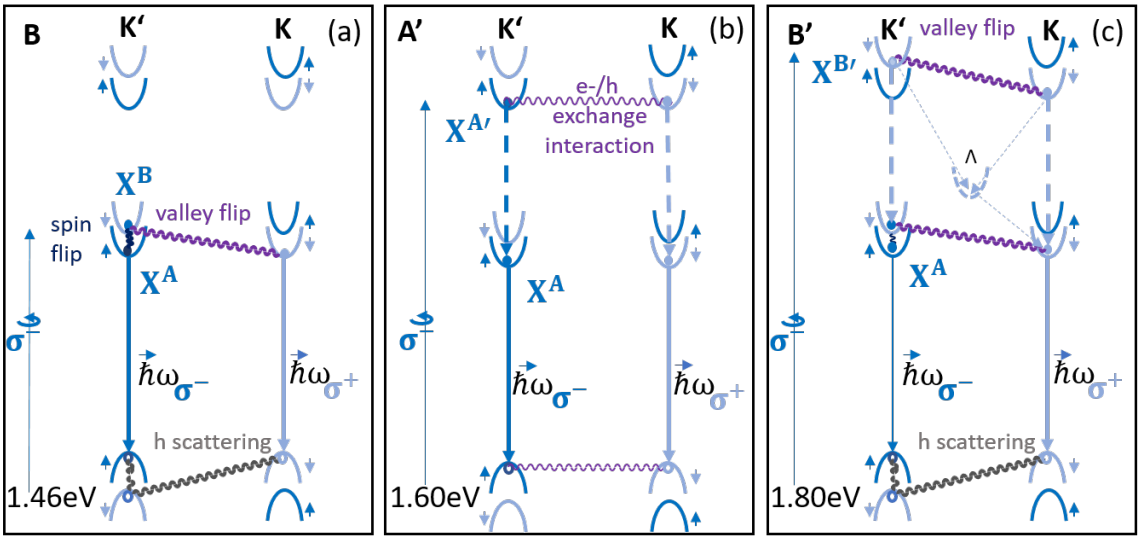

Fig. 5.12: Schematic illustration of phonon and exciton processes in ML $MoTe_2$ at 1.46 eV (B), 1.60 eV (A'), and 1.80 eV (B') excitation energy. Excitation with σ^- polarized light results in all cases in a population of the K' valley. Valley flip denotes spin conserved valley flip scattering of the electron. Spin flip induces a conservation of the valley.

a σ^--polarized excitation at 1.46 eV, we create a B exciton in the K' valley. For a better understanding we disentangle the interactions of electrons (e^-) and holes (h) and follow the rules implemented in Ref. [33] and [161]. For holes, inter-valley spin flip in the valence band is forbidden in 0th order due to optical selection rules. Therefore, only hole inter-valley spin-conserving and intra-valley spin-flip scattering is possible (cf. Fig. 5.12 B) and happens on comparable timescale. Following Ref. [161] there are two main assumptions for the electron: i) spin-conserving scattering is not affected by ZA phonons (cf. section 2.2.4) which dominate the scattering at low temperatures; ii) spin-flip scattering induced by ZA phonons is not vanishing and happens on highly temperature dependent timescales.

To investigate the temperature dependence of (ii), we calculate the electron spin flip scattering time τ_S^{e-} following Ref. [161] in the case of a substrate-supported ML with respect to temperature and the van der Waals interatomic force constant between ML and substrate $\kappa_S^{ML/sub}$. Our MLs are both connected to $MoTe_2$ bulk material as one can see in section 2.3.1, thus, we assume a reduced substrate coupling for our experimental conditions. As upper limit we use the value estimated for graphene on SiO_2 of $\kappa_S^{graph/sub} = 0.4\,Nm^{-1}$ [151]. According to Ref. [161], the spin flip scattering time is given by

$$\tau_S^{e-}(T, \kappa_S^{ML/sub}) = \frac{\hbar^3 \rho}{(2 m_K \Sigma_K^{SO})^2} \frac{1 + \exp(\frac{\Delta_K}{k_B T})}{4 + \frac{2\Delta_K}{k_B T}} \frac{\hbar^2 \kappa_S^{ML/Sub}/M_u}{(k_B T)^2}, \tag{5.1}$$

where the areal mass density is given by $\rho = \rho_{bulk}\, c/2 = 5.3 \cdot 10^{-7}\,\mathrm{g/cm^2}$ [156] with c being the lattice constant [138], $m_K = 0.53\ m_e$ is the effective mass in terms of the electron mass [204], $\Sigma_K^{SO} = 0.34$ eV is the small phonon wave vector in the zone edge and is estimated for $MoTe_2$

using Ref. [161], Δ_K is the conduction band splitting, and $M_u = 351.14\,u$ is the average atomic mass of the ML $MoTe_2$.

The calculated spin flip relaxation times are shown in Fig. 5.13 for different coupling strength of ML and substrate $\kappa_S^{ML/sub}$ and temperature. For comparison we also include the ML $MoSe_2$ and MoS_2 spin flip time for the same temperature and ML substrate coupling assuming either 13 meV or 4 meV conduction band splitting [39, 161]. The $MoTe_2$ spin flip scattering rate for temperatures below 40 K is higher than 1 ps and below 20 K higher than 1 ns for nearly free standing membranes (as we assume because of the connection to the bulk cf. section 2.3.1). Therefore, below 20 K, spin-conserving mechanisms dominate the exciton scattering resulting in the same circular polarization as the excitation light as sketched in Fig. 5.12 B. In contrast, for higher temperatures over $20 - 30$ K spin-flip valley conserved scattering dominates creating an opposite polarization compared to the excitonic emission. At high temperatures thus we measure a positive valley polarization across the B exciton. This perfectly agrees with the temperature dependence of the B exciton in Fig. 5.10. The values for $MoSe_2$ and MoS_2 in Fig. 5.13 show a different behavior. The valley conserving process in $MoTe_2$ observed in our experiment is stable up to 20 K i.e. for spin scattering times above 1 ns, whereas for ML $MoSe_2$ and MoS_2 the same timescales are observed for temperatures below ~ 13 K and ~ 5 K. That means in $MoSe_2$ and MoS_2 mostly valley conserving mechanisms should be observable in experiment. This is in perfect agreement with measurements on the B exciton for ML TMDCs in Ref. [107]. Moreover, it is also in agreement with pump probe measurements pumping the B exciton and probing the A exciton in WSe_2 [11] measuring a positive small polarization degree on the A exciton at room temperature.

Next, we investigate the A' excitonic transition in the energy range of 1.60 eV to 1.65 eV in Fig. 5.11. There we do not observe a valley polarization at any temperature. This is reasonable, as our calculations show a reduced polarization compared to the B, B' exciton. In addition, electron-hole exchange interactions happen on very short timescales below one picosecond, c.f. section 2.1.1. As sketched in Fig. 5.12 A', electrons and holes are more or less equally distributed in either the K' or K valley. The relaxation processes from the higher A' states to the lower A states happens due to cascade processes with phonons [17]. Thereby, especially the 2s exciton state is predominantly populated (within the first 100 fs) decaying within few picoseconds to the ground state exciton by optical and acoustical phonons. As scattering between excitons with the same angular momentum (i.e. best overlap of the excitonic wavefunctions) dominates, excitons in s states prefer to scatter to other excitonic s states. Consequently, we are observing either 2s than 2p excitonic states for both $X^{A'}$ and $X^{B'}$ resonances. In addition, there can be additional s scattering states in between the 1s and the 2s state, e.g. the 1s-KΛ state [17], where the hole is located in the K valley and the electron in the Λ valley (cf. Fig. 2.4).

Now we focus on the energy range in-between 1.72 eV and 1.85 eV in Fig. 5.11 related to the B' resonance. Here we consistently observe a large degree of polarization of up to -0.11 with the

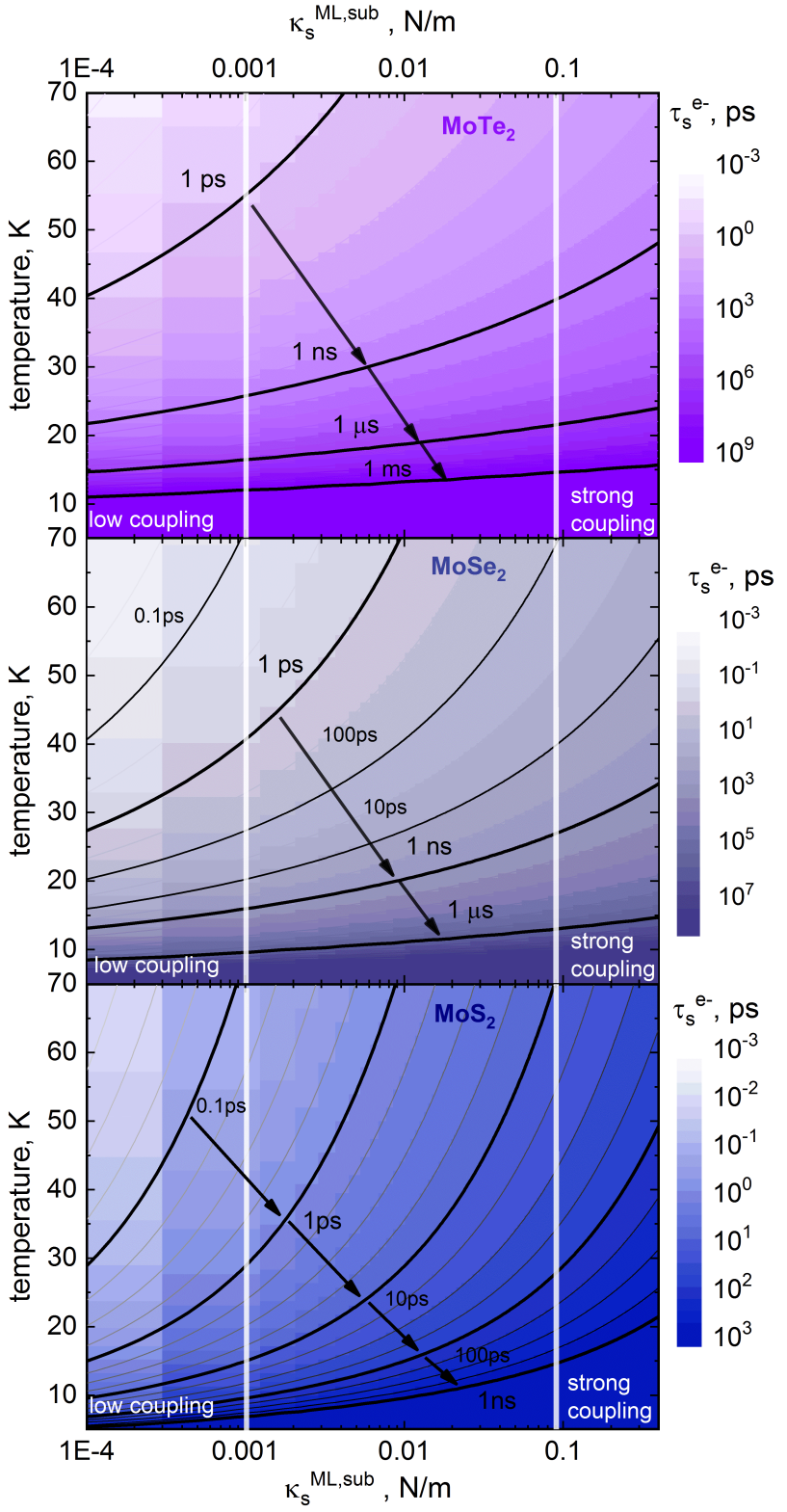

Fig. 5.13: Temperature and van der Waals interatomic force constant between ML and SiO_2 substrate $\kappa_S^{ML/sub}$ dependence of the spin flip relaxation rate for electrons in K valley due to interactions with phonons τ_S^{e-} for ML $MoTe_2$ (violet), MoSe2 (light blue), and MoS_2 (dark blue). The values are estimated by Ref. [161].

opposite helicity as the excitation light perfectly matching our DFT calculated polarization. In Fig. 5.12 B', excitation of the system with σ^- polarized light at 1.80 meV excites the $X^{B'}$ exciton in the K' valley. The hole mechanisms are comparable to the B exciton cases, the electron behaves differently. At low temperature we assume a preferred valley flip and a relaxation via a phonon cascade processes [17]. Increasing temperature results in a decreased polarization as spin-flip processes become significant. But phonon cascade processes have to considered additionally, for example cascade processes towards the Λ point which is energetically between the X^B and $X^{B'}$ resonance. Relaxation processes through this state preserve spin, being on really fast timescales of half a picosecond [17]. So, scattering towards the K valley is more likely emitting opposite circular polarized photons, resulting in a negative degree of polarization. These states are energetically not favorable in the B excitonic transition, this can explain the mismatch in B and B' polarization degree.

5.2.3 The degree of trion polarization

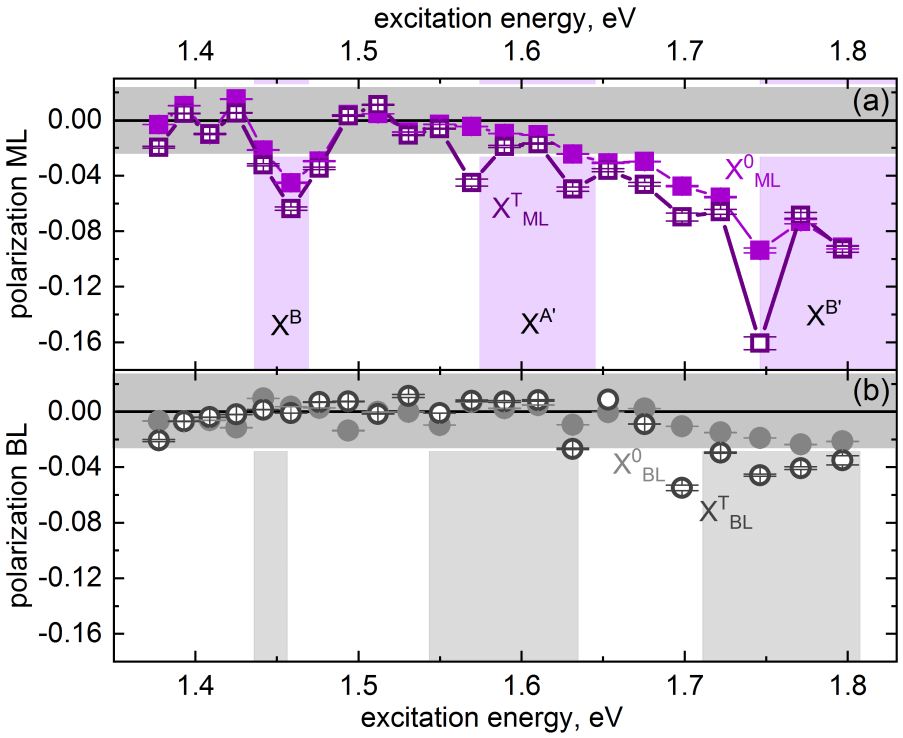

Fig. 5.14: Excitation energy dependence of PL circular polarization under σ^- polarized excitation for $MoTe_2$ ML (a, violet squares) and BL (b, gray circles) for excitons (closed symbols) and trions (open symbols).

In addition to measurements on the polarization degree of the A exciton, a non-zero trion polarization seems reasonable as we observe the same higher excitonic peaks in trion emission area, as seen before in Fig. 5.3. Therefore, we investigate trion degree of polarization similar to the exciton as described in the previous section. The results are presented in Fig 5.14 in

(a) as open violet squares (in (b) open gray circles) for ML (BL) $MoTe_2$. To compare with the trion, the closed symbols represents the exciton polarization investigated in the previous section. The shaded areas indicate the excitation energy range of the higher exciton states. We observe that the trion polarization degree follows the exciton degree of polarization with three major exceptions. (i) The observed polarization on the ML is stronger for the trion than for the exciton. (ii) We observe a negative degree of polarization across the $X^{A'}$ resonances in ML. (iii) There is a non-zero polarization degree measurable on the BL trion.

To understand the underlying processes at least for the ML, we include the trion processes in toFig. 5.12. The modified version is seen in Fig. 5.15. For all three different excitation energy ranges the excitation with σ^- polarized light not only excites excitons in the K' valley with a certain energy, it also excites electrons in the K' valley which can form a trion, together with an electron hole pair. In all three cases, we create excitons where the electron is not located in the lowest conduction band of the K' valley, but in higher conduction bands of the K' valley. The lowest conduction band, thus, can be populated with K'- spin up electrons (shown as yellow dots in Fig. 5.15). Due to the Pauli principle the exciton with its own electron now cannot relax in the lowest conduction band in the K' valley. It can either scatter to the next higher conduction band in the K' valley or to the lowest conduction band in the K valley. The latter is energetically and spin preferred. In case of the B exciton this is can be achieved by a valley flip of the electron and hole, maximizing the valley flip and spin conserving process dominating at lower temperatures in case of the A exciton emission. The same processes are observed for the B' exciton resulting in a for $MoTe_2$ high polarization degree of (-0.16 ± 0.03). For the $X^{A'}$ resonance we do not observe a polarization of the exciton, as electron hole exchange processes leads to equally distributed valleys. In case of an extra charge the K' lowest conduction band is blocked for other particles thus cascade processes toward the K valley dominate and we can detect more σ^+ polarized photons, resulting in a net polarization of (-0.05 ± 0.02). Besides, the larger polarization degree of the trion compared to the exciton is in agreement with measurements on WS_2 [52].

The polarization on the BL trion is harder to understand, and may result from inter-layer trions [208], where the electron hole pair is located in one valley and the extra charge is localized in the other layer, this can result in a non-zero polarization degree but is not associated to the previous introduced valley polarization. Near resonant (to the A exciton) magneto-PL measurements show a small trion polarization on natural bilayer $MoTe_2$ larger than from the exciton without applying a magnetic field [63]. This can explain the polarization degree of -0.04 to -0.05 we observed in experiment. To understand the physical processes in more complicated systems, van-der-Waals heterostructures with upper and lower layer consisting of different TMDCs can be a convenient system to study inter-layer effects.

In conclusion, by polarization resolved photoluminescence spectroscopy we measure for the first time a valley polarization in the A exciton emission of ML $MoTe_2$ and a polarization

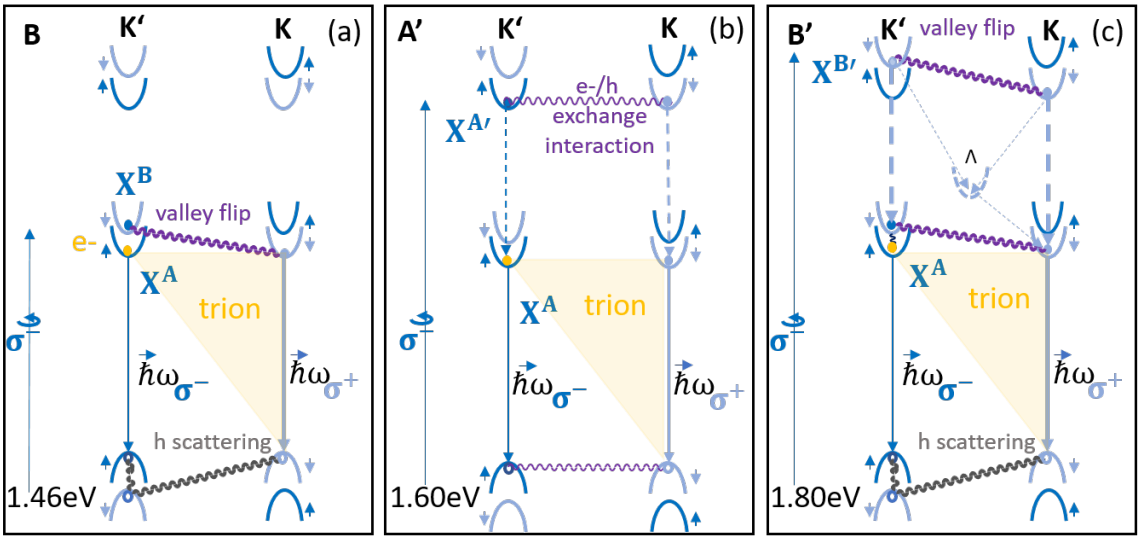

Fig. 5.15: Schematic illustration of phonon and exciton processes in ML $MoTe_2$ at 1.46 eV (B), 1.60 eV (A'), and 1.80 eV (B') excitation energy. Excitation with σ^- polarized light results in all cases in a population of the K' valley. Valley flip denotes spin conserved valley flip scattering of the electron. Spin flip induces a conservation of the valley. The yellow circles denote the extra electron and the yellow shaded area is the main light emitting trion.

transferred from the $X^{B'}$ resonance in all TMDCs. The polarization strongly dependent on the excitation energy. We measure a degree of polarization of (-0.04 ± 0.01) and (-0.11 ± 0.02) when exciting at the B and B' excitonic transitions at low temperature. An increase in temperature results in changes in the spin and valley conserving processes. At low temperature, valley flip, spin conserving processes dominates, whereas at higher temperatures the spin-flip valley conserving processes dominate. This results in a sign flip of valley polarization on the B exciton emission especially observable in $MoTe_2$ due to the large conduction band splitting and a massive chalcogenide atom. This temperature controllable flip in polarization can simplify binary selections in valley-tronic devices. Besides, we measure a high polarization of the trion of (-0.16 ± 0.03) compared to the exciton, giving rise to trion valley-tronic applications.

6 Exciton and trion formation, decay and polarization dynamics in $MoTe_2$

We study the pump energy dependence of two-color pump probe spectroscopy traces of the monolayer exciton and trion in molybdenum ditelluride in the temperature range between 5 K and 125 K. We focus on the amplitude and phase data, as the exciton amplitude data show a strong bandgap renormalization. We confirm that the trion decay time is larger than the exciton decay time, as previously assumed due to a faster exciton radiative decay compared to the trion in section 3.1.2. We extract a fast decay in the picosecond range, being strongly temperature-dependent, and attribute it to defect-bound electrons for both excitons and trions. The phase response of the exciton shows a formation process similar to the trion formation, thus the trion is an excellent scattering channel for the exciton. In addition to the fast quasiparticle decay, we find a long-lived component which we attribute to free carrier recombination. Moreover, we extract the trion formation time and explain this as a bimolecular formation, i.e. trions form by exciton to trion formation due to a capture of an extra charge on timescales of $1.5 - 2.5$ ps.

In the second part of this chapter, we investigate exciton and trion depolarization timescales and the degree of polarization. The exciton polarization degree is strongly influenced by renormalization effects and shows a depolarization within 1 ps due to electron-hole exchange interactions. The trion polarization is lost within 3 ps under quasi-resonant pump and probe energies at low temperature. For higher temperature, we observe a valley to spin flip conversion process. Moreover, we disentangle intra- and inter-valley trion processes for slightly different pump energies.

6.0.1 Introductory Remarks

The setup for the two-color pump probe (TCPP) experiments is presented in section 2.3.3. The TCPP spectroscopy is performed on ML $MoTe_2$, namely on flake 2, cf. section 2.3.1. The associated PL emission is shown in Fig. 6.1 (a, black line). We attribute the peaks to the exciton (X^0) and trion (X^T) emission. The properties of the emission like lineshape, broadening with temperature, emission energy and trion binding energy are similar to the properties of flake 1 discussed in chapter 3. We use a *FemtoFiber Pro* laser system with two synchronized pumped non-linear fiber amplifiers outputting white light supercontinua which are independently tunable in energy by amplitude masks in the Fourier plane of pulse shapers. The resulting pulses have a Gaussian-shaped spectrum of 10 nm FWHM width and 180 fs FWHM duration. The violet shaded Gaussian profiles in Fig. 6.1 (a) picture the spectral profiles of the pump and probe beams if centered resonant to the exciton and trion emission. The probe energy stays constant quasi-resonant to the exciton (1.180 eV) and trion (1.160 eV) emission energy. We measure pump probe spectra tuning the pump energy across the exciton and trion resonance, starting 11 meV below the trion emission up to 81 meV above the trion emission, in a pump energy range from 1.24 eV to 1.15 eV. The pump energies are indicated by violet arrows in Fig. 6.1 (a). In the second part of this chapter, we change the polarization of the pump beam (i.e. address K or K' valley), whereas we probe always at the K valley. If pump and probe beam have the same (opposite) circular polarization, we define this as co (cross) polarized. To obtain polarization resolution, polarizers and broadband $\lambda/2$ and $\lambda/4$ retarder plates were inserted in pump, probe, and reference beam paths. For polarization resolved measurement details we refer to sections 2.3.2 and 2.3.3.

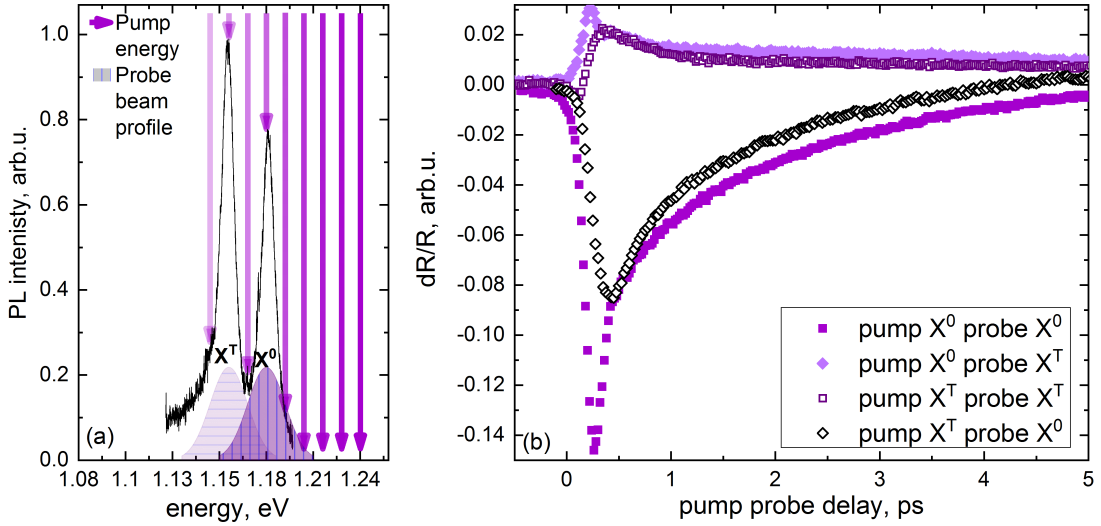

Fig. 6.1: (a) Exciton (X^0) and trion (X^T) photoluminescence spectrum (black line) of ML $MoTe_2$ at 15 K. The violet arrows indicate the different pump energies. The shaded Gaussian profiles indicate the energy profiles of the pump and probe beams and are centered at the probe energies resonant to the trion and exciton. (b) Normalized pump probe reflection data under different pump and probe energies at 15 K.

The TCPP measurements are performed using heterodyne balanced detection. This enables a simultaneous measurement of amplitude and phase unlike in most conventional pump probe measurements [36, 44, 33]. We measure in reflection geometry and the differential amplitude signal reads as differential reflection (dR/R), the differential phase signal ($\Delta\Phi/\Phi$) is called in the following for simplicity phase. Figure 6.1 (b) shows the delay-dependent differential amplitude change of the reflectivity for pumping and probing the exciton (XX, violet solid squares), pumping and probing the trion (TT, dark violet open squares), pumping the exciton and probing the trion (XT, light violet diamonds), and pumping the trion and probing the exciton (TX, black open diamond) in a two-color experiment. Note that the sign of the data taken at the exciton energy is inverted as the exciton resonance is shifted on an ultrafast timescale due to bandgap renormalization.

In this chapter, we study formation and decay processes of excitons and trions in ML $MoTe_2$ in ultrafast pump-probe experiments in a temperature range between 5 K and 125 K. We fit the decay of the spectra exemplary shown for 15 K in Fig. 6.1 (b) XX and TT three-exponentially as a function of temperature. We found in both cases an ultrafast component which we attribute to the pulse overlap of pump and probe pulses which we do not further analyze as it may contain coherent effects not accounted for by a multi-exponential decay. The fast component represents the decay of the quasiparticle and the slow decay component is associated with the free carrier decay. The timescales of the quasiparticles decrease with increasing temperature and are larger for the trion than for the exciton as shown for the radiative decay in chapter 3. Non-resonantly excited trion processes cannot be described without considering formation times of several picoseconds. By quasi-resonantly pumping the exciton and probing the trion (XT, light violet diamonds in Fig. 6.1), we measure trion formation times of $1.5 - 2.5$ ps. The last curve is measured by pumping the trion and probing the exciton. This theoretically should measure the trion to exciton scattering mechanisms. As the trion is around 24 meV energetically below the exciton, a scattering from trion to exciton seems to be unlikely, unless processes like annihilation of phonons are included. Especially optical phonons have matching energies, but at low temperatures there are not active. Therefore, we attribute the observed pump probe signal to state filling processes [62] and/or exciton up-conversion as observed in PL [119] and do not investigate the decrease of the signal further.

The analysis of the polarization degree is the topic of the second part of this chapter. We study the degree of circular polarization of the exciton and trion. The polarization of the exciton is strongly influenced by bandgap renormalization and bleaching effects leading to a reduced signal in the pumped valley and a counter-intuitive negative polarization of -65 %. The trion show less bandgap renormalization compared to the exciton. We measure a polarization degree of 95% resonantly to the trion transition. This maximum polarization by pumping and probing resonant to the trion is lost within 3 ps. This is in perfect agreement with previous experimental results [159] which shows that the trion polarization decays slower than the exciton.

6.1 Decay- and formation time of exciton and trion

In this section, we analyze the ultrafast decay processes of excitons and trion by investigating both phase and amplitude. $MoTe_2$ has so far not been studied in pump experiments. However, we can fit the exciton and trion decay by a three-exponential decay. We attribute the decay to a fast non-radiative decay be defects for both exciton and trion. In addition, the phase signal of the exciton shows a bimolecular trion formation process. The same formation process can be observed by pumping the exciton and probing the trion.

6.1.1 The mismatch of exciton amplitude and phase decay

Fig. 6.2 (b) shows the amplitude (dR/R, violet squares) and the phase (gray squares) signal at 15 K as a function of pump probe delay for a large time range and a smaller time range which is illustrated in the inset. There, we pump and probe at the excitonic transition X^0 as pictured in Fig. 6.2 (a). The amplitude and phase data in Fig. 6.2 (b) show a completely different evolution with delay time. For the amplitude signal the pump and probe energy is the resonance energy. For an energy smaller than the resonance energy the phase signal is negative due to a negative index of refraction which is the most usual situation. For energies below the phase signal has a positive sign. To both ends the phase diminishes slowly thus can scan a lager energy range than the amplitude [140]. This shows: Apart from the excitonic transition we pump and probe in the amplitude, we also create a set of other carriers off-resonantly resulting in a different phase behavior. However, in both cases the signal rises strongly with the laser duration of 180 fs (gray shaded Gaussian) and for the first few hundreds of femtoseconds the phase and amplitude are similar. Then the decay differs immensely.

The exciton amplitude can be fitted by a three-exponential decay

$$\frac{dR}{R} = A_{laser}\ e^{-\tau/\tau_{laser}} + A_{fast}\ e^{-\tau/\tau_{fast}} + A_{slow}\ e^{-\tau/\tau_{slow}}, \tag{6.1}$$

indicating more than one relaxation process. The fit is shown as solid blue line in Fig. 6.2. The first component (black box) decays with a time constant similar to the convolution of pump and probe pulses in all traces. It is attributed to coherent effects during the overlap of the pulses [154]. For illustration we insert the laser pulse envelope as gray Gaussian area. The remaining decay components are the fast (blue box) and the slow (yellow box) component. We extract values of (2.5 ± 0.5) ps and (40 ± 5) ps. These are the first pump probe data ever measured on $MoTe_2$, therefore we can only compare our results to previous measurements on other Mo and W based TMDCs. The values are in agreement with decay times of MoS_2 cf. Refs. [154, 184]. The fast component is thus attributed either to exciton decay by surface trap states [154], intrinsic exciton lifetimes, as the radiative exciton lifetime in this materials is found to be around 3-4 ps [85, 134], or non-radiative capture and recombination of photoexcited carriers

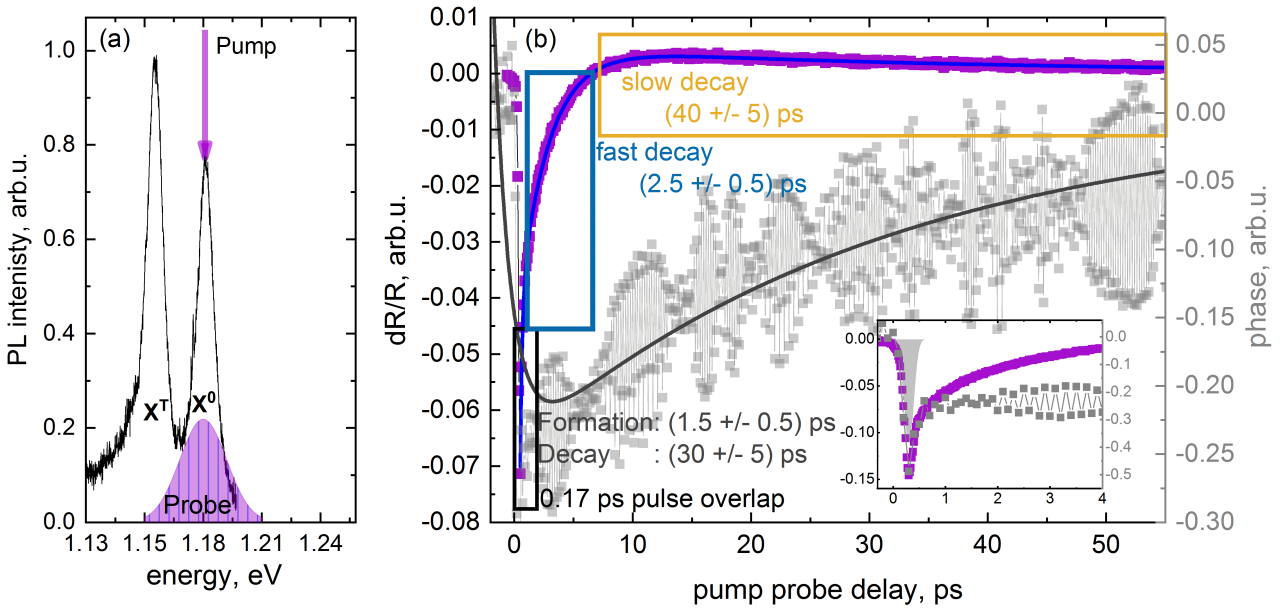

Fig. 6.2: (a) PL spectrum at 15 K the pump and probe energies are indicated. (b) Pump probe reflection data (violet squares) and phase data (gray squares) for pumping and probing the exciton fitted by a three-exponential decay (blue line) and formation-decay process by eq. 6.2 (gray line). The fit values are included. (Inset) Reflection and phase data at a smaller pump probe delay.

by defects e.g. transition metal or chalcogenide vacancies [184]. The slow decay component is determined by interband carrier-phonon scattering [154]. This means the energy resulting from the fast non-radiative decay is transferred to a phonon system, increasing the temperature of the lattice, shifting the excitonic transitions to smaller energies. The cooling -a heat transfer from the ML to the substrate- results in a decay of 10-100 of picoseconds [142]. Note, exciton decay mechanisms are highly dependent on the pump fluence attributed to exciton-exciton annihilation and Auger recombination [83, 168, 184]. For this reason, we kept our pump fluence as low as possible.

The phase signal behaves differently, the simultaneous rise and decay within the laser duration. The phase shows a formation-like process getting more pronounced by slightly tuning the pump energy to lower and higher energy values compared to the probe. To investigate the phase decay in detail, we subtract the signal corresponding to the pulse overlap. The remaining phase signal is fitted by a formation-decay equation established by Ref. [157]

$$\frac{\Delta\Phi}{\Phi} = A\left[1 - B \cdot \exp\left(\frac{\tau}{\tau_{form}}\right)\right] \exp\left(\frac{\tau}{\tau_{decay}}\right). \tag{6.2}$$

The resulting fit is shown as solid gray line in Fig. 6.2. We extract a formation time of (1.5 ± 0.5) ps and a decay of (30 ± 5) ps. The formation timescale is comparable to the fast decay of the exciton and the formation of trions as seen in the next subsection. Thus, a possible process is the formation of trions. Besides, we can either observe disintegration of excitons to electrons and holes, a transfer of carriers to dark excitonic states and lambda point excitons

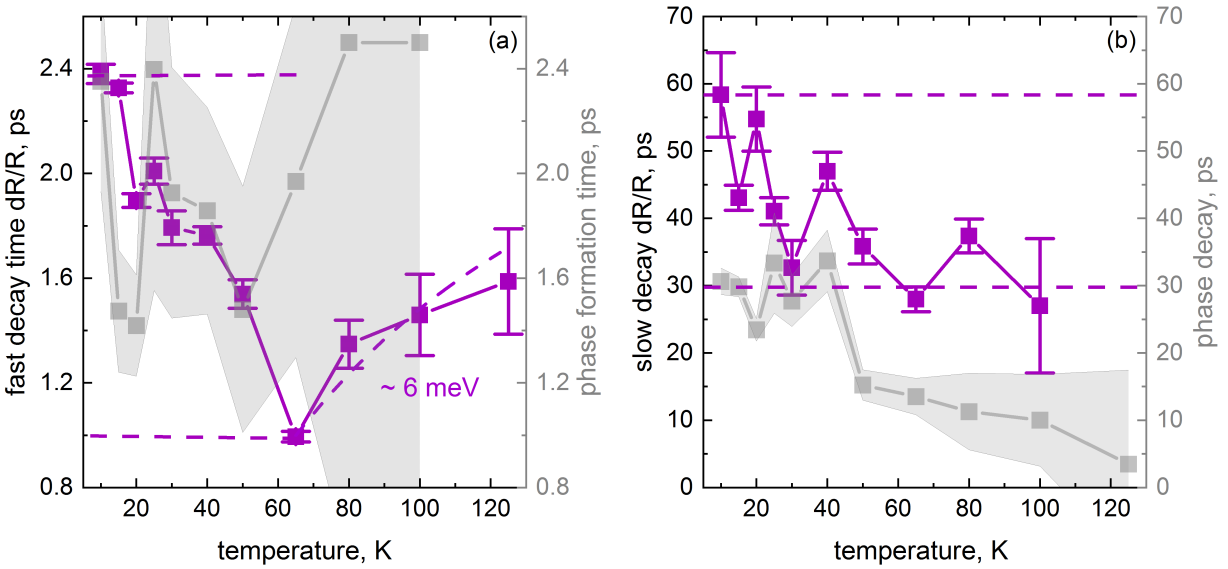

Fig. 6.3: Exciton amplitude decay time (violet squares) versus temperature out of three-exponential decay eq. 6.1 for the fast (a) and slow (b) component. Exciton phase time parameters (gray squares) out of the formation eq. 6.2 fit for the formation (a) and decay (b) time, where the error is shown as shaded area.

by phonons [102, 148] or a scattering towards defect states. To further investigate this, we measure temperature dependent exciton amplitude and phase pump probe signal.

Fig. 6.3 shows the temperature dependence of the fast (a, violet squares) and the slow (b, violet squares) time decay of the amplitude and the formation (a, gray squares) and decay (b, gray squares) of the phase signal. The fast time decreases with increasing temperature from 2.4 ps at 10 K to ∼1 ps at 65 K. A similar trend was observed for the acoustical phonon limited exciton relaxation time in PL measurements in chapter 4 in the same temperature range. For temperatures above 65 K the time constant increases with increasing temperature. We can explain this effect by weakly localized shallow potentials [157]. These states are weakly redshifted from the exciton state and lead to an inhomogeneous broadening of the linewidth. By increasing the temperature these states are thermally activated with an activation energy of ~ 6 meV extracted from an Arrhenius fit pictured as dashed line in Fig. 6.3 (a). We directly compare this activation process to the measurements of the inhomogeneous linewidth in section 4.1, Fig. 4.1. There we observe that the inhomogeneous linewidth has a minimum at ∼60 K and increases for higher temperatures, supporting the assumption of an activated shallow state. Such states capture carriers, which than decay non-radiative. The process below 60 K is also described by a non-radiative decay due to defects. An electron is captured into a bound state which is in our case a defect state, and then recombines with a hole in its original state most likely at the K or K' point. The released energy can be either transformed into lattice phonons or can excite other carriers (especially at high excitations powers) which is in principle the Auger process. The first process can be addressed by temperature resolved measurements. The strong temperature dependence we observe in Fig. 6.3 (a) supports the assumption of multiple

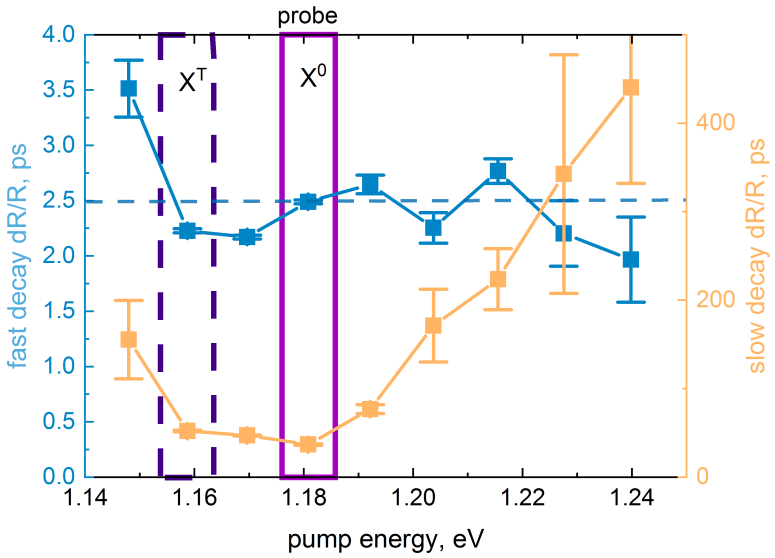

Fig. 6.4: Exciton decay time versus pump energy out of three-exponential decay fit (eq. 6.1) for probing resonantly to the exciton at 15 K. The fast component is pictured in blue the slow component in yellow.

phonon emission due to non-radiative electron capturing processes by defects [57]. The forming process in the phase data has comparable timescales to the trion formation process indicating that we can observe the formation of trions non-resonantly as the phase response is sensible to a wider energy range. The slow component in Fig. 6.3 (b) shows a similar behavior for both amplitude and phase decay decreasing with increasing temperature. The phase signal is limited for higher temperature to the radiative decay time of the trion of 12 ps (cf. section 3.1.2). This is reasonable, as the defect and shallow states are filled with excitons, therefore, trions cannot decay through this channel. This means that for higher temperatures scattering towards weakly localized shallow states is likely.

To further investigate exciton behavior, we perform pump energy resolved TCPP measurements. The results for the fast and slow decay component for the exciton are presented in Fig. 6.4. The fast (blue squares) component around 2.5 ps at 15 K in perfect agreement with the previous discussion. An exception is formed at 1.15 eV, where we pump slightly energetically below the trion resonance. The decay seems to be limited through the trion decay time, as the trion is the energetically favorable state, as seen in Fig. 6.2 (a) such that the measured value is dominated by signal from the trion. The slow component (yellow squares) is low for resonant pumping X^0 and X^T and gets slower for off-resonant excitation reflecting the cooling of the phonon-heated lattice. The higher values for off-resonant excitation previously measured by Ref. [154] and are attributed to direct interband electron-hole recombination.

To understand the nature of the quasiparticle decay in TMDCs, the trion decay processes needs to be investigated in more detail which will be done in the next subsection.

6.1.2 Trion formation and decay

In this section we quantify the trion decay time by a three-exponential decay and describe the formation of trions by pumping the exciton and probing resonantly to the trion. Both amplitude and phase show a comparable behavior confirming that we are investigating mostly trion decay processes.

Fig. 6.5 (b) shows the trion dynamics for the phase (gray squares) and amplitude (violet squares) for pumping and probing resonant to the trion X^T as pictured in Fig. 6.5 (a). The evolution of the phase and amplitude signal is remarkable similar. The phase normally reflects other states and carriers which are as well excited by pumping and probing a resonance. Therefore, in case of the trion mostly trions processes are investigated. This seems reasonable as the trion is the energetically lowest state. Moreover, this indicates that the trion has fewer scattering channels compared to the exciton. The trion decay can be described by a three-exponential decay with eq. 6.1 comparable to the exciton decay. We measure an ultrafast component of 0.17 ps due to the pump probe pulse overlap, as previously observed for the exciton. Besides, we extract a fast component of (3.9 ± 0.5) ps and a slow component of (45 ± 5) ps for both amplitude and phase. This is in good agreement with measurements of $MoSe_2$ [44] under the assumptions of low pump fluency. As the estimated radiative decay for trions in ML $MoTe_2$ is around 12 ps (cf. section 3.2.1) other processes dominate the trion decay. Thus, non-radiative process like defect assisted scattering is a possible additional mechanism [44, 95].

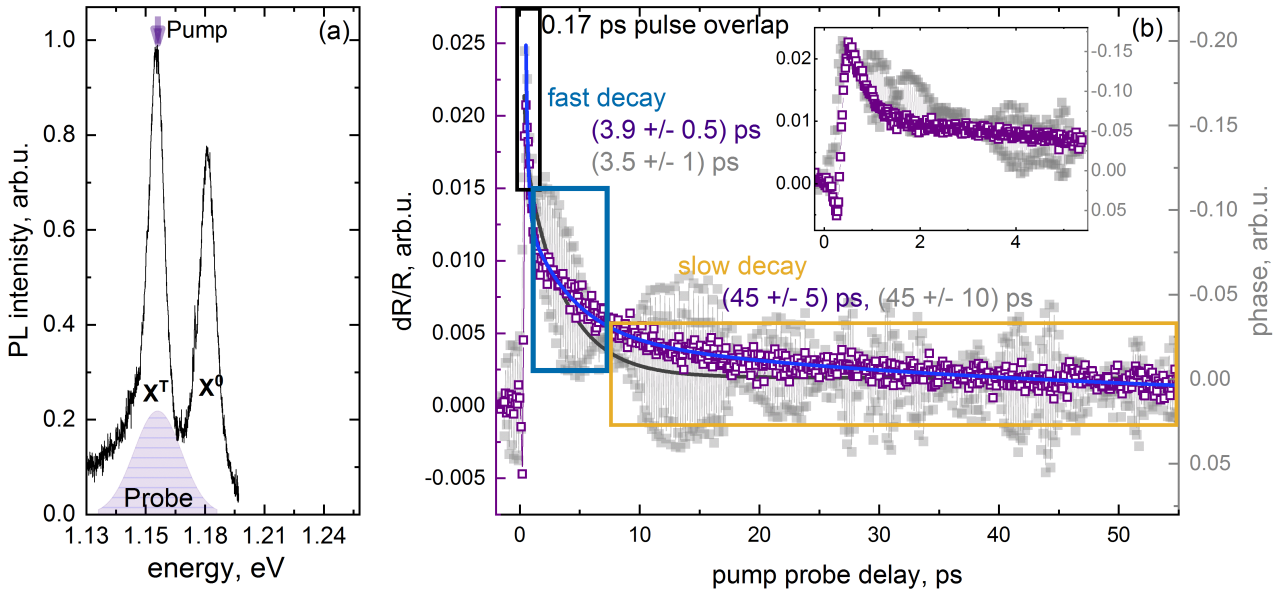

Fig. 6.5: (a) PL spectrum at 15 K, the pump and probe energies are indicated. (b) Trion amplitude (violet squares) and phase (gray square) pump probe signal as a function of pump probe delay. We fit both curves with the three-exponential decay eq. 6.1.

Analog to the exciton, we investigate the fast and slow component of the trion decay in Fig. 6.6. As amplitude and phase show a similar behavior, we concentrate here on the amplitude

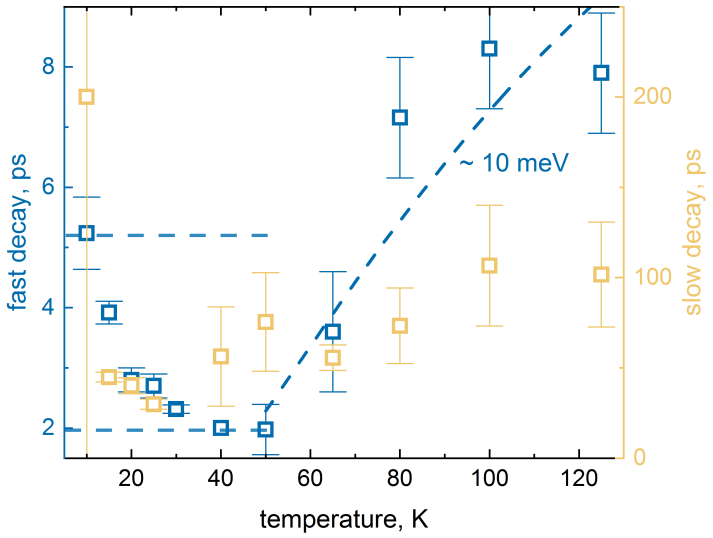

Fig. 6.6: Trion fast (blue squares) and slow (yellow square) decay time versus temperature out of three-exponential decay fit (eq. 6.1).

data. As for the exciton, the fast decay time decreases with increasing temperature from ∼5 ps at 10 K to ∼2 ps at 50 K and then increases again for higher temperatures to ∼8 ps. In very pure systems the radiative decay is slowed down with increasing temperature. Unlikely here, because the decay is faster than the radiative limit. The absolute change in decay time is larger in the trion compared to the exciton. The inhomogeneous linewidth in section 4.1, Fig. 4.1 shows a minimum at comparable temperature. There, the relative change in linewidth is stronger for the trion as for the exciton. This supports, non-radiative scattering processes and weakly localized shallow states are responsible for the trion decay. Moreover, it shows that the same defect and shallow states are influencing both exciton and trion. At lower temperatures we follow the trend of the acoustical phonon limited relaxation time in section 4.2.4. This means heating the material leads to a faster interaction with defects and other particles resulting in a faster decay. Fitting the higher temperature processes with the Arrhenius equation results in an activation energy comparable to the exciton of the shallow state of 10 meV. The trion decays slower than the exciton.

By pumping the exciton and probing the trion we can analyze trion formation. There are two main trion forming processes [44, 122, 157]: 1. directly from the electron-hole-plasma by three carrier formation, which is more likely at high excitation densities; 2. by exciton to trion formation. Several previous publications assume the latter one [44, 95]. The results of our TCPP measurements by pumping resonantly to the exciton and probing resonantly to the trion (named XT) are presented as violet squares in Fig. 6.7 (a). Note, we have subtracted the Gaussian component of the laser emission. The observed non-zero signal is a clear indication for a coupling between the exciton and the trion [158] in the ML $MoTe_2$. Two-dimensional coherent spectroscopy measurements will clarify whether they couple coherent or not as done in the next chapter for $MoSe_2$. We investigate the formation and decay processes in the amplitude

by a slightly modified version of formation equation in Ref. [157], expending the decay to a biexponential decay function. The formation equation reads then

$$\frac{dR}{R} = (A_1\ e^{-\tau/\tau_{fast}} + A_2\ e^{-\tau/\tau_{slow}}) \times (1 - A_3\ e^{-\tau/\tau_{form}}), \tag{6.3}$$

where, τ_{form} is the formation time.

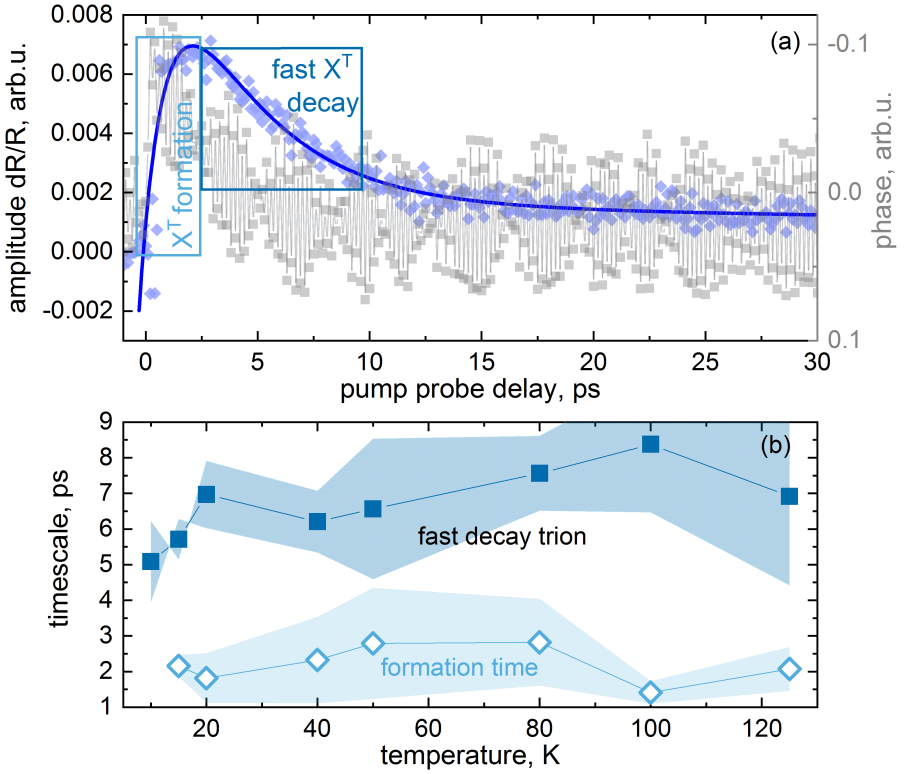

Fig. 6.7: (a) Two color pump probe measurements of pumping at the exciton and probing at the trion (XT) at 15 K (violet diamonds). The phase is pictures as gray squares. The amplitude data are fitted by a formation and decay equation 6.3. (b) Temperature dependence of trion formation and trion decay estimated by pump the exciton and probe the trion.

The extracted values are presented in Fig. 6.7 (b) for the formation (open blue diamonds) and the fast decay (blue closed squares) as a function of temperature. We extract a trion formation of 1.5-2.5 ps with a minimum formation time of (1.4 ± 0.3) ps at 100 K. The small variations in formation time are due to slightly different pump energies [157] as we tune the pump energy with temperature following the shift of the PL trion energy. The formation time is in good agreement with measurements on $MoSe_2$ [157] and is in between the ultrafast formation in carbon nanotubes [144] and the slow formation in quantum wells [81]. This means the trion binding energy limits the formation process [157]. As we directly excite the exciton and assume an instantaneous formation of the exciton seen in Fig. 6.2, we support the assumption of exciton to trion formation through exciton-electron interactions. The decay times slightly increase with increasing temperature and are limited to the fast time of the trion decay (cf. Fig. 6.6). Therefore, we attribute this process as trion formation.

In conclusion, we found a mismatch in phase and amplitude signal for the excitation at the exciton energy. The amplitude shows a three-exponential decay due to capturing of electrons from defect states, recombination of these excitons with holes, and the creation of phonons heating the lattice. In contrast, the phase data show a formation process which is attributed to the formation of the energetically lower trion. By pumping the exciton and probing the trion we find comparable timescales of 1.5-2.5 ps for the formation, if directly excited. The trion itself also shows a three-exponential decay due to defect states comparable to the exciton. The temperature dependence of the exciton and trion decay is strongly influenced by defects for lower temperatures acoustical phonon limited scattering by defect states is the main processes. For temperatures above 60 K weakly localized shallow states are activated and capture electrons resulting in an increase of the fast decay time.

6.2 Degree of polarization of exciton and trion for near-resonant excitation

In this section we investigate exciton and trion valley polarization dynamics under near-resonant excitation at low temperature. Valley polarization in pump probe is introduced in section 2.3.3 and the degree of polarization is estimated by eq. 2.18. We control the polarization of the pump and the probe beam to have the same (opposite) circular polarization and denote that with co (cross) polarized. In the first part of this section, we focus on the exciton polarization degree. This is rather difficult to handle as large bandgap renormalization is observed. The second part deals with trion valley polarization degree. The trion shows a large polarization of nearly 100 % decaying within ∼3 ps.

6.2.1 Bandgap renormalization effect in pump probe measurements

Photoluminescence measurements on MoS_2 and $MoSe_2$ promise a large polarization of 100 % and 84 %, respectively, by resonantly exciting the exciton [173]. By comparing this to the DFT calculations of polarized absorption from chapter 5 on $MoTe_2$ in Fig. 6.8, we also expect a large polarization of ∼ 85 % for resonantly exciting the exciton in $MoTe_2$. Thus, we assume to observe a large degree of valley polarization in pump probe measurements.

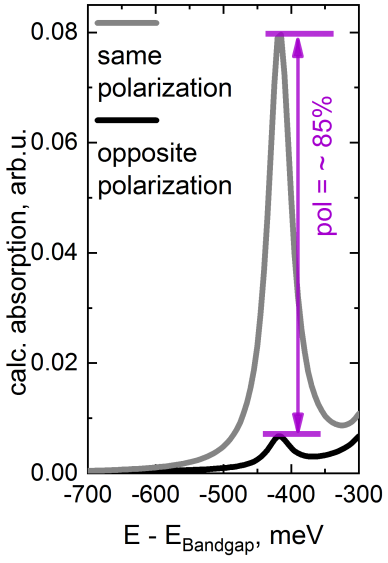

Fig. 6.8: From DFT calculatulations extraced polarization-resolved absorption spectra for the exciton in ML $MoTe_2$ from chapter 5.

The experimental results for pumping and probing the exciton resonance are presented in Fig. 6.9. We observe a larger signal from the cross polarized (black line) pump and probe pulses compared to the co polarized (gray line) case, resulting in a negative polarization degree (violet squares) of ∼ −65 %. The polarization is quickly lost within 1 ps due to electron-hole

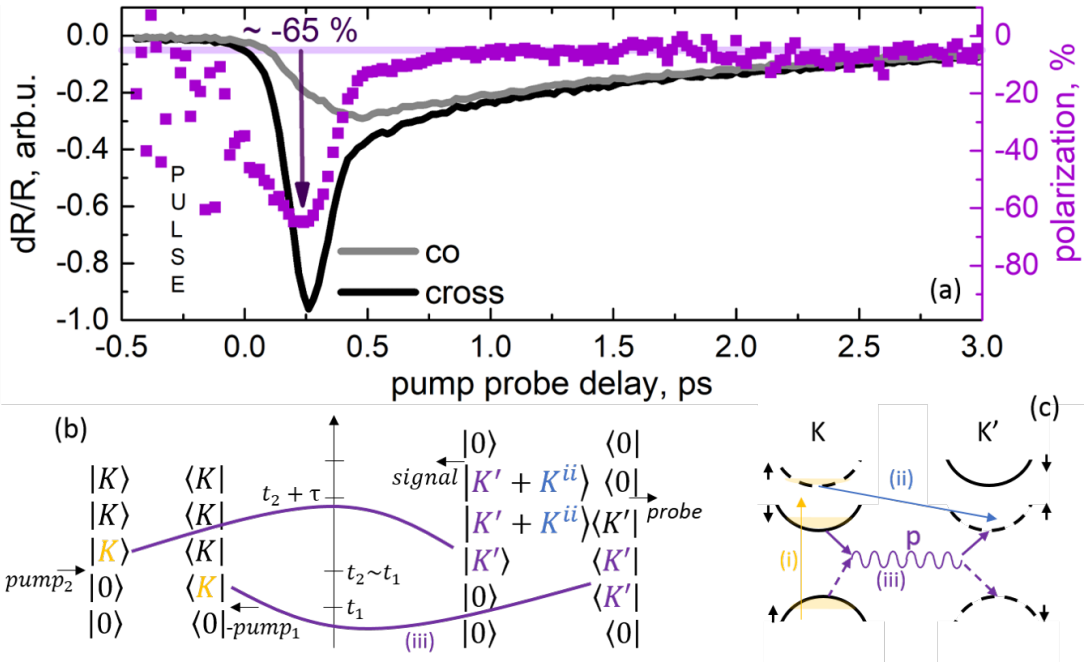

Fig. 6.9: (a) Normalized pump probe reflection data under co (gray line) and cross (black line) circular polarized pump and probe beams at 15K. The pump and probe beams are centered quasi-resonant to the excitonic transition. The de-polarization (violet squares) is calculated by eq. 2.18. Feynman diagrams (b) and valley schema (c) of (i) excitation, (ii) inter-valley scattering and (iii) exchange interactions by a virtual photon p.

exchange interactions [159, 199] as introduced in chapter 2.1.1 and sketched in (c) of Fig. 6.9. The excitons exchange extremely fast a virtual photon p without violation of spin and valley conservation. So, excitons are equally distributed through the valleys for timescales longer than one picosecond. However, the negative polarization does not agree with the assumptions of valley polarization transfer sketched in section 2.3.3 in terms of Feynman diagrams, that the unpumped valley does not show a population for a zero pump probe delay. The effect of negative polarization has been previously observed by Refs. [97, 98, 121, 145, 186, 196] and is mainly addressed to Coulomb induced bandgap renormalization which is also sensitive to valley.

There are three main Coulomb induced effects sketched in terms of Feynman diagrams Fig. 6.9 (b) and a valley scheme (c): (i) the intrinsic intra-valley population; (ii) the intrinsic inter-valley scattering for states with the same spin and (iii) electron-hole exchange coupling [145, 149]. Electron-hole exchange interaction induces both a microscopic polarization and population transfer from K to K' as sketched in the Feynman diagrams by the violet lines. The pumped valley is populated by (i). The excited carriers induce a bandgap change which red-shifts the exciton resonance, called bandgap renormalization. Together with absorption bleaching (introduced in section 2.3.3) this leads to a reduced signal in the pumped channel. The unpumped valley is populated through processes (ii) and (iii). Process (ii) is not probable as the energetically upper dark state is $\sim$ 34 meV separated. Besides, the unpumped valley

shows less renormalization and bleaching because of less excited carriers by the (iii) transfer process. After a few 100 fs the unpumped valley is populated strongly (polarization of -65 %) inducing a strong bandgap renormalization in K' resulting in a signal decrease. Besides, the exciton resonance shift of the unpumped valley is reduced and the K valley is repopulated for timescales larger than 250 fs, creating a maximal population in K at 400 fs, and so the polarization is lost at ∼1 ps. We do not expect a strong trion bandgap renormalization effect as beside the electron-hole pair an extra carrier needs to be transported and the extra carrier already renormalizes the gap. The trion polarization will be the point of discussion in the next subsection.

6.2.2 High degree of valley polarization in the trion

For PL measurements as done in the previous chapter, the trion shows a polarization similar to the exciton. This trend is confirmed in near-resonant PL measurements on $MoSe_2$ measuring a valley polarization of 79% [173]. Our previous measurements on WSe_2 show a strong valley polarization of ∼ 70 %, decreasing quickly within ∼ 4 ps for inter-valley trions and long lived > 25 ps for intra-valley trions [159].

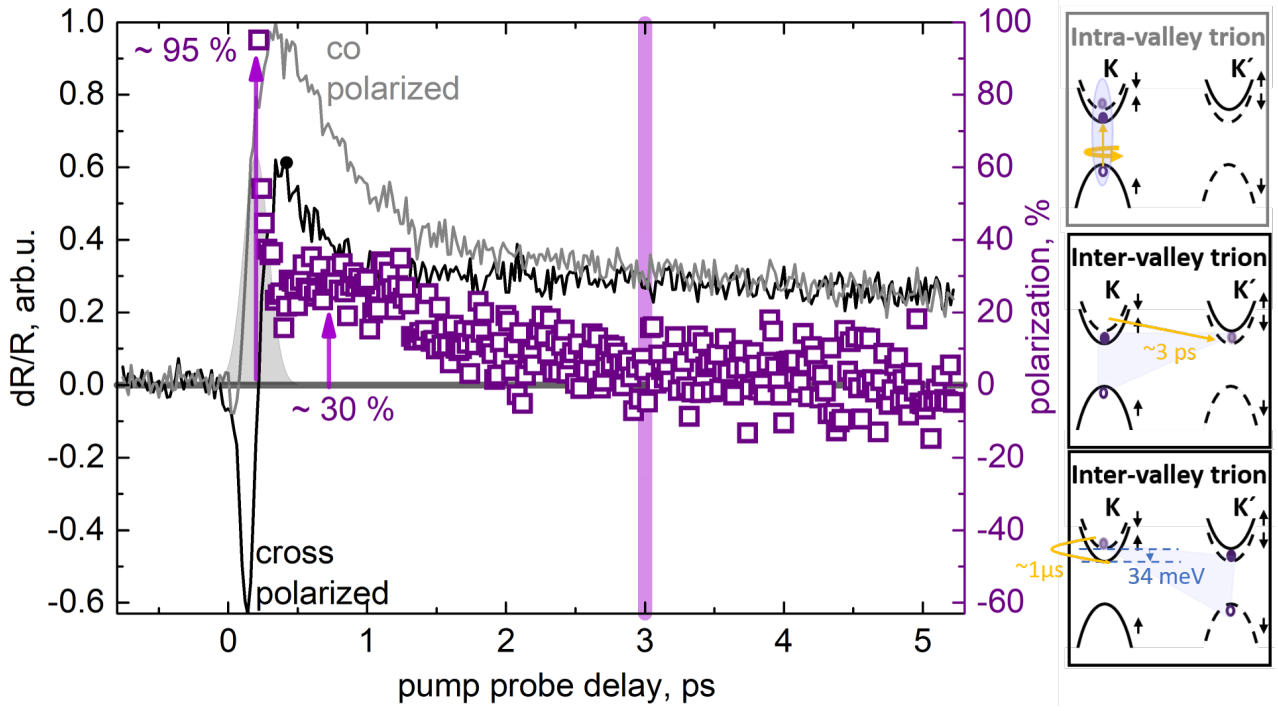

Fig. 6.10: Normalized pump probe reflection data under co (gray line) and cross (black line) circular polarized pump and probe beams at 15 K. The pump and probe beams are centered quasi-resonant to the trionic transition. The pump beam is shown as shaded gauss profile. The polarization degree is calculated by eq. 2.18. Trion valley schemata are sketched on the right side.

Similar to exciton polarization we estimate the degree of polarization from the co and cross polarized pump probe signal by eq. 2.18. The resulting differential reflection spectra for pump

and probe quasi-resonant to the trion are represented in Fig. 6.10 for co (gray line) and cross (black line) polarized pulses. The gray shaded Gauss profile represents the pump pulse. At low pump probe delay co and cross signals differ clearly. We measure a polarization of nearly 100 % directly after the excitation pulse decreasing within the pulse width of 180 fs to 30 % and depolarize completely within 3 ps. This means that scattering of particles from the K valley to the K' valley starts on fast timescales of hundreds of femtoseconds. The depolarization time agrees very well with previous measurements on WSe_2 [159]. By pumping one valley, intra-valley trions, which were introduced in detail in section 3.1, form immediately after excitation. The intra-valley trion is sketched in Fig. 6.10 in the gray box, consisting of two electrons and one hole. After excitation an exciton is selectively excited in the K valley capturing an electron and forming a trion. There are three possible transitions to form inter-valley trions (black boxes). First, the electron scatters through the other valley forming inter-valley trions via spin conserving scattering mechanisms at low temperature, which is the primary scattering channel for excitons in Mo-based TMDCs as shown in section 5.2.2 at low temperatures and happens on several picoseconds. Second, the exciton changes valley due to electron-hole exchange interactions on timescales below one picosecond. Then the extra electron needs to spin flip to be energetically resonant to our measurement, this happens at 15 K on a microsecond timescale (cf. Fig. 5.13), therefore, it is non-likely. Third, all three particles simultaneous transfer to the other valley. This takes place on long timescales (more than 25 ps) [159]. So, intra-valley trions are investigated by co polarized measurements and inter-valley trions by cross polarized light. Therefore, we can attribute the valley depolarization timescale of $\sim$3 ps to the valley transfer spin-conserving scattering mechanism of the extra electron.

Now we change the temperature to 40 K consistent with our measurements in section 5.2.2. The resulting co and cross polarized signal is shown in Fig. 6.11 as gray and black lines. In contrast to the measurements at 15 K, the signal shows a pronounced cross polarized response and thus a negative polarization. We attribute this effect to the change in the spin flip relaxation time with temperature as seen in Fig. 5.13 (a). At 40 K we observe a spin flip time of the exciton of $\sim$1 ps, sketched as yellow line in the inset. So ultrafast electron-hole exchange interactions of the exciton from K to K' and fast transfer of the electron lead to a population of the K' valley. This is quickly lost within 1 ps due to bandgap renormalization comparable to the exciton. Beside the PL valley- to spin-flip converting mechanism, we also measure a valley- to spin-flip converting mechanism in pump probe measurements.

By tuning the pump energy across the trion resonance trion formation processes can be investigated. The results for nine different detuning energies (i.e. the separation of pump energy and trion emission energy) are presented in Fig. 6.12 for co (gray lines) and cross (black lines) polarized pump probe beams at 15 K. At zero time delay the differential reflection signal is zero and rises to its maximum within the first 200 fs. The behavior with increasing delay time is strongly pump energy dependent. For under-bandgap excitation (-11 meV) the amplitude data

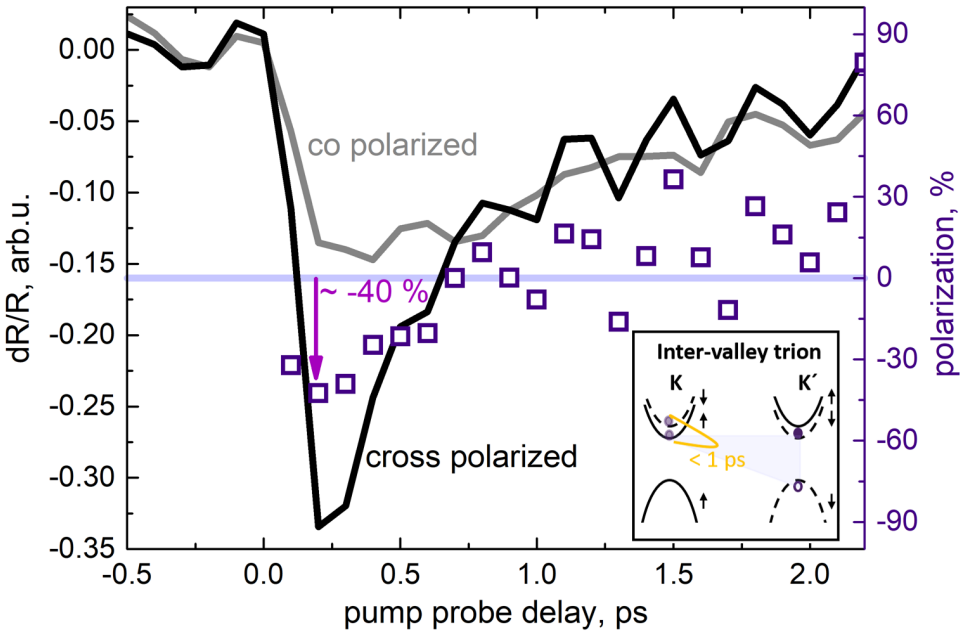

Fig. 6.11: Normalized pump probe reflection data under co (gray line) and cross (black line) circular polarized pump and probe beams at 40 K. The pump and probe beams are centered quasi-resonant to the trionic transition. The polarization degree is calculated by eq. 2.18. Trion valley schemata are sketched in the inset.

are dominated by the cross polarized signal which we assign to a creation of inter-valley trions. The inter-valley and intra-valley trion differ by the position of the extra charge as sketched on the right side of Fig. 6.12. As already introduced in section 2.2.2 the $MoTe_2$ ML has the largest conduction band splitting in Mo-based TMDC family ($\sim 34\,\text{meV}$ [39]). Therefore, both types of trions are energetically different. The intra-valley trion is energetically higher than the inter-valley trion. As we excite slightly off-resonant, the population energy for the higher conduction band state is significantly higher, explaining the pronounced cross polarized signal. As we tune the energy above the bandgap (pumping in between exciton and trion) the spectra look similar to the ones from pumping the exciton. This is not surprising as our laser has a spectral full width of half maximum of 10 nm, so the exciton is stimulated in part. Following the previous section, trion formation can be observed by pumping the exciton and probing the trion resonance. We investigate this in more detail in Fig. 6.12 (b). We observe for both, co (gray line) and cross (black line) polarized measurements a sharp peak which is attributed to the laser, followed by a formation of trions by capturing an extra charge as illustrated in (c) within $1.5 - 2.5$ ps. During the formation process, we measure a polarization of 25-30 % (violet squares). After the successful forming of the trion we do not observe a polarization, meaning the particles are equally distributed through the valleys. This can be either due to capturing of the electron by the K valley or transfer of the electron from the K to the K' valley. By further increasing the detuning energy, we observe a change of sign. Co and cross polarized signal get negative far apart from the pulse overlap. This was also observed

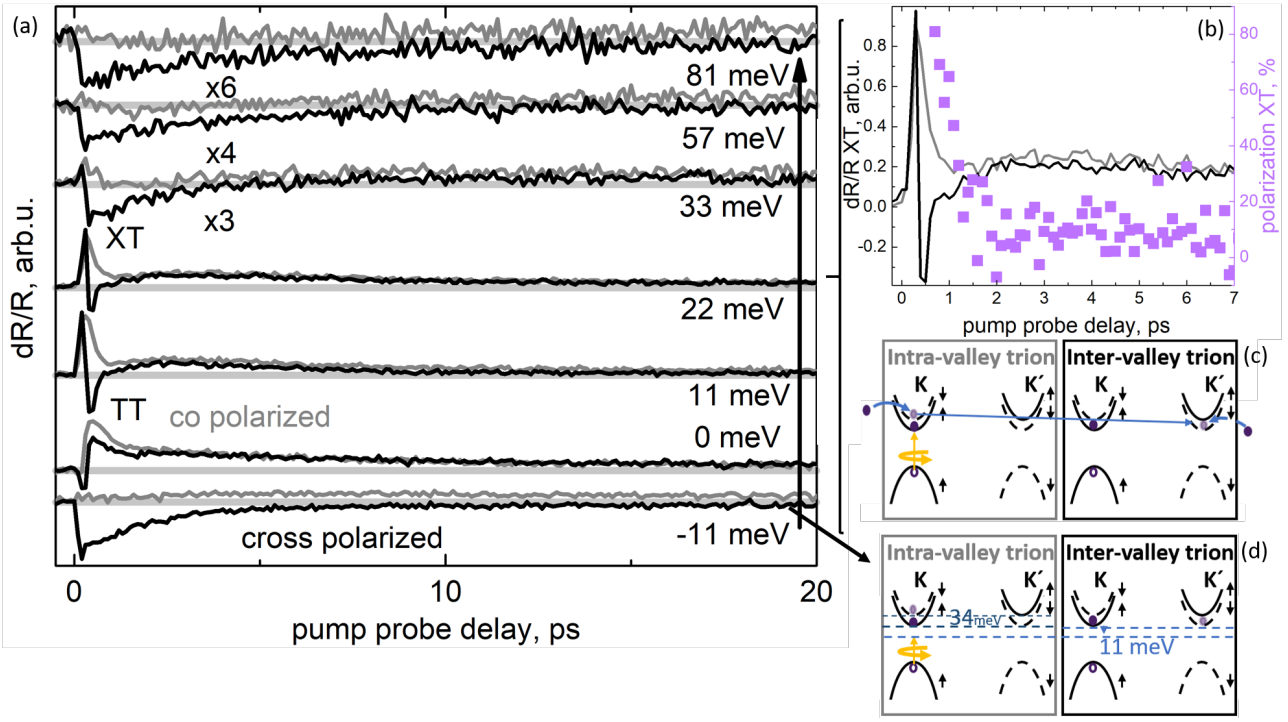

Fig. 6.12: (a) Detuning energy resolved pump probe signal for different pump probe delays under co (gray lines) and cross (black lines) polarized pump probe beams at 15 K. The values for the detuning energy are calculated relatively to the trion transition energy. XT (TT) denotes pump the exciton (trion) and probe the trion (trion) resonance. (b) Zoom into the XT measurements where the violet squares show the polarization. (c+d) Sketches of intra- and inter-valley trion for XT (c) and for under-bandgap excitation (d).

in Ref. [196], attributing this effect to blocking of states by phase-space filling of excitons. Moreover, for off-resonant excitation we enable measurement of higher energetic bright and dark excitonic and trionic states as discussed in section 3.1.1. Especially dark quasiparticle states have longer depolarization timescales as they do not couple to photons and electron-hole exchange interaction is suppressed. This matches the observed increase in polarization (that mean co and cross signal overlap) decay time for these higher detuning energies.

In conclusion, we investigate exciton and trion degree of polarization. The exciton shows strong bandgap renormalization effects in the pumped valley and due to ultrafast electron-hole interactions a high cross polarized response. We measure a polarization degree of -65 % decaying within 1 ps due to bandgap renormalization and the filling of the unpumed valley. The trion shows for low temperature and resonant excitation a less populated unpumped valley so the observed effect of bandgap renormalization is weaker than as in case of the exciton. We can extract an electron valley flip time of 3 ps. By increasing the temperature, we observe a valley- to spin-flip converting process similar as in chapter 5. Moreover, we change the trion valley depolarization by off-resonantly pumping the trion observing that valley polarization is lost on timescales comparable to trion formation.

7 Coherent exciton dynamics and dephasing in mono- and bilayer $MoSe_2$

In this chapter, we use two-dimensional coherent spectroscopy to resolve dynamics on ultrashort timescales beyond the limitations of the pulse overlap in pump probe measurements presented in the previous chapter. The measurements were performed during my stay abroad at the *University of Texas at Austin* in cooperation with the group of *Prof. Xiaoqin Li*. The measurements have been performed together with *Kevin Sampson* and *Dr. Kai Hao*. As the lab is specialized in measurements in the visible range of the titan-sapphire laser, we switch from molybdenum ditelluride to molybdenum diselenide. We measure the homogenous linewidth (γ) which is related to the coherent dephasing time $T_2 = \hbar/\gamma$ of both monolayer and bilayer direct exciton in molybdenum diselenide at low temperatures. Moreover, we address the relaxation time T_1 by linewidth cuts through the zero-quantum energy map.

In case of the monolayer, we confirm a direct excitonic transition. At ultrafast timescales, the monolayer is a two level system and features in two-dimensional coherent spectroscopy arise from ground state bleaching and excited state emission. The relaxation time in the monolayer reflects the exciton population decay time of 220 fs where the relation $T_2 \sim 2 \cdot T_1$ is valid. In the bilayer, the dephasing time is attributed to an ultrafast electron dephasing of 24 fs from the K to the Λ point. The relaxation time T_1 reflects the hole depopulation time of 400 fs caused by acoustical phonon mediated scattering from the K to the Γ point. Moreover, the bilayer coherent spectroscopy measurements exhibit an additional feature in the bilayer induced by excited state absorption of a doubly excited state. This can be either an intra-layer biexciton or an inter-layer exciton. From polarization resolved measurements, we determine the biexciton binding energy in the monolayer and a valley polarization of 43 %. The bilayer shows a layer polarization of -27 %, increasing toward the above-mentioned feature in the bilayer signal which supports the biexciton behavior of this feature.

7.0.1 Why and how to investigate the indirect transition in bilayer $MoSe_2$

TMDCs are a class of semiconducting 2D material crystals with a direct optical bandgap in the ML-limit as described in the previous chapters. This class of materials has potential for the use in opto- and valley-tronics devices. The basis of such devices is the stacking of different material MLs to form so called heterostructures [45, 174]. In heterostructures, two materials of slightly different band structure are combined to induce a smaller indirect bandgap transition. The understanding of indirect TMDCs is still at the beginning. Recently, it have been found that heterostructures have a momentum-direct inter-layer exciton at the K point and a momentum-indirect inter-layer exciton at the indirect bandgap [46, 108]. Natural BLs of MoS_2, $MoSe_2$, WS_2, and WSe_2 show an indirect excitonic transition from the Λ-point in conduction band to the K-point in valence band [55, 94, 135, 201] as sketched in Fig. 7.1 (c). In BL $MoSe_2$, scattering of carriers by phonons is highly pronounced compared to other TMDCs [66] due to a smaller separation of Λ (in CB) and K (in VB) points in energy. This makes BL $MoSe_2$ a perfect material to investigate optical transitions as a starting point to understand optical transitions in heterostructures. The ML is pictured in Fig. 7.1 (a) and shows a direct intra-layer exciton emitting an energy E_g. In addition, the BL is a structure consisting of two Bernel stacked MLs (cf. section 2.2). Therefore, there are several excitonic states in addition to the states of the ML. The BL in Fig. 7.1 (b) shows an upper layer intra-layer exciton and a lower layer intra-layer exciton. The lower layer intra-layer exciton is influenced stronger by substrate screening as the upper one. Therefore, the upper intra-layer exciton has a higher bandgap energy [91, 146]. Moreover, the BL shows an indirect inter-layer exciton comparable to the one in heterostructures [58] with the difference that the exciton in the BL has a similar energy as the direct intra-layer excitons. Thus, they are hard to distinguish energetically.

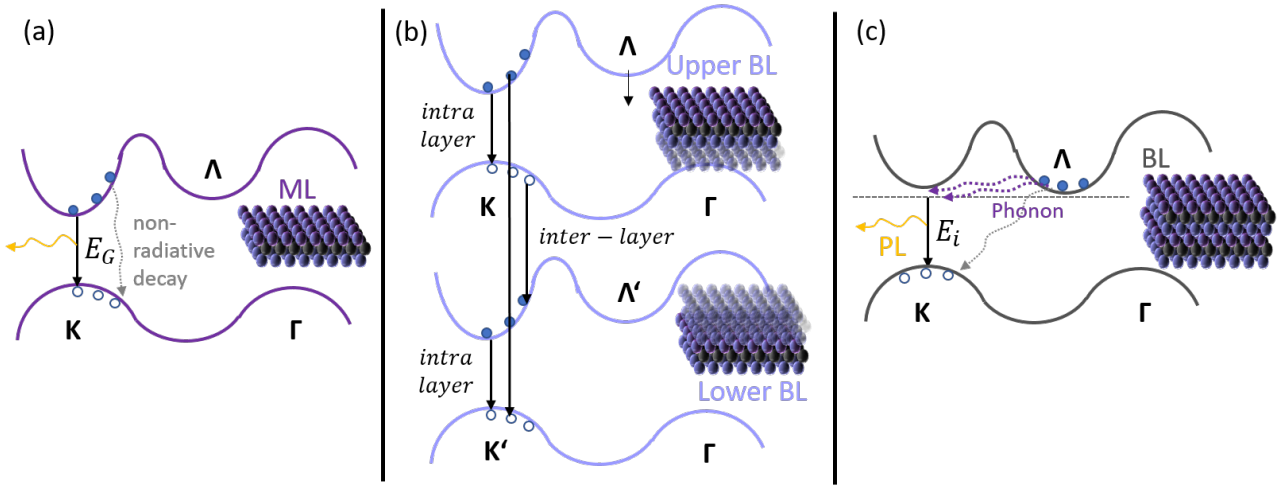

Fig. 7.1: Sketch of decay pathways for ML and BL $MoSe_2$, including direct exciton recombination, phonon induced indirect exciton recombination, and other non-radiative scattering pathways.

Using absorption spectroscopy, direct excitons in ML and BL can be observed [141]. We use

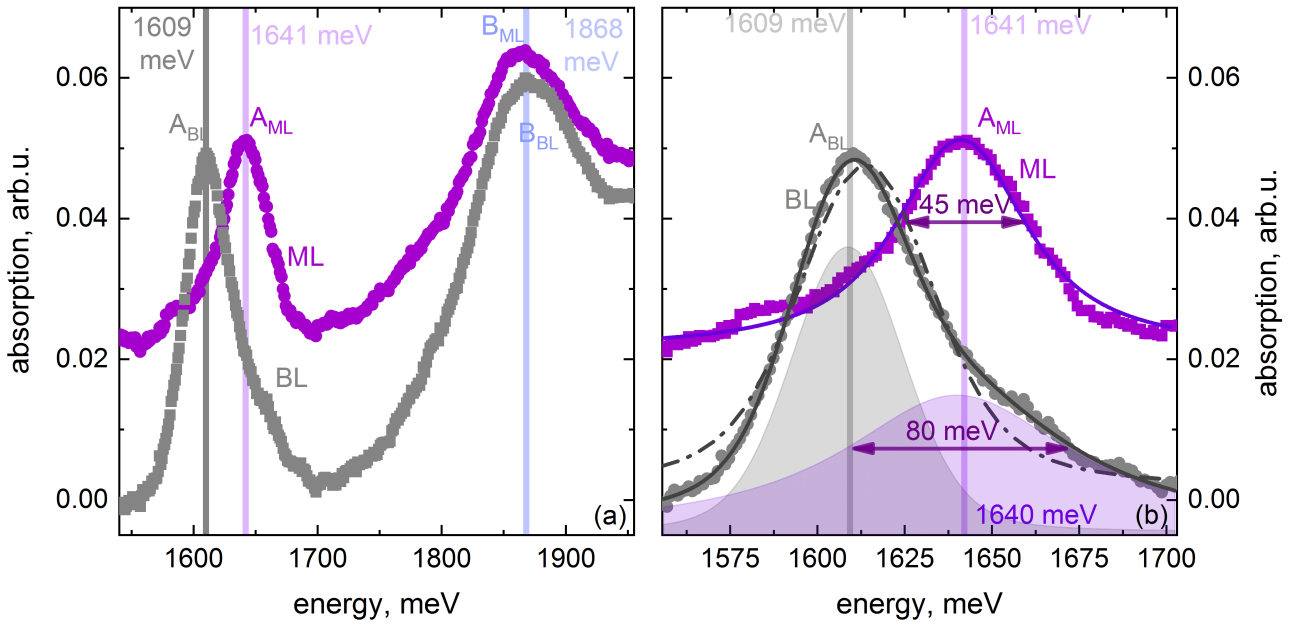

Fig. 7.2: (a) Absorption measurement of ML (violet) and BL (gray) $MoSe_2$ versus energy at 30 K. A_{ML} and A_{BL} denote the lowest direct excitonic feature. B_{ML} and B_{BL} is the B exciton separated towards the A exciton by valence and conduction band spitting. (b) Zoom to the A excitonic transition. ML (solid violet line) and BL (dashed gray line) fit by the Voigt function. The BL is additionally fitted with a set of two functions (solid gray line) where the parts are pictured as shaped profiles.

white light absorption spectroscopy to locate the direct excitonic transitions in ML and BL $MoSe_2$. The resulting spectra at 30 K are shown in Fig. 7.2 (a). We observe two absorption peaks in ML and BL $MoSe_2$ and attribute them to the direct A and B excitons as introduced in section 2.2. The B exciton does not change the position from ML to BL. This seems to be a general behavior of TMDCs which is investigated in detail in section 5.1. The center position of the A exciton shifts slightly from ML to BL to lower energies by ∼32 meV in agreement with Ref. [3]. Having a closer look at the A excitons in Fig. 7.2 (b), we fit the data of ML and BL with a Voigt function. Details of the Voigt profile are found in section 3.1. The ML is fitted with a single Voigtian (violet line) centered in energy at 1641 meV with a FWHM of 45 meV. The BL cannot be fitted with a single Voigtian as illustrated by the dashed gray line. A set of two Voigtian components fits the BL absorption centered at 1609 meV and 1640 meV. The former perfectly matches the maximum of A_{BL}, whereas the latter is centered at the ML A excitonic signal and is significantly broadened to 80 meV. Ref. [131] observes a similar effect on heterostructures: a broadening of the direct excitonic absorption from ML to the heterostructure. Following their assignment, we calculate a broadening difference of 35 meV corresponding to a lifetime of ∼ 20 fs. This lifetime is identified as intra-layer exciton decay of one of the two layers in BL. This raises the questions of exciton lifetime in BL.

For the first time, we investigate dephasing and population dynamics in natural BL $MoSe_2$ by two-dimensional coherent spectroscopy (2DCS). We measure both coherence dephasing and population decay of ML and BL $MoSe_2$ to directly compare their lifetimes. We study ML and BL

flakes of $MoSe_2$ (cf. flake 3 and 4 in Fig. 2.13) mechanically exfoliated onto a sapphire substrate for optical transmission measurements. ML and BL are transferred to the same substrate facilitating direct comparison of ML and BL emission within the same cooling cycle procedure. We prefer separated ML and BL flakes to avoid in particular mixtures of the ML trion and BL exciton emission, as they emit in the same energy range. For our 2DCS experiments we use a transient four-wave mixing technique. The details can be found in section 2.3.4.

7.1 Dephasing time in ML and BL $MoSe_2$

In this section, we investigate the excitation energy versus emission energy spectra from 2DCS measurements. We identify the exciton and the trion in the ML map and attribute the exciton feature to the direct excitonic transition at the K point. The ML exciton behaves like a two-level system where processes like ground state bleaching and excited state emission can explain the measured feature. In contrast, the BL shows two overlapping peaks. The main peak shows a strong dephasing due to ultrafast scattering of the direct exciton into indirect excitonic states as the conduction band has its minimum at the Λ point. The second feature is induced by the excited state absorption due to an extra doubly excited state, as will be shown later. This state can be either a biexciton in the upper or lower layer or an inter-layer exciton.

To measure the dephasing time, we scan the time delay t_1 between the first and the second pulse producing a 2D excitation spectrum of the Signal $S(\hbar\omega_{t_1}, t_2, \hbar\omega_{t_3})$ while keeping the delay between the second and the third pulse t_2=0 fs constant.

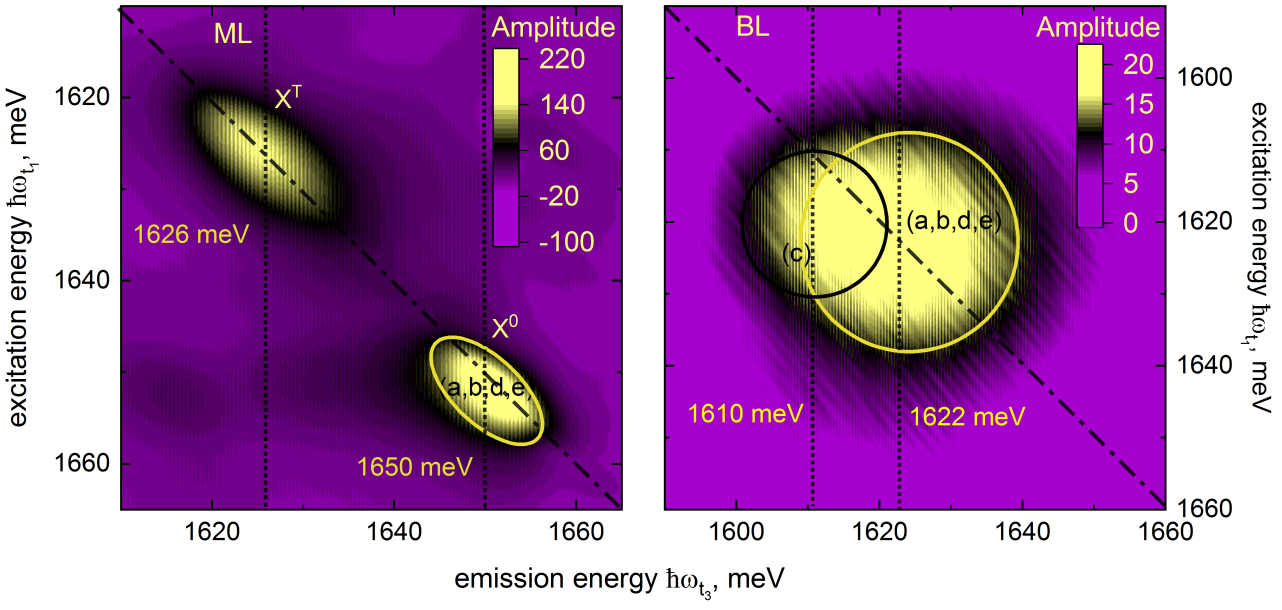

Fig. 7.3: 2D spectra of ML and BL $MoSe_2$ at 300 μW excitation power and 30 K. The exciton and trion resonances are highlighted by X^0 and X^T. The off-diagonal linewidth (homogenous linewidth) of X^0 is extracted at ten energy positions ±2 meV around the dotted line.

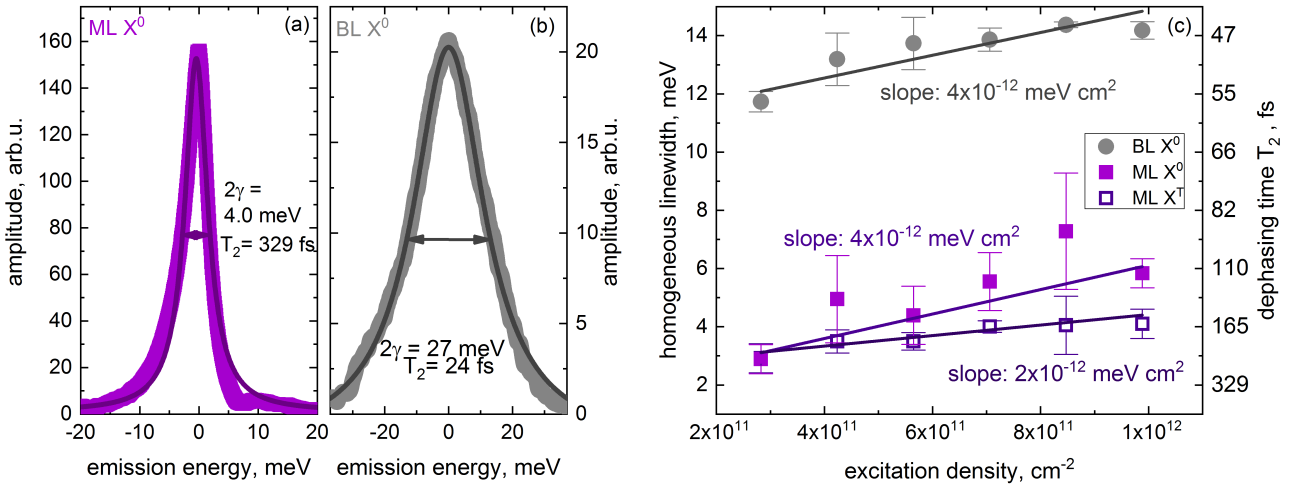

Fig. 7.4: (a+b) The extracted homogenous linewidth with respect to the emission energy fitted by a Lorentzian at 30 K. (c) Linearly fitted (solid lines) homogenous linewidth and dephasing time T_2 for ML exciton and trion and BL exciton as a function of excitation density.

Exemplary 2D spectra for ML and BL $MoSe_2$ are shown in Fig. 7.3. The x (y) axis corresponds to the emission $\hbar\omega_{t_3}$ (excitation $\hbar\omega_{t_1}$) energy. The dot-dashed line indicates equal excitation and emission energy. Peaks occurring on this line represent coherent ground or excited state population. The ML spectrum (left) shows two prominent peaks associated to the exciton X^0 (1650 meV) and trion X^T (1626 meV) in accordance with Ref. [54]. Comparing the 2D center energy to the absorption measurements in Fig. 7.2, the 2D-signal is blue-shifted by ∼10 meV. The 2D and absorption measurements are performed on two different flakes which can explain the mismatch in energy position. The broadening along the diagonal of the 2D spectrum is due to inhomogeneous effects like impurities or defects. The cross-diagonal broadening is related homogenous linewidth γ which is related to the coherent dephasing time $T_2 = \hbar/\gamma$. By averaging across ten linewidth cuts around the center emission energy ±2 meV, we extract a homogenous broadening of $\gamma_X = (2.0 \pm 0.2)$ meV ($T_2^X = (329 \pm 33)$ fs) from a Lorentzian fit of the exciton as seen in Fig. 7.4 (a). The trion is treated similarly and we estimate a trion linewidth of $\gamma_T = (2.9 \pm 0.5)$ meV ($T_2^T = (227 \pm 39)$ fs). Exciton and trion homogenous linewidth are in perfect agreement with previous measurements on $MoSe_2$ for comparable excitation density and temperature [170, 54].

The BL spectrum, however, has one roundish main emission peak related to the direct excitonic transition of the BL as seen in Fig. 7.3. The BL direct resonance is centered at 1622 meV emission energy. In agreement with the ML exciton, the BL exciton shows an energy blue-shifting from absorption to 2D measurement. Therefore, we attribute the main peak to the direct K point exciton. In addition, the BL shows a second feature at 1610 meV shifted in emission energy compared to the main peak. The origin of this peak will be discussed in the next subsection. As the ML trion and BL exciton emit at a comparable energy, it is it even more important to separate the ML and BL from each other to avoid mixtures of states.

BL $MoSe_2$ is known to be an indirect semiconductor [137]. In 2D spectroscopy, we investigate the direct K_{VB} to K_{CB} exciton as it is still an allowed direct transition even if it is energetically unfavorable in emission. The indirect exciton from K_{VB} to Λ_{CB} is lower in energy and, therefore, a preferred scattering channel for excitons. In contrast to $MoTe_2$, where the BL and ML show the same behavior in PL (cf. chapter 3 and 4). Therefore, we expect that in $MoSe_2$ the BL feature is less intense compared to the ML 2D signal despite that we excite the direct exciton in both cases. We extract a broadening in Fig. 7.4 (b) of $\gamma_X = (13 \pm 0.8)$ meV ($T_2^X = (24 \pm 2)$ fs) for the BL exciton. The BL dephasing time is ten times faster compared to the ML and agrees with the estimated lifetime of ∼20 fs extracted from the linewidth analysis of the absorption spectra. We interpret this ultrashort lifetime as scattering of direct excitons to indirect excitons where the electrons are located at the Λ point in the conduction band as sketched in Fig. 7.1 (c). We cover a range of 120 meV in our 2DCS measurements and do not observe a second feature. DFT calculations throughout literature predict several different energy separations of K and Λ, so corresponding band structure separations range from 300 meV [55] to zero [201] K-Λ separation. We can extract a lower bound for the K-Λ splitting of 80 meV.

By changing the excitation density we investigate excitation induced dephasing [111]. The results for the homogenous linewidth versus excitation energy are shown in Fig. 7.4 (c) for ML (exciton: closed violet squares; trion: open violet squares) and BL (gray circles). By linear fitting (solid lines), we can extract the excitation density induced dephasing rate of $4 \cdot 10^{-12}$ meV cm^2 for both ML and BL exciton and $2 \cdot 10^{-12}$ meV cm^2 for the ML trion. This further confirms the excitonic nature of the BL feature in the 2D spectrum. The values are slightly larger than results on WSe_2 at 10 K [111] and slightly smaller than trion results on $MoSe_2$ [170]. This indicates that similar many-body effects influence the optical response of our sample compared to samples in literature.

7.1.1 The second feature in 2DCS spectra of the BL

Here, we have a closer look at the second feature of the BL centered at ∼1610 meV, corresponding to in a red-shift of 12 meV with respect to the main feature. Similarly shaped features have been previously observed in 2DCS in quantum wells [19, 160] and have been attributed to biexcitons. To understand the nature of this feature we follow the investigations from the thesis of *Dr. Galan Moody* [110]. Depending on how many possible states one can excite there will be different features in the 2D map as illustrated in Fig. 7.5. By excluding X^T, the ML acts as a two level system consisting of a ground state $|G\rangle$ and an excited state $|K\rangle$ sketched in (A). That means in the ML we can investigate either ground state excitons or excitons where the electron and the hole are located in the K valley. In our measurements, we have a fixed pulse time ordering so that the pulses k_1, k_2, k_3 interact with the sample to generate a four-wave mixing signal $k_S = -k_1 + k_2 + k_3$. The resulting possible pathways are sketched using Feynman

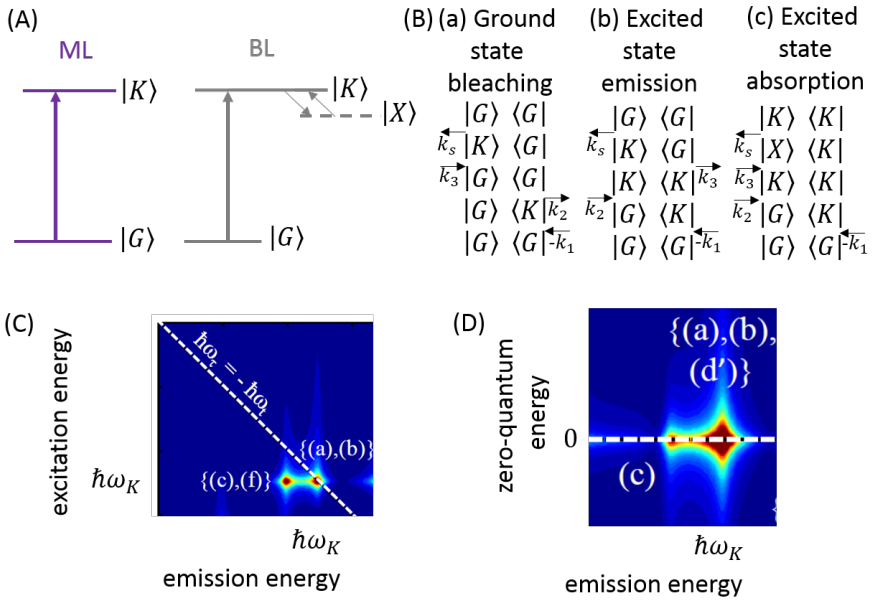

Fig. 7.5: (A) Level schema for ML and BL where $|G\rangle$ is the ground state, $|K\rangle$ is the excited state associated to a exciton in the K valley, and $|X\rangle$ is an extra BL excited state only excitable via the $|K\rangle$ state. (B) Feynman diagram for possible 2D states. (C+D) Simulated 2D (C) and zero-quantum (D) map from Ref. [110] where (a,b,c) are connected to the Feynman diagrams in (B).

diagrams in (B). A detailed description of Feynman diagrams can be found in section 2.3.3. For the ML, as a two level system, only ground state bleaching and excited state emission (a+b) are possible processes. Each process can be attributed to a feature in either the 2D map (C) or the zero-quantum map (D). Bleaching (a) and excited state emission (b) occur as diagonal peak in (C) at the energy of the direct optical transition at the K point ($\hbar\omega_K$). In the zero-quantum energy map this results in a feature along zero zero-quantum energy. This agrees with our measurements in Fig. 7.3 and Fig. 7.8 in the next section.

In the BL in Fig. 7.3, we attribute the main feature to ground state bleaching and excited state emission of the direct K point exciton. In addition, a second feature can be observed. By comparing this to the simulated 2D map, we assign the additional feature to the (c) process, the so-called excited state absorption. Excited state absorption is only possible if there is an additional excited state $|X\rangle$ which cannot be excited directly from the ground state. We call this a doubly excited state. There are three possible implementations: (i) An indirect exciton where the hole is located in the Γ valley or the electron in the Λ valley. We can rule out this possibility as the energy separation to the direct exciton is too large [55]. (ii) An indirect inter-layer exciton where one carrier is in the upper layer and the other carrier is in the lower layer as sketched in Fig. 7.1 (b). As the lower layer is influenced by increased screening compared to the upper they are energetically separated by 10-30 meV in $MoSe_2$ [146]. Thus, a separation of several meV from intra- to inter-layer, is possible. Moreover, inter-layer hopping of holes is pronounced at low temperatures [38] inducing an exciton layer polarization in BL $MoSe_2$. (iii)

Biexcitons (cf. section 2.1.3) where all carriers are either in the upper layer or in the lower layer, as all three pulses have the same polarization in these first experiments. As found in quantum wells, biexcitons show a comparable feature in 2D measurements [19, 160]. In addition, in ML TMDCs biexcitons have been found to have a binding energy of ~ 10 meV [164] and have been previously observed in 2D measurements in the ML $MoSe_2$ [53]. The investigation of valley and layer polarization can help to further support our assumptions.

7.1.2 Valley vs. layer polarization in ML and BL $MoSe_2$

In ML TMDCs, valley polarization occurs due to the locking of spin and valley selection rules. These are based on the breaking of inversion symmetry as introduced in section 2.2. So by choosing the helicity of circular polarized light, individual valleys can be addressed specifically. In 2DCS we measure the valley polarization by changing the circular polarization of the four beams from $\sigma^+\sigma^+\sigma^+\sigma^+$ (short: $++++$) to $\sigma^+\sigma^+\sigma^-\sigma^-$ (short: $++--$) [54]. The resulting homogenous linewidth is shown in Fig. 7.6 (a). We measure a valley-polarization of ~ 43 % in agreement with zero t_2 time measurements of Ref. [54]. This shows that by exciting resonantly to the K valley we mainly populate the K valley and we obtain a high valley polarization.

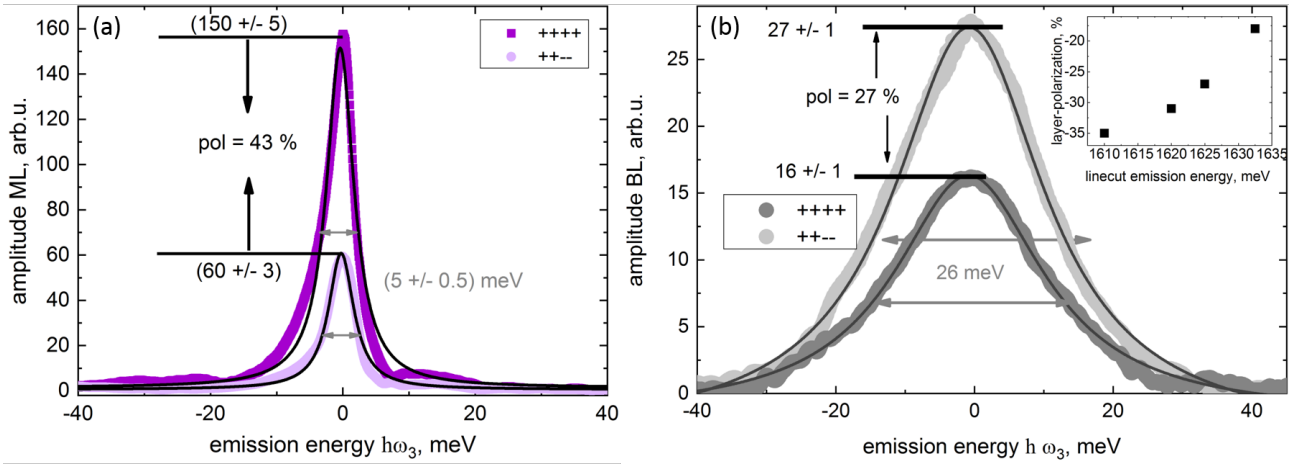

Fig. 7.6: Polarization measurements of ML (a) and BL (b) homogenous linewidth cuts. The inset shows the BL layer-polarization for different linewidth cuts in emission energy.

In the BL the inversion symmetry is restored, therefore, spin and valley are not coupled, and valleys are not selectively addressable by circular polarized light, as introduced in section 2.2. Thus, the BL is excepted show zero valley polarization. However, due to the Bernal stacking (AA'), the upper and the lower layer show a different k vector such that the upper (lower) layer is associated to the K (K'). As a consequence, one layer carries more particles than the other one, the population ratio between the layers being referred to as layer polarization [37, 38, 64, 67, 195]. In our case we measure a negative layer polarization. Within the dephasing time, a microscopic polarization is induced to the not-excited layer. Moreover, the polarization

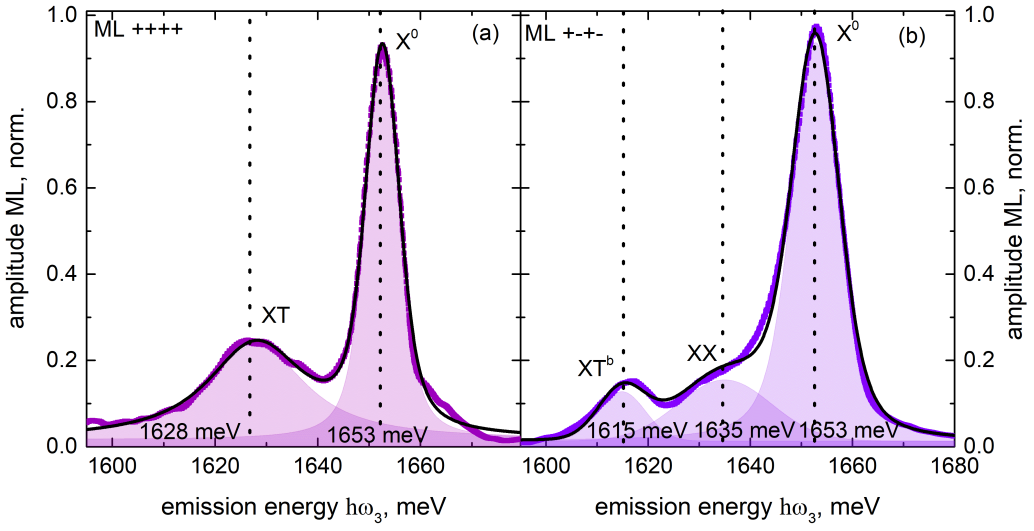

Fig. 7.7: Slices along the emission axis at an excitation energy of 1652 meV for $++++$ (a) and $+-+-$ (b) circular polarization. The lines are fitted by Voigt function. Where XX, XT, and XT^b are associated to the neutral biexciton, exciton-trion coupling, and charge bound biexciton.

changes when scanning across the BL feature in Fig. 7.3 (b, inset). At the main feature we measure a polarization of -27 %. At the second BL feature the polarization has increased to -35 %. A non-zero polarization indicates that particles are not equally distributed to the layers, thus, opposing the interpretation of the inter-layer exciton presented in the previous section.

In addition, the ML at a closer look shows a trace of the biexciton as shown in Fig. 7.7 (b) in perfect agreement with previous measurements in Ref. [53]. This means we observe in the measurements with circular polarized beams $+-+-$ the natural biexciton XX and the charged bound exciton XT^b missing in the $++++$ case. The signal of the biexciton in ML supports the appearance of biexcitons in BL. However, only careful calculations for the BL can clarify the origin of the second peak.

In summary, the analyzed 2D maps and find that the ML shows as expected an exciton, a trion, and exciton-trion coupling terms. The BL feature consists of two peaks: The main peak is attributed to a direct exciton at the K point showing an ultrafast dephasing time of 24 fs. This means electrons scatter ultrafast to the energetically lower lying Λ point conduction band minima on ultrafast timescales. The second peak is attributed to either inter-layer excitons or intra-layer biexcitons, where we assume the latter to be dominant.

7.2 Depopulation in ML and BL $MoSe_2$

In this section, we additionally analyze the zero-quantum energy map of ML and BL to confirm the assumption of a second peak in the BL. Moreover, we discuss the relaxation rate associated with the linewidth at a certain emission energy for ML and BL. We find that the relaxation rate is connected to the population decay rate in agreement with previous publications for the ML. In the case of the BL, this rate is associated to the hole transfer rate from the K to the Γ point via acoustical phonon processes.

To measure the relaxation rate, we scan the time delay t_2 between the second and the third pulse reproducing a zero-quantum spectrum of the Signal $S(t_1, \hbar\omega_{t_2}, \hbar\omega_{t_3})$, keeping the delay between the first and the second pulse t_1=0 constant. The resulting spectra for ML and BL are shown in Fig. 7.8. The dashed line indicates the center position of the excitonic peaks in ML and BL. For simplicity we omit the trion peak in ML. The ML shows a symmetrically shaped signature of the exciton centered at 1658 meV in agreement with our measurements in section 7.1. The high frequency patterns at this feature are a ringing artifact related to the finite duration of the scan. We attribute this peak to a ground state bleaching and excited state emission, as shown in Fig. 7.5 (B, D). The BL in Fig. 7.8 shows two features centered at 1624 meV and 1610 meV associated to the direct exciton and a doubly excited state $|X\rangle$ as explained in section 7.1.1. Therefore, we attribute the second feature as excited state absorption of the either intra-layer biexciton or inter-layer exciton.

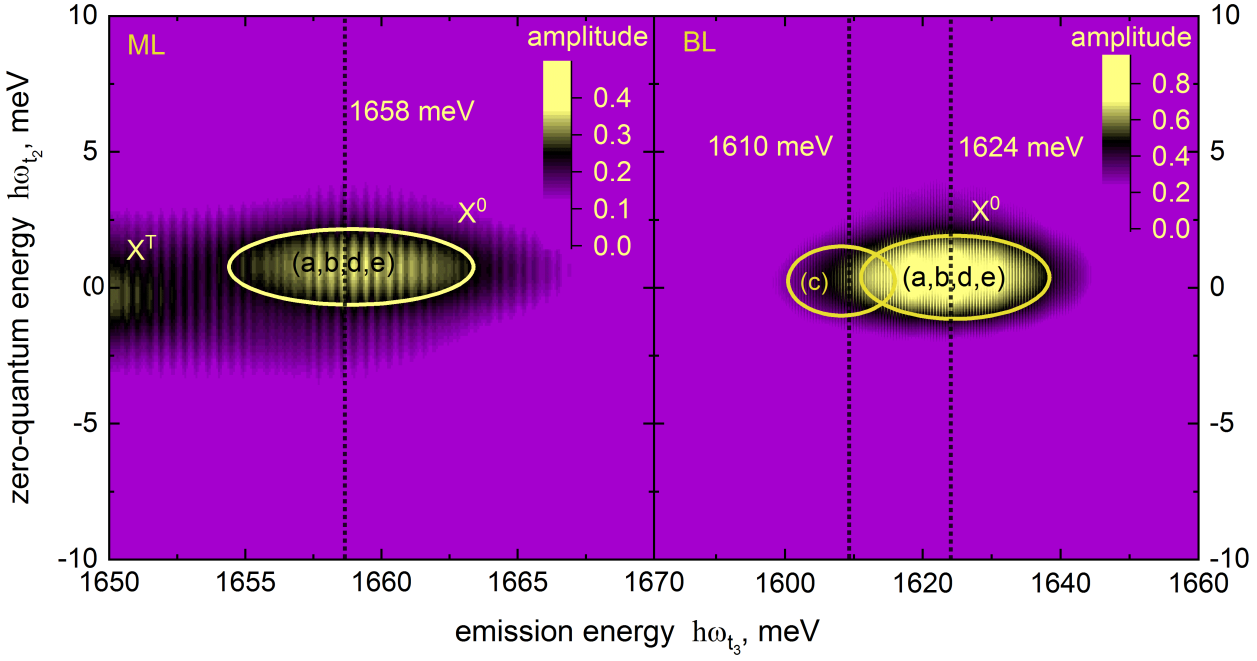

Fig. 7.8: Optical 2DCS zero-quantum spectrum of ML and BL $MoSe_2$ at 300 μW excitation power and 30 K. The exciton resonances are highlighted by X^0 and a dotted line.

By averaging across ten linewidth cuts around the center emission energy ±2 meV shown in

Fig. 7.9 (a) we extract a relaxation rate of $\Gamma_p^X = (3 \pm 0.5)$ meV ($T_1^X = (219 \pm 37)$ fs) for the ML. The quantum dynamics of excitons in ML TMDCs are mainly characterized by two fundamental processes: Firstly, dephasing which can be measured by the homogenous linewidth (γ) and, secondly, the population decay rate (Γ_p) related to the coherent dephasing time $T_2 = \hbar/\gamma$ and the population decay time $T_1 = \hbar/\Gamma_p$. In ML, $2 \cdot T_1$ gives an upper limit for T_2 [54], indicating that quantum coherence is mainly lost due to population decay such that $T_2 \sim 2 \cdot T_1$. We can confirm this relation by measuring the population decay rate and the dephasing rate as a function of temperature. The results are presented in Fig. 7.9 (c). T_2 (open violet squares) consistently equals two times T_1 (light violet squares). In addition, we can fit the homogenous linewidth by a linear version of eq. 3.4 introduced in section 3.2.2 for low temperatures. We assume that mainly acoustical phonons broaden the linewidth. We find an acoustic phonon-exciton coupling of $\gamma_A = (11.4 \pm 0.2)\,\mu$eV K^{-1}. The coupling is smaller than the coupling in ML $MoTe_2$ extracted in section 3.2.

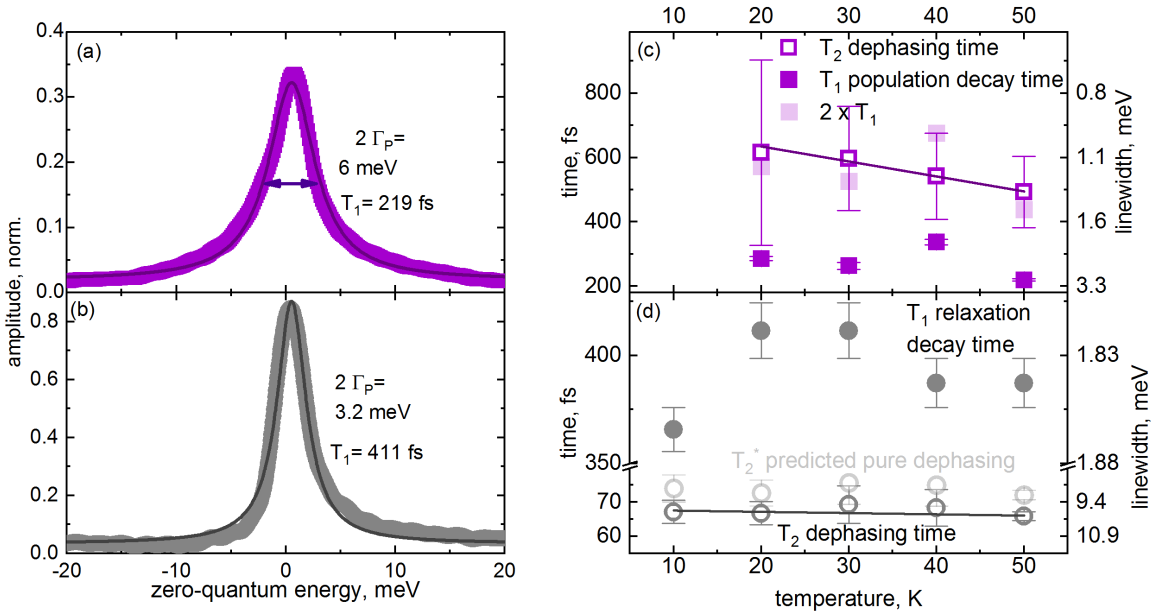

Fig. 7.9: (a+b) Linewidth cuts at the center emission energy from zero-quantum energy maps. Extracted homogenous linewidth $\gamma(T)$ (dephasing time T_2) and relaxation rate Γ_P (relaxation time T_1) of the exciton emission of ML (c) and BL (d) $MoSe_2$ versus temperature. The solid lines indicate fits via the linear exciton-acoustic phonon interaction equation.

Analog to the investigations of the ML, we extract a relaxation rate of $\Gamma_p^X = (1.6 \pm 0.3)$ meV ($T_1^X = (411 \pm 77)$ fs) for the BL as shown in Fig. 7.9 (b). As analyzed in heterostructures, holes transfer on timescales of hundreds of femtosecond [24]. Moreover, ARPES measurements of $MoSe_2$ resolve the band structure splitting of the ML and BL valence band. They estimate an energy splitting Γ to K of ~90 meV, where the valance band maximum is located at the Γ point [205]. Therefore, we attribute this lifetime to a hole transfer time from the K to the Γ point in valence band. The scattering is induced by phonon processes, mainly M-acoustical phonon-hole scattering mechanisms of energies at about 9 meV [66, 126]. By changing the temperature, we

observe a similar trend as in $MoTe_2$ in section 3.2.2, namely that the BL shows an acoustical phonon-exciton coupling of half of the value of the ML. In our case, we measure a coupling of $(6 \pm 4)\,\mu$eV K^{-1}, confirming the excitonic nature of the BL feature in Fig. 7.3. In contrast to the ML, the BL is not a two level system, such that $T_2 \sim 2 \cdot T_1$ relation is not valid. In most semiconductors there are other processes such as elastic exciton-exciton or exciton-phonon scattering influencing the dephasing. These processes are called pure dephasing γ^* and add to the relaxation decay $\gamma = \Gamma_p/2 + \gamma^*$ [111]. The pure dephasing energy perfectly matches the M-phonon energy of 9 meV as seen in Fig. 7.9 d (light gray circles). So the T_1 time is attributed to the scattering of holes from the K to the Γ point.

In conclusion, we confirm that the second feature in the BL signal occurs from excited state absorption of a doubly excited state $|X\rangle$. Moreover, we find the dephasing time to be similar to twice the population decay time in the ML as expected for high quality TMDC MLs. The BL shows a totally different trend; we attribute the relaxation time to the scattering time of holes from the K to the Γ point in the valence band. This is a starting point to investigate the direct transition in BL, giving hints towards the indirect BL exciton and, thus, for the design of heterostructures.

8 Summary

This thesis examines the optical properties of quasiparticles in transition metal dichalcogenides (TMDCs) and their interactions with phonons based on photoluminescence (PL), pump probe (PP) and two-dimensional coherent spectroscopy (2DCS). In the introduction of this thesis we posed a number of questions regarding the excitonic and trionic properties of $MoTe_2$ and TMDCs in general. We answer these questions by summarizing the results presented in the previous chapters.

Which ultrafast dynamics and dephasing processes are observable in BLs of TMDCs?

Ultrashort timescales can be accessed by two-dimensional coherent spectroscopy. Such experiments were performed on $MoSe_2$, where ML and BL differ in their respective band alignment. For TMDC MLs, we confirm that the dephasing time is limited by twice the population decay time for the exciton, as typical for a two level system. The bilayer differs in three aspects from the ML: (i) The dephasing is ten times faster than in the ML due to the electron dephasing towards the energetically favored Λ point. (ii) An additional intermediate relaxation time which is not describing depopulation of excitons but rather hole scattering from the K to the Γ point. (iii) An excited state absorption signal from an additional intra-layer biexciton or inter-layer exciton coupling to the main exciton. In particular, the last point needs further investigation in both experiment and theory.

Does the BL of $MoTe_2$ feature a direct excitonic transition?

The properties of the BL of $MoTe_2$ differ from all other TMDCs. We analyze temperature-dependent PL spectra and carefully compare the lineshape of the emission of ML and BL. Thereby, we find that in particular (acoustical) phonons influence the quasiparticles. Phonons and their coupling to excitons are the processes responsible for the bandgap redshift, linewidth broadening, and population decrease with increasing temperature. Differences in the temperature-dependence of the emission of ML and BL can be fully accounted for by including a well-width dependence well known from classical quantum wells in the coupling of excitons and phonons. Our findings prove a similar (direct) band alignment of ML and BL in $MoTe_2$.

Is there a trion in the BL $MoTe_2$?

We examine the nature of an emission peak on the low energy side of the exciton by simultaneously fitting the temperature- and excitation density-dependent PL with the mass action law: For the first time in Mo-based TMDCs, we confirm the existence of trions in the BL. Moreover, we confirm that ML and BL trion have similar bandgap shifts compared to the exciton. The inhomogeneous linewidth analysis predicts two trion states (inter- and intra-layer trion) in the BL separated by 2.2 meV.

Do exciton and trion mobilities in $MoTe_2$ approach the theoretical limit?

We connect phonon induced homogenous linewidth broadening with phonon limited mobility and relaxation time of quasiparticles for both acoustical and optical phonons. This tool enables us to determine a high acoustical phonon limited mobility of 6000 $cm^2V^{-1}s^{-1}$ (2000 $cm^2V^{-1}s^{-1}$) and 4300 $cm^2V^{-1}s^{-1}$ at low temperature for the ML exciton (trion) and BL exciton, respectively which are the highest values found so far in TMDCs. For the optical phonon mobility at room temperature we find that mainly the zero-order deformation potential determines the mobility of 300 $cm^2V^{-1}s^{-1}$ and 150 $cm^2V^{-1}s^{-1}$ in ML and BL.

Is there a measurable valley polarization degree in $MoTe_2$?

The theoretically predicted valley polarization decreases with the mass of the chalcogenide. For $MoTe_2$ a valley polarization has not been observed up to now. We measure polarization off-resonantly in PL and quasi-resonantly in PP. In the case of PL we measure a maximum polarization in the ML of -11 % for exciton and -16 % for the trion in agreement with spin-dependent density functional theory calculations. Quasi-resonant excitation in PP results in a degree of polarization of -65 % for the exciton which is induced by strong bandgap-renormalization. For the trion, we estimate values of 95 % immediately after excitation which depolarizes within 3 ps.

Can we measure a polarization of higher excitonic states?

We resonantly excite higher excitonic transitions, namely the B, A', and B' and find that population can be transferred to the ground state exciton and trion by phonon cascade processes. Since the hole transfer is slow, the electron transfer processes mainly define the polarization of the emitted light. Electrons undergo a change from spin-conserving processes to valley-conserving processes with increasing temperature. We find that spin-transfer processes are dominating at temperatures above 40 K.

Which processes determine the decay dynamics of excitons and trions in $MoTe_2$?

Excitons and trions show a three-exponential decay in PP. We find that defect-assisted recombination is ultrafast, namely 2.5 ps and 5 ps for exciton and trion. The evolution with temperature follows the acoustical phonon limited relaxation time and decreases to 1 ps and 2 ps for exciton and trion below 60 K. Refractive index change measurements in pump probe enables us to resolve scattering channels of the resonantly created state. We find that by exciting the exciton we also create trions within 1.5-2.5 ps, in agreement with the bimolecular formation of trions in amplitude.

In summary, this thesis presents the first comprehensive spectroscopic study and dynamics analysis of ML and BL $MoTe_2$.

"P.S. As far as the white rabbit is concerned, it might be better to compare it with the whole universe. We who live here are microscopic insects existing deep down in the rabbit's fur. But philosophers are always trying to climb up the fine hairs of the fur in order to stare right into the magician's eyes."

-Jostein Gaarder- Sophie's World: A Novel About the History of Philosophy

Danksagung

Ich möchte mich ganz herzlich bei allen Menschen bedanken, die mir geholfen haben, ein Stückchen aus dem Fell des Kaninchens herauszuklettern.

Als erstes möchte ich meiner Betreuerin und Gutachterin Prof. Dr. Ulrike Woggon bedanken. Neben ihrer fachlichen Qualifikation bewundere ich ihre Fähigkeit, eine Arbeitsgruppe aufzubauen und weiterzuentwickeln, hervorragendes Equipment zu beschaffen und die finanzielle Förderung sicherzustellen. In dem gesteckten Rahmen habe ich sowohl eine weitreichende Freiheit bekommen, mein Thema zugestalten als auch fachliche Leitung bei der Klärung schwieriger Fragen. Ich freue mich sehr, Teil dieser Arbeitsgruppe zu sein und bedanke mich für meine Zeit hier.

Des weiteren danke ich Prof. Dr. Janina Maultzsch und Prof. Dr. Ursula Wurstbauer für ihre Unterstützung insbesondere durch die Begutachtung dieser Arbeit und hoffe, sie mögen mir den einen oder anderen (Schreib-)Fehler verzeihen. Ich bedanke mich bei Prof. Dr. Kathy Lüdge für Ihre Bereitschaft, meiner Verteidigungskommission vorzustehen.

In ganz besonderem Maße bedanke ich mich bei Dr. Nina Owschimikow, ohne die diese Arbeit so nicht existieren würde. Ihre fabelhaften Ideen und ihr umfassendes Verständnis der Thematik haben mir dutzende Male geholfen, Zusammenhänge klarzustellen und einzuordnen. Darüberhinaus bedanke ich mich für die vielen tollen Gespräche und die schöne Zeit in- und außerhalb der Uni.

Außerdem möchte ich mich bei meiner Arbeitsgruppe bedanken. Ich danke Dr. Oliver Schöps für seine Hilfe in allen Lebenslagen, sei es im Labor, beim Korrigieren dieser Arbeit, oder den aufmunternden Worten, wenn es mal nicht so einfach war. Er ist der beste Büropartner der Welt und es wird mir sehr fehlen mit ihm über Filme, Bücher und die Welt zu fachsimpeln. Ich danke Dr. Mirco Kolarczik und Dr. Bastian Herzog für ihre große Unterstützung beim Messen der Pump Probe und Photolumineszenzdaten und für die schöne und witzige Zeit im Kaffeeraum. Dr. Alexander W. Achtstein danke ich dafür, dass er sein umfassendes Wissen mit mir geteilt hat, jede seiner Ideen und Beiträge führten zu einem verbessertem fachlichem Verständnis. Ich danke meinen Studenten Hery Ahmad und Matthias Kunz für ihre tolle Arbeit und ihren Einsatz. Ich bedanke mich bei Dr. Karsten Pufahl, Jenny Schwadtke, Leo und Michael Quick für die schöne gemeinsame Zeit in der AG.

Diese Arbeit wäre nicht möglich gewesen ohne die vielen Kooperationspartner. Ich bedanke mich ganz herzlich bei Prof. Dr. Xiaoqin Li für ihre Gastfreundschaft und die ausgezeichnete Betreuung während meines Auslandsaufenthalts in Texas. Sie ist für mich sowohl menschlich als auch wissenschaftlich ein großes Vorbild. Ein großes Dankeschön geht an Kevin Sampson und Dr. Kai Hao dafür, dass sie die 2D Messungen mit mir durchgestanden haben incl. einiger Nachtschichten. Ich bedanke mich bei Dr. Kha Tran, Marshall Campbell, Matthew Staab für

die Herstellung der ausgezeichneten $MoSe_2$ ML und BL. Außerdem bedanke ich mich bei der gesamten Arbeitsgruppe und den Mädels vom Tanzen für die herzliche Aufnahme in Texas, Ihr habt die Zeit dort für mich einzigartig gemacht.

Ich bedanke mich bei den Arbeitsgruppen von Prof. Dr. Tim Wehling und Prof. Dr. Frank Jahnke von der Universität Bremen, insbesondere bei Dr. Matthias Florian und Dr. Alexander Steinhoff für ihre wundervollen Rechnungen zur Polarisation und den vielen fruchtbaren Diskussionen.

Ich bedanke mich bei der Arbeitsgruppe von Prof. Dr. Rudolf Bratschitsch von der Westfälischen Wilhelms-Universität Münster, insbesondere bei Dr. Robert Schneider, Dr. Ashish Arora und Dr. Steffen Michaelis de Vasconcellos für das Herstellen der $MoTe_2$ Proben insbesondere des Wunder-Flakes und der fruchtbaren Paperdiskussionen.

Ich bedanke mich beim GRK 1558, SfB 787 und der DFG für die finanzielle Förderung.

Darüberhinaus bedanke ich mich bei meinen Freunden, allen voran Franzi & Malte & Charlotte, Felix, Flori, Martin & Natalie & Joshi, Anna & Christian, Britta, Sahra, Lisa, Bettina, Luisa und Melanie. Ihr habt mir Halt, Mut und Zeit gegeben diese Doktorarbeit durchzustehen.

Abschließend möchte ich mich bei meiner Familie bedanken: Bei meiner süßen Schwester Theresia, meinen Eltern Ines und Uwe, meinen Omas Brigitte und Elisabeth und meiner restlichen Familie für ihren Rückhalt, ihre tröstenden Worte und Umarmungen in schwierigen Zeiten. Und ich danke von ganzem Herzen meinem Freund Mäx für Alles, vom Korrigieren dieser Arbeit bis hin zum Trost, Aufmunterung und den ganzen Kleinigkeiten, die mir das Leben gerade in den letzten Monaten unglaublich erleichtert und verschönert haben.

Publications

Peer Reviewed Publications

- A Singh, K. Tran, M. Kolarczik, J. Seifert, Y. Wang, K. Hao, D. Pleskot, N. M. Gabor, S. Helmrich, N. Owschimikow, U. Woggon, and X. Li, "Long-Lived Valley Polarization of Intravalley Trions in Monolayer WSe_2", Phys. Rev. Lett. 117, 257402 (2016)

- S. Helmrich, R. Schneider, A. W. Achtstein, A. Arora, B. Herzog, S. M. de Vasconcellos, M. Kolarczik, O. Schöps, R. Bratschitsch, U. Woggon and N. Owschimikow, "Exciton-phonon coupling in mono- and bilayer $MoTe_2$", 2D Mater. 5, 045007 (2018).

- A. Steinhoff, M. Florian, A. Singh, K. Tran, M. Kolarczik, S. Helmrich, A. W. Achtstein, U. Woggon, N. Owschimikow, F. Jahnke and X. Li, "Biexciton fine structure in monolayer transition metal dichalcogenides", Nature Physics. 14, 1199 (2018).

- B. Herzog, B. Lingnau, M. Kolarczik, S. Helmrich, A.W. Achtstein, K. Thommes, F. Alhussein, D. Quandt, A. Strittmatter, U. W. Pohl, O. Brox, M. Weyers, U. Woggon, K. Lüdge and N. Owschimikow, "Broadband Semiconductor Light Sources Operating at 1060 nm Based on InAs:Sb/GaAs Submonolayer Quantum Dots", IEEE J. Select. Top. Quantum Electron. 25, 1900310 (2019).

Conference Proceedings

- A. Singh and K. Tran and J. Seifert and Y. Wang and K. Hao and X. Li and D. Pleskot and N. M. Gabor and S. Helmrich and M. Kolarczik and N. Owschimikow and U. Woggon. "Long-Lived Valley Polarization of Intra-Valley Trions in Monolayer WSe_2," APS March Meeting, New Orleans, Louisian, USA abstract id. C48.003 (2017).

- A. Singh and K. Tran and J. Seifert and Y. Wang and K. Hao and X. Li and D. Pleskot and N. M. Gabor and S. Helmrich and M. Kolarczik and N. Owschimikow and U. Woggon. "Valley polarization dynamics of inter- and intra-valley trions in monolayer WSe_2," Conference on Lasers and Electro-Optics (CLEO), San Jose, CA, USA, pp. 1-2 (2017).

- A. Singh, K. Tran, J. Seifert, Y. Wang, K. Hao, X. Li, D. Pleskot, N. M. Gabor, N. Owschimikow, S. Helmrich, M. Kolarczik, and U. Woggon, "Trion valley dynamics in monolayer WSe_2," European Conference on Lasers and Electro-Optics and European Quantum Electronics Conference, Munich, Germany, paper EI_3_2 (2017).

- M. Kolarczik, K. Thommes, B. Herzog, S. Helmrich, N. Owschimikow, U. Woggon. "Ultrafast photonics in coherently coupled III-V semiconductor nanostructures," Proc. SPIE 10638, Orlando, FL, USA (2018).

- B. Herzog, B. Lingnau, M. Kolarczik, S. Helmrich, U.Woggon, K. Lüdge, and N. Owschimikow. "Role of Mixed-dimensional Excitons in Phase Dynamics of Semiconductor Lasers based on InAs(Sb)/GaAs Submonolayer Quantum Dots," Conference on Lasers and Electro-Optics (CLEO), San Jose, CA, USA, paper JW2A.24 (2019).

- M. Kolarczik, A. Koulas-Simos, B. Herzog, B. Lingnau, S. Helmrich, K. Lüdge, N. Owschimikow, and U. Woggon. "Heterodimensionally confined carriers in III-V semiconductor nanostructures in multidimensional spectroscopy," Conference on Lasers and Electro-Optics (CLEO), San Jose, CA, USA, paper FM3D.2 (2019).

Conference Contributions

- B. Herzog, M. Kolarczik, S. Helmrich, B. Lingnau, K. Lüdge, J.-H. Schulze, U. Pohl, A. Strittmatter, O. Brox, M. Weyers, N. Owschimikow, U. Woggon. "Exciton dynamics and state splitting in antimony-doped InAs submonolayer agglomerations," Fundamental Optical Processes in Semiconductors (FOPS), Stevenson, WA, USA (2017).

- S. Helmrich, R. Schneider, A. W. Achtstein, A. Arora, B. Herzog, S. M. de Vasconcellos, M. Kolarczik, O. Schöps, R. Bratschitsch, U. Woggon and N. Owschimikow. "Exciton-phonon coupling in mono- and bilayer $MoTe_2$," DPG Spring Meeting, Berlin, (2018)

- M. Kunz, S. Helmrich, R. Schneider, A. W. Achtstein, A. Arora, B. Herzog, S. M. de Vasconcellos, M. Kolarczik, O. Schöps, R. Bratschitsch, U. Woggon and N. Owschimikow. "Spatially resolved photoluminescence of mono- and bilayer molybdenum ditelluride," DPG Spring Meeting, Berlin, (2018)

- S. Helmrich, R. Schneider, A. W. Achtstein, A. Arora, B. Herzog, S. M. de Vasconcellos, M. Kolarczik, O. Schöps, R. Bratschitsch, U. Woggon and N. Owschimikow, "Exciton-phonon coupling in mono- and bilayer $MoTe_2$", PCNSPA Photonic Colloidal Nanostructures, St. Petersburg, Russia (2018).

- S. Helmrich, M. Kunz, R. Schneider, A. W. Achtstein, A. Arora, B. Herzog, S. M. de Vasconcellos, M. Kolarczik, O. Schöps, R. Bratschitsch, U. Woggon and N. Owschimikow. "Coupling of excitons and phonons in mono- and bilayer $MoTe_2$," NOEKS14, Berlin, Germany (2018)

- A. Steinhoff, M. Florian, A. Singh, K. Tran, M. Kolarczik, S. Helmrich, A. W. Achtstein, U. Woggon, N. Owschimikow, F. Jahnke and X. Li. "Induced absorption reveals biexciton fine structure in monolayer WSe_2," NOEKS14, Berlin, Germany (2018)

- S. Helmrich, M. Kunz, R. Schneider, A. W. Achtstein, A. Arora, B. Herzog, S. M. de Vasconcellos, M. Kolarczik, O. Schöps, R. Bratschitsch, U. Woggon and N. Owschimikow. "Valley Polarization in mono- and bilayer $MoTe_2$" NECD 18, International Conference of GRK 1558,Potsdam, Germany (2018)

- S. Helmrich, M. Kolarczik, A. W. Achtstein, B. Herzog, O. Schöps, U. Woggon and N. Owschimikow. "Optical properties of mono- and bilayer Molybdenum Ditelluride," Fundamental Optical Processes in Semiconductors (FOPS), Banff, Alberta, CA (2019).

- B. Herzog, A. Nelde, M. Kolarczik, A. W. Achtstein, S. Helmrich, U. Woggon and N. Owschimikow. "From chaotic lasing to photon statistics: Small and large scale fluctuations in the emission of quantum dot lasers," Fundamental Optical Processes in Semiconductors (FOPS), Banff, AB, Canada (2019).

Bibliography

[1] Alexander W. Achtstein, Andrei Schliwa, Anatol Prudnikau, Marya Hardzei, Mikhail V. Artemyev, Christian Thomsen, and Ulrike Woggon. Electronic Structure and Exciton-Phonon Interaction in Two-Dimensional Colloidal CdSe Nanosheets. *Nano Lett.*, 12:3151, 2012.

[2] Hery Ahmad. Linienformanalyse der Photolumineszenz-Spektren von Mono- und Doppellage $MoTe_2$. Master's thesis, Technische Universität Berlin, 2019.

[3] Ashish Arora, Karol Nogajewski, Maciej Molas, Maciej Koperski, and Marek Potemski. Excitonic band structure in layered $MoSe_2$: from a monolayer to bulk limit. *Nanoscale*, 7:20769, 2015.

[4] Ashish Arora, Robert Schmidt, Robert Schneider, Maciej R. Molas, Ivan Breslavetz, Marek Potemski, and Rudolf Bratschitsch. Valley Zeeman Splitting and Valley Polarization of Neutral and Charged Excitons in Monolayer $MoTe_2$ at High Magnetic Fields. *Nano Lett.*, 16(6):3624–3629, 2016.

[5] Tomoya Asaba, Yongjie Wang, Gang Li, Ziji Xiang, Colin Tinsman, Lu Chen, Shangnan Zhou, Songrui Zhao, David Laleyan, Yi Li, Zetian Mi, and Lu Li. Magnetic Field Enhanced Superconductivity in Epitaxial Thin Film WTe_2. *Sci. Rep.*, 8:6520, 2018.

[6] C. Ataca, H. Şahin, and S. Ciraci. Stable, Single-Layer MX_2 Transition-Metal Oxides and Dichalcogenides in a Honeycomb-Like Structure. *J. Phys. Chem. C*, 116(16):8983, 2012.

[7] M. Balkanski and R.F. Wallis. *Semiconductor Physics and Applications*. Oxford Univ. Press, 2000.

[8] M. Baranowski, A Surrente, D.K. Maude, M. Ballotti, A.A. Mitioglu, P.C.M. Christianen, Y.C. Kung, D. Dumcenco, A. Kis, and P. Plochocka. Dark excitons and the elusive valley polarization in transition metal dichalcogneides. *2D Mater.*, 4(2):025016, 2017.

[9] J. Bardeen and W. Shockley. Deformation Potentials and Mobilities in Non-Polar Crystals. *Phys. Rev.*, 80:72, 1950.

[10] P. K. Basu. *Theory of Optical Processes in Semiconductors*. Oxford Science Publications, 1997.

[11] Gunnar Berghäuser, Ivan Bernal-Villamil, Robert Schmidt, Robert Schneider, Iris Niehues, Paul Erhart, Steffen Michaelis de Vasconcellos, Rudolf Bratschitsch, Andreas Knorr, and Ermin Malic. Inverted valley polarization in optically excited transition metal dichalcogenides. *Nature Commun.*, 9:971, 2018.

[12] Timothy C. Berkelbach, Mark S. Hybertsen, and David R. Reichman. Theory of neutral and charged excitons in monolayer transition metal dichalcogenides. *Phys. Rev. B*, 88:045318, 2013.

[13] J. Berney, M.T. Portella-Oberli, and B. Deveaud-Plédran. Theoretical derivation of the bi- and tri-molecular trion formation coefficients. *arXiv*, 0901.3645, 2009.

[14] W. Bludau, A. Onton, and W. Heinke. Temperature dependence of the band gap of silicon. *J. Appl. Phys.*, 45:1846, 1974.

[15] K.I. Bolotin, K.J. Sikes, Z. Jiang, M. Klima, G. Fudenberg, J. Hone, P. Kim, and H.L. Stormer. Ultrahigh electron mobility in suspended graphene. *Solid State Commu.*, 146:351, 2008.

[16] P. Borri, W. Langbein, J. M. Hvam, and F. Martelli. Well-width dependence of exciton-phonon scattering in $In_xGa_{1-x}As$/GaAs single quantum wells. *Phys. Rev. B*, 59:2215, 1999.

[17] Samuel Brem, Malte Selig, Gunnar Berghäuser, and Ermin Malic. Exciton Relaxation Cascade in two-dimensional Transition Metal Dichalcogenides. *Sci. Rep.*, 8:8238, 2018.

[18] A. D. Bristow, D. Karaiskaj, X. Dai, T. Zhang, C. Carlsson, K. R. Hagen, R. Jimenez, and S. T. Cundiff. A versatile ultrastable platform for optical multidimensional Fourier-transform spectroscopy . *Rev. Sci. Instrum.*, 80:073108, 2009.

[19] Alan D. Bristow, Denis Karaiskaj, Xingcan Dai, Richard P. Mirin, and Steven T. Cundiff. Polarization dependence of semiconductor exciton and biexciton contributions to phase-resolved optical two-dimensional Fourier-transform spectra. *Phys. Rev. B*, 79:161305, 2009.

[20] Samantha Bruzzone and Gianluca Fiori. Ab-initio simulations of deformation potentials and electron mobility in chemically modified graphene and two-dimensional hexagonal boron-nitride. *Appl. Phys. Lett.*, 99:222108, 2011.

[21] F. Cadiz, E. Courtade, C. Robert, G. Wang, Y. Shen, H. Cai, T. Taniguchi, K. Wantanabe, H. Carrere, D. Lagarde, M. Manca, T. Amand, P. Renucci, S. Tongay, X. Marie, and B. Urbaszek. Excitonic Linewidth Approaching the Homogeneous Limit in MoS_2-Based van der Waales Heterostructures. *Phys. Rev. X*, 7:021026, 2017.

[22] Ting Cao, Gang Wang, Wenpeng Han, Huiqi Ye, Chuanrui Zhu, Junren Shi, Qian Niu, Pingheng Tan, Enge Wang, Baoli Liu, and Ji Feng. Valley-selective circular dichroism of monolayer molybdenum disulphide. *Nat. Commun.*, 3:887, 2012.

[23] L. S. R. Cavalcante, D. R. da Costa, G. A. Farias, D. R. Reichman, and A. Chaves. Stark shift of excitons and trions in two-dimensional materials. *Phys. Rev. B*, 98:245309, 2018.

[24] Frank Ceballos, Matthew Z. Bellus, Hsin-Ying Chiu, and Hui Zhao. Ultrafast Charge Separation and Indirect Exciton Formation in a MoS_2-$MoSe_2$ van der Waals Heterostructure. *ACS Nano.*, 8:12717, 2014.

[25] Soonyoung Cha, Ji Ho Sung, Sangwan Sim, Jun Park, Hoseok Heo, Moon-Ho Jo, and Hyunyong Choi. 1s-intraexcitonic dynamics in monolayer MoS_2 probed by ultrafast mid-infrared spectroscopy. *Nat. Commun.*, 7:10768, 2016.

[26] Bin Chen, Hasan Sahin, Aslihan Suslu, Laura Ding, Mariana I. Bertoni, F. M. Peeters, and Sefaattin Tongay. Enviromental Changes in $MoTe_2$ Excitonic Dynamics by Defects-Activated Molecular Interaction. *ACS Nano*, 9(5):5326, 2015.

[27] Ke Chen, Anupam Roy, Amritesh Rai, Hema C. P. Movva, Xianghai Meng, Feng He, Sanjay Banerjee, and Yaguo Wang. Accelerated Carrier Recombination by Grain Boundary/Edge Defects in MBE Grown Transition Metal Dichalcogenides. *APL Materials*, 6(5):056103, 2018.

[28] Shao-Yu Chen, Thomas Goldstein, Jiayue Tong, Takashi Taniguchi, Kenji Watanabe, and Jun Yan. Superior Valley Polarization and Coherence of 2 s Excitons in Monolayer WSe_2. *Phys. Rev. Lett.*, 120:046402, 2018.

[29] A. Chiari, M. Colocci, F. Fermi, Yuzhang Li, R. Querzoli, A. Vinattieri, and Weihua Zhuang. Temperature Dependence of the Photoluminescence in GaAs-GaAlAs Multiple Quantum Well Structure. *Phys. stat. sol.*, 147:421, 1988.

[30] Jason W. Christopher, Bennett B. Goldberg, and Anna K. Swan. Long tailed trions in monolayer MoS_2: Temperature dependent asymmetry and resulting red-shift of trion photoluminescence spectra. *Scien. Rep.*, 7:14062, 2017.

[31] Monique Combescot and Shiue-Yuan Shiau. *Excitons and Cooper Pairs - Two Composite Bosons in Many-Body Physics*. Oxford Univ. Press, 2016.

[32] Hiram J. Conley, Bin Wang, Jed I. Ziegler, Richard F. Haglund Jr., Sokrates T. Pantelides, and Kirill I. Bolotin. Bandgap Engineering of Strained Monolayer and Bilayer MoS_2. *Nano Lett.*, 13(8):3626, 2013.

[33] S. Dal Conte, F. Bottegoni, E. A. A. Pogna, D. De Fazio, S. Ambrogio, I. Bargigia, C. D'Andrea, A. Lombardo, M. Bruna, F. Ciccacci, A. C. Ferrari, G. Cerullo, , and M. Finazzi. Ultrafast valley relaxation dynamics in monolayer MoS 2 probed by nonequilibrium optical techniques. *Phys. Rev. B*, 92:235425, 2015.

[34] OriginLab Corporation. OriginLab Corporation, 2012.

[35] E. Courtade, M. Semina, M. Manca, M. M. Glazov, C. Robert, F. Cadiz, G. Wang, T. Taniguchi, K. Watanabe, M. Pierre, W. Escoffier, E. L. Ivchenko, P. Renucci, X. Marie, T. Amand, and B. Urbaszek. Charged excitons in monolayer WSe_2: Experiment and theory. *Phys. Rev. B*, 96:085302, 2017.

[36] Qiannan Cui, Frank Ceballos, Nardeep Kumar, and Hui Zhao. Transient Absorption Microscopy of Monolayer and Bulk WSe_2. *Nature Nano.*, 8(3):2970, 2014.

[37] Hanan Dery and Yang Song. Polarization analysis of excitons in monolayer and bilayer transition-metal dichalcogenides. *Phys. Rev. B*, 92:125431, 2015.

[38] Luojun Du, Tingting Zhang, Mengzhou Liao, Guibin Liu, Shuopei Wang, Rui He, Zhipeng Ye, Hua Yu, Rong Yang, Dongxia Shi, Yugui Yao, and Guangyu Zhang. Temperature-driven evolution of critical points, interlayer coupling, and layer polarization in bilayer MoS_2. *Phys. Rev. B*, 97:165410, 2018.

[39] J. P. Echeverry, B. Urbaszek, T. Amand, X. Marie, and I. C. Gerber. Splitting between bright and dark excitons in transition metal dichalcogenide monolayers. *Phys. Rev. B*, 93:121107(R), 2016.

[40] Axel Esser, Erich Runge, Roland Zimmermann, and Wolfgang Langbein. Photoluminescence and radiative lifetime of trions in GaAs quantum wells. *Phys. Rev. B*, 62:8232, 2000.

[41] H. Y. Fan. Temperature Dependence of the Energy Gap in Semiconductors. *Phys. Rev.*, 82:900, 1951.

[42] J. Frenkel. On the Transformation of light into Heat in Solids. I. *Phys. Rev.*, 37:17, 1931.

[43] Guillaume Froehlicher, Etienne Lorchat, and Stéphane Berciaud. Direct versus indirect band gap emission and exciton-exciton annihilation in atomically thin molybdenum ditelluride ($MoTe_2$). *Phys. Rev. B*, 94:085429, 2016.

[44] Feng Gao, Yongji Gong, Michael Titze, Raybel Almeida, Pulickel M. Ajayan, and Hebin Li. Valley Trion Dynamics in Monolayer $MoSe_2$. *Phys. Rev. B*, 94:245413, 2016.

[45] A. K. Geim and I. V. Grigorieva. Van der Waals heterostructures. *Nature*, 499:419, 2013.

[46] Roland Gillen and Janina Maultzsch. Interlayer excitons in $MoSe_2/WSe_2$ heterostructures from first principles. *Phys. Rev. B*, 97:165306, 2018.

[47] Thorlabs GmbH. Thorlabs GmbH, 2019.

[48] Huaihong Guo, Teng Yang, Mahito Yamamoto, Lin Zhou, Ryo Ishikawa, Keiji Ueno, Kazuhito Tsukagoshi, Zhidong Zhang, Mildred S. Dresselhaus, and Riichiro Saito. Double resonance Raman modes in monolayer and few-layer $MoTe_2$. *Phys. Rev. B*, 91:205415, 2015.

[49] Garima Gupta, Sangeeth Kallatt, and Kausik Majumdar. Direct observation of giant binding energy modulation of exciton complexes in monolayer $MoSe_2$. *Phys. Rev. B*, 96:081403(R), 2017.

[50] Tetsuro Habe and Mikito Koshino. Spin-dependent refraction at the atomic step of transition-metal dichalcogenides. *Phys. Rev. B*, 91:201407, 2015.

[51] Bernhard Halle. B.Halle Nachfl. GmbH, 2017.

[52] A.T. Hanbicki, G. Kioseoglou, M. Currie, C. Stephen Hellberg, K.M. McCreary, A.L. Friedman, and B.T. Jonker. Anomalous temperature-dependent spin-valley polarization in monolayer WS_2. *Sci. Rep.*, 6:18885, 2016.

[53] Kai Hao, Judith F. Specht, Philipp Nagler, Lixiang Xu, Kha Tran, Akshay Singh, Chandriker Kavir Dass, Christian Schüller, Tobias Korn, Marten Richter, Andreas Knorr, Xiaoqin Li, and Galan Moody. Neutral and charged inter-valley biexcitons in monolayer $MoSe_2$. *Nature Commun.*, 8:15552, 2017.

[54] Kai Hao, Lixiang Xu, Fengcheng Wu, Philipp Nagler, Kha Tran, Xin Ma, Christian Schüller, Tobias Korn, Allan H MacDonald, Galan Moody, and Xiaoqin Li. Trion valley coherence in monolayer semiconductors. *2D Mater.*, 4:025105, 2017.

[55] Jiangang He, Kerstin Hummer, and Cesare Franchini. Stacking effects on the electronic and optical properties of bilayer transition metal dichalcogneides MoS_2, $MoSe_2$, WS_2 and WSe_2. *Phys. Rev. B*, 89:075409, 2014.

[56] S. Helmrich, R. Schneider, A. W. Achtstein, A. Arora, B. Herzog, S. M. de Vasconcellos, M. Kolarczik, O. Schöps, R. Bratschitsch, U. Woggon, and N. Owschimikow. Exciton-phonon coupling in mono- and bilayer $MoTe_2$. *2D Mater.*, 5:045007, 2018.

[57] C. H. Henry and D. V. Lang. Nonradiative capture and recombination by multiphonon emission in GaAs and GaP. *Phys. Rev. B*, 15:989, 1977.

[58] Xiaoping Hong, Jonghwan Kim, Su-Fei Shi, Yu Zhang, Chenhao Jin, Yinghui Sun, Sefaattin Tongay, JunqiaoWu, Yanfeng Zhang, and Feng Wang. Ultrafast charge transfer in atomically thin MoS_2/WS_2 heterostructures. *Nature Nano.*, 9:682, 2014.

[59] S. Y. Hu, Y. C. Lee, J. L. Shen, K. W. Chen, K. K. Tiong, and Y. S. Huang. Temperature dependence of absorption edge anisotropy in 2H-$MoSe_2$ layered semiconductors. *Solid State Commun.*, 139(4):176, 2006.

[60] Jiani Huang, Thang B. Hoang, and Maiken H. Mikkelsen. Probing the origin of excitonic states in monolayer WSe_2. *Sci. Rep.*, 6:22414, 2016.

[61] Zhishuo Huang, Wenxu Zhang, and Wanli Zhang. Computational Search for Two-Dimensional MX2 Semiconductors with Possible High Electron Mobility at Room Temperature. *Mater.*, 9(9):716, 2016.

[62] S. Hunsche, K. Leo, H. Kurz, and K. Köhler. Exciton absorption saturation by phase-space filling: Influence of carrier temperature and density. *Phys. Rev. B*, 49:16565, 1994.

[63] Chongyun Jiang, Fucai Liu, Jorge Cuadra, Zumeng Huang, KeLi, Abdullah Rasmita, Ajit Srivastava, Zheng Liu, and Wei-Bo Gao. Zeeman splitting via spin-valley-layer coupling in bilayer $MoTe_2$. *Nature Commun.*, 8:802, 2017.

[64] Tao Jiang, Hengrui Liu, Di Huang, Shuai Zhang, Yingguo Li, Xingao Gong, Yuen-Ron Shen, Wei-Tao Liu, and Shiwei Wu. Valley and band structure engineering of folded MoS_2 bilayers. *Nature Nano.*, 9:825, 2014.

[65] Wencan Jin, Po-Chun Yeh, Nader Zaki, Datong Zhang, Jerzy T. Sadowski, Abdullah Al-Mahboob, Arend M. van der Zande, Daniel A. Chenet, Jerry I. Dadap, Irving P. Herman, Peter Sutter, James Hone, and Richard M. Osgood. Direct Measurement of the Thickness-Dependent Electronic Band Structure of MoS_2 Using Angle-Resolved Photoemission Spectroscopy. *Phys. Rev. Lett.*, 111:106801, 2013.

[66] Zhenghe Jin, Xiaodong Li, Jeffrey T. Mullen, and Ki Wook Kim. Intrinsic transport properties of electrons and holes in monolayer transition-metal dichalcogenides. *Phys. Rev. B*, 90:045422, 2014.

[67] Aaron M. Jones, Hongyi Yu, Jason S. Ross, Philip Klement, Nirmal J. Ghimire, Jiaqiang Yan, David G. Mandrus, Wang Yao, and Xiaodong Xu. Spin-layer locking effects in optical orientation of exciton spin in bilayer WSe_2. *Nature Phys.*, 10:130, 2014.

[68] Aaron M. Jones, Hongyi Yu, Jason S. Ross, Philip Klement, Nirmal J. Ghimire, Jiaqiang Yan, David G. Mandrus, Wang Yao, and Xiaodong Xu. Intrinsic Circular Polarization

in Centrosymmetric Stacks of Transition-Metal Dichalcogenide Compounds. *Phys. Rev. Lett.*, 114:087402, 2015.

[69] Kristen Kaasbjerg, Kristian S. Thygesen, and Karsten W. Jacobsen. Phonon-limited mobility in n-type single-layer MoS_2 from first principles. *Phys. Rev. B*, 85:115317, 2012.

[70] Kristen Kaasbjerg, Kristian S. Thygesen, and Antti-Pekka Jauho. Acoustic phonon limited mobility in two-dimensional semiconductors: Deformation potential and piezoelectric scattering in monolayer MoS_2 from first principles. *Phys. Rev. B*, 87:235312, 2013.

[71] Y. Kaptan, H. Schmeckebier, B. Herzog, D. Arsenijevic, M. Kolarczik, V. Mikhelashvili, N. Owschimikow, G. Eisenstein, D. Bimberg, and U. Woggon. Gain dynamics of quantum dot devices for dual-state operation. *Appl. Phys. Lett.*, 104:261108, 2014.

[72] Marjan Khamesian, Ignacio Fdez.Galvan, Mickaël G.Delcey, Lasse Kragh Sorensen, and Roland Lindh. Chapter Three - Spectroscopy of linear and circular polarized light with the exact semiclassical light-matter interaction. *Annu. Rep. Comput. Chem.*, 15:39–76, 2019.

[73] G. Kioseoglou, A. T. Hanbicki, M. Currie, A. L. Friedman, D. Gunlycke, and B. T. Jonker. Valley polarization and intervalley scattering in monolayer MoS_2. *App. Phys. Lett.*, 101:221907, 2012.

[74] G. Kioseoglou, A. T. Hanbicki, M. Currie, A. L. Friedman, and B. T. Jonker. Optical polarization and intervalley scattering in single layers of MoS_2 and $MoSe_2$. *Sci. Rep.*, 6:25041, 2016.

[75] Sandhaya Koirala, Shinichiro Mouri, Yuhei Miyauchi, and Kazunari Matsuda. Homogeneous linewidth broadening and exciton dephasing mechanism in $MoTe_2$. *Phys. Rev. B*, 93:075411, 2016.

[76] Mirco Kolarczik. *Broadband ultrafast spectroscopy on mixed-dimensional InAs/GaAs systems.* PhD thesis, Technical University of Berlin, 2019.

[77] Mirco Kolarczik, Nina Owschimikow, Bastian Herzog, Florian Buchholz, Y. I. Kaptan, and Ulrike Woggon. Exciton dynamics probe the energy structure of a quantum dot-in-a-well system: The role of Coulomb attraction and dimensionality. *Phys. Rev. B*, 91:235310, 2015.

[78] Andor Kormányos, Guido Burkard, Martin Gmitra, Jaroslav Fabian, Viktor Zolyomi, Neil D Drummond, and Vladimir Falko. k*p theory for two-dimensional transition metal dichalcogenide semiconductors. *2D Mater.*, 2:022001, 2015.

[79] T. Korn, S. Heydrich, M. Hirmer, J. Schmutzler, and C. Schüller. Low-temperature photocarrier dynamics in monolayer MoS_2. *Appl. Phys. Lett.*, 99:102109, 2011.

[80] K. Kośmider, J.W. González, and J. Fernández-Rossier. Large spin splitting in the conduction band of transition metal dichalcogneide monolayers. *Phys. Rev. B*, 88:245436, 2013.

[81] Takeshi Koyama, Satoru Shimizu, Yasumitsu Miyata, Hisanori Shinohara, and Arao Nakamura. Ultrafast formation and decay dynamics of trions in p-doped single-walled carbon nanotubes. *Phys. Rev. B*, 87:165430, 2013.

[82] A. Kumar and P. K. Ahluwalia. Electronic structure of transition metal dichalcogenides monolayers 1H-MX_2 (M=Mo, W; X=S, Se, Te) from ab-initio theory: new direct band gap semiconductors. *Eur. Phys. J. B*, 85:186, 2012.

[83] Nardeep Kumar, Qiannan Cui, Frank Ceballos, Dawei He, Yongsheng Wang, and Hui Zhao. Exciton-exciton annihilation in $MoSe_2$ monolayers. *Phys. Rev. B*, 89:125427, 2014.

[84] Matthias Felix Kunz. Ortsaufgelöste Photolumineszensspektroskopie am Monolayer-Bilayer Übergang vom TMD $MoTe_2$. Master's thesis, Technische Universität Berlin, 2018.

[85] D. Lagarde, L. Bouet, X. Marie, C. R. Zhu, B. L. Liu, T. Amand, P. H. Tan, and B. Urbaszek. Carrier and Polarization Dynamics in Monolayer MoS_2. *Phys. Rev. Lett.*, 112:047401, 2014.

[86] Murray A. Lampert. Mobile and Immobile Effective-Mass-Particle Complexes in Nonmetallic Solids. *Phys. Rev. Lett.*, 1:450, 1958.

[87] N. A. Lanzillo, A. G. Birdwell, M. Amani, F. J. Crowne, P. B. Shah, S. Najmaei, Z. Liu, P. M. Ajayan, J. Lou, M. Dubey, S. K. Nayak, and T. P. O'Regan. Temperature-dependent phonon shifts in monolayer MoS_2. *Appl. Phys. Lett.*, 103:093102, 2013.

[88] Johnson Lee, Emil S. Koteles, and M. O. Vassell. Luminescence linewidths of excitons in GaAs quantum wells below 150 K. *Phys. Rev. B*, 33:5512, 1986.

[89] Ignacio Gutiérrez Lezama, Ashish Arora, Alberto Ubaldini, Céline Barreteau, Enrico Giannini, Marek Potemski, and Alberto F. Morpurgo. Indirect-to-Direct Band Gap Crossover in Few-Layer $MoTe_2$. *Nano Lett.*, 15(4):2336, 2015.

[90] Tianshu Li and Giulia Galli. Electronic Properties of MoS_2 Nanoparticles. *J. Phys. Chem. C*, 111:44, 2007.

[91] Yuxuan Lin, Xi Ling, Lili Yu, Shengxi Huang, Allen L. Hsu, Yi-Hsien Lee, Jing Kong, Mildred S. Dresselhaus, and Tomás Palacios. Dielectric Screening of Excitons and Trions in Single-Layer MoS_2. *Nano Lett.*, 14:5569, 2014.

[92] Gui-Bin Liu, Di Xiao, Yugui Yao, Xiaodong Xu, and Wang Yao. Electronic structures and theoretical modelling of two-dimensional group-VIB transition metal dichalcogenides. *Chem. Soc. Rev.*, 44:2643, 2015.

[93] Gui-Binn Liu, Wen-Yu Shan, Yugui Yao, Wang Yao, and Di Xiao. Three-band tight-binding model for monolayers of group-VIB transition metal dichalcogenides. *Phys. Rev. B*, 88:085433, 2013.

[94] Ning Lu, Hongyan Guo, Lei Li, Jun Dai, Lu Wang, Wai-Ning Mei, Xiaojun Wu, and Xiao Cheng Zeng. MoS_2/MX_2 heterobilayers: bandgap engineering via tensile strain or external electrical field. *Nanoscale*, 6:2879, 2014.

[95] C.H. Lui, A.J. Frenzel, D.V. Pilon, Y.-H. Lee, X. Ling, G.M. Akselrod, J. Kong, and N. Gedik. Trion-Induced Negative Photoconductivity in Monolayer MoS_2. *Phys. Rev. Lett.*, 113:166801, 2014.

[96] G.G. Macfarlane, T.P. McLean, J.E. Quarrington, and V. Roberts. Exciton and phonon effects in the absorption spectra of germanium and silicon. *J. Phys. Chem. Solids*, 8:388, 1959.

[97] Cong Mai, Andrew Barrette, Yifei Yu, Yuriy G. Semenov, Ki Wook Kim, Linyou Cao, and Kenan Gundogdu. Many-Body Effects in Valleytronics: Direct Measurement of Valley Lifetimes in Single-Layer MoS_2. *Nano Lett.*, 14:202, 2014.

[98] Cong Mai, Yuriy G. Semenov, Andrew Barrette, Yifei Yu, Zhenghe Jin, Linyou Cao, Ki Wook Kim, and Kenan Gundogdu. Exciton valley relaxation in a single layer of WS_2 measured by ultrafast spectroscopy. *Phys. Rev. B*, 90:041414(R), 2014.

[99] Kin Fai Mak, Keliang He, Changgu Lee, Gwan Hyoung Lee, James Hone, Tony F. Heinz, and Jie Shan. Tightly bound trions in monolayer MoS_2. *Nature Mat.*, 12:207–211, 2013.

[100] Kin Fai Mak, Keliang He, Jie Shan, and Tony F. Heinz. Control of valley polarization in monolayer MoS_2 by optical helicity. *Nat. Nano.*, 7:494, 2012.

[101] Kin Fai Mak, Changgu Lee, James Hone, Jie Shan, and Tony F. Heinz. Atomically Thin MoS_2: A New Direct-Gap Semiconductor. *Phys. Rev. Lett.*, 105:136805, 2010.

[102] Ermin Malic, Malte Selig, Maja Feierabend, Samuel Brem, Dominik Christiansen, Florian Wendler, Andreas Knorr, and Gunnar Berghäuser. Dark excitons in transition metal dichalcogenides. *Phys. Rev. Mat.*, 2:014002, 2018.

[103] A. Manassen, E. Cohen, A. Ron, and E. Linder L.N. Pfeiffer. Exciton and trion spectral line shape in the presence of an electron gas in GaAs/AlAs quantum wells. *Phys. Rev. B*, 54(15):10609, 1996.

[104] M. Manca, M.M. Glazov, C. Robert, F. Cadiz, T. Taniguchi, K. Watanabe, E. Courtade, T. Amand, P. Renucci, X. Marie, G. Wang, and B. Urbaszek. Enabling valley selective exciton scattering in monolayer WSe_2 through upconversion. *Nat. Commun.*, 8:14927, 2017.

[105] A. Manoogian and A. Leclerc. Determination of the dilation and vibrational contributions to the energy band gaps in germanium and silicon. *Phys. stat. solid.*, 92:K23, 1979.

[106] Toshio Matsusue and Hiroyuki Sakaki. Radiative recombination coefficient of free carriers in GaAs-AlGaAs quantum wells and its dependence on temperature . *Appl. Phys. Lett.*, 50:1429, 1987.

[107] Kathleen M. McCreary, Aubrey T. Hanbicki, Saujan V. Sivaramb, and Berend T. Jonker. A- and B-exciton photoluminescence intensity ratio as a measure of sample quality for transition metal dichalcogenide monolayers . *APL Materials*, 6:111106, 2018.

[108] Bastian Miller, Alexander Steinhoff, Borja Pano, Julian Klein, Frank Jahnke, Alexander Holleitner, and Ursula Wurstbauer. Long-Lived Direct and Indirect Interlayer Excitons in van der Waals Heterostructures. *Nano Lett.*, 17:5229, 2017.

[109] G. Moody, C. K. Dass, K. Hao, C.-H. Chen, L.-J. Li, A. Singh, K. Tran, G. Clark, X. Xu, G. Berghäuser, E. Malic, A. Knorr, and X. Li. Intrinsic homogeneous linewidth and broadening mechanisms of excitons in monolayer transition metal dichalcogenides. *Nat. Comm.*, 6:8315, 2015.

[110] Galan Moody. *Confinement Effects on the Electronic and Optical Properties of Semiconductor Quantum Dots Revealed with Two-Dimensional Coherent Spectroscopy.* PhD thesis, University of Colorado, 2013.

[111] Galan Moody, Chandriker Kavir Dass, Kai Hao, Chang-Hsiao Chen, Lain-Jong Li, Akshay Singh, Kha Tran, Genevieve Clark, Xiaodong Xu, Gunnar Berghäuser, Ermin Malic, Andreas Knorr, and Xiaoqin Li. Intrinsic homogeneous linewidth and broadening mechanisms of excitons in monolayer transition metal dichalcogenides. *Nature Commun.*, 6:8315, 2015.

[112] Shaul Mukamel. *Principles of nonlinear optical spectroscopy.* Oxford Univ. Press, 1995.

[113] S. B. Nam, D. C. Reynolds, C. W. Litton, R. J. Almassy, T. C. Collins, and C. M. Wolfe. Free-exciton energy spectrum in GaAs. *Phys. Rev. B*, 13:761, 1976.

[114] K. S. Novoselov, D. Jiang, F. Schedin, T. J. Booth, V. V. Khotkevich, S. V. Morozov, and A. K. Geim. Two-dimensional atomic crystals. *PNAS*, 102:10451, 2005.

[115] K. P. O'Donnell and X. Chen. Temperature dependence of semiconductor band gaps. *Appl. Phys. Lett.*, 58:2924, 1991.

[116] Nina Owschimikow, Mirco Kolarczik, Y. I. Kaptan, Nicolai B. Grosse, and Ulrike Woggon. Crossed excitons in a semiconductor nanostructure of mixed dimensionality. *Appl. Phys. Lett.*, 105:101108, 2014.

[117] R. Pässler. Parameter Sets Due to Fittings of the Temperature Dependencies of Fundamental Bandgaps in Semiconductors. *Phys. Stat. Sol.*, 216:975, 1999.

[118] Bo Peng, Hao Zhang, Hezhu Shao, Yuchen Xu, Xiangchao Zhang, and Heyuan Zhu. Thermal conductivity of monolayer MoS_2, $MoSe_2$, and WS_2: interplay of mass effect, interatomic bonding and anharmonicity. *RSC Adv.*, 6:5767, 2016.

[119] Aurélie Pierret, Hans Tornatzky, and Janina Maultzsch. Anti-Stokes Photoluminescence of Monolayer WS_2. *Phys. Stat. Solid. b*, 256:1900419, 2019.

[120] Gerd Plechinger, Philipp Nagler, Julia Kraus, Nicola Paradiso, Christoph Strunk, Christian Schüller, and Tobias Korn. Identification of excitons, trions and biexcitons in single-layer WS_2. *Phys. Status Solidi RRL*, 9:457, 2015.

[121] Eva A. A. Pogna, Margherita Marsili, Domenico De Fazio, Stefano Dal Conte, Cristian Manzoni, Davide Sangalli, Duhee Yoon, Antonio Lombardo, Andrea C. Ferrari, Andrea Marini, Giulio Cerullo, and Deborah Prezzi. Photo-Induced Bandgap Renormalization Governs the Ultrafast Response of Single-Layer MoS_2. *ACS Nano*, 10:1182, 2016.

[122] M. T. Portella-Oberli, J. Berney, L. Kappei, F. Morier-Genoud, J. Szczytko, and B. Deveaud-Plédran. Dynamics of Trion Formation in $In_xGa_{1-x}As$ Quantum Wells. *Phys. Rev. Lett.*, 102:096402, 2009.

[123] M. T. Portella-Oberli, V. Ciulin, S. Haacke, J.-D. Ganière, P. Kossacki, M. Kutrowski, T. Wojtowicz, and B. Deveaud. Diffusion, localization, and dephasing of trions and excitons in CdTe quantum wells. *Phys. Rev. B*, 66:155305, 2002.

[124] Diana Y. Qiu, Felipe H. da Jornada, and Steven G. Louie. Optical Spectrum of MoS_2: Many-Body Effects and Diversity of Exciton States. *Phys. Rev. Lett.*, 111:216805, 2013.

[125] B. Radisavljevic, A. Radenovic, J. Brivio, V. Giacometti, and A. Kis. Single-layer MoS2 transistors. *Nature Nano.*, 6:147, 2011.

[126] Archana Raja, Malte Selig, Gunnar Berghäuser, Jaeeun Yu, Heather M. Hill, Albert F. Rigosi, Louis E. Brus, Andreas Knorr, Tony F. Heinz, Ermin Malic, and Alexey Chernikov. Enhancement of Exciton-Phonon Scattering from Monolayer to Bilayer WS_2. *Nano. Lett.*, 18:6135, 2018.

[127] Ashwin Ramasubramaniam. Large excitonic effects in monolayers of molybdenum and tungsten dichalcogenides. *Phys. Rev. B*, 86:115409, 2012.

[128] Filip A. Rasmussen and Kristian S. Thygesen. Computational 2D Materials Database: Electronic Structure of Transition-Metal Dichalcogenides and Oxides. *J. Phys. Chem. C*, 119(23):13169, 2015.

[129] N. M. Ravindra and V. K. Srivastava. Temperature dependence of the energy gap in semiconductors. *J. Phys. Chem. Solids.*, 40(10):791, 1979.

[130] Ali Hussain Reshak and Sushil Auluck. Band structure and optical response of 2H-MoX_2 compounds (X= S, Se, and Te). *Phys. Rev. B*, 71:155114, 2005.

[131] Albert F. Rigosi, Heather M. Hill, Yilei Li, Alexey Chernikov, and Tony F. Heinz. Probing Interlayer Interactions in Transition Metal Dichalcogenide Heterostructures by Optical Spectroscopy: MoS_2/WS_2 and $MoSe_2/ WSe_2$. *Nano Lett.*, 15:5033, 2015.

[132] D. Robart, X.Marie, B. Baylac, T. Amand, M. Brousseau, G. Bacquet, G. Debart, R. Planel, and J.M. Gerard. Dynamical equilibrium between excitons and free carriers in quantum wells. *Solid State Commun.*, 95:287, 1995.

[133] C. Robert, D. Lagarde, F. Cadiz, G. Wang, B. Lassagne, T. Amand, A. Balocchi, P. Renucci, S. Tongay, B. Urbaszek, and X. Marie. Exciton radiative lifetime in transition metal dichalcogenide monolayers. *Phys. Rev. B*, 93:205423, 2016.

[134] C. Robert, R. Picard, D. Lagarde, G. Wang, J. P. Echeverry, F. Cadiz, P. Renucci, A. Högele, T. Amand, X. Marie, I. C. Gerber, and B. Urbaszek. Excitonic properties of semiconducting monolayer and bilayer $MoTe_2$. *Phys. Rev. B*, 94:155425, 2016.

[135] Rafael Roldàn, Jose A. Silva-Guillén, M. Pilar Lòpez-Sancho, Francisco Guinea, Emmanuele Cappelluti, and Pablo Ordejón. Electronic properties of single-layer and multilayer transition metal dichalcogenides MX_2 (M = Mo, W and X = S, Se) . *Phys. Rev. B*, 526:347, 2014.

[136] Arza Ron, H.W. Yoon, M.D. Sturge, A. Manassen, E. Cohen, and L.N. Pfeiffer. Thermodynamics of free trions in mixed type GaAsAlAs quantum wells. *Solid State Commun.*, 97:741, 1996.

[137] Jason S. Ross, Sanfeng Wu, Hongyi Yu, Nirmal J. Ghimire, Aaron M. Jones, Grant Aivazian, Jiaqiang Yan, David G. Mandrus, Di Xiao, Wang Yao, and Xiaodong Xu. Electrical control of neutral and charged excitons in a monolayer semiconductor. *Nature Commun.*, 4:1474, 2013.

[138] Anupam Roy, Hema C. P. Movva, Biswarup Satpati, Kyounghwan Kim, Rik Dey, Amritesh Rai, Tanmoy Pramanik, Samaresh Guchhait, Emanuel Tutuc, and Sanjay K. Banerjee. Structural and Electrical Properties of $MoTe_2$ and $MoSe_2$ Grown by Molecular Beam Epitaxy. *ACS Appl. Mater. Interfaces*, 8:7396, 2016.

[139] S. Rudin, T. L. Reinecke, and B.Segall. Temperature-dependent exciton linewidths in semiconductors. *Phys. Rev. B*, 42:17, 1990.

[140] Claude Rullière. *Femptosecond Laser Pulses: Principles and Experiments*. Springer Science and Bisiness, 2005.

[141] Claudia Ruppert, Ozgur Burak Aslan, and Tony F. Heinz. Optical Properties and Band Gap of Single- and Few-Layer $MoTe_2$ Crystals. *Nano Lett.*, 14(11):6231, 2014.

[142] Claudia Ruppert, Alexey Chernikov, Heather M. Hill, Albert F. Rigosi, and Tony F. Heinz. The Role of Electronic and Phononic Excitation in the Optical Response of Monolayer WS2 after Ultrafast Excitation. *Nano Lett.*, 17:644, 2017.

[143] G. Sallen, L. Bouet, X. Marie, G. Wang, C.R. Zhu, W.P. Han, Y. Lu, P.H. Tan, T. Amand, B.L. Liu, and B. Urbaszek. Robust optical emission polarization in MoS_2 monolayers through selective valley excitation. *Phys. Rev. B*, 86:081301(R), 2012.

[144] D. Sanvitto, R.A. Hogg, A.J. Shields, M.Y. Simmons, D.A. Ritchie, and M. Pepper. Formation and Recombination Dynamics of Charged Excitons in a GaAs Quantum Well. *Phys. stat. solid. b*, 227:297, 2001.

[145] Robert Schmidt, Gunnar Berghäuser, Robert Schneider, Malte Selig, Philipp Tonndorf, Ermin Malic, Andreas Knorr, Steffen Michaelis de Vasconcellos, and Rudolf Bratschitsch. Ultrafast Coulomb-Induced Intervalley Coupling in Atomically Thin WS_2. *Nano Lett.*, 16:5, 2016.

[146] Lorenz Maximilian Schneider, Jan Kuhnert, Simon Schmitt, Wolfram Heimbrodt, Ulrich Huttner, Lars Meckbach, Tineke Stroucken, Stephan W. Koch, Shichen Fu, Xiaotian Wang, Kyungnam Kang, Eui-Hyeok Yang, and Arash Rahimi-Iman. Spin-Layer and Spin-Valley Locking in CVD-Grown AA'- and AB-Stacked Tungsten-Disulfide Bilayers. *J. Phys. Chem. C*, 123:21813, 2019.

[147] Giovanni Scuri, You Zhou, Alexander A. High, Dominik S. Wild, Chi Shu, Kristiaan De Greve, Luis A. Jauregui, Takashi Taniguchi, Kenji Watanabe, Philip Kim, Mikhail D. Lukin, and Hongkun Park. Large Excitonic Reflectivity of Monolayer $MoSe_2$ Encapsulated in Hexagonal Boron Nitride. *Phys. Rev. Lett.*, 120:037402, 2018.

[148] M. Selig, G. Berghäuser, A. Raja, P. Nagler, C. Schüller, T. F. Heinz, T. Korn, A. Chernikov, E. Malic, and A. Knorr. Excitonic linewidth and coherence lifetime in monolayer transition metal dichalcogenides. *Nat. Comm.*, 7:13279, 2016.

[149] Malte Selig, Florian Katsch, Robert Schmidt, Steffen Michaelis de Vasconcellos, Rudolf Bratschitsch, Ermin Malic, and Andreas Knorr. Ultrafast dynamics in monolayer transition metal dichalcogenides: Interplay of dark excitons, phonons, and intervalley exchange. *Phys. Rev. Res.*, 1:022007, 2019.

[150] 2D Semiconductor. 2Dsemiconductors Inc., 2019.

[151] J.Hun Seol, Insun Jo, Arden L. Moore, Lucas Lindsay, Zachary H. Aitken, Michael T. Pettes, Xuesong Li, Zhen Yao, Rui Huang, David Broido, Natalio Mingo, Rodney S. Ruoff, and Li Shi. Two-Dimensional Phonon Transport in Supported Graphene. *Science*, 328:213, 2010.

[152] R. A. Sergeev, R. A. Suris, G. V. Astakhov, W. Ossau, and D. R. Yakovlev. Universal estimation of X^- trion binding energy in semiconductor quantum wells. *Eur. Phys. J. B*, 47:541, 2005.

[153] W. Z. Shen and S. C. Shen. Exciton-longitudinal-optical phonon coupling in quantum wells. *Infrared Phys. Technol*, 37:655, 1996.

[154] Hongyan Shi, Rusen Yan, Simone Bertolazzi, Jacopo Brivio, Bo Gao, Andras Kis, Debdeep Jena, Huili Grace Xing, and Libai Huang. Exciton Dynamics in Suspended Monolayer and Few-Layer MoS_2 2D Crystals. *ACS Nano*, 7:1072, 2013.

[155] Hajime Shibata. Negative Thermal Quenching Curves in Photoluminescence of Solids. *Jpn. J. Appl. Phys.*, 37:550, 1998.

[156] S. Shree, M. Semina, C. Robert, B. Han, T. Amand, A. Balocchi, M. Manca, E. Courtade, X. Marie, T. Taniguchi, K. Watanabe, M. M. Glazov, and B. Urbaszek. Exciton-phonon coupling in $MoSe_2$ monolayers. *arXiv*, page 1804.06340v1, 2018.

[157] Akshay Singh, Galan Moody, Kha Tran, Marie E. Scott, Vincent Overbeck, Gunnar Berghäuser, John Schaibley, Edward J. Seifert, Dennis Pleskot, Nathaniel M. Gabor, Jiaqiang Yan, David G. Mandrus, Marten Richter, Ermin Malic, Xiaodong Xu, and

Xiaoqin Li. Trion formation dynamics in monolayer transition metal dichalcogenides. *Phys. Rev. B*, 93:041401, 2016.

[158] Akshay Singh, Galan Moody, Sanfeng Wu, Yanwen Wu, Nirmal J. Ghimire, Jiaqiang Yan, David G. Mandrus, and Xiaoqin Li. Coherent Electronic Coupling in Atomically Thin $MoSe_2$. *Phys. Rev. Lett.*, 114:216504, 2014.

[159] Akshay Singh, Kha Tran, Mirco Kolarczik, Joe Seifert, Yiping Wang, Kai Hao, Dennis Pleskot, Nathaniel M. Gabor, Sophia Helmrich, Nina Owschimikow, Ulrike Woggon, and Xiaoqin Li. Long-Lived Valley Polarization of Intravalley Trions in Monolayer WSe_2. *Phys. Rev. Lett.*, 117:257402, 2016.

[160] Rohan Singh, Marten Richter, Galan Moody, Mark E. Siemens, Hebin Li, and Steven T. Cundiff. Localization dynamics of excitons in disordered semiconductor quantum wells. *Phys. Rev. B*, 95:235307, 2017.

[161] Yang Song and Hanan Dery. Transport Theory of Monolayer Transition-Metal Dichalcogenides through Symmetry. *Phys. Rev. Lett.*, 111:026601, 2013.

[162] Andrea Splendiani, Liang Sun, Yuanbo Zhang, Tianshu Li, Jonghwan Kim, Chi-Yung Chim, Giulia Galli, and Feng Wang. Emerging Photoluminescence in Monolayer MoS_2. *Nano Lett.*, 10:1271, 2010.

[163] Vivek Srinivas, John Hryniewicz, Yung Jui Chen, and Colin E.C. Wood. Intrinsic linewidths and radiative lifetimes of free excitons in GaAs quantum wells. *Phys. Rev. B*, 46(16):10193, 1992.

[164] A. Steinhoff, J.-H. Kim, F. Jahnke, M. Rösner, D.-S. Kim, C. Lee, G. H. Han, M. S. Jeong, T. O. Wehling, and C. Gies. Efficient Excitonic Photoluminescence in Direct and Indirect Band Gap Monolayer MoS_2. *Nano Lett.*, 15(10):6841, 2015.

[165] A. Steinhoff, J.-H. Kim, F. Jahnke, M. Rösner, D.-S. Kim, C. Lee, G. H. Han, M. S. Jeong, T. O. Wehling, and C. Gies. Efficient Excitonic Photoluminescence in Direct and Indirect Band Gap Monolayer MoS_2. *Nano Lett.*, 15:6841, 2015.

[166] Alexander Steinhoff, Matthias Florian, Akshay Singh, Kha Tran, Mirco Kolarczik, Sophia Helmrich, Alexander W. Achtstein, Ulrike Woggon, Nina Owschimikow, Frank Jahnke, and Xiaoqin Li. Biexciton fine structure in monolayer transition metal dichalcogenides. *Nature Phys.*, 14:1199, 2018.

[167] Frank Stern. Calculated Temperature Dependence of Mobility in Silicon Inversion Layers. *Phys. Rev. Lett.*, 44:1469, 1980.

[168] Dezheng Sun, Yi Rao, Georg A. Reider, Gugang Chen, Yumeng You, Louis Brézin, Avetik R. Harutyunyan, and Tony F. Heinz. Observation of Rapid Exciton Exciton Annihilation in Monolayer Molybdenum Disulfide. *Nano Lett.*, 14:5625, 2014.

[169] Yan Sun, Junpei Zhang, Zongwei Ma, Cheng Chen, Junbo Han, Fangchu Chen, Xuan Luo, Yuping Sun, and Zhigao Sheng. The Zeeman splitting of bulk 2H-$MoTe_2$ single crystal in high magnetic field. *Appl. Phys. Lett.*, 110:102102, 2017.

[170] Michael Titze, Bo Li, Xiang Zhang, Pulickel M. Ajayan, and Hebin Li. Intrinsic coherence time of trions in monolayer $MoSe_2$ measured via two-dimensional coherent spectroscopy. *Phys. Rev. Mater.*, 2:054001, 2018.

[171] Sefaattin Tongay, Jian Zhou, Can Ataca, Kelvin Lo, Tyler S. Matthews, Jingbo Li, Jeffrey C. Grossman, and Junqiao Wu. Thermally Driven Crossover from Indirect toward Direct Bandgap in 2D Semiconductors: $MoSe_2$ versus MoS_2. *Nano Lett.*, 12(11):5576, 2012.

[172] Philipp Tonndorf, Robert Schmidt, Philipp Böttger, Xiao Zhang, Janna Börner, Andreas Liebig, Manfred Albrecht, Christian Kloc, Ovidiu Gordan, Dietrich R. T. Zahn, Steffen Michaelis de Vasconcellos, and Rudolf Bratschitsch. Photoluminescence emission and Raman response of monolayer MoS_2, $MoSe_2$, and WSe_2. *Opt. Express*, 21(4):4908, 2013.

[173] Hans Tornatzky, Anne-Marie Kaulitz, and Janina Maultzsch. Resonance Profiles of Valley Polarization in Single-Layer MoS_2 and $MoSe_2$. *Phys. Rev. Lett.*, 121:167401, 2018.

[174] Kha Tran, Galan Moody, Fengcheng Wu, Xiaobo Lu, Junho Choi, Kyounghwan Kim, Amritesh Rai, Daniel A. Sanchez, Jiamin Quan, Akshay Singh, Jacob Embley, André Zepeda, Marshall Campbell, Travis Autry, Takashi Taniguchi, Kenji Watanabe, Nanshu Lu, Sanjay K. Banerjee, Kevin L. Silverman, Suenne Kim, Emanuel Tutuc, Li Yang, Allan H. MacDonald, and Xiaoqin Li. Evidence for moiré excitons in van der Waals heterostructures. *Nature*, 567:71, 2019.

[175] D. Valerini, A. Creti, M. Lomascolo, L. Manna, R. Cingolani, and M. Anni. Temperature dependence of the photoluminescence properties of colloidal CdSe/ZnS core/shell quantum dots embedded in a polystyrene matrix. *Phys. Rev. B*, 71:235409, 2005.

[176] Y. P. Varshni. Temperature dependence of the energy gap in semiconductors. *Physica*, 34(1):149, 1967.

[177] L. Viña, S. Logothetidis, and M. Cardona. Temperature dependence of the dielectric function of germanium. *Phys. Rev. B*, 30(4):1979, 1984.

[178] Y. Wan, H. Zhang, K. Zhang, Y. Wang, B. Sheng, X. Wang, and L. Dai. Large-Scale Synthesis and Systematic Photoluminescence Properties of Monolayer MoS_2 on Fused Silica. *ACS Appl. Mater. Interfaces*, 8:18570, 2016.

[179] G. Wang, L. Bouet, M.M. Glazov, T. Amand, E.L. Ivchenko, E. Palleau, X. Marie, and B. Urbaszek. Magneto-optics in transition metal diselenide monolayers. *2D Mater.*, 2(3):034002, 2015.

[180] G. Wang, I. C. Gerber, L. Bouet, D. Lagarde, A. Balocchi, M. Vidal, T. Amand, X. Marie, and B. Urbaszek. Exciton states in mololayer $MoSe_2$: impact on interband transitions. *2D Mater.*, 2(4):045005, 2015.

[181] G. Wang, M. M. Glazov, C. Robert, T. Amand, X. Marie, and B. Urbaszek. Double Resonant Raman Scattering and Valley Coherence Generation in Monolayer WSe_2. *Phys. Rev. Lett.*, 115:117401, 2015.

[182] G. Wang, X. Marie, I. Gerber, T. Amand, D. Lagarde, L. Bouet, M. Vidal, A. Balocchi, and B. Urbaszek. Giant Enhancement of the Optical Second-Harmonic Emission of WSe_2 Monolayers by Laser Excitation at Exciton Resonances. *Phys. Rev. Lett.*, 114:097403, 2015.

[183] G. Wang, E. Palleau, T. Amand, S. Tongay, X. Marie, and B. Urbaszek. Polarization and time-resolved photoluminescence spectroscopy of excitons in MoS_2 monolayers. *Appl. Phys. Lett.*, 106(11):112101, 2015.

[184] Haining Wang, Changjian Zhang, and Farhan Rana. Ultrafast Dynamics of Defect-Assisted Electron-Hole Recombination in Monolayer MoS_2. *Nano Lett.*, 1:339, 2015.

[185] Qinsheng Wang, Shaofeng Ge, Xiao Li, Jun Qiu, Yanxin Ji, Ji Feng, and Dong Sun. Valley Carrier Dynamics in Monolayer Molybdenum Disulfide from Helicity-Resolved Ultrafast Pump-Probe Spectroscopy. *ACS Nano*, 7(12):11087, 2013.

[186] Yu-Ting Wang, Chih-Wei Luo, Atsushi Yabushita, Kaung-Hsiung Wu, Takayoshi Kobayashi, Chang-Hsiao Chen, and Lain-Jong Li. Ultrafast Multi-Level Logic Gates with Spin-Valley Coupled Polarization Anisotropy in Monolayer MoS_2. *Sci. Rep.*, 5:8289, 2015.

[187] Jakob Wierzbowski, Julian Klein, Florian Sigger, Christian Straubinger, Malte Kremser, Takashi Taniguchi, Kenji Watanabe, Ursula Wurstbauer, Alexander W. Holleitner, Michael Kaniber, Kai Müller, and Jonathan J. Finley. Direct exciton emission from atomically thin transition metal dichalcogenide heterostructures near the lifetime limit. *Sci. Rep.*, 7:12383, 2017.

[188] J. A. Wilson and A. D. Yoffe. The transition metal dichalcogenides discussion and interpretation of the observed optical, electrical and structural properties. *Advances in Physics*, 18:193, 1969.

[189] Di Xiao, Gui-Bin Liu, Wanxiang Feng, Xiaodong Xu, and Wang Yao. Coupled Spin and Valley Physics in Monolayers of MoS_2 and Other Group-VI Dichalcogenides. *Phys. Rev. Lett.*, 108:196802, 2012.

[190] Di Xiao, Wang Yao, and Qian Niu. Electrical tuning of valley magnetic moment through symmetry control in bilayer MoS_2. *Nature Phys.*, 9:149, 2013.

[191] Di Xiao, Wang Yao, and Qian Niu. Valley contrasting physics in graphene: magnetic moment and topological transport. *Phys. Rev. Lett.*, 99:236809, 2014.

[192] Xiaodong Xu, Wang Yao, Di Xiao, and Tony F. Heinz. Spin and pseudospins in layered transition metal dichalcogenides. *Nature Physics*, 10:343, 2014.

[193] Jiong Yang, Tieyu Lü, Ye W. Myint, Jiajie Pei, Daniel Macdonald, Jin-Cheng Zheng, and Yuerui Lu. Robust Excitons and Trions in Monolayer $MoTe_2$. *ACS Nano*, 9(6):6603, 2015.

[194] Wang Yao, Di Xiao, and Qian Niu. Valley-dependent optoelectronics from inversion symmetry breaking. *Phys. Rev. B*, 77:235406, 2008.

[195] Jialiang Ye, Ying Li, Tengfei Yan, Guihao Zhai, and Xinhui Zhang. Ultrafast Dynamics of Spin Generation and Relaxation in Layered WSe_2. *J Phys. Chem. Lett.*, 10:2963, 2019.

[196] Jialiang Ye, Tengfei Yan, Binghui Niu, Ying Li, and Xinhui Zha. Nonlinear dynamics of trions under strong optical excitation in monolayer $MoSe_2$. *Sci. Rep.*, 8:2389, 2018.

[197] Hongyi Yu, Gui-Bin Liu, Pu Gong, Xiaodong Xu, and Wang Yao. Dirac cones and Dirac saddle points of bright excitons in monolayer transitionmetal dichalcogenides. *Nat. Commun.*, 5:3876, 2014.

[198] Peter Y. Yu and Manuel Cardona. *Fundamentals of Semiconductors: Physics and Materials Properties*. Springer-Verlag Berlin Heidelberg, 2010.

[199] T. Yu and M. W. Wu. Valley depolarization due to intervalley and intravalley electron-hole exchange interactions in monolayer MoS_2. *Phys. Rev. B*, 89:205303, 2014.

[200] Won Seok Yun, S. W. Han, Soon Cheol Hong, In Gee Kim, and J. D. Lee. Thickness and strain effects on electronic structures of transition metal dichalcogenides: 2H-MX_2 semiconductors (M = Mo, W; X = S, Se, Te). *Phys. Rev. B*, 85:033305, 2012.

[201] Won Seok Yun, S. W. Han, Soon Cheol Hong, In Gee Kim, and J. D. Lee. Thickness and strain effects on electronic structures of transition metal dichalcogenides: 2H-MX_2 semiconductors (M = Mo, W; X = S, Se, Te). *Phys. Rev. B*, 85:033305, 2012.

[202] Hualing Zeng, Junfeng Dai, Wang Yao, Di Xiao, and Xiaodong Cui. Valley polarization in MoS_2 monolayers by optical pumping. *Nat. Nano.*, 7:490, 2012.

[203] Changjian Zhang, Haining Wang, Weimin Chan, Christina Manolatou, and Farhan Rana. Absorption of light by excitons and trions in monolayers of metal dichalcogenide MoS_2: Experiments and theory. *Phys. Rev. B*, 89:205436, 2014.

[204] Wenxu Zhang, Zhishuo Huang, Wanli Zhang, and Yanrong Li. Two-dimensional semiconductors with possible high room temperature mobility . *Nano Research*, 7:1731, 2014.

[205] Yi Zhang, Tay-Rong Chang, Bo Zhou, Yong-Tao Cui, Hao Yan, Zhongkai Liu, Felix Schmitt, James Lee, Rob Moore, Yulin Chen, Hsin Lin, Horng-Tay Jeng, Sung-Kwan Mo, Zahid Hussain, Arun Bansil, and Zhi-Xun Shen. Direct observation of the transition from indirect to direct bandgap in atomically thin epitaxial $MoSe_2$. *Nature Nano.*, 9:111, 2014.

[206] Youwei Zhang, Hui Li, Haomin Wang, Ran Liu, Shi-Li Zhang, and Zhi-Jun Qiu. On Valence-Band Splitting in Layered MoS_2. *ACS Nano*, 9(8):8514, 2015.

[207] Weijie Zhao, R. M. Ribeiro, M. Tho, A. Carvalho, C. Kloc, A. H. C. Neto, and G. Eda. Origin of Indirect Optical Transitions in Few-Layer MoS_2, WS_2, and WSe_2. *Nano Lett.*, 13(11):5627, 2013.

[208] Bairen Zhu, Hualing Zeng, Junfeng Dai, Zhirui Gong, and Xiaodong Cui. Anomalously robust valley polarization and valley coherence in bilayer WS_2. *PNAS*, 111:11606, 2014.

[209] Z. Y. Zhu, Y. C. Cheng, and U. Schwingenschlögl. Giant spin-orbit-induced spin splitting in two-dimensional transition-metal dichalcogenide semiconductors. *Phys. Rev. B*, 84:153402, 2011.

Statement of Authorship

I hereby certify that this thesis has been composed by myself, and describes my own work, unless otherwise acknowledged in the text. All references and verbatim extracts have been quoted, and all sources of information have been specifically acknowledged. It has not been accepted in any previous application for a degree.

After positive appraisal of this thesis, I agree that one copy of my presented thesis may remain at the disposal of the library of Technical University of Berlin.

Berlin, 12 March 2020